UNIVERSITY OF DUBLIN, TRINITY COLLEGE

DOCTORAL THESIS

Carbon Nanomaterials for Improved Performance of Perovskite Solar Cells Processed under High Humidity

---

Author:
John James Magan

Supervisor:
Werner Blau

A thesis submitted in fulfilment of the requirements
for the degree of Doctor of Philosophy
in the

School of Physics

2019

Declaration

I declare that this thesis has not been submitted as an exercise for a degree at this or any other university and it is entirely my own work.

I agree to deposit this thesis in the University's open access institutional repository or allow the library to do so on my behalf, subject to Irish Copyright Legislation and use and acknowledgement.

Elements of this work that have been carried out jointly with others or by collaborators have been duly acknowledged in the text wherever included.

Signed:

_____

Date:

_____

"I believe there is no philosophical high-road in science, with epistemological signposts. No, we are in a jungle and find our way by trial and error, building our road behind us as we proceed."

Max Born (1882-1970)

"Civilization is in a race between education and catastrophe. Let us learn the truth and spread it as far and wide as our circumstances allow. For the truth is the greatest weapon we have."

H.G. Wells (1866-1946)

Abstract

The work documented in this thesis concerns optimization of stacks of semiconducting materials for photovoltaic purposes. Hybrid organic-inorganic metal halide perovskite (MHP) is a promising semiconducting material for thin film solar cells, offering both high solar to electrical energy conversion efficiencies and cheap fabrication costs. However, several issues have so far acted as constraints to development of the technology such as sensitivity of commonly pursued fabrication techniques to atmospheric moisture and use of high temperature-processed porous metal oxides which add to manufacturing costs and are incompatible with high-throughput roll-to-roll processing on flexible substrates. In addition, many of the prototypical charge selective materials used to achieve high performance are known to be inherently reactive with perovskites, especially in the presence of oxygen, moisture and even ultraviolet light in some cases. In order to fully realise the potential of perovskite solar cells it would be extremely advantageous to improve device performance, reproducibility and stability in uncontrolled humid environments; both from the perspective of commercialisation and of rendering the technology accessible to less specialist research labs. Initially, work focuses on finding optimal electron selective materials for planar solution processed perovskite devices under humid conditions. It is found that many of the most commonly used metal oxides are not well suited to the task, presenting large barriers to charge extraction resulting in low photocurrents. In addition, zinc oxide is found to accelerate perovskite decomposition to varying degrees depending on the method used for thin film fabrication. On the other hand, introduction of solution-processed C_{60} as a surface modifier is found to reduce the barrier to charge extraction for all of the metal oxides studied. Consequently, efforts are made to avoid metal oxide electron transport layers (ETLs) by optimizing C_{60}-based ETLs. Thin layers of the polymer polyethyleneimine (PEI) are found to be effective in achieving consistently high photovoltaic conversion efficiencies (PCE) with champion cells delivering over 15.2mW/cm^2 under AM1.5 illumination. Furthermore, these polymer-fullerene bilayers are demonstrated to be versatile ETLs by fabricating flexible photovoltaic devices on ITO-coated PET and PEDOT:PSS-coated PET as well as aluminium-doped zinc oxide (AZO) as a low cost solution-processed alternative to ITO. PEI is also found suitable for stabilizing

graphene at concentrations of approximately 0.66mg/mL in butanol, thereby permitting the deposition PEI-graphene composite films via spin coating. Optimized composites act as an effective barrier to perovskite decomposition whilst maintaining high PCE. Introduction of $PbCl_2$ into perovskite precursor mix improved both photocurrent output and open circuit voltage for devices made using single-step deposited perovskite via solvent-solvent extraction, although two-step deposition ultimately led to less cell-to-cell variability. Addition of 30 weight% lead chloride ($PbCl_2$) is found to be crucial in guaranteeing full perovskite crystallization in highly humid environments, leading to much improved batch-to-batch reproducibility. Higher $PbCl_2$ content is also demonstrated to improve performance of devices based on transparent AZO electrodes deposited by spray pyrolysis. Cells showed good stability, retaining 75% of initial PCE after over 600 hours of storage in ambient without encapsulation. Performance reproducibility issues are also raised regarding the hole transport layer (HTL) P3HT, with carbon nanotube (CNT)-PMMA composite layers found to give consistently high photocurrents. Champion devices with HTL stacks of P3HT / CNT / PMMA delivered a PCE of 16.2% and outperformed P3HT-only HTLs by maintaining 80% of initial PCE after 900 hours. A thicker PEI-C_{60} ETL is also demonstrated to improve device fill factor leading to a stabilized PCE of 15.5% for P3HT-free devices containing only thin CNT-PMMA HTLs. Finally, efforts are made to incorporate graphene as a p-doped material for hole transport.

Acknowledgements

I would like to thank Werner Blau for giving me the opportunity to undertake work as part of his group and for his patience and support. It was very much appreciated.

I am extremely grateful to the generosity and understanding shown to me first by Louise Bradley and then especially by Mauro Ferreira and Marie Kinsella (and Ciara and Susanna in the Finance Office). I cannot thank you enough. Thanks also to Science Foundation Ireland and the School of Physics in particular for financial support.

Another person who really went out of their way for me is Johnny Coleman, his insights were extremely valuable to me and his encouragement helped more than I think he knew.

Yong Zhang was a tremendous help to me in my early days in the group and to him I will always be grateful. Special thanks to Karsten Fleischer for all of the time and effort we went through growing metal oxide films together and to David Caffrey for his help with Hall measurements, four-probe and handling XRD files. A very big thank you also to Ramsankar Senthamaraikannan for his generosity and skill in taking such good SEM images. I only hope that I can repay the debt. Thanks to Georg Duesberg and to all his team for being so friendly, especially John McManus for all of the help with CVD graphene. Thanks to Gwenael Atcheson for sputtering TiO_2 and to Colm McManamon for letting me join his gold evaporation sessions. Also thanks to Cornelia Rodenburg and her team for SEM imaging.

Thank you Gaozhong for being a good friend, willing to help however you can and always with a joke and a smile. Thanks Beata for the many long therapeutic talks we've had over the years and for all of the little ways you've helped me - whether it be sending me papers, bringing back coffee from your travels or giving sound advice generally. Thanks to Katja Zibrek for helping me out in a tough time and to James Creel for his positivity. Thanks to Katarzyna Siewierska for always being so friendly and to Brian Jennings. I am also very grateful to Giulio Brunetti for the coffees and constant encouragement over the last few weeks.

Thanks to Andrew Harvey for his help with UV-vis to Adam Kelly for help with spray coating CNTs and to all of the Coleman group for just being sound in general. It's only a shame that we didn't get to hang out more.

Romina has been a shining light - thank you for the many meaningful talks over the years and for helping me so so much with getting usable data. Not to mention the endless tasty treats (and full meals) you've given me over the years. A warm thank you also to Damien Howard; the best housemate I could have asked for.

Last but not least I must thank my family. To my turbo-charged godmother Antoinette thanks for being a second mother. Much love also to Marie and Bernard for the cards, newspaper clippings and discussions over tea and cake. Mum, whatever good that I am is down to you. I'm very proud to have you as a mother and I'm sorry for all of the stress I've caused you. Dad, I'm still waiting for the day that I don't learn something from you. It may not always seem like it, but I've tried to do you proud. Alex and Isabelle, I love you both and my only regret is that we haven't spent nearly enough time together in recent years - hopefully I can remedy that soon. Finally, to Aisling who was there at the very beginning and especially to Cora who I've had the great fortune to have had as my companion these last couple of years, thank you for the unconditional care and support. I would not have gotten through this without you. I love you long time.

Publications

1. *Intensity-dependent nonlinear refraction of antimonene dispersions in the visible and near-infrared region*, Gaozhong Wang, Sean Higgins, Kangpang Wang, Daniel Bennett, Nina Milosavljevic, John James Magan, Saifeng Zhang, Xiaoyan Zhang, Jun Wang and Werner J. Blau, Appl. Opt. 57, 22, 2018.

2. *Ultrafast Nonlinear Excitation Dynamics of Black Phosphorus Nanosheets from Visible to Mid-Infrared*, Kangpend Wang, Beata Szylowska, Gaozhong Wang, Xiaoyan Zhang, Jing Jing Wang, John J. Magan, Long Zhang, Jonathan Coleman, Jun Wang and Werner J. Blau, ACS Nano, 2016, 10 (7) 2016.

3. *A General Strategy for Hybrid Thin Film Fabrication and Transfer onto Arbitrary Substrates*, Yong Zhang, John J. Magan and Werner J. Blau, Scientific Reports 4, 4822, 2014.

Contents

1 Introduction and Thesis Outline

1.1 Motivation

FIGURE 1.1: View of Earth from the Moon taken during the Apollo 11 mission.

Scientific and technological breakthroughs made in the last couple of centuries have led to an apparent dichotomy in the modern world. On the one hand, humankind has learnt of the interconnectedness of all matter on our tiny fragile world. On the other hand, the tools of science and engineering have largely been used to exploit and destroy in the name of security and progress. There is strong evidence to suggest that humanity is heading for catastrophe. The famous "Doomsday Clock" set by the Bulletin of Atomic Scientists primarily to assess the risk of imminent global destruction by nuclear weapons was set to 2 minutes to midnight in 2018. In addition to increasingly hostile rhetoric by leading politicians and nations' investments in their nuclear arsenals, the perils posed by anthropomorphic climate change was cited as a contributing factor to moving clock to the closest it has ever been

to midnight [1]. It is becoming widely accepted that the Earth is entering a new geological epoch characterised by human activities and domination over its surface, atmosphere, oceans and systems of nutrient cycling [2] [3]. Formalization of the so-called Anthropocene hinges on whether the effects of humans on the biosphere and geosphere are substantial enough to appear in rock strata as many scientists now believe to be the case. Concern stems largely from measurements of global atmospheric carbon dioxide (CO_2) levels. CO_2 is the most important long-lived greenhouse gas (GHG), absorbing thermal infrared energy radiated from the Earth's surface and releasing it gradually. The example of baking temperatures on the surface of Venus illustrates the dangers of a runaway greenhouse effect. In the 1960s Dave Keeling demonstrated annual oscillations in CO_2 superimposed on a rising background which has since come to be known as the Keeling curve as shown at the top of Figure 1.2. Ice core data has revealed that this relentless rise in recent years has resulted in CO_2 levels not seen in over a million years (bottom of Figure 1.2). In fact the last time that global atmospheric CO_2 was at a comparable level was more than 3 million years ago, when global average temperature was 2 °C to 3 °C higher than pre-industrial levels and sea level was 15-25 meters higher than today [4]. There is growing concern from some in the scientific community that the 2 °C "Charney Sensitivity" (response of the climate system to a doubling of CO_2 concentrations including all fast feedbacks) upon which Intergovernmental Panel on Climate Change (IPCC) work is based, is an underestimate. Even the figure of 2 °C has been suggested as being highly dangerous based on a combination of paleoclimate data, climate modelling and modern observations [5]. This conclusion is even more alarming when it is considered that climate sensitivity may vary nonlinearly, being significantly higher during warm phases [6]. Furthermore, in addition to loss of albedo and direct heating as a result of retreating ice sheets, the melting of permafrost may release huge quantities of methane which is itself a much more potent GHG than CO_2 [7]. These factors have so far proven difficult to quantify but that only adds to the conservative nature of predictions made to date. As if this wasn't enough, there are worrying signs that entire ecosystems may be collapsing with for example an estimated loss of between 76% and 82% in flying insect biomass in Germany over the last 27 years [8] prompting talk of Earth's ongoing sixth mass extinction event which may have dire consequences for human civilization [9].

Given the central position of fossil fuels in the global economy, it may be argued that the single most important measure that can be taken to combat the crisis is to replace CO_2 producing fossil fuels with clean sources of energy. Not only is this important from an environmental point of view but also from an economic standpoint as fossil fuels are a finite resource that is being depleted by an ever growing demand for energy. Many countries have

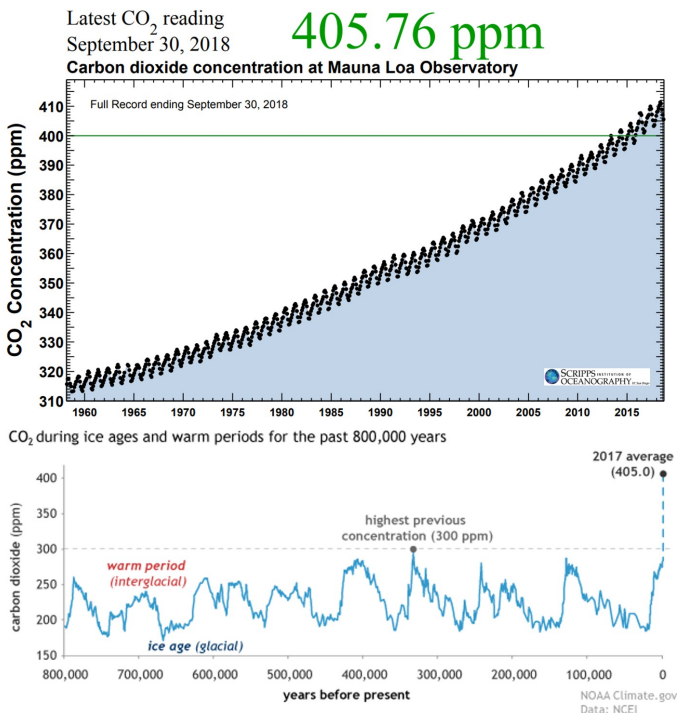

FIGURE 1.2: Variation in atmospheric carbon dioxide levels in parts per million (ppm) over the past 60 years (top) [10] and over the last 800,000 years (bottom) [4].

made pledges to this end, with the Parliament of the European Union for example having recently voted to double Europe's 2015 renewable energy levels by 2030. However, care must be taken in this regard as scientists have warned that the European directive, which treats wood harvested directly for bioenergy use as a carbon-free or carbon-neutral fuel, would likely accelerate deforestation and result in a net increase in atmospheric-CO_2 [11]. Solar and wind energy on the other hand are advocated as more effective alternatives, with solar costs already dropping below $US 0.02/kWh in some locations thereby making it more attractive for electricity generation in particular, even with bioenergy's incorrect GHG accounting [12] [11].

Looking at the energy landscape today, it can be seen that renewables are providing more and more energy with an estimated total contribution in 2017 of 2195 Gigawatts as shown in Figure 1.3. Looking at the breakdown of different technologies it can be seen that most of the growth in recent years has been in the use of solar photovoltaic (PV) and wind power. However, considering renewable energies as a share of global electricity production at the end of 2017 shows that fossil fuels still make up the lion's share of global production with solar PV accounting for less than 2%. This is a highly inefficient situation when one considers that with the exception of geothermal and nuclear fission, the entire spectrum from non-renewable fossil fuels to medium-term renewable biomass and on to renewables

such as wind, wave, tidal, hydro and solar power all ultimately derive their energy from light radiating from the Sun.

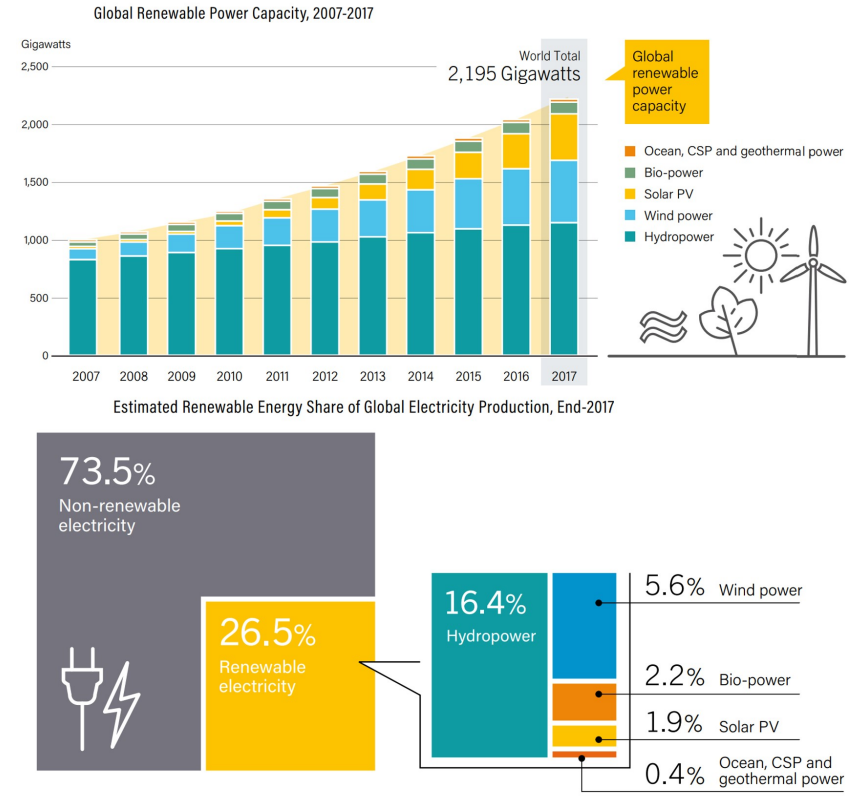

FIGURE 1.3: Global renewable power capacity between 2007 and 2017 (top) and estimated breakdown by energy technology of global electricity production at the end of 2017 (bottom) [13].

It therefore follows that effectively tapping even a modest fraction of the energy contained in sunlight would meet the world's needs. For example, covering just 0.3-0.4% of the Earth's surface with photovoltaic devices operating at a 20% light-to-electricity conversion efficiency would meet current global requirements. Not only is such an efficiency attainable with commercial modules but maximum theoretical efficiencies are as high as 31-33% [14] for what are called single junction devices and efficiencies of 40-43% should be attainable in a so-called "tandem" device by stacking materials in a multi-junction arrangement [15]. Although module costs have dropped substantially in recent decades, high efficiency devices currently available remain expensive to process and fabricate (particularly tandem cells) resulting in long payback times. This is the main factor hampering widespread adoption of solar PV and highlights the need to develop even lower cost solar cells with high efficiencies. In order to achieve this goal, it would be extremely advantageous to use photovoltaic materials that are both abundant and can be dispersed or dissolved in appropriate solvents. In this way, inks or paints of these materials could ultimately be deposited using high throughput

printing techniques which would dramatically lower device fabrication costs.

In recent years, many candidate materials having one or the other of these characteristics to varying degrees have been identified and studied as detailed in Chapter 3. Of these, hybrid organic-inorganic perovskite semiconductors have shown particular promise by combining optoelectronic properties similar to many of the inorganic devices used commercially with easy solution-processability and abundance of their constituent elements. Champion device efficiencies for perovskite solar cells have already surpassed the 20% mark, thereby fulfilling one of the major requirements for commercial application. However, long-term stability of the technology has yet to be definitively demonstrated, with most of the highest efficiencies having been reported using device structures and materials that are inherently reactive upon exposure to moisture, oxygen and light. In addition, sensitivity of the perovskite material to processing conditions (particularly humidity level) has resulted in reliance on carefully controlled environments and glovebox conditions to guarantee high performance. These are both obstacles to rapid commercialisation of the technology. Another family of materials that has been much studied in the field of photovoltaics is that of low dimensional carbon allotropes, as they display many superlative optoelectronic properties in addition to impressive mechanical strength and chemical stability. Much less explored on the other hand is the potential for carbon nanomaterials to enable simple low-temperature fabrication and operation of perovskite devices under ambient (humid) conditions. Atmospheric carbon (in the form of CO_2) is significant danger to the continued existence of organised human life; how fitting it would be if (nanostructured) carbon was also the source of humanity's salvation.

1.2 Thesis outline

Given the needs outlined in the previous section, the work in this thesis will focus on optimizing the performance of planar perovskite solar cells using simple processing techniques in uncontrolled humid conditions. A variety of materials are examined for use in device stacks with the general aim of minimizing fabrication cost. Chapter 2 introduces the principle materials used in devices fabricated over the course of the project. A general overview of the development of photovoltaics is first given before introducing some of the major characteristics and challenges associated with perovskite solar cells. A brief history on the discovery and processing of carbon nanomaterials is then covered as is their applicability towards photovoltaic devices. Chapter 3 explains the physics of charge transport in organic and inorganic materials before introducing the basics of light-matter interactions and the behaviour

at junctions of different materials. The main techniques used to process and characterise devices are also covered. Experimental results are grouped largely by device layer, although some overlap exists between chapters due to the iterative nature of device optimization. Chapter 4 deals with establishing an effective electron accepting and hole-blocking layer for planar devices. Zinc oxide nanoparticles (ZnO-NPs) are first examined as a candidate electron transport layer (ETL) material in low-temperature processed devices. Spray pyrolysis and sputter coating are also considered to deposit ZnO and titanium dioxide (TiO_2) films. Solution-processed C_{60} is also investigated both in conjunction with the metal oxides or simply with thin polymer layers. Liquid-phase exfoliated (LPE) graphene is then studied as a dopant to improve the barrier properties of otherwise insulating polymer layers. Chapter 5 focusses on optimization of solution-processed perovskite films in humid environments. Single-step deposited layers are studied first, varying the ratio between organic and inorganic precursors as well as the halide composition to determine the effect on optical and electrical performance. Chapter 6 looks at improving the hole transport layer by addition of carbon nanotubes. Several methods are developed and implemented to obtain polymer-nanotube composites and the advantages and disadvantages of each relating to devices are discussed. Efforts to p-dope graphene for application as top contact in regular architecture devices are also made. Conclusions from all of the work carried out are drawn in Chapter 7 and used to outline future work.

2 Materials and Background

2.1 Overview of solar cell development

2.1.1 Three generations of photovoltaics

Humans have been harnessing the power of the Sun in various forms for millennia. There are numerous accounts from antiquity of reflective surfaces being used to concentrate sunlight to light fires, such as the famous example of the Greek philosopher Archimedes who used the polished bronze shields of the defenders of Syracuse to set fire to Roman vessels besieging the city in 212BC. However, for most of recorded history the energy extracted from sunlight was restricted to thermalisation processes. In 1839, a young French physicist named Edmond Becquerel reported that an electric current was produced when a silver coated platinum electrode immersed in an electrolyte was exposed to light. This came to be known as the "Photovoltaic Effect". The discovery of photoconductivity of selenium by the English engineer Willoughby Smith in 1873 was followed three years later by the discovery that a photocurrent could be produced from selenium contacted between two heated platinum contacts [16]. Charles Fritts made the first solar photovoltaic cell in 1883 using selenium and over the next decade attempted to demonstrate viability of the technology to compete with coal-fired power plants. However, efficiencies below 1% meant that photovoltaic action would remain little more than a scientific curiosity and attention was instead focused on exploiting the photoconductive effects of selenium and other materials for such applications as photographic light meters. The theory of metal-semiconductor barrier layers was developed by Walter Schottky, Nevill Mott and others during the 1930s. It described the rectifying action that exists at the interface between a metal and a semiconductor such that current flows preferentially in one direction and provided the basis for understanding that all of the early photovoltaic cells were in fact thin film Schottky barrier devices.

The inadvertent discovery of a p-n junction in silicon by Russell Ohl in 1940 led to development of a 6% efficient silicon solar cell by Chapin, Fuller and Pearson fourteen years later in which a thin p-type layer was formed on top of n-type silicon by exposing it to

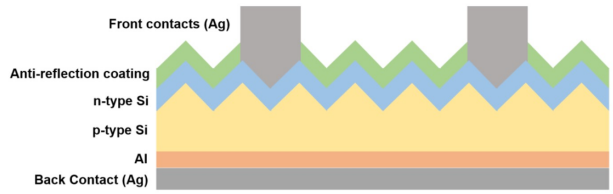

FIGURE 2.1: Simplified cross-section showing the general components of a silicon photovoltaic device.

the gas boron trichloride [17][18]. Solar cell efficiencies rose significantly over the following decades due to the superior photovoltaic behaviour and rectifying characteristics of p-n junctions over Schottky barrier diodes. A simplified cross-section of a typical crystalline silicon (Si) solar cell, as shown in Figure 2.1, consists of relatively thick p-type Si layer (a few μm) coated with a thinner n-type window layer on one side and metallic layers on the other. Photogenerated charges in the Si are separated by an electric field that acts across the junction and are collected by the metallic contacts and used to do work in an external circuit.

However, for many years implementation of the technology was reserved for power generation in remote areas (such as on satellites in space) due to the prohibitively high cost per Watt compared to fossil fuels. The oil crisis in the 1970s spurred the western world to fund alternative methods for energy production and strategies for producing photovoltaic devices more cheaply and with greater conversion efficiency were explored. Benefiting from knowledge and expertise accrued by over half a century of tremendous investment and development of the semiconductor industry, crystalline Si cells now reach record efficiencies of over 25%, approaching the theoretical maximum for a single junction solar cell (32%) known as the Shockley-Queisser limit[14]. In addition, the price of modules has dropped significantly in recent years, reaching (as of 2017) below $3 (US) per watt for residential systems and below $1 for fixed-tilt utility-scale systems[19]. However, gains have been largely due to economies of scale and it is an open question how much further prices can drop and it is quite possible that the cost of producing the high quality silicon needed for devices may prove prohibitive.

As part of the effort to increase the commercial viability of solar energy, a range of alternative photovoltaic technologies have been developed. Devices can now be grouped into one of three generations, the first being those based on silicon. The second generation consists of "thin film" materials (typically $\approx 1\mu$m) such as amorphous silicon, gallium arsenide (GaAs), cadmium telluride (CdTe) and copper indium gallium diselenide (CIGS) as active component. One attractive aspect is that the thinner layers of these materials, made possible by more efficient light absorbance (for reasons discussed in 3), can reduce fabrication costs

and efficiencies for some of these devices are competitive with crystalline silicon. There are, however, other concerns due to the scarcity and toxicity of elements used in these solar cells, hampering widespread adoption.

The third generation of photovoltaics is made up of a broad group of technologies that have the potential to avoid many of the limits associated with the previous generations. In addition to abundance of the raw materials generally used, many of these technologies are solution processable and thus hold great promise in providing extremely low cost devices with high throughput manufacturing. Furthermore, many third generation technologies offer tunability of optoelectronic properties have the potential to surpass the Shockley-Queisser limit by means of physical processes such as multiple exciton generation whereby a single photon excites more than one electron. The main categories comprising third generation photovoltaics will be dealt with in turn in the following sections.

2.2 Organic photovoltaics

As with silicon-based solar technology, the field of organic photovoltaics (OPV) was studied as far back as the 1950s[20], although very low efficiencies were achieved in small organic molecule-based devices owing largely to the fact absorbed photons formed tightly bound excitons (electron-hole pairs) that were far more likely to recombine than dissociate and drive an electric current. A milestone was reached in 1986 with the first "donor-acceptor" device consisting of a bi-layer structure in which a heterojunction between two materials aided exciton dissociation resulting in an efficiency of around 1% [21]. The first polymer solar cells were reported in the early 90s and soon the now popular "bulk heterojunctions" (illustrated on the right of Figure 2.2) emerged as a means to reduce the path length to the interface for any point in the cell and hence increase efficiency. Organic semiconductors can be treated using similar principles as inorganic semiconductors and metals; instead of being excited between conduction and valence bands (as detailed in 3), electrons are excited between the highest occupied molecular orbital (HOMO) and the lowest unoccupied molecular orbital (LUMO).

Unlike small molecules which generally require thermal evaporation for device processing, polymers offer the advantage of more facile solution processability and thus have attracted considerable attention by the research community. However, among the disadvantages of polymers is inherent variation in molecular weight and polydispersity which make

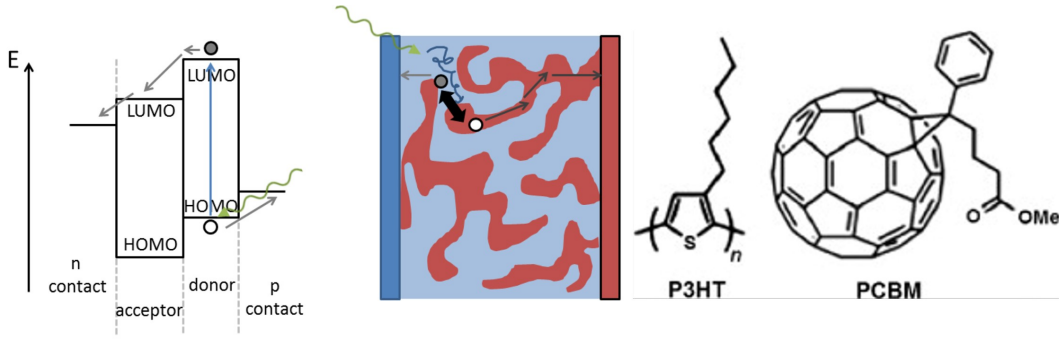

FIGURE 2.2: Representation of energy level diagram (left) and bulk heterojunction (right) with distributed donor (red) and accepter (blue) phases in a typical organic solar cell under illumination. The most studied donor and acceptor materials, P3HT and PCBM are also shown.

batch-to-batch reproducibility difficult[22]. OPVs are typically built in a "bottom illuminated" design in a stack consisting most commonly of an ITO-glass substrate onto which a p-type material is deposited such as the conducting polymer poly(3,4-ethylenedioxythiophene) poly(styrenesulfonate) (PEDOT:PSS) followed by a blend of poly-3-hexyl thiophene (P3HT) as donor and phenyl-C61-butyric acid methyl ester (PCBM) as acceptor with n-type materials like ZnO, LiF or bathocuproine and a metallic cathode. These materials offer the advantages of simple roll-to-roll processing on flexible substrates of low weight semi-transparent devices. However, these cells are limited by the energy required to drive efficient exciton splitting at the interface, resulting in lower efficiencies (generally less than 10%) relative to other technologies. Furthermore, materials tend to be very sensitive to oxygen and moisture both during fabrication and operation resulting in glovebox processing and encapsulation techniques being commonly employed.

2.3 Dye-sensitized solar cells

Dye-sensitized solar cells (DSSC) have a somewhat similar device architecture to bulk heterojunction solar cells in that a large surface area junction is employed for charge dissociation. This is achieved by means of a mesoporous wide bandgap n-type semiconductor (generally TiO_2) onto which a thin layer of light sensitive dye is anchored as shown by the red dots in Figure 2.3. Electron-hole pairs are dissociated with electrons travelling through the n-type material and holes toward the counter electrode via the electrolyte. A built-in field arises from the difference between the conduction band of the semiconductor and reduction level of the electrolyte which blocks transfer of electrons to the electrolyte.

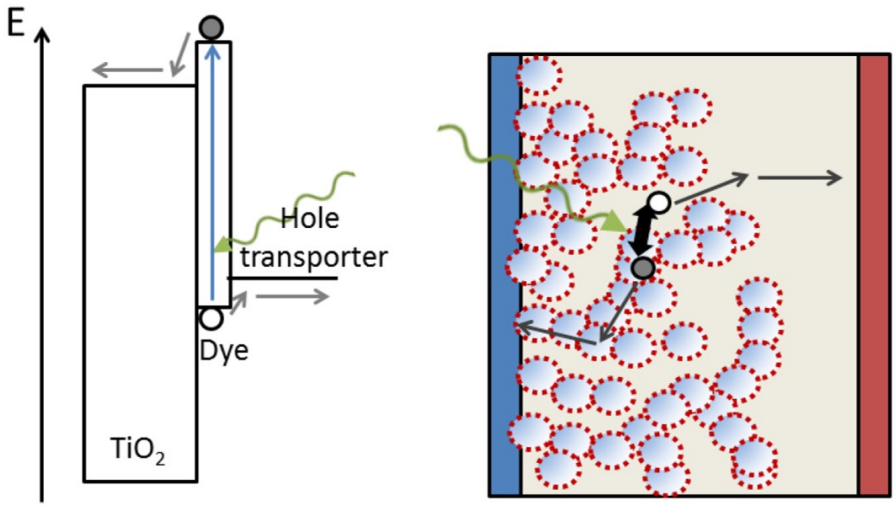

FIGURE 2.3: Schematic representation of energy level diagram (left) and operation (right) of a dye sensitized solar cell. Excitons in the dye are dissociated with electrons transferred into TiO_2 and holes to the hole transporter which has traditionally been a liquid electrolyte, although solid state hole transporters have been developed in recent years.

2.4 Perovskite solar cells

In 1839 Gustav Rose published a report on a mineral that he had come across during an expedition through the Russian Empire a decade before [23]. He identified the mineral calcium titanate (CaTiO3) and named it "Perovskite" in honour of the Russian Mineralogist Lev Perovski [24][25]. The term "perovskite" has come to lend its name to a crystallographic family with a general stoichiometry ABX_3. The B-site is traditionally coordinated octahedrally in a BX_6 configuration as shown in Figure 2.4, with the A component situated in the cuboctahedral cavity formed by the nearest neighbour X atoms in the AX_{12} polyhedron[26]. Of particular interest for photovoltaic applications are metal halide perovskites, in which the B-site is usually occupied by a divalent metal such as Pb^{2+} or Sn^{2+}, Ge^{2+}, Cu^{2+} or Ni^{2+}, with lead the most widely employed for photovoltaics to date. Halide perovskites are generally solution-processable semiconductors, typically employing an organic A site cation CH_3NH_{3+} (MA) or H_2NCNH_{2+} (FA) and X site occupied by I^-, Br^-, Cl^- and F^-.

Organic-inorganic hybrid perovskites have been studied since the late 1970s, although the first report featuring an organometal trihalide perovskite in a device analogous to a DSSC was not until 2006 [27] followed in 2009 by an improvement to 3.8% [28] and to 6.5% by 2011[29]. However, these perovskite devices suffered from rapid decomposition due in part to the presence of liquid electrolyte and so it was the demonstration in 2012 of a solid state perovskite device using $CH_3NH_3PbI_3$ on a mesoporous TiO_2 scaffold with an efficiency of 9.7% that drew much greater interest and made perovskite research the hot topic that it is

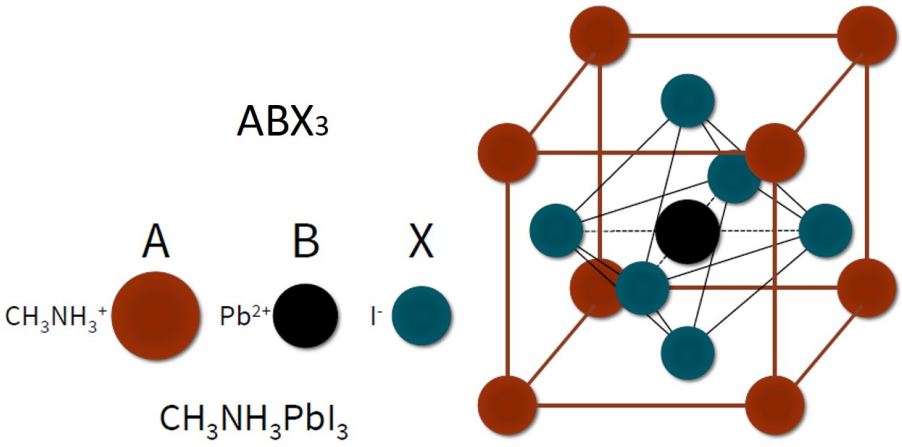

FIGURE 2.4: A generic representation of the crystal structure of the form ABX_3. Lines are a guide to represent crystal orientation rather than bonding patterns.

today[30]. Soon after it was demonstrated that long-range electron transport must occur in within a continuous layer of perovskite by replacing TiO_2 with an inert Al_2O_3 mesoporous scaffold achieving even greater efficiency[31]. This, coupled with the realisation that perovskite devices free from a hole-selective layer still display reasonable efficiency[32], suggested that $MAPbX_3$ was a high-quality semiconductor capable effective transport of both electrons and holes.

This led to the possibility of fabricating planar devices in which perovskite is sandwiched between electron and hole-selective layers, resulting also to adoption by researchers of materials and processing techniques developed for OPV. This trend in historical development is illustrated in Figure 2.5. Consequently, the operating mechanism for perovskite solar cells, as illustrated in Figure 2.6, can be described as effectively a p-i-n junction in which photons absorbed in the intrinsic perovskite layer excite electrons (create holes) into the conduction

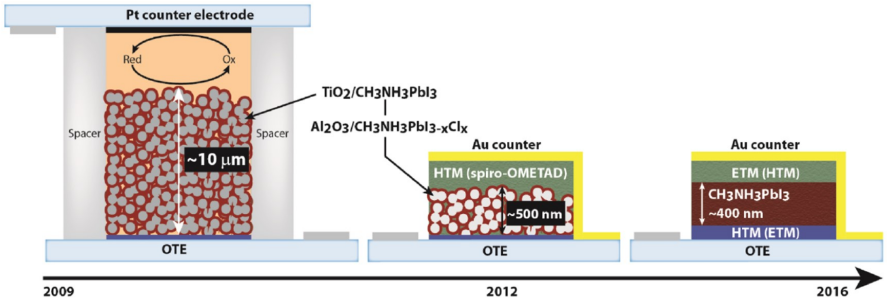

FIGURE 2.5: Schematic representation (not to scale) of the development of device structure for perovskite solar cells where OTE is optically transparent electrode, and ETM and HTM are electron and hole transport materials respectively[26].

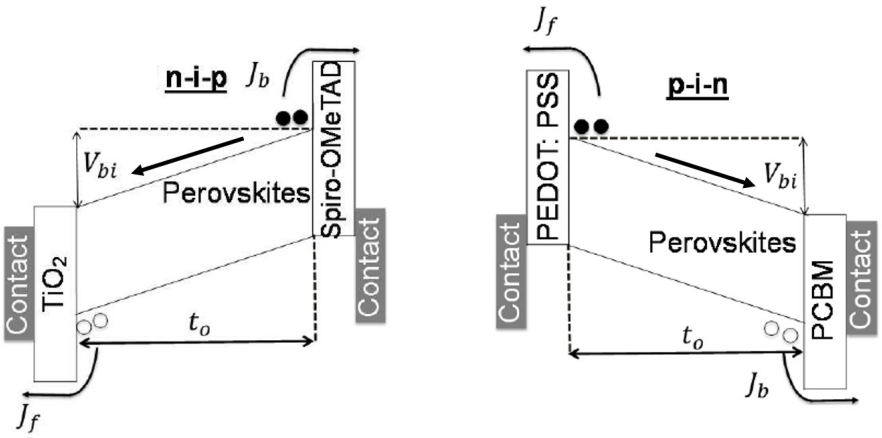

FIGURE 2.6: Operating mechanism of planar perovskite solar cell in traditional titania-based structure (left) and inverted OPV-based structure (right). In both structures an intrinsic perovskite layer is sandwiched between n-type and p-type materials. J_f and J_b are leakage currents reflecting imperfect minority carrier blocking at the front and back transport layer where the front is defined as the illuminated side[33].

band (valence band) which, due to low binding energy, immediately separate and diffuse through the material in the direction of the built in electric field. When carriers reach the correct selective layer it is energetically favourable for them to be collected whereas the opposite is true for the wrong selective contact.

2.4.1 Device fabrication

There are various methods for forming metal halide perovskites. The earliest technique employed was that used in dye-sensitized solar cells (DSSC) and involved spin coating a stoichiometric solution of the inorganic component, namely PbI_2 or $PbBr_2$, and the organic component CH_3NH_3I or CH_3NH_3Br onto a mesoporous titanium dioxide scaffold [28] [34] [31] [30] [35]. In this method, crystallisation is achieved with evaporation of the solvent which typically occurs fully only upon annealing due to the high boiling point of solvents employed. Although stoichiometry can be carefully controlled, morphological variations due to uncontrolled precipitation may hamper reproducibility. In order to combat this fact, fabrication is often undertaken in low humidity or inert conditions within glovebox [36] [37] [38] or else anti-solvents are employed for more instantaneous precipitation [39] [40] [38] [41] [42]. Another of the most widely reported techniques which mitigates this issue involves spin coating the inorganic component, namely PbI_2, onto a mesoporous titanium dioxide scaffold and then immersing the substrate in an alcoholic solution containing the organic methylammonium iodide component to achieve crystallisation [43] [44] [45]. Variants on this two stage method have evolved over time including thermal evaporation of

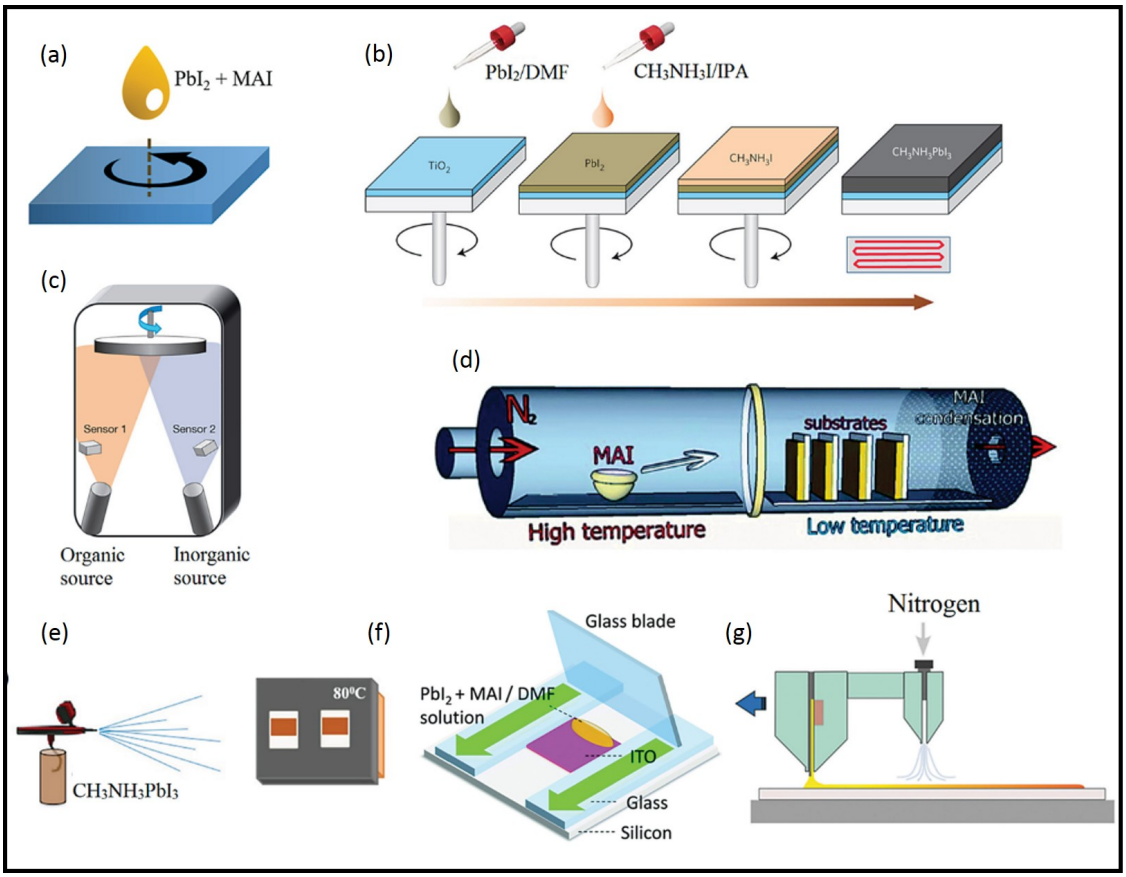

FIGURE 2.7: Various techniques used to fabricate organic-inorganic perovskite films. (a) Single-Step spin coating from common solvent. (b) Sequential or Two-Step deposition . (c) Co-evaporation. (d) Vapour deposition in a furnace. (e) Spray coating. (f) Blade-coating. (g) Slot-die coating. [42].

the inorganic component [46], vapour-assisted crystallisation[47] [48] . Additionally, dual-evaporation [49], and even layer-by-layer evaporation and conversion [50] have been used. In addition to these methods, more commercially attractive high throughput techniques are possible such spray deposition, blade coating and slot-die coating as shown in Figure 2.7.

2.4.2 Role of halide

Although PbI_2 remains the predominant halide source (in conjunction with methylammonium iodide or MAI) in high efficiency perovskite solar cells reported in the literature, other important halide sources include both compounds containing bromide and chloride. Owing to the different ionic radii of halides, the bandgap of perovskites varies with halide type and so for example, mixed iodide-bromide mixtures in $CH_3NH_3Pb(I_{1-x}Br_x)_3$ enable tuning of the bandgap from 1.55eV at $x = 0$ to 2.2eV at $x = 1$[26]. Conflicting results have emerged for the case of perovskites denoted in the literature by the formula $CH_3NH_3PbI_{3-x}Cl_x$, with some studies claiming the presence of chlorine in the final film and others failing to detect

it. Further confusion arises from the fact that Cl could be present in some capacity as for example residual MACl or unconverted $PbCl_2$ rather than in the perovskite phase. However in any case, the consensus seems to be that "mixed halide" using iodide and chloride precursors does in fact form the same material as the triiodide version. That being said, the use of $PbCl_2$ instead of Pb_2 in a 3:1 molar ratio with MAI in single-step deposited perovskites has been repeatedly shown to result in increased grain size and film coverage with more preferential crystallographic orientation[51] [52] [53]. This has been translated into longer diffusion lengths and device performance [54]. Any difference between "mixed halide" and triiodide perovskite films thus appears to be due to properties of the polycrystalline films rather than the materials themselves.

2.4.3 Hysteresis

Solar cell performance is typically assessed via measurement of a JV-curve which is derived explained in 3. The measurement involves sweeping an applied voltage and recording the resulting current either in the dark or in the presence of a standard light source and is designed to represent the steady-state power output from a cell at any given bias regardless of scan speed or direction. However, hysteresis is a common phenomenon in perovskite solar cells and involves differences arising in the current measured in the forward and the reverse scan direction as shown in Figure 2.8. Despite a large body of research devoted to the topic, the exact mechanism behind hysteresis remains an open question. Also, many proposals have been put forward including interfacial capacitive effects, ferroelectric properties of perovskites, delayed electronic trapping and slow ion migration [55] [56] [57]. For example, holding a cell at forward bias before measuring can result in an enhanced PCE obtained while a reduced efficiency is attained by holding the cell at reverse bias before measuring. Furthermore, the magnitude of the hysteresis generally depends on the scan rate with very fast rates recording high PCE in both directions with low hysteresis, middle-rates demonstrating high efficiency in the reverse bias direction and low in the forward bias and very slow scans recording lower efficiencies in both direction with little hysteresis. The simplest viable solution to obtain reliable device parameters reflecting performance under true operating conditions is thus to apply slow scans speeds or better still to hold the device at its maximum power point (MPP) voltage and measure the photocurrent over time until a steady value of PCE is reached. The issue of hysteresis was encountered frequently throughout this project, particularly for devices studied in 4 and so the measures detailed here were employed to avoid erroneous extracted devices parameters as much as possible.

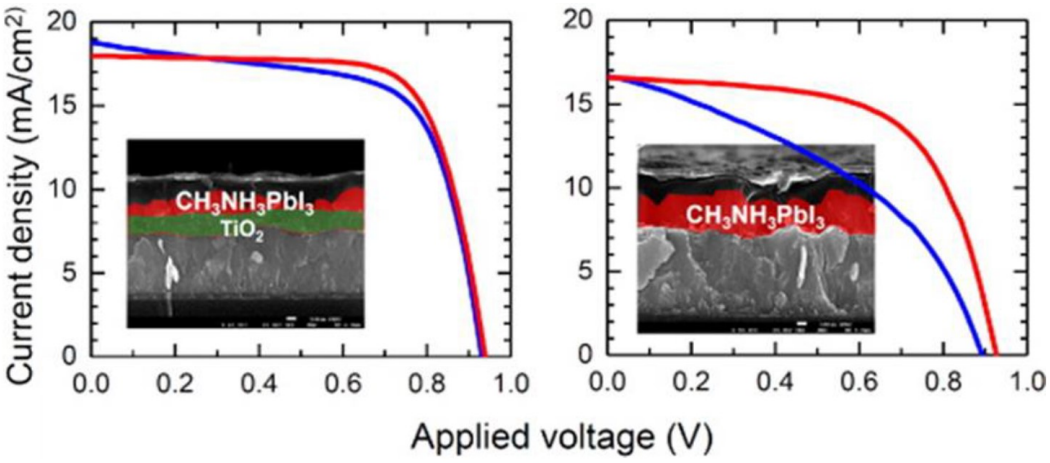

FIGURE 2.8: Scan-dependent hysteresis commonly observed in the current-voltage characteristics of perovskite solar cells (reverse bias direction in red, forward bias in blue). Hysteresis tends to be particularly pronounced planar devices where perovskite directly contacts compact TiO_2 (shown on the right) compared to devices with a mesoporous TiO_2 scaffold (shown in green on the left) [55] .

2.4.4 Stability and toxicity

Stability is a major concern for hybrid-organic-inorganic perovskite and represents a barrier to commercialisation of the technology. Humidity for example, plays a critical role in degrading perovskite solar cell performance via the generally accepted overall reaction

$$CH_3NH_3PbI_3(s) \rightarrow CH_3NH_2(g) + HI(g) + PbI_2 \tag{2.1}$$

which shows that H_2O deprotonates CH_3NH_3 resulting in the formation of degradation products leaving behind PbI_2. It is worth noting that there is evidence of many intermediate and partially reversible degradation products formed during perovskite decomposition but the above equation is satisfactory for most practical purposes [58][59]. This effect causes problems during device fabrication to a greater or lesser extent depending on the exact device architecture employed as well as on the long term stability. It is thus commonplace to undertake cell preparation within a glovebox or at least within a controlled humidity environment to reduce moisture exposure. The use of these systems, though feasible on a laboratory scale, would likely prove costly and difficult for large scale production. Another consequence is that devices are routinely encapsulated to prevent oxygen and moisture ingress. However, it is clear that care must also be taken in the choice of materials as many of the prototypical charge selective layers are known to further degrade perovskites. For example, under UV light exposure encapsulated devices featuring mesoporous TiO_2 have been shown to degrade more quickly than control devices using Al_2O_3 due to light induced desorption of

surface-adsorbed oxygen [60]. It is for these reasons that efforts were made throughout this project to use simple processing techniques and relatively stable materials wherever possible with the aim of optimizing device performance and reproducibility under high humidity processing conditions.

Another concern frequently raised is toxicity of lead used as part of devices. Even quite low levels of lead exposure can lead to neurological, renal, cardiovascular and reproductive problems with a particular risk to the nervous system amongst children and infants especially [61]. The PbI_2 left behind after perovskite decomposition is partially soluble in water and so rainwater on unencapsulated devices could cause lead to leach into soil and groundwater. However, due to the thin film nature of the technology, it has been calculated that even complete dissolution of perovskite modules would only result in an increase of $\tilde{7}0$ ppm of lead to surrounding soil compared to the 50-200 ppm typically found in urban areas [62]. It has similarly been argued that the quantities of lead within perovskite solar cells is much lower than that produced annually by other industries. For example, it has been calculated that to power the entire US economy for one year using perovskites would require 160 t of lead which is dwarfed by the 6200 t already used in the electronics industry and the 5900 - 93000 t generated through processing and combustion of coal [63]. Furthermore, from a recycling the life-cycle perspective, the fact that perovskite cells of equally high efficiency can be produced using lead from recycled lead-acid batteries is highly encouraging [64]. Taken together these facts suggest that suitable encapsulation coupled with an end-of-life recycling system should prevent a major risk from lead pollution, and could under optimal conditions reduce environmental lead exposure.

2.5 Carbon nanotubes and buckminsterfullerene

2.5.1 Synthesis and properties

In 1985, during vaporization experiments of graphite by laser irradiation (in an attempt to understand the creation of long chain carbon molecules in interstellar dust), Kroto and Smalley discovered a remarkably stable molecular cluster of 60 carbon atoms [65]. The structure was identified as a cage made up of 20 hexagonal and 12 pentagonal faces, resembling the surface of a football in which every corner is occupied by a carbon atom. The molecule was named "buckminsterfullerene" after the geodesic domes of architect R. Buckminster Fuller and the discovery spurred more intense study by the scientific community to determine what other carbon allotropes were possible. Iijima identified "helical microtubules of graphitic carbon" in 1991 produced via arc-discharge evaporation [66]. These nanoscale

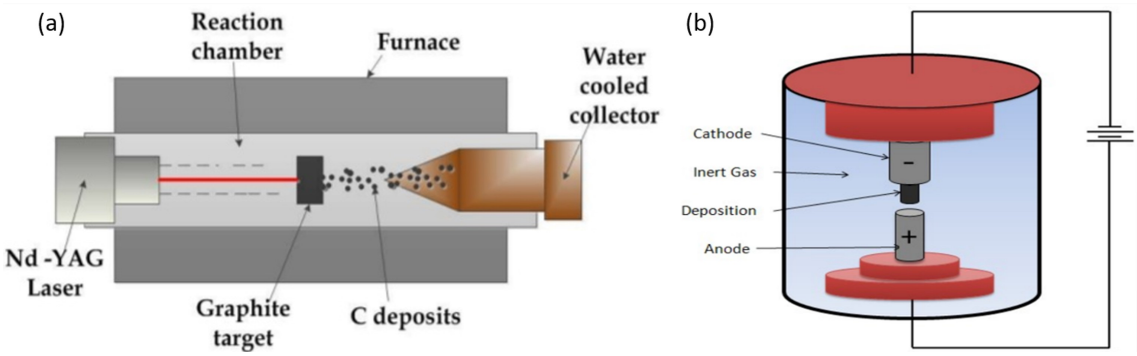

FIGURE 2.9: Methods for producing carbon allotropes (a) laser ablation and (b) arc-discharge.

structures were arranged in concentric cylinders and came to be called "multi-wall carbon nanotubes"(MWCNTS). Two years later Iijima reported production of 1nm diameter single-walled carbon nanotubes (SWCNTS)[67]. The alternating double and single bonds between carbon atoms coupled with the low dimensionality of these materials (effectively zero dimensional C_{60} and one-dimensional CNTs) results in their outstanding optoelectronic properties.

As mentioned in the previous section, the earliest methods used for producing carbon allotropes were laser ablation and arc-discharge. In laser ablation, intense laser pulses are directed towards a piece of graphite within a tube-furnace at elevated temperature and a flow of inert gas is used to direct the produced CNTs, fullerenes and other carbonaceous material towards a cooled copper collector for further purification as shown in Figure 2.9(a). In arc-discharge, two graphite rods housed in a chamber containing inert gas at low pressure are held at a potential difference and then distance between them is reduced until an arc is formed. The elevated temperature of the electric arc causes sublimation of the anode with most of the nanotubes grown on the cathode. This set up is illustrated in Figure 2.9(b).

Although these methods can provide large quantities of material, they do not allow for much control of structure and length of nanotubes and much subsequent purification is needed. Other methods such as High Pressure carbon monoxide (HiPco) growth which is closely related to many Chemical Vapour Deposition (CVD) processes have largely replaced these preliminary methods of nanotube production. The HiPCO process can produce SWCNTs of high quality and selectivity via thermal decomposition of iron pentacarbonyl using a continuous flow of carbon monoxide as feedstock within a highly pressurized reactor [68][69]. In CVD, hydrocarbon precursors such as CH_4, C_2H_2 and alcohols are dissociated and carbon atoms are precipitated upon metal catalyst particles such as iron, cobalt and nickel [70][71][72].

The spherical caged structure of 60 carbon atoms known as C_{60} has been confirmed as one of the largest molecules identified in space [73] suggesting that buckminsterfullerene is a remarkably stable and durable molecule as has indeed been demonstrated through collisions experiments [74]. Theoretical predictions and experimental results have indicated that crystals formed from C_{60} are n-type semiconductors with direct bandgap and the close packing of C60 molecules in face-centred-cubic crystals results in a relatively high electron mobility of the order of $0.1cm^2/Vs$ [75] [76]. C_{60} and its derivatives have been investigated for use organic transistors [77] and superconductivity applications when alkali-doped [78][79]. The ability of hollow cage to entrap atoms of any size as well as the catalytic and anti-oxidant properties of $C60$ also have potential applications in fuel cells [80], spin dynamics for quantum computing [81] as well as in the biomedical sector in drug delivery systems, pharmaceuticals and targeted cancer therapies [82] [83] [84]. However, by far the most successful application of fullerenes to date has been as electron acceptor in the field of photovoltaics due to their high ionization potential and the stability of the anion [76][85]. Carbon nanotubes have attracted a great deal of interest for a diverse set of applications due to their superlative optical, electrical, thermal and mechanical properties. Depending upon chirality (the arrangement of the carbon honeycomb with respect to the tube axis discussed further in Chapter 3), CNTs can be either metallic or semiconducting with near ballistic transport and intrinsic mobilities for the latter exceeding $100000cm^2/Vs$ which is amongst the highest for any known semiconductor [86]. All CNTs have a direct bandgap which is zero in the case of metallic tubes and a finite value for semiconducting CNTs that takes on a range of values depending upon tube diameter and chirality.They have been constructed with a very large length-to-diameter ratio (up to 132000000:1) [66][87] [88] and can thus their large molecular size means that they can be studied as well defined engineering structures, being discussed in traditional terms of moduli and stiffness. The geometry of their sp^2-hybridized carbon honeycomb lattice imparts exceptional mechanical strength, making them the strongest and stiffest materials yet known in terms of their tensile strength and elastic modulus respectively [89]. As such they have been used to considerably improve the strength of polymers even at modest loading levels [90] and their high aspect ratio can prove useful in the presence of a percolating pathway for excellent thermal and electrical conduction.

2.5.2 Exfoliation and deposition

In order to study and exploit the many fascinating properties of fullerenes and CNTs, the van der Waals bonds that typically cause aggregation of the materials into clusters on the macroscopic scale must be overcome. There are various methods for manipulating carbon

allotropes. For example, a common approach to form C_{60} films of arbitrary thickness is to thermally evaporate fullerene powder under vacuum, thereby coating any substrate placed above it in the chamber. Another more versatile approach is to disperse these molecular-sized materials in organic solvents via liquid-phase exfoliation (LPE). In LPE, the choice of solvent is crucial in determining both the quantity of material that can be exfoliated and the stability of the resulting dispersion. The solubility parameters that govern the suitability of a given solvent for dispersing a solute will be detailed later in the chapter but an ideal solvent is one whose surface energy matches that of the nanomaterial. If the interfacial tension [Nm^{-1}] between liquid and nanomaterial is low then the solvent will be capable of stabilizing the material against re-aggregation. C_{60} is only sparingly soluble in the vast majority of common solvents and so the fullerene derivative PCBM is typically used for solution processing. Carbon nanotubes can be directly exfoliated in solvents with surface tension of approximately $40\mathrm{mNm}^{-1}$ such as the polar solvents N-methylpyrrolidone (NMP), dimethylformamide (DMF) and γ-butyrolactone (GBL). Exfoliated CNTs can also be stabilized against re-aggregation in solvents such as water, isopropanol, acetone, and chloroform by Coulomb repulsion using linear chain surfactants such as sodium dodecylbenzene sulfonate (SDBS) [91], bile salts such as sodium cholate [92] or polymers.

2.5.3 Applicability in PV

Fullerenes were predicted to be relatively electronegative molecules and it was soon learned that they are capable of accepting as many as six electrons[93]. The redox properties of C_{60} were first harnessed in a manner relevant to photovoltaics in 1992 when photoinduced electron transfer was demonstrated in a mixture with the conducting polymer polyl2- methoxy,5-(2'-ethyl-hexyloxy)-p-phenylenevinylene] (MEH-PPV) [94]. Early devices using a planar polymer-fullerene junction yielded efficiencies well below 1% [85][95] due to low exciton diffusion lengths in π-conjugated polymers. Higher efficiencies have been achieved by forming a bulk heterojunction blend in which the donor and acceptor are intimately mixed with optimized phase separation. As such, the fullerene derivative [6,6]-phenyl-C_{60}-butyric acid methyl ester ($PC_{60}BM$) has been widely used due to its improved solubility in organic solvents.

Carbon nanotubes have been incorporated into virtually every part of the structure of photovoltaic cells with varying degrees of success. The majority of devices studied to date have exploited the low resistivity of CNTs by creating transparent electrodes composed of debundled CNT networks arranged in a porous interpenetrating mesh. The high work function ($4.8 - 5eV$) of CNTs [96] [97] means that they have mostly found application as p-type

contact electrodes[98][99], or else as hole selective contact in conjunction with a metallic (gold) or metal oxide (ITO or FTO) anode [100][101] [102] [103] [104]. CNTs have also been incorporated into the active layer in solar cells as an additive or as part of a hybrid structure to improve charge separation and transport [105][106][107]. Semiconducting CNTs typically exhibit p-type behaviour under ambient conditions [108] and as such, all-carbon heterojunctions have been used to generate photocurrents [108][109][110] in which exciton dissociation occurs primarily between CNTs and n-type fullerenes and an all-carbon solar cell has even been demonstrated[111]. Implementing careful nanotube sorting and blending with [6,6]-phenyl-C_{71}-butyric acid methyl ester (PC_{71}BM) has been shown to yield a certified efficiency of 2.5% by through broadband optical absorption offered by the polychiral nanotubes and the smaller bandgap fullerene[112].

2.6 Graphene

2.6.1 Fabrication methods

The method first used to identify monolayer graphene was through micromechanical cleavage of graphite using adhesive tape [113][114]. Mechanical exfoliation of graphene ("Scotch tape method") is illustrated in Figure 2.10(a). It remains the preferred method for fundamental studies as it produces graphene flakes of high quality. However, flake size is limited to the size of single grains in the starting graphite (which is of the order of millimeters [115]) and it is a time consuming process with low throughput and thus is impractical for large-scale applications. Other dry exfoliation methods include anodic bonding [116][117] and photoexfoliation with laser ablation [118] [119].

Other top-down techniques to produce graphene are lithium ion intercalation in which layers are exfoliated from the bulk crystal by means of the insertion of lithium ions and liquid phase exfoliation (LPE), depicted in Figure 2.10(b), in which energy is supplied to graphite powder in organic solvents (typically via ultrasonication) which exfoliates mono- and few-layer graphene in a liquid dispersion. LPE is an attractive technique as it is capable of producing large quantities of exfoliated material relatively simply. As for fullerenes and CNTs, the solvent is chosen to match the surface energy of graphene and as such, polar solvents such as NMP and DMF are suitable for direct exfoliation. A common bottom-up technique is chemical vapour deposition (CVD) in which a hydrocarbon gas (typically methane) is injected into a high temperature furnace and is deposited on a metal foil (typically copper) as shown in Figure 2.10(c)

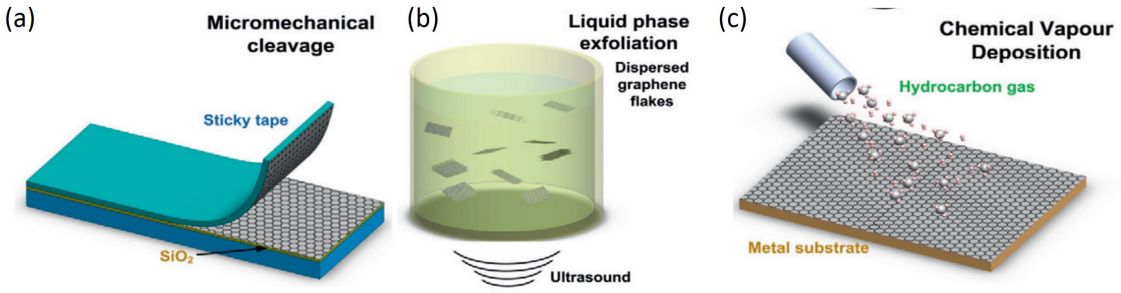

FIGURE 2.10: Common methods used to produce graphene. (a) Micromechanical cleavage. (b) Liquid phase exfoliation (LPE). (c) Chemical vapour deposition (CVD). Adapted from [120].

2.6.2 Graphene photovoltaics

The identification of graphene and its superlative properties came at a time of heightened interest in cheap renewable energy sources and so it is of no surprise that there has been much work done to date on incorporating graphene into solar cells. Organic photovoltaic devices in particular have proven fertile ground for demonstrating the potential of graphene as they tend to suffer from lower mobilities and poor ambient stability compared to inorganic devices, both deficiencies that graphene may help to address. In fact, graphene has many favourable characteristics for application in photovoltaic devices. Its high conductivity coupled with the intrinsically high transparency afforded by its atomically thin nature make it attractive as a transparent electrode. Its high mobility and ability to be easily doped by heteroatoms has resulted in graphene being incorporated into every layer of photovoltaic devices, either replacing existing commonly used materials or else in conjunction with them.

The solution processability of organic photovoltaic materials has naturally led to much work using liquid-phase exfoliated (LPE) graphene as electrode and or charge selective material. The difficulties in solution processing graphene in its pristine form has resulted in the majority of device research using graphene oxide (GO) or reduced graphene oxide (RGO) following from various forms of the Hummers method [121]. For example there have been reports of using LPE graphene as anode to replace ITO. Xu et al. [122] made 25nm thick graphene oxide (GO) films and then used hydrazine and various annealing treatments to reduce the films before making solar cells with a P3HT:PCBM blend as active layer, achieving a conversion efficiency of 0.13%. Wang et al. [123] used thermal reaction of nanographene molecules of giant polycyclic aromatic hydrocarbons to grow graphene films and obtained an efficiency of 0.29% under one Sun illumination. Zhang et al. [124] made a graphene mesh via standard photolithography and ozone etching and used it in a device to obtain 2.04% conversion efficiency. At least part of the improvement in efficiency relative to other devices

with solution processed graphene electrodes was due to a low sheet resistance without compromising too much on transparency ($150\Omega/sq$ and 8% transmittance ay 550nm respectively before mask-based etching versus $750\Omega/sq$ and 65% after etching). Konios et al. [125] used a laser-based patterning technique to create a graphene micromesh, achieving an efficiency of 3.05%.

Liu et al. [126] used P3HT as donor together with RGO as acceptor and obtained a maximum efficiency of 0.88% for 10wt% of functionalised graphene oxide, with lower concentrations being insufficient for a continuous donor-acceptor interface and significant graphitic aggregation and hence reduced hole mobility occurring at higher concentrations. Yu et al. chemically grafted C_{60} onto RGO to act as a hybrid acceptor together with P3HT as donor[127]. The barrier properties of graphene have also been demonstrated. For example, Kim et al. [128] directly spin-coated graphene oxide on top of an aluminium contacted OPV and found that the device was more stable than control devices, demonstrating the barrier properties of graphene.

Although oxidizing graphene offers several advantages such as improved solubility in a wider range of solvents and creation of a tunable bandgap depending on the degree of oxidation, it also destroys the π-conjugation of the lattice resulting in reduced electron mobility[129][130]. There is also evidence that the presence of hydroxide and carboxylic groups hamper device stability [131]. These groups may be removed and the conductivity improved by chemical and thermal reduction but such treatments cannot fully restore the properties of graphene in its pristine form.

Graphene grown by chemical vapour deposition has shown greater promise for high performance transparent electrode applications primarily because it does not have to contend with many of the difficulties associated with conductivity of solution-processed films such as structural defects induced during redox treatments, removal of surfactants and significant flake-to-flake contact resistance and lateral disorder [132][133].

3 Theory and Experimental Methods

3.1 Introduction

The aim of this chapter is to explain the theory behind materials used in this work as well as the operating principles of tools used to characterise them. The focus is on determining the optoelectronic properties of a variety of materials and their composites whilst paying attention to morphology. Materials are examined both individually and as composites or in stacked arrangement. A semi-classical approach to understanding electron transport in solids if first adopted before introducing the effects of orbitals, crystal lattice structure and resulting energy bands on charge distribution and transport. These concepts and the derived equations are then used to explain the superlative properties of carbon nanomaterials and perovskites used in this work before introducing the basic physics of semiconductor devices and solar photovoltaics in particular. Finally, the main methods used to fabricate and characterise materials and devices are outlined.

3.2 Charge Transport in thin films

The Free Electron Model, combining the semi-classical Drude Model and quantum mechanical Fermi-Dirac statistics, provides a simple and yet effective method of understanding electrical and thermal conductivity in metals. The valence electrons in a metal are assumed to be completely detached from their ion and so are free to move throughout the crystal lattice which, when coupled with the assumption that electron-electron interactions are negligible, results in the notion of an "electron gas". If a particle is considered to have three degrees of freedom in which to move (x, y and z) then Boltzmann's law states that each particle has thermal energy (E_t) given by

$$E_T = \frac{3}{2} k_B T \tag{3.1}$$

where the energy is measured in joules and k_B is Boltzmann's constant ($k_B = 1.38 * 10^{-23}$ J/K). In the absence of a potential field, the kinetic energy of a particle of mass m moving with average velocity v is $mv^2/2$ and so

$$\frac{1}{2}mv^2 = \frac{3}{2}k_BT \tag{3.2}$$

therefore

$$v_T = \sqrt{\frac{3k_BT}{m}} \tag{3.3}$$

where v_T is the thermal velocity. However, this motion is random and does not result in any net current. Applying a potential for a time t across a solid containing free electrons results in an electric field that accelerates the electrons in a direction opposite to that of the applied field. Treating the electrons as classical particles, Newton's law gives

$$F = m_e a = m_e \frac{dv}{dt} = Eq_e \tag{3.4}$$

where E is the vector electric field, q_e is the charge of an electron ($-e = -1.6 * 10^{-19}C$) and the effective mass m_e is introduced to account for the forces experienced by the electrons due to the crystal lattice. m_e differs from the mass of a free electron in a vacuum, with a large m_e implying that the conduction electrons are strongly influenced by the atomic potentials. Integrating with respect to time gives

$$v(t) = \int_0^t (\frac{q_e}{m_e}E)dt = \frac{q_e t}{m_e}E = v_d(t) \tag{3.5}$$

where E is assumed to be independent of time. This component of velocity (v_d) due to the electric field is called the drift velocity and so the net motion of an electron in an applied electric field is the sum of the thermal and dift velocities or

$$v = v_T + v_d \tag{3.6}$$

However, 3.5 would predict an indefinitely linearly increasing velocity with time which is clearly not the case. This is due to the fact that collisions and obstructions originating from the presence of the material lattice have not been taken into account. Defining the mean time between collisions τ as the relaxation or scattering time and assuming that each collision results in the electron losing all of its momentum gained by the electric field means that 3.5 can simply be altered by integrating between time $t = 0$ to $t = \tau$ so that the drift

velocity is given as

$$v_d = \frac{q_e \tau}{m_e} E = \mu E \tag{3.7}$$

where μ is the mobility of the material with units m^2/Vs^{-1}. A consequence of this picture of charge transport is that a high μ is a result of low effective mass and low scattering. The classical current density J through a material can be obtained by multiplying the unit charge q_e by the total number of electrons crossing a unit plane through the material per second $N_e v_d$, where N_e is the number of electrons per unit volume.

$$J = q_e N_e v_d = q_e N e \frac{q_e \tau}{m_e} E = \frac{q_e^2 \tau}{m_e} N_e E \tag{3.8}$$

with units A/m^2. All of the terms in 3.8 are properties of the material and can be grouped together to define the conductivity σ so that

$$\sigma = \frac{q_e^2 \tau}{m_e} N_e \tag{3.9}$$

with units of Siemens per meter ($S/m = 1/\Omega m$). It can thus be seen that a large conductivity can result from a high mobility, large electron density or a combination of the two.

In order to get a more expansive understanding of charge dynamics it is necessary to introduce the ideas of quantization and electron orbitals. Electrons surrounding the nucleus of an atom occupy discrete energy levels. Atomic orbitals are described by a unique combination of three quantum numbers n, l and m_l which correspond to electron energy (known as the principal quantum number), angular momentum and magnetic quantum number (gives the spatial variation of the angular momentum) respectively. Electrons can also be thought of as spinning on their own axis with a constant spin angular momentum m_s which varies only in direction ($m_s = +/-1$). Each orbital can accommodate two electrons, each with opposite spin. The naming convention for $l = 0, 1, 2, 3$ is "s,p,d,f" and so on alphabetically.

When a pair of atoms is brought together, their atomic orbitals combine to form pairs of molecular orbitals with energy slightly higher and lower than they were in isolation. This is illustrated for the simple case of molecular hydrogen in Figure 3.1. When a large number of atoms come together in a solid, the atomic orbitals split into a large number of levels so close in energy that they effectively form a continuum which can be thought of as an energy band of allowed energies. These bands are due to the atomic or molecular orbitals and as such their energy distribution depends upon the electronic properties of the atoms and the bond strength between them. Likewise the bands are occupied or not depending upon whether the original molecular orbitals were occupied. The lowest unoccupied band

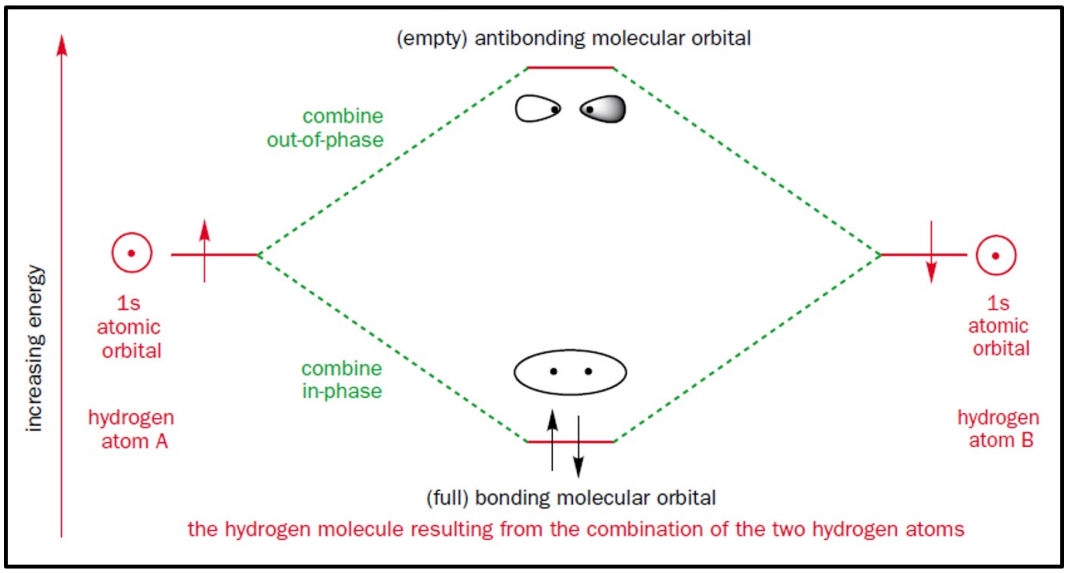

FIGURE 3.1: Bonding in molecular hydrogen [134].

is referred to as the conduction band (CB) and the valence electrons are contained in the highest occupied band or valence band (VB). If the VB is partly full or if it overlaps with the CB then the material behaves like a metal under an applied field as there is an availability of empty states at similar energies make it easy for an electron to be excited or scattered into neighbouring states resulting in good conduction of heat and electricity at a macroscopic level. If the valence band is separated from the conduction band by an energy gap (E_g) and is completely occupied then the solid is a either a semiconductor or an insulator, with the former being distinguished roughly by an E_g in the range 0.5 to 3eV. The band structure can be predicted exactly when the solid forms a regular crystal, with the adopted crystal structure depending on such factors as the number of valence electrons.

A primitive cell represents the smallest assembly of atoms that can be repeated to form the entire crystal. Three primitive basis vectors a_1, a_2 and a_3 define the cell and the direct lattice sites can be defined by the set

$$R = ma_1 + na_2 + pa_3 \tag{3.10}$$

where R is a position vector and m, n and p are integers. In three dimensions there are 14 different types of lattice that can be generated by this set, some of which are illustrated in Figure 3.2. Compounds can be considered as combinations of one or more of these lattices. The wurtzite structure often taken by zinc oxide for example can be considered as two interpenetrating hexagonal close-packed lattices and the zincblende structure as two interpenetrating face-centered cubic lattices. Miller indices are a convenient way to define the

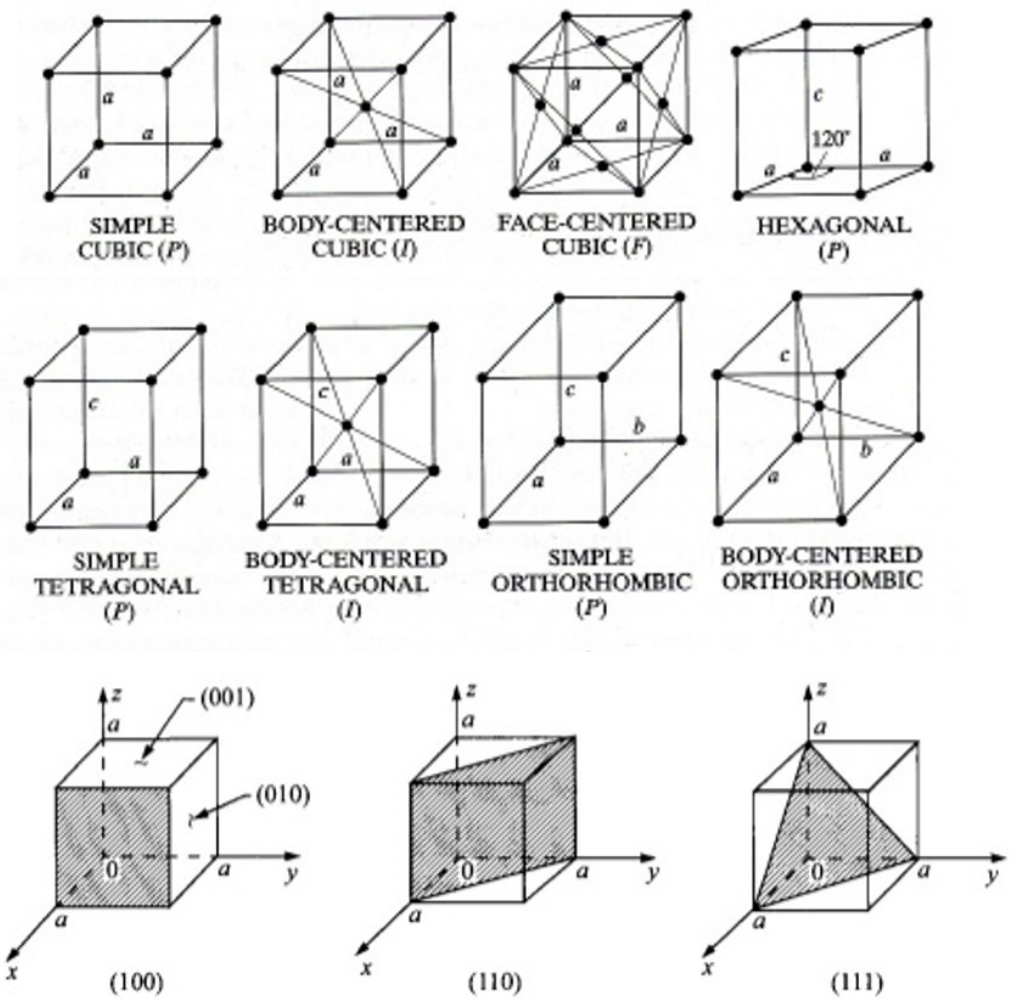

FIGURE 3.2: Common lattice structures of crystalline materials with graphical illustration of Miller indices.

various planes in a crystal lattice and can be determined by finding the intercept of the plane with the basis axes of the primitive cell and then taking the reciprocal of these numbers and reducing to the smallest integers that maintain the ratio. This is illustrated for a simple cubic crystal at the bottom of Figure 3.2.

A reciprocal lattice is a useful mathematical representation of planes within a crystal and is defined in relation to the primitive basis vectors as follows

$$b_1 = 2\pi \frac{a_2 * a_3}{a_1.(a_2 * a_3)} \qquad b_2 = 2\pi \frac{a_3 * a_1}{a_1.(a_2 * a_3)} \qquad b_3 = 2\pi \frac{a_1 * a_2}{a_1.(a_2 * a_3)} \tag{3.11}$$

The corresponding general reciprocal lattice vector G is given by

$$G = hb_1 + kb_2 + lb_3 \tag{3.12}$$

where h, k and l are integers. Each vector in the reciprocal lattice is normal to a set of planes in the direct lattice and volume of a primitive cell in the reciprocal lattice is inversely proportional to that in the direct lattice. A Wigner-Seitz cell is constructed by choosing a lattice point and drawing a perpendicular bisector plane across each line joining the chosen point to its nearest equivalent neighbours. This technique can be applied to the direct lattice and the reciprocal lattice. In the case of the reciprocal lattice, the resulting cell is called the first Brillouin zone. All of the information about the reciprocal lattice is contained in the first Brillouin zone. Reciprocal space is also variously referred to as momentum space, Fourier space and k-space. The reciprocal lattice is useful for visualising the relationship between energy and periodically varying wave vectors as the coordinates of the wave vectors k can be mapped against the coordinates of the reciprocal lattice.

The Schrödinger equation can be used to locate the energy levels of an atom or molecule. It is essentially a statement of conservation of energy in a system, using a wavefunction as a mathematical tool to determine the probability distribution of particles.

$$[-\frac{\hbar^2}{2m_e}\nabla^2 + V(r)]\Psi(r,k) = E(k)\Psi(r,k) \tag{3.13}$$

where $\hbar$ is the reduced Plank constant, k is the wavevector and $V(r)$ is the potential energy. In a crystalline solid we are able to take advantage of the fact that atomic potentials vary periodically over an infinite periodic lattice and thus the probability distribution of the electrons must also be periodic. Bloch's theorem states that if the potential energy $V(r)$ is periodic in the direct lattice space then the solutions for the wavefunction $\Psi(r,k)$ in the Schrödinger

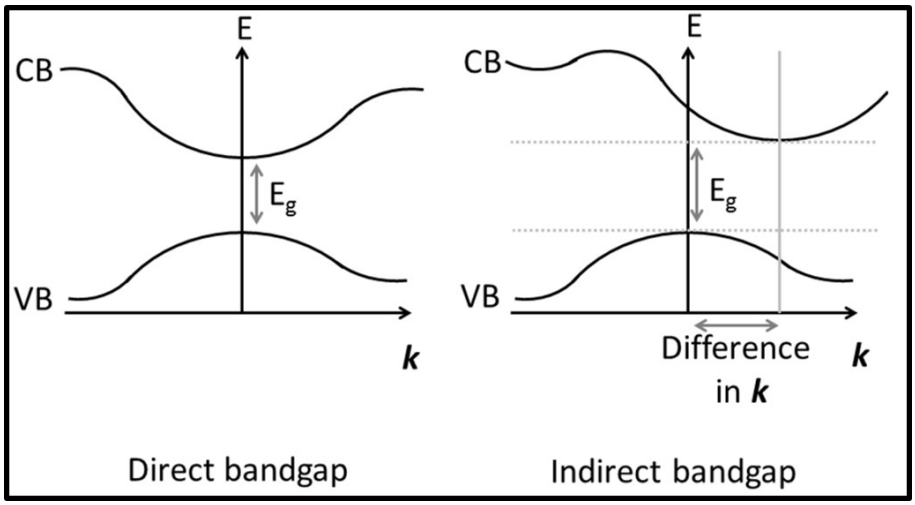

FIGURE 3.3: Diagram of direct and indirect bandgap materials, represented in k-space. The CB minimum and VB maximum take have the same k values in a direct gap material, and different ones in an indirect gap material.

equation are of the form of a Bloch function given as

$$\Psi(r,k) = u_{ik}(r)e^{ikr} \tag{3.14}$$

where u_{ik} possesses the periodicity of the lattice and is found (along with eigenenergies $E(k)$) by solving the Schrödinger equation for each band i and for each k. The resulting map of energies E vs wavevector k is the crystal band structure and is usually visualized by plotting $E(k)$ against $|k|$ for the most important directions in the crystal.

Within the conduction band, a minimum of energy $E(k)$ may occur at a value of k corresponding to an important direction in the crystal. Near to such a minimum (k=k_{c0}), $E(k)$ may be approximated by a quadratic equation

$$E(k) = E_{c0} + \frac{\hbar^2|k-k_{c0}|^2}{2m_{ce}} \tag{3.15}$$

where $E_{c0} = E_c(k_c0)$ and m_{ce} is the effective mass introduced earlier for conduction band electrons and is defined by the atomic potentials. For a hole near a valence band maximum at $k = k_{v0}$ a similar energy approximation can be made as

$$E(k) = E_{v0} - \frac{\hbar^2|k-k_{v0}|^2}{2m_{ve}} \tag{3.16}$$

where $E_{v0} = E_v(k_v0)$. Equations 3.15 and 3.16 are also statements of conservation of energy in that the first and second terms represent the potential and kinetic energy respectively. This has important implications for optoelectronic devices as semiconductors are described

either as direct or indirect depending on whether momentum transfer via phonons (crystal lattice vibrations) are involved in absorption and emission processes. If the conduction band minimum (CBM) and valence band maximum (VBM) have the same value of k (direct bandgap) then momentum is not involved and electron transfer between energy states is relatively simple. However absorption and radiative recombination require momentum transfer in the case of indirect bandgap materials, making the process less likely. The two situations are illustrated in Figure 3.3. This is reflected in the absorption coefficient α which in real terms means that indirect bandgap material solar cells such as those based on crystalline silicon (Si) must be thicker to absorb enough photons whereas direct bandgap materials may be much thinner.

As mentioned previously, each quantum state can be occupied by two electrons of different spin (this is in accordance with the Pauli exclusion principle). This means that there should be two electrons per value of k so that a crystal volume with dimensions $L*L*L$ can support $(L/2\pi)^3$ different values of k. Following from the requirement that $kL/2\pi$ must be an integer for a wavefunction confined in a region of width L and including spin degeneracy, the density of states (DOS) per unit crystal volume $g(k)$ is given as

$$g(k)d^3k = \frac{2}{(2\pi)^3}d^3k \tag{3.17}$$

where it is assumed that the electron levels are close enough for the integral over k to be a good approximation to the sum of k states. Using the band structure $E(k)$ to convert the integral over wavevector space into an integral over energy and assuming band structure isotropy about the band minimum at $k = 0$ results in

$$g(k)d^3k = g(k) * 4\pi k^2 dk \tag{3.18}$$

from which

$$g(E)dE = g(k) * 4\pi k^2 * \frac{dk}{dE}dE \tag{3.19}$$

Substituting for $g(k)$ results in

$$g(E) = \frac{2}{(2\pi)^3} * 4\pi k^2 * \frac{dk}{dE} \tag{3.20}$$

where k^2 is obtained from 3.15 and is given as

$$k^2 = \frac{2m_{ce}}{\hbar^2}(E - E_{c0}) \tag{3.21}$$

This means that the DOS for the conduction band is given as

$$g_c(E) = (\frac{1}{2\pi^2})(\frac{2m_{ce}}{\hbar^2})^{3/2}(E - E_{c0})^{3/2} \tag{3.22}$$

In order to understand how the states are filled, it is worth introducing a distribution function $f(k, r)$ such that f is the probability that at a point r the electron state of wavevector k is occupied. For the case in which a system is in thermal equilibrium, the distribution is spatially invariant and Fermi Dirac statistics may be employed. In this approach, f is dependent upon k only implicitly through the electron energy as follows

$$f(k, r) = f_0(E(k), E_F, T) \tag{3.23}$$

where E_F is is the Fermi energy, defined as the energy level up to which states are filled in a material at absolute zero and is a measure of the statistical potential energy of the distributed electrons. The Fermi Dirac distribution function $f_0(E, E_F, T)$ gives the probability that an electron state at energy E will be occupied at some temperature T and takes the form

$$f_0(E, E_F, T) = \frac{1}{e^{(E-E_F)/k_BT} + 1} \tag{3.24}$$

Electron and hole density distribution can thus be obtained by multiplying the density of states by the appropriate probability distribution function. The total density of electrons in a conduction band of minimum energy E_c is given by

$$n = \int_{E_c}^{\infty} g_c(E) f_0(E, E_F, T) dE \tag{3.25}$$

Similarly, the density of holes in the valence band is given by

$$p = \int_{-\infty}^{E_v} g_v(E)(1 - f_0(E, E_F, T)) dE \tag{3.26}$$

If the Fermi level is far enough from the band edges (a reasonable assumption given that it lies somewhere in the bandgap at absolute zero) then f_0 can be approximated by the Maxwell-Boltzmann form. Therefore, in the conduction band where $E >> E_F$,

$$f_0(E, E_F, T) \approx e^{(E_F-E)/k_BT} \tag{3.27}$$

and in the valence band where $E << E_F$

$$1 - f_0(E, E_F, T) \approx e^{(E-E_F)/k_BT} \tag{3.28}$$

Using these approximations simplifies the expressions for the integrals in equations 3.25 and 3.26, allowing n and p to be solved directly as

$$n = N_c e^{(E_F-E_c)/k_BT} \qquad p = N_v e^{(E_v-E_F)/k_BT} \tag{3.29}$$

where N_c and N_v are constants given by

$$N_{c(v)} = 2(\frac{m_{ce(ve)}k_bT}{2\pi\hbar^2})^{\frac{3}{2}} \tag{3.30}$$

From these equations it can be seen that the electron and hole densities vary exponentially with position of the Fermi level and that for any material at a given temperature the product np is constant and given by

$$np = N_c N_v e^{-E_g/k_BT} \tag{3.31}$$

This constant property of the material can be defined as the intrinsic carrier density n_i. At finite temperatures, thermal agitation occurs in intrinsic semiconductors resulting in continuous excitation of electrons from the valence band to the conduction band, with an equal number of holes left behind in the valence band. This is balanced by recombination of electrons in the conduction band with holes in the valence band such that at steady state the net result is $n = p = n_i$. Likewise, it is sometimes convenient to write n and p in terms of n_i and the intrinsic potential energy E_i,

$$n = n_i e^{(E_F-E_i)/k_BT} \qquad p = n_i e^{(E_i-E_F)/k_BT} \tag{3.32}$$

3.2.1 Organic materials

The Free electron Model provides a good approximation to electrical conduction in metals but deviations may arise in cases where strong electron-phonon interactions are present, electron-hole scattering is non-negligible or charge hopping occurs, among others. Such phenomena occur in electron conduction in organic materials.

Carbon is a material of special significance as it can exist in different phases depending upon the hybridization of its valence electrons. For example, carbon atoms are bonded in

tetrahedral arrangement in diamond by forming four sp^3 orbitals which is the same structure as crystalline silicon. Carbon atoms can also take the semimetallic graphitic structure in which three valence electrons are involved in sp^2 hybridized σ-bonds, leaving the fourth orbital p_z which is oriented perpendicular to the other three loosely involved in bonding with another plane of carbon atoms and relatively mobile. Organic materials in which the carbon backbone has alternating double and single bonds (where a double bond consists of one σ-bond and one π-bond) allows for effective electron delocalization and is said to be π-conjugated. Many π-conjugated polymers become highly conducting upon redox treatment and can thus be tailored for optoelectronic processes. Some crystalline organic solids can be treated using similar principles as inorganic semiconductors and metals as intermolecular forces are strong and carriers may be considered to occupy bands much like inorganic crystals. However, in more amorphous organic solids and polymers intramolecular forces dominate and electron-hole pairs are considered tightly bound.

3.2.2 Carbon nanotubes

As mentioned in the previous chapter, carbon nanotubes can be thought of as sheets of sp^2-hybridized carbon atoms rolled into a cylindrical shape. This is illustrated in Figure 3.4. An individual nanotube can be defined by the particular axis with a circumference vector C given by

$$\hat{C} = \hat{a_1} + m\hat{a_2} \tag{3.33}$$

so that nanotubes are identified by (n, m) and categorised as either "arm-chair" for $n = m$ and $\theta = 30°$, "zigzag" for n or $m = 0$ and $\theta = 0°$ and "chiral" for all other intermediate angles. Nanotubes are metallic if $(m - n)/3$ is an integer or else semiconducting for other chiral angles. This is a consequence of the fact that although the wavevectors along the axis of the nanotube remain continuous (for an infinite tube), the wavevectors along the circumference of the nanotube have periodic boundary conditions and are quantized. Plotting the allowed vectors into the Brillouin zone for graphene results in a set of parallel lines whose length, number and orientation depend on the chirality (n, m) of the nanotube. This is illustrated in the map of density of states (DOS) versus energy for a $(9, 0)$ and $(10, 0)$ nanotube shown in Figure 3.4. This confinement in directions perpendicular to the nanotube axis means that the sum over k states in equation 3.20 must be taken in one direction resulting in

$$g_{c,1D}(E) = (\frac{1}{2\pi})(\frac{2m_{ce}}{\hbar^2})^{1/2}(E - E_c)^{-1/2} \tag{3.34}$$

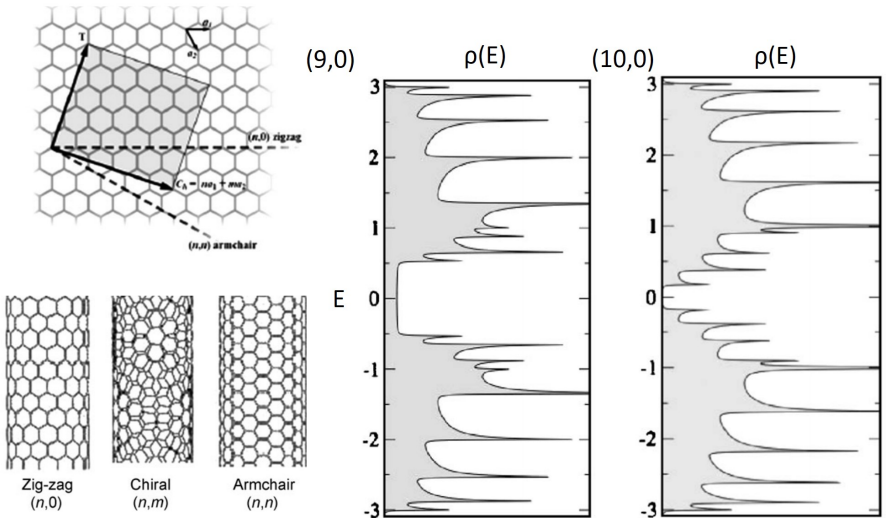

FIGURE 3.4: Illustration of nanotube chiralities (left) with density of states for a (9,0) and (10,0) nanotube [135][136].

It can be seen that close to band extrema, the DOS diverges as the inverse root of the energy and the "spiky" behaviour at energies close to the band edges are referred to as "Van Hove singularities". The DOS at the Fermi level (E = 0) is finite for metallic nanotube and null for semiconducting one, with the bandgap of the latter depending inversely on the nanotube diameter. The dependence of band structure on chirality means that the majority of as-produced carbon nanotubes are semiconducting, with one third being metallic.

3.2.3 Graphene

The structure of graphene can be described as a triangular lattice with a basis of two atoms per cell. This is illustrated in Figure 3.5. The bonding and anti-bonding σ-bands are well separated in energy ($> 10eV$ at the Brillouin zone centre Γ) and can thus be neglected from consideration, leaving only the two π-bands. The electronic wavefunctions from different atoms in the hexagonal lattice overlap and the p_z electrons can be treated as independent of the other valence electrons. The obtained dispersion relation is thus

$$E \pm (k_x, k_y) = \pm\gamma_o \sqrt{1 + 4\cos(\frac{\sqrt{3}k_x a}{2})\cos(\frac{k_y a}{2}) + 4\cos^2(\frac{k_y a}{2})} \tag{3.35}$$

for nearest-neighbour interactions only, where $a = \sqrt{3}a_{cc}$ (with carbon-carbon distance $a_{cc} = 1.42$ Angstoms) and $\gamma_o = 2.9 - 3.1eV$ is the transfer integral between first-neighbour π-orbitals. With one p_z electron per atom, the negative energy branch (-) in equation 3.35 is completely full and the positive $\pi*$ branch is completely empty. The occupied and unoccupied bands touch at K and K' points at the corners of the first Brillouin zone shown

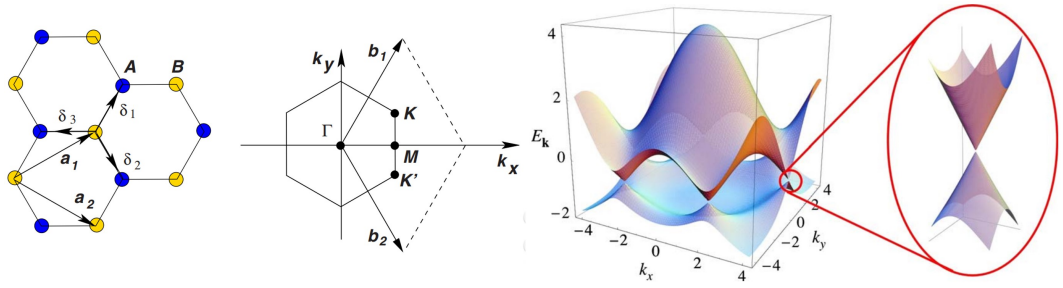

FIGURE 3.5: Illustration of graphene unit cell and brillouin zone .

in Figure 3.5. Expanding equation 3.35 about $K(K')$ gives linear π and $pi*$ bands near the Dirac points as shown to the right in Figure 3.35(c) with energy

$$E \pm (\kappa) = \pm \hbar v_F |\kappa| \tag{3.36}$$

where $\kappa = k - K$ and v_F is the electronic group velocity or Fermi velocity given as $v_F = \sqrt{3}\gamma_o a/(2\hbar) \approx 10^6 m/s$. This represents a striking departure from the usual quadratic approximation as in such cases the velocity depends upon both energy and momentum with $v = \sqrt{2E/m}$ whereas v_F in graphene results in massless Dirac quasiparticle behaviour. In effect the p_z electrons behave as if they have no mass, travelling at relativistic speed of approximately $c/300$ which would predict very high charge mobilities in pristine graphene.

Pristine graphene can be chemically doped at doping levels of $N_i = 1^{12}$ cm^{-2} while maintaining charge carrier mobilities of $\mu = 10^5$ cm^2/(Vs) or higher in which case the theoretical lower bound for sheet resistance (R_{sheet}) of graphene is [137]

$$R_{sheet} = \frac{1}{e\mu N_i N} = \frac{62.4\Omega}{N} \tag{3.37}$$

where N is the number of stacked graphene monolayers. It is for this reason that graphene is believed to be a potential replacement for ITO in some transparent electrode applications.

3.3 Perovskites

The term "perovskite" has come to lend its name to a crystallographic family with general stochiometry ABX_3. The B-site is traditionally coordinated octahedrally in a BX_6 configuration, with the A component situated in the cuboctahedral cavity formed by the nearest neighbour X atoms in the AX_{12} polyhedron[26]. In metal halide perovskites, the B-site is usually occupied by a divalent metal such as Pb^{2+} or Sn^{2+}, Ge^{2+}, Cu^{2+} or Ni^{2+}, with lead the most widely employed for photovoltaics to date. Chlorine (Cl) and the heavier halides

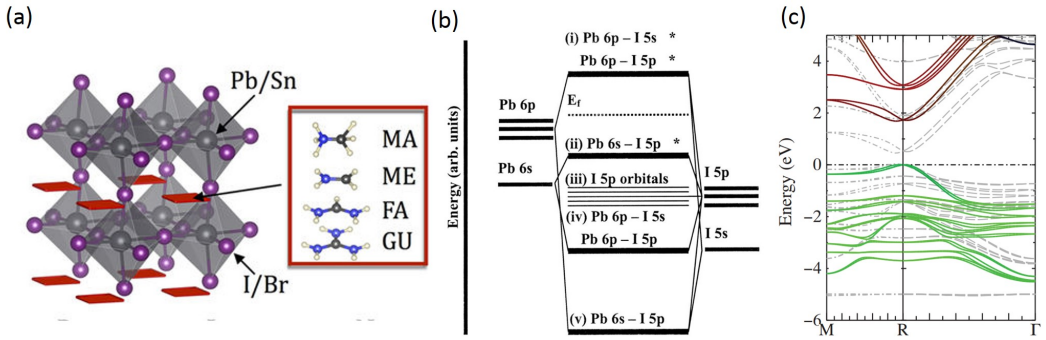

FIGURE 3.6: (a) Illustration of the crystal structure of perovskites relevant to the current work where in the organic cation blue = N, black = C and white = H [140]. (b) Bonding diagram for $[PbI_6]^{4-}$ octahedra without considering spin-orbit coupling (SOC)[141]. (c) Electronic band structure of $CH_3NH_3PbI_3$ calculated using quasiparticle self-consistent GW theory (QSGW) including the effects of SOC. Zero denotes the valence band maximum (VBM) and orbital contributions are indicated by I 5p (green), Pb 6p (red) and Pb 6s (blue). [142].

bromine (Br) and iodine (I) generally occupy the X-site. The typically monovalent A-site cation can range from a single atom to a variety of organic molecules such as formamidium (FA) and methylammonium (MA) as shown in Figure 3.6(a). The lack of covalent bonds between the organic and inorganic species offers some degree of flexibility in the overall geometry of the structure, as well as a low barrier to reorientation and contributes to dielectric and ferroelectric properties [138] [139] .

The exciting properties of metal lead halide perovskites for optoelectronic applications stem largely from material band structure and density of states (DOS). The basic BX_6 building blocks primarily determine the electronic band structure near the band edge and so orbital diagrams of isolated $[BX_6]^{4-}$ clusters provide a solid foundation for understanding the structure at higher dimensions[141][26]. Accordingly, as shown in Figure 3.6(b), for $[PbI_6]^{4-}$ units the Pb 6s-I 5p σ-antibonding orbital comprises the HOMO while Pb 6p-I 5p π-antibonding and Pb 6p-I 5s σ-antibonding orbitals constitute the LUMO[141]. Comparable character is retained in 3D $CH_3NH_3PbI_3$ perovskite where the valence band maximum (VBM) is approximately 3:1 I 5p to Pb 6s and the conduction band minimum (CBM) is nonbonding with majority Pb 6p along with contribution from I p states[26]. Furthermore, as illustrated in Figure 3.6(c), the VBM and CBM lie on the point in reciprocal space (k-space) resulting in a direct gap semiconductor with strong optical absorption and luminescence.

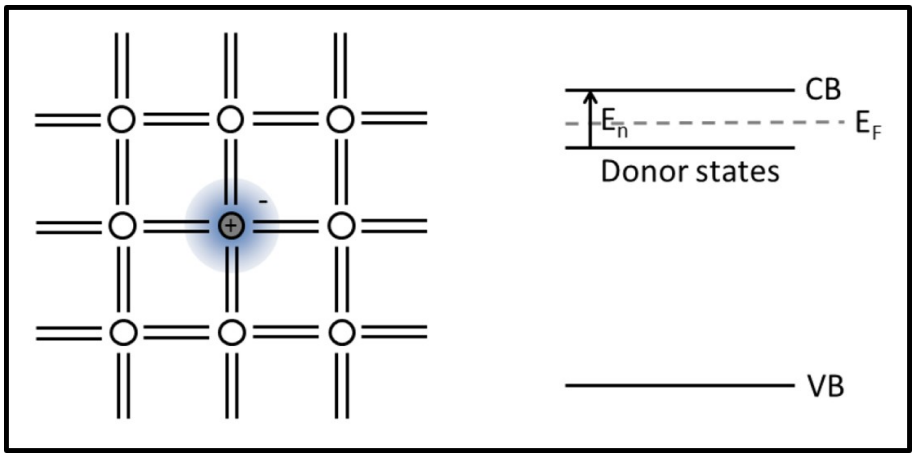

FIGURE 3.7: Illustration of n-type impurity doping in the crystal bonding of Si (left) and the band diagram (right). The extra electron is loosely bound to the donor atom and is thus delocalised. The Fermi level is shifted closer to the conduction band (CB) such that the supply of an ionization energy E_n would result in complete delocalisation of electrons promoted to the CB and net current flow.

3.4 The p-n junction

The true value in semiconductors lies in two important properties that set them apart from other materials. The first is that they can be doped with impurities, thereby allowing the resistivity to be varied. The second is that when these impurities are ionized, and the carriers are depleted, they leave behind a charge density that results in an electric field and sometimes in a potential barrier. In intrinsic silicon, each Si atom shares its four valence electrons in sp^3 hybridized bonds with four other Si atoms in a highly ordered tetrahedral arrangement. As such, the electrons are all part of stable directional covalent bonds and the material has poor conductivity at ambient temperatures under low light intensity. Introducing an impurity atom into the crystal lattice with a higher number of valence electrons results in electrons being donated to the lattice in the conduction band. This is illustrated in Figure 3.7 where the extra valence electron of phosphorous is donated to the lattice as a negative charge, resulting in n-type silicon. Similarly, when an impurity atom with fewer valence electrons is introduced into the lattice (such as boron with three valence electrons) then a vacancy is created with a positive charge. This positively charged hole in the valence band will accept additional electrons to form four covalent bonds and results in p-type silicon. When materials doped with different quantities or types of impurity atoms are brought into intimate contact, band bending occurs in order to equalize the Fermi level as shown in Figure 3.8.

The electron and hole carrier densities at thermal equilibrium were derived at the end of Section 3.2. Under the presence of an applied voltage however, carrier densities on both sides

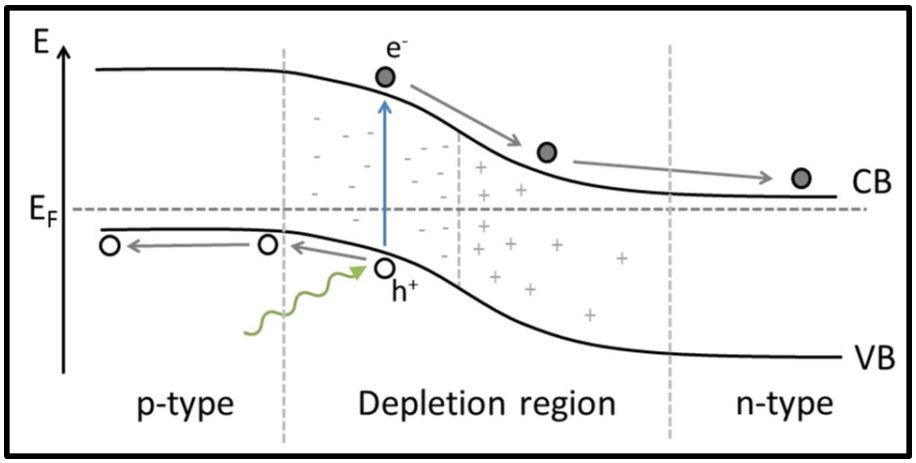

FIGURE 3.8: Schematic representation of a p-n junction solar cell under open circuit conditions.

of a junction are changed and the product pn no longer equals n_i^2. Replacing the Fermi level at equilibrium E_F with the quasi-Fermi levels for electrons (E_{Fn}) and holes (E_{Fp}) results in

$$n \equiv n_i e^{\frac{E_{Fn}-E_i}{k_B T}} \qquad p \equiv n_i e^{\frac{E_i-E_{Fp}}{k_B T}} \tag{3.38}$$

and the product becomes

$$np \equiv n_i^2 e^{\frac{E_{Fn}-E_{Fp}}{k_B T}} \tag{3.39}$$

Inside the depletion region, E_{Fn} and E_{Fp} remain relatively constant therefore the following relation may be used

$$qV = E_{Fn} - E_{Fp} \tag{3.40}$$

This situation is shown schematically in Figure 3.9(b). Combining this with 3.39 gives the electron density at the boundary of the depletion-layer region on the p-side where $x = -W_{dp}$ as

$$n_p(W_{dp}) = \frac{n_i^2}{p_p} e^{(\frac{qV}{k_B T})} \approx n_{po} e^{(\frac{qV}{k_B T}} \tag{3.41}$$

where n_{po} is the equilibrium electron density on the p-side and where $p \approx p_{po}$. Similarly at the n-type depletion boundary (where $x = W_{dn}$)

$$p_n(W_{dn}) = p_{no} e^{(\frac{qV}{k_B T})} \tag{3.42}$$

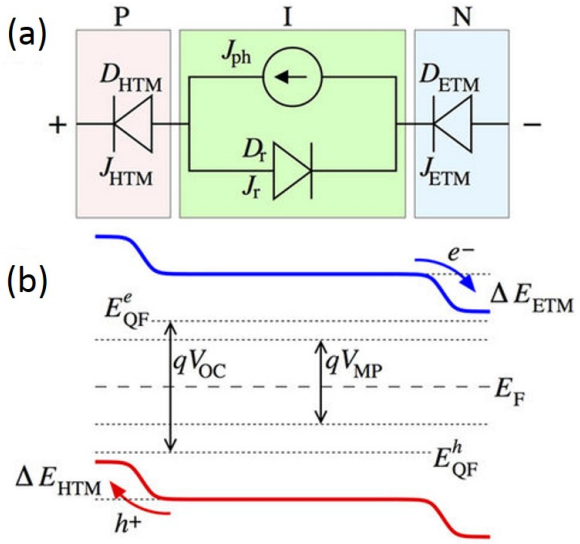

FIGURE 3.9: (a) Equivalent circuit of a p-i-n photo absorbing heterostructure such as perovskite-based devices used in this work. (b) Energy level diagram of the intrinsic part shown in (a) showing band offsets with the n and p-type layers as well as quasi Fermi levels under illumination[140].

In the neutral region there is no electric field and assuming low-injection, the continuity equations in the n-type material reduce to

$$\frac{d^2 p_n}{dx^2} - \frac{p_n - p_{no}}{D_p \tau_p} = 0 \tag{3.43}$$

This equation can be solved using 3.42 and $p_n(x = \infty) = p_{no}$ as boundary conditions resulting in

$$p_n(x) - p_{no} = p_{no}[e^{(\frac{qV}{k_B T})} - 1]e^{(-\frac{x - W_{dn}}{L_p})} \tag{3.44}$$

where $L_p \equiv \sqrt{D_p \tau_p}$ At $x = W_{dn}$ the hole diffusion current J_p is given as

$$J_p = -qD_p \frac{dp_n}{dx} \mid W_{dn} = \frac{qD_p p_n o}{L_p}[e^{(\frac{qV}{k_B T})} - 1] \tag{3.45}$$

Similarly, for electron diffusion current on the p-side

$$J_n = -qD_n \frac{dp_p}{dx} \mid W_{dp} = \frac{qD_n n_n o}{L_n}[e^{(\frac{qV}{k_B T})} - 1] \tag{3.46}$$

The total current is then

$$J = J_p + J_n = J_0[e^{(\frac{qV}{k_B T})} - 1] \tag{3.47}$$

where $J_0 \equiv \frac{qD_p p_n o}{L_p} + \frac{qD_n n_n o}{L_n} \equiv \frac{qD_p n_i^2}{L_p N_d} + \frac{qD_n n_i^2}{L_n N_a}$. This is the ideal diode law and it is widely

used to describe the behaviour of a solar cell without illumination. For a cell under reverse bias, the current will quickly approach J_0 which is termed the reverse saturation dark current whereas the current through the cell increases in an exponential fashion with voltage under forward bias. In this way the cell preferentially allows current to flow in one direction over the other and is thus a rectifying diode.

3.4.1 Equivalent circuits and modelling

As discussed in the previous section, a solar cell behaves like a diode in the dark due to doping asymmetry of its constituent layers and resultant band bending near the junction(s). Within an electrical circuit under illumination, an ideal solar cell is best modelled as a diode in parallel with a constant current provider. Given that photocurrent scales directly with area, it is useful in this context to replace current I with current density J. This is illustrated in Figure 3.10 where the diode and current source are connect to an external load R_L which provides a voltage drop V. As can be seen from the arrows in the figure, the total current $J(V)$ is equal to the diode current J_D minus the constant current provided by the current source (J_{sc}). This is captured in the following equation

$$J(V) = J_D - J_{sc} \tag{3.48}$$

Inserting the ideal diode equation yields

$$J(V) = J_o[e^{\frac{qV}{k_B T}} - 1] - J_{SC} \tag{3.49}$$

Under illumination in the absence of an external load (i.e. $V = 0$) the solar cell acts as a current provider and the current density across the cell $J(V) = J_{sc}$ which is the condition of short circuit (SC) and explains the naming convention of J_{sc}. Another consequence of this equation is that under conditions in which no current is flowing in the external circuit (i.e. $J(V) = 0$ as illustrated in Figure 3.8) then J_D equals J_{sc} and the open circuit voltage V_{oc} is obtained as

$$V_{oc} = \frac{k_B T}{q} \ln(\frac{J_{SC}}{J_o} + 1) \approx \frac{k_B T}{q} \ln(\frac{J_{SC}}{J_o}) \tag{3.50}$$

In either of these cases (V_{oc} or J_{sc}) the power density P delivered by the solar cell is zero. There must exist a load between these two conditions where the power extracted is greatest, that is $P_m = J_m V_m$. The fill factor FF can thus be defined as

$$FF = \frac{J_m V_m}{J_{sc} V_{oc}} \tag{3.51}$$

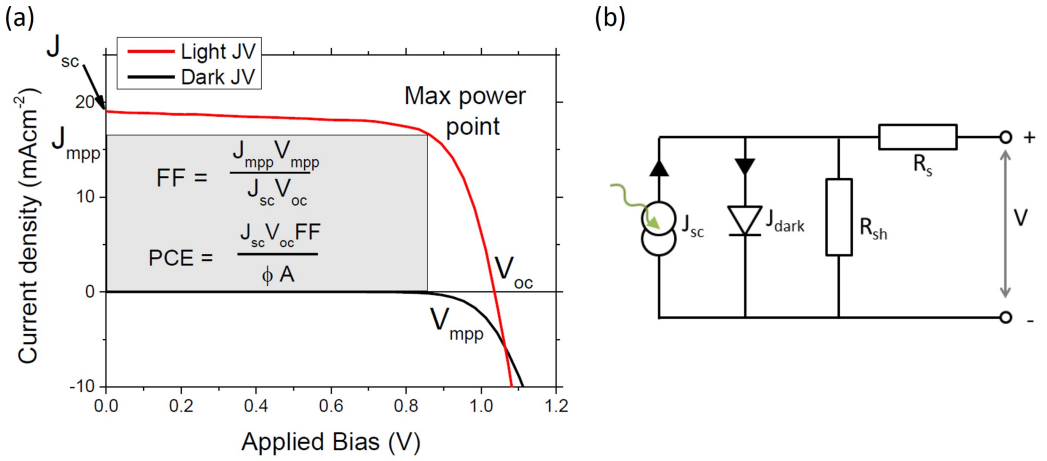

FIGURE 3.10: General parameters used to characterise the behaviour of solar cells. (a) Current-voltage curve for photovoltaic device under illumination (red) and in the dark (black) where the shaded area represents the maximum power attainable. (b) An equivalent circuit diagram for a solar cell where J_{sc} represents current generated from absorbed photons, J_{dark} represents the diode dark current and R_s and R_{sh} are parasitic resistances.

which gives an idea of how well the solar cell performs. The power conversion efficiency (η) can be defined as the ratio of of the maximum power output to the incident power density P_{in} of the incoming radiation. It is given as

$$\eta = \frac{J_m V_m}{P_{in}} = \frac{J_{sc} V_{oc} FF}{P_{in}} \tag{3.52}$$

where P_{in} is usually taken as 1000W/m^2 as this is the standard Air Mass 1.5 spectrum.

In real cells however, power is dissipated through non-idealities in the device. One source of losses is due to the choice of materials used such as resistance to charge flow through the plane and across the interface between individual layers as well as along the plane of electrodes. Another source of losses mainly reflects imperfections in device geometry where holes within and non-homogeneous thickness of layers compromise effective rectifying action. These imperfections can be represented electrically by two parasitic resistances, one in series (R_s) and one in parallel (R_{sh}) with the cell in the equivalent circuit as shown in Figure 3.10(b). From the diagram it is evident that series resistance should be minimized (i.e. $R_s \to 0$) and shunt resistance maximized ($R_{sh} \to \infty$) if solar cell output is not to be compromised. The resulting current through the cell is then given as

$$J = J_0[e^{\frac{q(V-JR_s)}{k_B T}} - 1] + \frac{V - JR_s}{R_{sh}} - J_{sc} \tag{3.53}$$

Additional recombination mechanisms are accounted for by introducing an ideality factor

n_{id} which may take a minimum value of 1. Many practical devices are better described by placing an additional diode in parallel with the diode shown in the equivalent circuit in Figure 3.10(b) resulting in

$$J = J_{01}[e^{\frac{q(V-JR_s)}{n_{id1}k_BT}} - 1] + J_{02}[e^{\frac{q(V-JR_s)}{n_{id2}k_BT}} - 1] + \frac{V - JR_s}{R_{sh}} - J_{sc} \tag{3.54}$$

A variety of approaches may be used to obtain values for the various parameters in equations 3.53 and 3.54. Polynomial fits to small portions of the current-voltage curve may be used to extract J_{sc}, V_{oc}, J_{mpp} and V_{mpp}. Additionally, series and shunt resistances may be approximated by taking the inverse slope of such fits near V_{oc} and J_{sc} respectively. More sophisticated approaches involve fitting current-voltage data directly using equation 3.53 or 3.54.

For a data sequence such as current density measurements J_1, J_2,...,J_N, the Method of Least Squares assumes that measurements are samples from a normal distribution with mean $\overline{J}$ and standard deviation $\sigma(J_i)$ where

$$\overline{J} = \frac{1}{N}\sum_{i=1}^{N} J_i \qquad \sigma(J_i) = \sqrt{\frac{1}{N}\sum_{i=1}^{N}(J_i - \overline{J})^2} \tag{3.55}$$

Therefore, in order to fit data to an equation with parameters to be determined $\vec{p}$ where $\vec{p}$ is a vector consisting of R_s, R_{sh}, J_{sc}, J_{01}, J_{02} and n_{id}, it follows that J can be determined as a function of V and $\vec{p}$ by minimizing the sum

$$\vec{p_0} = \min_{\vec{p}} \sqrt{\frac{1}{N}\sum_{i=1}^{N}(\frac{1}{\sigma(J_i)}|J_i - J(V_i, \vec{p})|)^2} \tag{3.56}$$

where $\vec{p_0}$ is the optimum set of parameters for the fit. In the case where noise exists in both voltage and current measurements, equation 3.56 may be modified using the method of Orthogonal Distance Regression such that

$$\vec{p_0} = \min_{\hat{V}_i, \hat{J}_i, \vec{p}} \sqrt{\frac{1}{N}\sum_{i=1}^{N}\left(\left[\frac{V_i - \hat{V}_i}{\sigma(V)}\right]^2 + \left[\frac{J_i - \hat{J}_i}{\sigma(J)}\right]^2\right)} \tag{3.57}$$

where $\sigma(V)$ and $\sigma(J)$ are noise levels in current and voltage and fitted values are represented by $\hat{V}_i$ and $\hat{J}_i$. Fits to data in this work were obtained via the software "IVFIT" which makes use of equations 3.53, 3.54 and 3.57.

The amount of photocurrent generated at zero applied bias (i.e. J_{sc}) depends on the incident light spectrum and the amount of light that the cell can absorb. The wavelengths

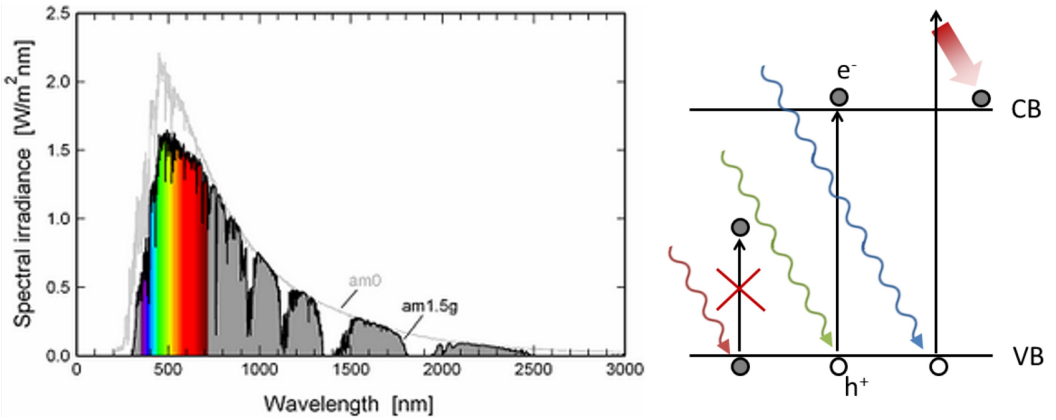

FIGURE 3.11: Solar spectral irradiance at AM1.5 ([143]) with the coloured area corresponding to visible wavelengths (left) and diagram of photon absorption in a semiconductor (right). Photons with energy equal to E_g promote electrons with no energy wastage, leaving a hole in the valence band. Photons with energy greater than E_g promote an electron to a higher state resulting in loss of excess energy as heat.

absorbed depend upon the bandgap of the semiconductor where photons with energy larger than the bandgap may be absorbed by exciting an electron from the VB to the CB or a higher energy state. Photons with energy below the bandgap are generally not absorbed as there is no suitable state to which electrons may be excited. However, photons that excite electrons to states much greater than the CBM will undergo rapid thermal decay as depicted in the band diagram in Figure 3.11 with excess energy being lost as heat. Therefore there is a certain trade-off in material bandgap between capturing as much of the spectrum as possible whilst minimizing thermal losses. V_{oc} is likewise affected as the maximum voltage generated is that held by extracted electrons (U =qV) and is thus at best equal to the material bandgap.

Given the dependence of photocurrent on the incident energy spectrum, a fixed reference is required. The solar spectrum is of most interest for photovoltaic energy conversion and is defined as representing the solar spectrum at ground level for mid-latitude regions at a solar zenith angle of 48 °. This definition is useful as it represents the overall yearly average for mid-latitudes and is referred to as the Air Mass 1.5 spectrum (AM1.5), with a total irradiance of 100W/m^2. The AM1.5 spectrum is shown in Figure 3.11. Another important consideration, as introduced previously, is the absorption coefficient (α) of the semiconductor. In general the absorption coefficient is related to the integral of the DOS in the CB and VB so that for a direct bandgap semiconductor where the DOS vary parabolically, it is given by

$$\alpha(E) = A(E - E_g)^{1/2} \tag{3.58}$$

where A is a material-dependent constant. Indirect bandgap materials can be described by the same equation but by increasing the exponent to 2 to account for the necessary presence of a phonon during the absorption event.

The photocurrent density can thus be calculated by integrating the product of the absorbance of a particular material and the AM1.5 spectrum with the wavelength-dependent External Quantum Efficiency (EQE) which is the probability of an incident photon of energy E delivering one electron to the external circuit. Accordingly, the total short-circuit current density generated by the cell is given by

$$J_{sc} = q \int EQE(E)\Phi_{AM1.5}(E)dE \tag{3.59}$$

3.5 Electrical measurements

The Four-probe method was used to measure film resistance as contact resistance made between probe and the material surface is accounted for and removed by the inclusion of the two additional probes. The method works by applying current to the two outer probes and measuring the potential drop between the two inner probes as shown schematically in Figure 3.12(b). In this way, both the contact and spreading resistances associated with two-probe methods are eliminated. Equations 3.8 and 3.9 define Ohm's Law as

$$J = \sigma E \tag{3.60}$$

In the case of describing current flowing in a wire, equation 3.60 can be expressed in the more recognizable form

$$V = IR \tag{3.61}$$

where V is the potential drop along the wire and R is the resistance which dependent on the dimensions of the wire. For a wire with length L and cross-sectional area A as shown in Figure 3.12(a), the resistance can be defined as

$$R = \rho\frac{L}{A} = \frac{1}{\sigma} \times \frac{L}{A} \tag{3.62}$$

where the resistivity ρ is a material-dependent constant equal to the inverse of the conductivity. For the case of thin films of width W and thickness t, equation3.62 becomes

$$R = \frac{\rho}{t}\frac{L}{W} = R_{sheet}\frac{L}{W} \tag{3.63}$$

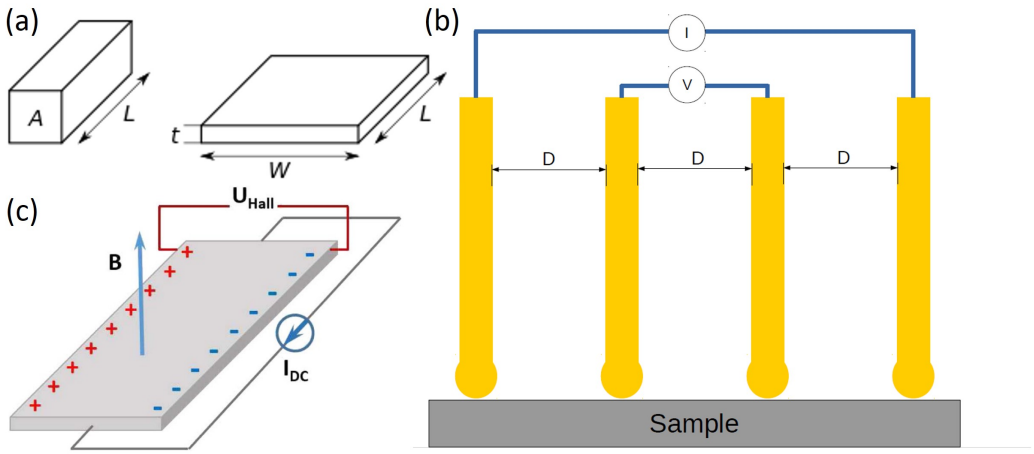

FIGURE 3.12: (a) Geometry of thin films relative to bulk conductors as defined in the text. (b) Four-point probe. (c) Schematic of the electrical Hall effect in thin conducting materials. An applied magnetic field B causes a Lorentz force on charge carriers driven by a DC current through the sheet, resulting in a transverse voltage which varies with B and depends on carrier type[144].

where R_{sheet} is the dimensionally independent (where t is assumed small) quantity known as the sheet resistance. For four equally spaced probes with separated by a distance D on a square sample shown in Figure 3.12(b) where D $\gg t$, the sheet resistance may be approximated as

$$R_{sheet} = \frac{\pi}{ln(2)} \frac{V}{I} \tag{3.64}$$

The mobility and charge type of films was determined by measuring the Hall effect. The setup is shown in Figure 3.12(c) where a current is passed along a thin film in the presence of a magnetic field B perpendicular to the surface. Under such conditions the carriers experience a Lorentz force $F_L = q(v \times B)$ leading to a build up a transverse electric field and thus of charge carriers. The resulting potential is referred to as the Hall voltage and is given by

$$V_H = IB\mu_H R_{sheet} \tag{3.65}$$

Therefore the Hall mobility (μ_H) can be determined from the Hall voltage and sheet resistance as

$$\mu_H = \frac{V_H}{IBR_{sheet}} \tag{3.66}$$

A Keithley 2400 digital multimeter in four-wire mode generally used for all electrical measurements, including device current-voltage testing of devices in conjunction with custom built labview software and a Xenon lamp calibrated to AM1.5 intensity using a silicon reference cell (ReRA Solutions Model RR-1002).

3.6 Absorption Spectroscopy

Light can interact with matter in a number of different ways. Some light will be reflected from the surface while the rest propagates through it. If the energy of the radiation is close to that of the molecular transitions then it will be absorbed by the material and any light that reaches the back surface will again either be reflected or transmitted. The combination of these interactions determines the amount of light transmitted through the material and thus the incident and transmitted light can be related to one another. If an incident beam I_0 is propagating in the x-direction and represents the optical intensity at $x = 0$ and I is the transmitted light. This defines the transmittance as

$$T = \frac{I_0}{I} \tag{3.67}$$

If the intensity of the beam at position x is $I(x)$ then the decrease in intensity in an incremental slice dx is given by:

$$dI = -\alpha I(x)dx \tag{3.68}$$

where α is the absorption coefficient of the medium. Integrating over the entire intensity range and over the entire path length l gives Beer's Law:

$$I(x) = I_0 e^{-\alpha x} \tag{3.69}$$

In the case of solutions or colloidal dispersions this relation can be used to determine concentration C via the empirical Beer-Lambert Law:

$$I = I_0 10^{-\epsilon C l} \tag{3.70}$$

where ϵ is the extinction coefficient which depends on the frequency of the incident light and is greatest where it is most intense. Absorbance can thus be defined as:

$$A = -\ln fracII_0 = -\ln T \tag{3.71}$$

combining with equation 3.70 we see that for a solution or colloidal dispersion

$$A = \epsilon C l = \sigma N l \tag{3.72}$$

where σ is the optical cross section [m^2] and N is the number of molecules per volume. The units for ϵ is [$Lg^{-1}m^{-1}$] for C is [$mgml^{-1}$] and the sample thickness l is in [m]. In the case

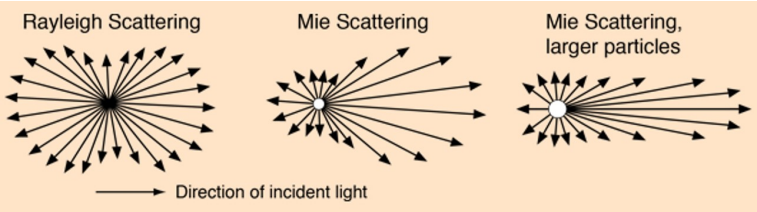

FIGURE 3.13: Light scattering processes.

of solid samples, ϵ and C are replaced with α $[m^{-}1]$ yielding

$$A = \alpha l \tag{3.73}$$

In general, absorption is measured as a function of wavelength λ or equivalently by photon energy E of incident radiation. As discussed in the previous sections, the energy levels in an atom or molecule are discrete as are the vibrational and rotational energies. Electrons must acquire sufficient energy in order to make a jump to a higher level and therefore the incident photons must have at least this energy in order to be absorbed. This is given by

$$E = \frac{hc}{\lambda} \tag{3.74}$$

The result is an absorption spectrum. The vibrational energy levels of a molecule are much more closely spaced than the electronic energy levels. Photons of lower energy than that required for a change in electronic structure (infra red light)can thus still be absorbed by causing vibrational energy changes. Rotational energy levels are closer still and can thus cause absorption of far infra red and microwave radiation. These phenomena help explain the broad humps (as opposed to sharp peaks) typically observed in the absorption spectrum of a UV-visible spectrophotometer. Spectra were measured using a Perkin Elmer UV-vis NIR Lambda 1050 spectrophotometer.

The above discussion concerning absorption spectroscopy assumes that the difference in incident and transmitted light intensities is entirely due to absorption in the material. However, Rayleigh and Mie scattering events (depicted in Figure 3.13) can cause a significant change in the intensity of light reaching the detector in a manner that may or may not be wavelength dependent. The use of an integrating sphere can account for these scattering events. The sphere is approximately 150mm in diameter and the inner wall is coated with a diffuse white reflective coating. The difference between an ordinary spectrophotometer and one equipped with an integrating sphere is that in the former, scattered light leaving the sample is lost and is thus incorrectly attributed to absorption by the material whereas

in the latter the scattered light is re-scattered and accounted for. The term used to describe and quantify the light emanating from a diffuse surface is the radiance L, the flux density per unit solid angle. For input flux Φ_i, reflectance ρ, illuminated area A and total solid reflectance angle π, the radiance is given as

$$L = \frac{\Phi_i \rho}{\pi A} \tag{3.75}$$

Expanding to an infinite power series after multiple reflections results in

$$L = \frac{\Phi_i}{\pi A} \times \frac{\rho}{1 - \rho(1 - f)} \tag{3.76}$$

where the port fraction f represents the area of the opening ports from which light can escape. The first term is similar to equation 3.75 and the second is a unitless quantity which can be referred to as the sphere multiplier M which accounts for the increase in radiance due to multiple reflections. Accounting for the geometrical setup in this manner allows the true absorbance spectra to be obtained.

3.7 X-Ray Diffraction

Crystallographic information can be derived by analysing X-ray diffraction (XRD) patterns. As already mentioned, the periodic arrangement of atoms in a crystalline structure leads to the presence of periodic atomic planes referred to as lattice planes where the type of atoms and length of unit cell vectors determines lattice spacing (d). When ordered materials are illuminated with plane wave electromagnetic radiation of appropriate wavelength, interference occurs following Bragg's Law such that

$$n\lambda = 2dsin\theta \tag{3.77}$$

where d is typically on the order of a couple of Angstroms meaning that X-rays must be used. As shown in Figure 3.14, a of 2θ should reveal intensities positions where Bragg's Law is satisfied resulting in small broad peaks for materials with short range order (amorphous) and sharp peaks for materials with long range order (crystalline). The peak positions and the d-spacings that they represent thus provide information about the location of lattice planes in the crystal structure. Although the height of peaks may be used as a qualitative measure of relative intensity, relationships between peaks in a given pattern provides a more accurate measure with the strongest peak assigned an intensity of 100 by convention[145].

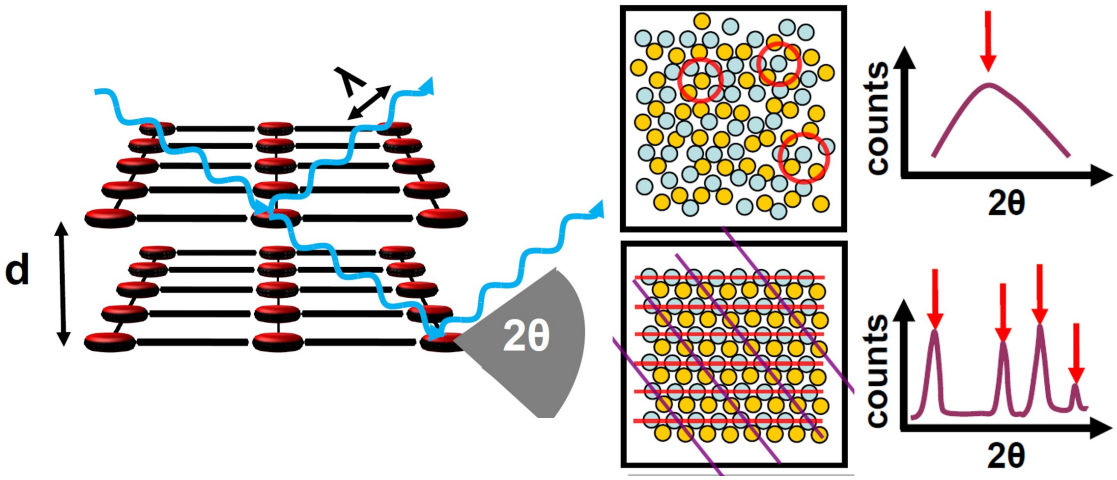

FIGURE 3.14: Illustration of Bragg diffraction (left) and general XRD patterns for amorphous and crystalline materials (right).

XRD patterns were obtained either from a PANalytical X'Pert Pro or a Bruker D8 Advance with monochromized Cu $K\alpha 1$ radiation.

3.8 Spin Coating

Spin coating is a process whereby solution containing a desired solute is spread on a horizontal rotating substrate resulting in ejection and evaporation of the solvent leaving a liquid or solid film. The simplicity and relative ease with which the process can be set up coupled with the thin and uniform films of controllable thickness that can be achieved has made spin coating a widely used technique both in laboratory environments and in the microelectronics industry[146][147]. The general process is illustrated in Figure 3.15(b). The ink is first dispensed either on a static substrate (1) or on a substrate rotating at high speed (generally at least 1500rpm) (2) such that the majority of the ink is flung off and the remaining material is dried by airflow leaving a plasticised film (3) before the solvent is fully removed to leave the dissolved or dispersed molecules on the surface (4). The thickness t of resulting films generally follows an inverse relationship with spin speed squared or $t \propto 1/\sqrt{\omega}$ where ω is the angular velocity. An important consideration for spin coating is wettability of ink on the desired substrate which is characterised by the contact angle of the liquid on the surface. A high contact angle means that the ink will tend not to spread out resulting in poor substrate coverage and film uniformity. Contact angle is increased by use of high surface tension solvents or low energy substrates and so UV/ozone or oxygen plasma treatment of the substrate is commonly employed. Limitations and disadvantages of spin coating are

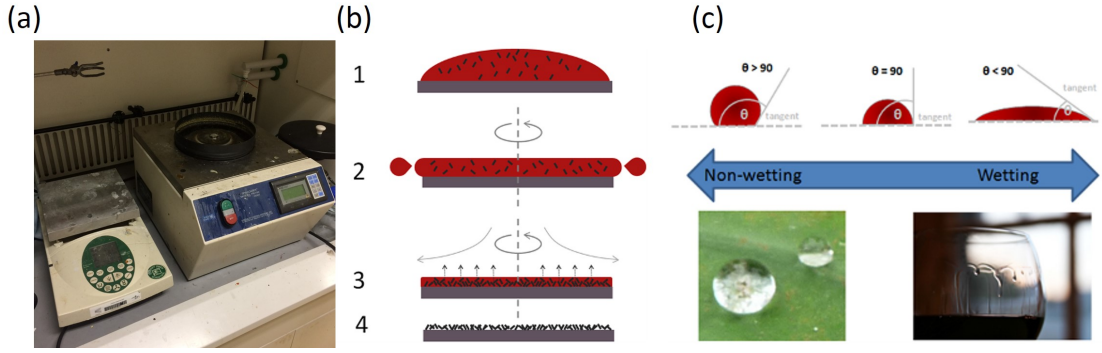

FIGURE 3.15: (a) Image of the spin coating set up.(b) Step-by-step illustration of the spin coating process. (c) Surface wetting considerations where a large contact angle means poor wettability and a low contact angle means good coating of the substrate[147].

low throughput (single substrate at a time) relatively high concentrations generally necessary and high material wastage with more than 90% of ink lost during coating.

3.9 Spraying

Spray coating is an extremely attractive deposition technique as it offers the possibility to deposit high purity products over large areas at low cost[148][149][150]. Other advantages include that uniform thin films of arbitrary thickness may be grown with high material usage and that due to the solution-processed nature of films, dopants may intentionally be added with relative ease. Figure 3.16 shows the home-built set up used along with an illustration of the general method of spray pyrolysis. Deposition of metal oxides was carried out in a custom built confined environment (Abbess 18" Cube) at atmospheric pressure, employing an air blast atomizer nozzle (PNR model MAD 0331) with N_2 as carrier gas (15l/min) placed at a distance of 26cm from the deposition substrate. Undoped and doped metal oxides were deposited on glass slides heated at 420 °C during the deposition process and oxygen concentration inside the chamber was monitored using an O_2 sensor (Sensortechnics, model XYA1). For aluminium ad indium-doped ZnO films, thermal postgrowth treatments were carried out in full nitrogen atmosphere in a separate Bell-jar chamber.

Spray coating is also a useful technique for depositing coatings of organic materials. The process involves a very sharp needle being inserted into nozzle of either 150μm or 600μm (depending on the material being sprayed). As the needle is withdrawn from the nozzle an annulus is formed and the nanomaterial ink can then run down the needle and escape through the annulus. Nitrogen at high pressure is directed through the a gap around the annulus, forcing the solution to atomise with droplet size depending on the pressure of N_2.

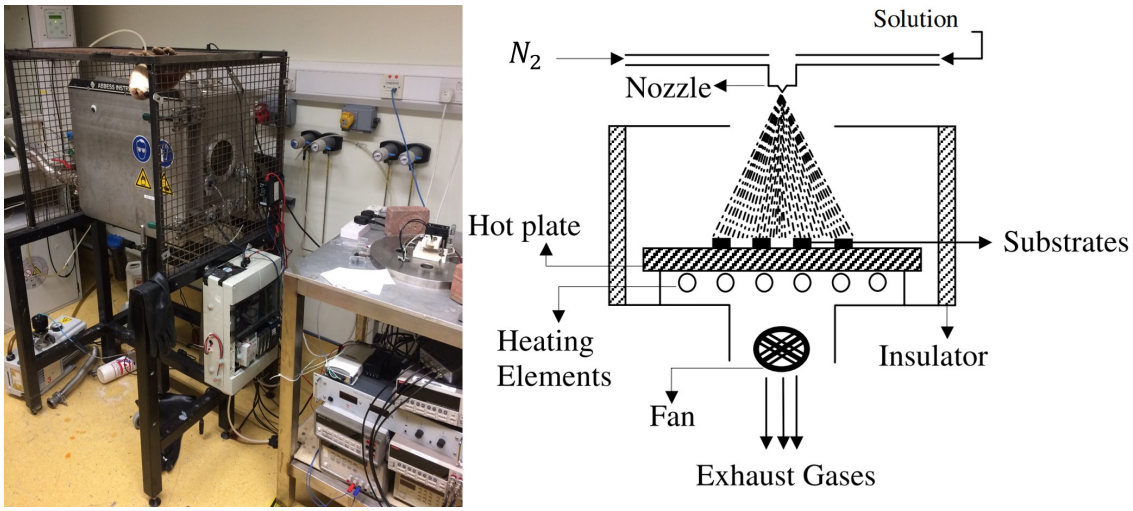

FIGURE 3.16: Set up used for deposition of metal oxides by spray pyrolysis (left) and illustration of the deposition process (right)[151].

The resulting mist is directed towards a target substrate which may or may not be heated depending on the desired film qualities and the nature of the solvent. In Chapter 6, dispersions of CNTs in chloroform (0.1375mg/mL) were spray deposited onto device stacks using a Harder & Steenbeck infinity airbrush secured to a JANOME JR2300N robot as shown in Figure 3.17. The flow-rate was 2.5 $mm^3.s^{-1}$ and the back-pressure was between 30 and 55psi. The nozzle had a diameter of 150μm and the substrate was either kept at room temperature or heated to 60 °C during deposition.

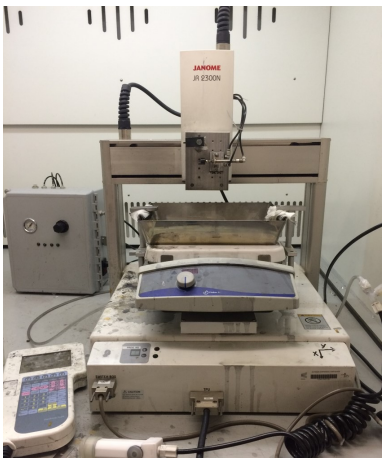

FIGURE 3.17: Set up used for spray deposition of CNT networks.

4 Optimizing Electron Extraction Materials for Improved Solar Cell Characteristics with Reduced Hysteresis

4.1 Introduction

As discussed in Chapter 2, most high efficiency perovskite solar cells to date have relied either on high temperature processed porous metal oxide scaffolds or on an inverted structure using acidic and hygroscopic PEDOT:PSS and evaporated ETLs processed in glovebox conditions. The aim of work carried out in this chapter was to optimize ETL performance for ambient processed planar perovskite solar cells. Zinc oxide nanoparticles produced using a sol-gel technique are the first material considered for this purpose. Various spray pyrolized metal oxides are then studied both as ETL and as transparent cathode in the case of binary oxides doped with donor impurities. Solution-processed fullerenes are also combined with metal oxides in devices followed by optimization of metal oxide-free polymer-fullerene ETLs. Finally, polymer-graphene composites are considered towards the improvement of device stability.

4.2 Zinc oxide nanoparticles for facile deposition at low temperatures

Zinc oxide has been much studied as an n-type contact material in the field of organic photovoltaics [153, 154, 155, 112, 156, 157, 158] and more recently in perovskite solar cells [159] [160] [161] [162] [163] [164]. Interest in the use of zinc oxide over the more traditionally used titanium dioxide (TiO_2) stems primarily from its superior intrinsic mobility and the fact that

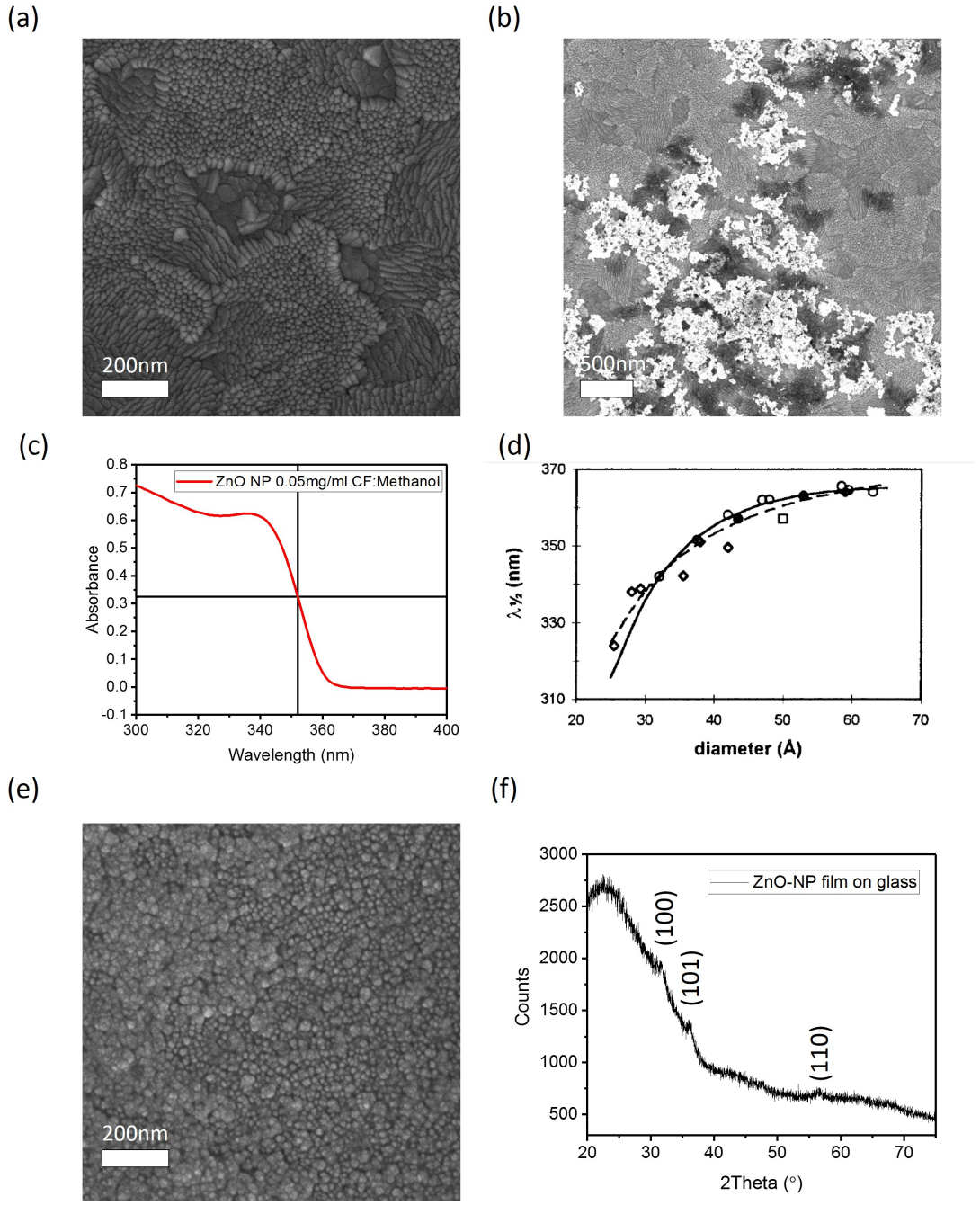

FIGURE 4.1: SEM image of plain ITO (a) and ITO coated with ZnO-NPs from an aggregated dispersion (b). (c) Absorption spectrum of ZnO-NP dispersion. (d) Size dependence of the optical band gap taken from [152]. (e) ITO coated three times with an optimized ZnO-NP dispersion. (f) XRD pattern of ZnO-NP film on glass.

it can be grown in a large variety of nanostructured morphologies by a number of different wet and dry methods, many of which are low cost. Additionally, there is the possibility to tune its conductivity by extrinsic doping which is attractive for certain applications such as transparent electrodes [155]. Zinc oxide nanoparticles are of particular interest as they can be deposited from solution at room temperature and may be processed below 150 °C, which is compatible with flexible substrates.

Zinc oxide nanoparticles were produced by adapting a published procedure [165]. Briefly, zinc acetate dihydrate (2.95g) was first dissolved in methanol (125mL) at 60 °C. A solution of potassium hydroxide (1.48g) in methanol (65mL), also at 60 °C, was then added to the acetate solution in a dropwise fashion over 10 minutes under vigorous stirring. Some precipitates formed but dissolved again. After 5 minutes the solution became and remained translucent. After 90 minutes the nanoparticles started to precipitate and the solution became turbid. After 135 minutes the heater and stirrer were removed and the nanoparticles were left to precipitate. The mother liquor was removed and the precipitate was washed in fresh methanol (60mL) for 5 minutes before being placed in equal volume vials. Centrifugation was carried out (4000rpm, 4 minutes) to better separate nanoparticles from solution, and the process was repeated a minimum of four times to minimize residual hydroxides and acetates in the sediment.

Previous reports of similarly prepared zinc oxide nanoparticles have used different solvents to disperse them, such as butanol or chloroform or combinations of butanol and chloroform and methanol at concentrations generally between 6mg/mL and 50mg/mL for spin coating [166] [167] [168]. However, it was found that these solvent combinations (at least in the volume ratios reported) caused rapid aggregation of the ZnO sol resulting in precipitation and non-homogeneous coverage of substrates for any combination of (nominal) concentration and spin speed as illustrated in Figure 4.1(b). In our case it was found that a chloroform-methanol mixture with a 90:10 ratio by volume provided almost optically clear dispersions even at concentrations greater than 100mg/ml. UV-visible absorption spectroscopy can provide a convenient way to quantify particle size in the colloid due to quantum size effects below approximately 7nm[169]. The absorption spectrum for a dispersion diluted to 0.05mg/mL is shown in Figure 4.1(c). The bandgap E_g can be determined quite simply by identifying the excitonic peak (or shoulder) and recording the wavelength at which absorption is 50% of that at the peak (called $\lambda_{1/2}$) as illustrated in the Figure. By comparing $\lambda_{1/2}$ with data collected by other researchers [152] of the size dependence of the optical gap as shown in Figure 4.1(d), the ZnO nanoparticle size in the colloid was determined to be approximately 3.8nm. The presence of methanol was found to improve the

stability of the dispersions relative to neat chloroform. Additionally it was found that lower concentrations coated repeatedly resulted in better coverage films as shown in Figure 4.1(e) therefore ZnO films were formed by spin coating 5mg/mL dispersions at 3000rpm. The thin nature of the films produced coupled with the small size of the nanoparticles resulted in short broad peak in the X-ray diffraction patterns (Figure 4.1(f)), however the hexagonal wurtzite structure of ZnO was discernible.

4.2.1 Optimizing zinc oxide layer thickness

In order to ascertain the optimum ETL thickness, devices with structure ITO/ ZnO NP/ Perovskite/ P3HT/ TiAu were fabricated with 1, 3, 5 and 7 coats of ZnO and all other parameters left unchanged. The general device stack is illustrated in Figure 4.2(a). During perovskite fabrication it was noticed that the typically employed thermal annealing step (100 °C for 10min to 1 hour) used to increase grain size resulted in complete degradation of the film in less than one minute when the perovskite was in direct contact with ZnO. Given the fact that perovskite could not be annealed upon the ZnO nanoparticle films, devices were fabricated without the typically employed annealing step as the role of perovskite stoichiometry is still an open question. Indeed, a slight excess of PbI_2 has been observed to be beneficial in some device configurations [170] [171] [172].

Figure 4.2(b) shows representative JV-curves for each of the ZnO coatings and device characteristics extracted from fits to these curves are displayed in Table 4.1. Looking at the JV-curves it is apparent that the cells with three coats of ZnO have the highest photocurrent due to their lower series resistance, implying a more complete coverage of underlying ITO than in the case of a single coat. Increasing the number of coats further resulted in increased R_s and hence decreased J_{sc} as would be expected for a thicker ETL.

As the number of ZnO-NP coats increased there was a trend towards an increasingly pronounced anomalous peak in the vicinity of the maximum power point (MPP). This indicated the presence of a barrier to carrier extraction resulting in a build-up of charge carriers. This phenomenon was found to be more pronounced for initial consecutive reverse

	$R_s(\Omega cm^2)$	$R_{sh}(\Omega cm^2)$	PCE(%)
1× ZnO	46	2×10^4	2.7
3× ZnO	16	4×10^4	3.3
5× ZnO	29	4.5×10^4	2.54
7× ZnO	36	4.5×10^4	2.79

TABLE 4.1: Extracted device parameters for devices with different number of ZnO NP coatings as ETL.

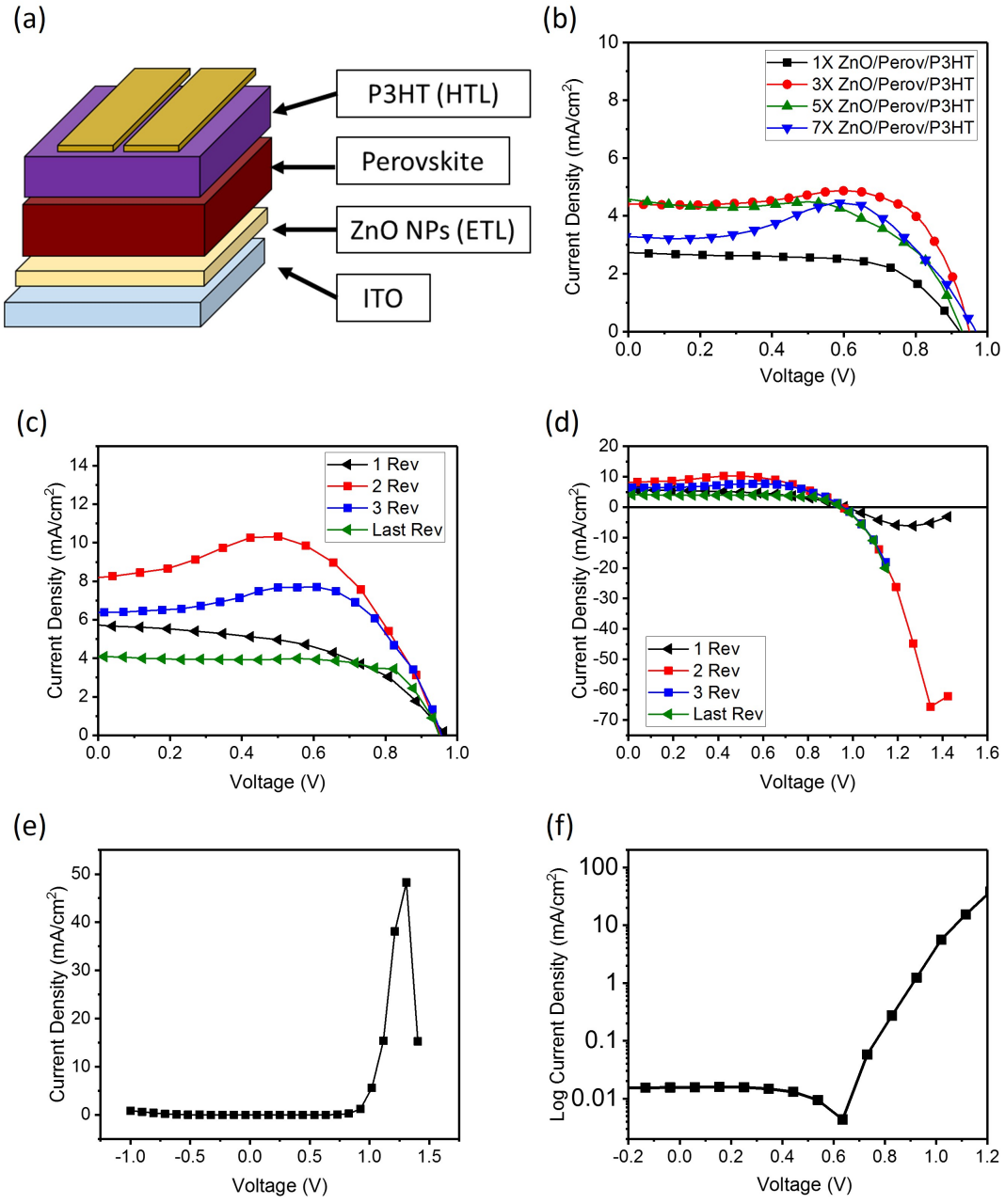

FIGURE 4.2: (a) Schematic of device stack. (b) Variation of photovoltaic response with the number of ZnO nanoparticle coatings. (c) Typical JV response under repeated reverse bias scans for a device with 3 ZnO-NP coats as ETL. (d) Influence of scan range on photocurrent observed in (c) showing roll-over effect at large forward bias. (e) Current-voltage response in the dark for the device shown in (c).(f) Semilog plot of data shown in (e).

bias scans as shown in Figure 4.2(c) and especially when sweeping over a wider voltage range (Figure 4.2(d)). However, even for the case of 3 coats of ZnO, the calculated R_s was in excess of 20Ω cm^2 which signified significant carrier recombination in this device configuration. Scans in the dark showed decent rectification behaviour (Figure 4.2(e)) though a semilog plot (Figure 4.2(f)) suggesting a capacitive effect remained even in the absence of light whereby charge built-up in the reverse bias scan direction. This was consistent with the roll-over effect observed at large forward bias both under illumination and in the dark.

4.2.2 Fullerenes as surface modifier

The aforementioned charge accumulation phenomenon suggested by scan direction, range and rate-dependent hysteresis lead to the conclusion that energy level mismatch at the interface between the active layer and ETL must be at least partly responsible for the limited photocurrent densities. Fullerenes and their derivatives have been widely documented to reduce hysteresis and passivate boundaries in perovskite cells, usually being employed in inverted devices as a solution-processed PCBM layer or a thermally evaporated C_{60} layer. Though C_{60} is less soluble than its derivatives, it has sufficiently high solubility in dichlorobenzene (DCB) to be simply spin coated on the ZnO film. Additionally, the low solubility of C_{60} in most solvents is a useful quality for withstanding the deposition of subsequent solution-processed layers for device fabrication.

When 10mg/mL C_{60} was spun on the ZnO nanoparticle layer before depositing perovskite as depicted in Figure 4.3(a), a dramatic effect on device performance was observed. As seen in Figure 4.3(b), the presence of C_{60} resulted in a much higher photocurrent in both scan directions due to a reduced R_s. This improvement can be attributed to a reduction in recombination at the interface between ETL and active layer. There are two likely explanations for this result; either the fullerenes promote effective electron extraction towards ITO due to improved band level matching or they provide more effective hole blocking from their low lying HOMO and thus suppress electron injection from ITO into the active layer through defect levels in ZnO. Of course there is also the possibility that C_{60} fills pinholes to better prevent direct contact between the ITO and higher layers of the device stack but this is unlikely as suggested by relatively large dark currents under low bias in the dark (Figure 4.3(b)).

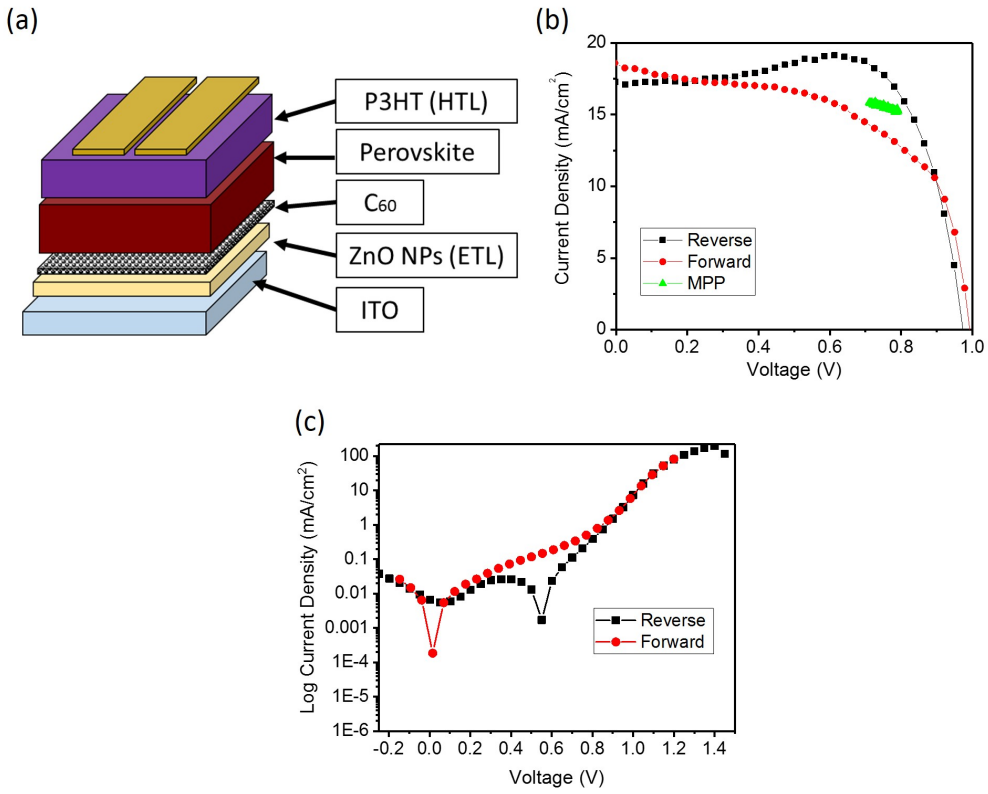

FIGURE 4.3: Effect of C_{60} as surface modifier. (a) Schematic of device stack. (b) Current-voltage curves for champion device with structure ITO/ZnO/C_{60}/Perovskite/P3HT/TiAu. "MPP" represents with current extracted under constant bias at the maximum power point. (c) Scans performed in the dark on the same cell in (b).

4.2.3 Effect on perovskite stability

As mentioned in section 4.2.1, the thermal annealing step typically employed after perovskite deposition to increase grain size and remove residual solvent resulted in complete degradation of the film in less than one minute when the perovskite was in direct contact with ZnO. This was a somewhat surprising finding given the number of high efficiency perovskite solar cells reported in the literature. Thermogravimetric analysis (TGA) was performed on the ZnO-NPs in the hope of ascertaining probable causes of this effect. As seen in the inset of Figure 4.4(a), the nanoparticle samples lost approximately 5% of their mass as they were heated to 200 °C with significant mass loss between in the range 150 °C - 350 °C before stabilizing at 80% of the original mass at temperatures above 600 °C. This indicated the presence of a substantial amount of other material. To get a better qualitative understanding of the nature of the impurities, Fourier-transform infrared spectroscopy (FTIR) was also carried out as shown in Figure 4.4(a). The FTIR spectrum revealed a broad band at 3340cm^{-1} which may be attributed ti the O-H mode of vibration signifying the presence of hydroxides, likely due at least partly to absorbed water.

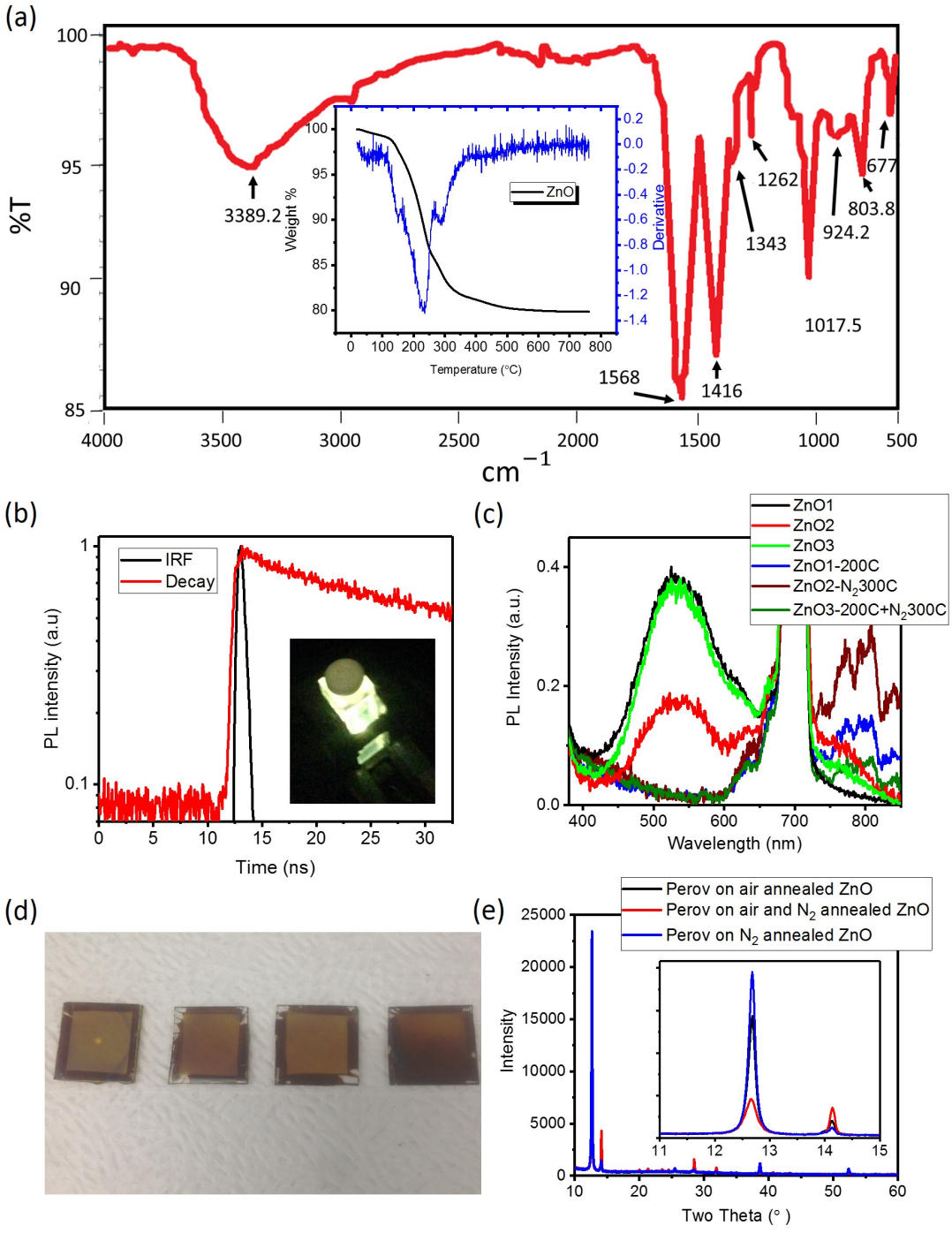

FIGURE 4.4: (a) FTIR spectrum of ZnO-NPs with prominent peaks indicated. Inset shows TGA of the same material. (b) Fluorescence lifetime of ZnO nanoparticles (ZnO-NPs) measured using TRSPC setup showed a relatively long-lived emission around 520nm. (c) Steady-state photoluminescence measurements of ZnO-NP films on glass slides before and after applying annealing treatments. (d) Image of perovskite films on ZnO substrates after 6 minutes annealing on a hot plate at 100 °C (left to right: Untreated ZnO, annealed at 200 °C in air, annealed at 300 °C in N_2, annealed in air followed by annealing in N_2. (e) XRD measurements of treated films shown in (d).

Many peaks associated organic species were also detected, particularly stretching modes of C-O and C=0 between ∼1340 cm^{-1} and ∼1600 cm^{-1} as well as wide absorption bands in the region ∼800-1100 cm^{-1}. ZnO-NP films were also measured using steady-state photoluminescence as shown in Figure 4.4(c) as it has been shown that the presence of various defects and impurities can be identified using this simple characterisation technique [173]. A broad peak in the green ($\tilde{5}$20nm) can be attributed to emission involving oxygen vacancies (V_O) due to incomplete oxidation during ZnO synthesis which would result in chemisorbed species such as OH^-, consistent with TGA and FTIR results. Time-resolved photoluminescence of the ZnO revealed a long-lived decay as shown in Figure 4.4(b). Presence of oxygen vacancies, hydroxide groups (OH^-) and residual acetate ligands on the ZnO nanoparticle surface would likely hamper device performance and cause degradation of perovskite as has since been reported [174] [167] [158].

In order to reduce the hydroxide content and fill oxygen vacancies as well as burn off any residual organic species on the ZnO surface, the films were annealed at 200 °C for 1 hour in air, 1 hour in N_2 and 1 hour in air followed by 1 hour in N_2. All three annealing treatments resulted in removal of the V_O related emission but introduced twin peaks in the near-infrared (∼770nm and 800nm), particularly for the N_2 annealed film as shown in Figure 4.4(c). To assess the effectiveness of the annealing treatments, perovskite films were deposited on each of the ZnO layers and annealed on a hot plate at 100 °C for 6 minutes. Figure 4.4(e) shows X-ray diffraction (XRD) measurements of films after the short annealing treatment. It can be seen that the peak at 12.7 ° belonging to PbI_2 is particularly prominent for the film on N_2 annealed ZnO and that the peak at 14.1 ° associated with the (110) plane of perovskite is almost completely suppressed. The perovskite film on air annealed ZnO fared slightly better, with a stronger peak at 14.1 ° and a weaker PbI_2 peak and the air and N_2 annealed ZnO resulted in the least decomposition into PbI_2. This result can be observed visually in the degree of yellowing visible in the films as shown in Figure 4.4(d).

4.3 Spray-pyrolysis of metal oxides

Spray pyrolysis has been used extensively as a relatively simple, low cost technique for depositing transparent conductive oxides [175] [176] [177] [178] [179] [180] [181] [149]. The method generally involves directing a fine spray of an alcoholic solution containing metal salts towards a heated substrate such that pyrolytic decomposition in the vicinity of the substrate forms the desired product, with the escape of associated volatile bi-products in the vapour phase. In the field of perovskite solar cells, the spraying technique has been applied

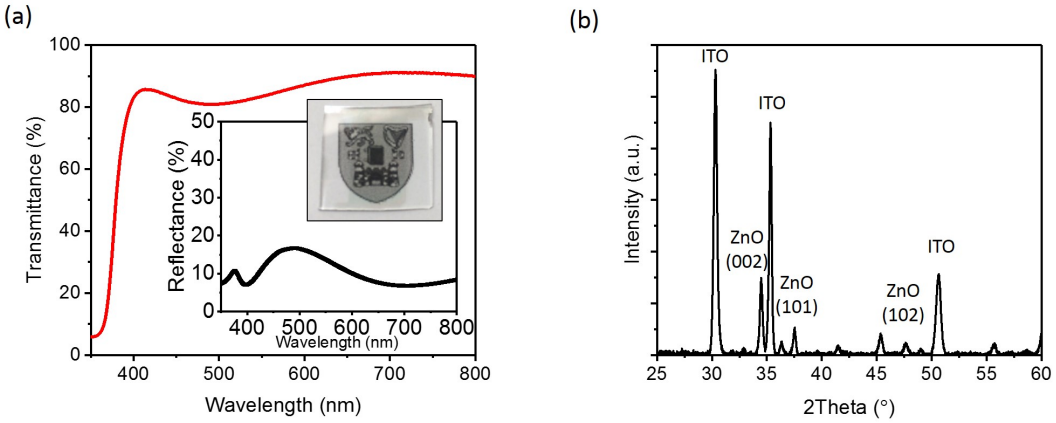

FIGURE 4.5: (a) Transmittance spectrum of intrinsic ZnO grown by spray pyrolysis (iZnO) with inset showing reflectance spectrum and high optical transparency of the film. (b) XRD pattern of 60nm thick iZnO film on ITO-glass substrate.

mostly for depositing dense hole blocking layers of TiO_2 on sputtered fluorine-doped tin oxide (FTO) substrates.

Films of undoped (intrinsic) zinc oxide (60nm thick) were grown in ITO for comparison with the sol-gel ZnO nanoparticle films. From Figure 4.5(a) and (b) it can be seen that the films were highly transparent and displayed the characteristic wurtzite structure of ZnO. Devices comprised of ITO/ iZnO/ Perov/ P3HT/ TiAu were fabricated as depicted in Figure 4.6(a). Typical cell response for such devices under one sun illumination (Figure 4.6(b)) was poor with a small inverse slope near V_{oc} indicating a large series resistance. Dark JV-scans (Figure 4.6(d)) showed a degree of hysteresis, suggesting charge build-up but also low dark current in the low to medium voltage range which together indicate a pinhole-free film with decent hole-blocking ability. However, fitting revealed that the cells had very high series resistance, particularly for scans measured in the forward bias direction as shown in Table 4.2. This resulted in low fill factor and short circuit current which can be explained either by excessive thickness of an insufficiently conductive ZnO film or by band level mismatch in the vicinity of the interface between active layer and the ETL. Given that the thickness of sprayed ZnO films (60nm) was in the typically reported range, the latter explanation is more convincing. Energy level mismatch could be due either to a shallower ZnO conduction band relative to perovskite or possibly from partial decomposition of the active layer itself resulting in an energy barrier for electron extraction imposed by lead iodide.

Annealing metal oxides under nitrogen atmosphere has been shown to decrease sheet resistance which can be attributed to removal of chemisorbed species such as OH, O_2^-, O^- O^{--} and trap passivation at grain boundaries by neutral nitrogen molecules [150] [148].

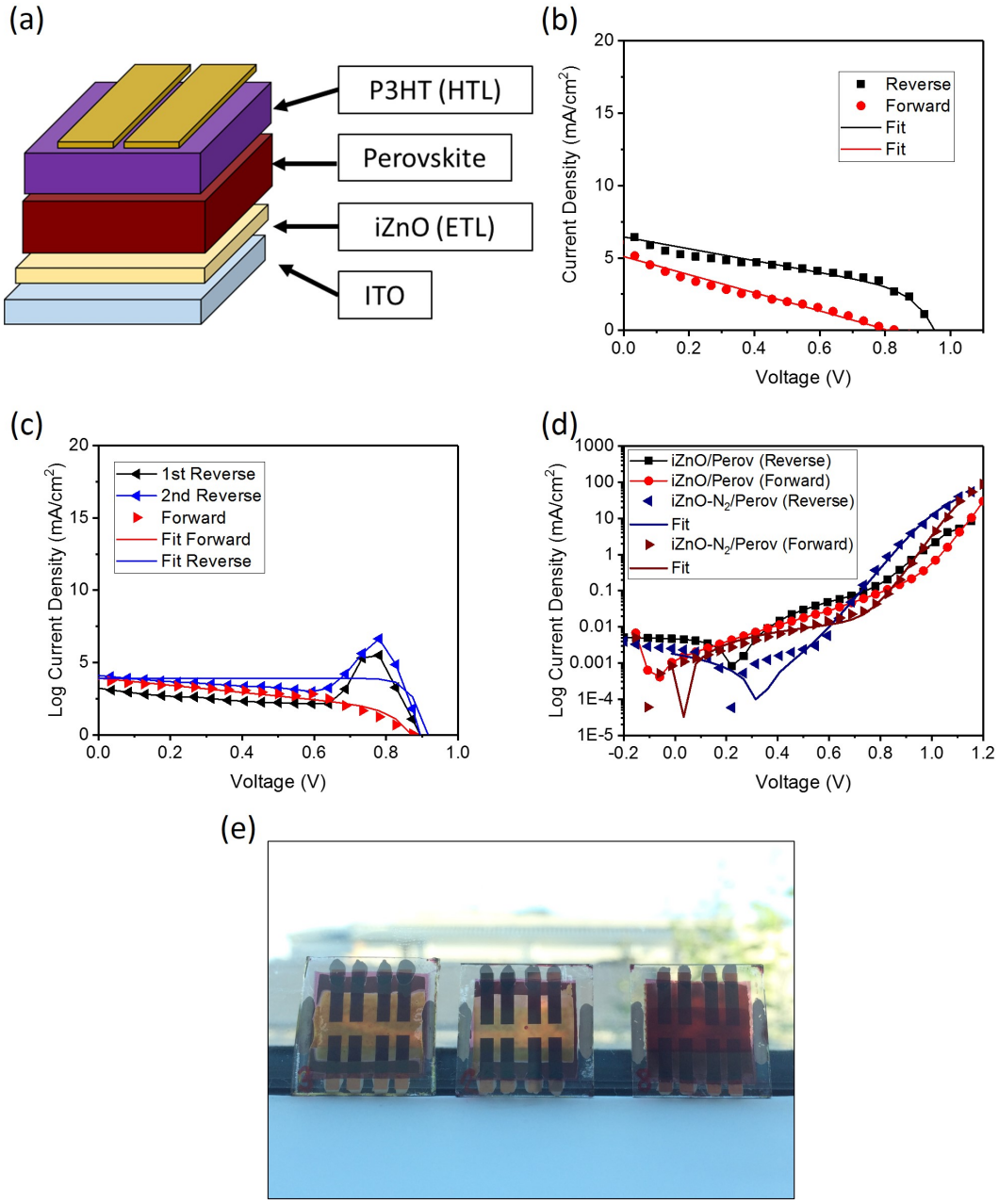

FIGURE 4.6: (a) Schematic of device stack where "iZnO" refers to intrinsic ZnO deposited by spray pyrolysis. (b) Current-voltage curves for devices consisting of ITO/iZnO/Perov/HTL/TiAu. (c) Current-voltage curves for devices in which iZnO was subjected to 30 minutes annealing at 320 °C under N_2. (d) Semilog plot of scans performed in the dark on devices shown in (b) and (c). (e) Devices from (b) (left) and (c) (middle) compared to a ZnO-free device (right) after 3 months storage in ambient in the dark.

	$R_s(\Omega cm^2)$	$R_{sh}(\Omega cm^2)$	PCE(%)
iZnO (Rev.)	19.5	1×10^4	2.7
iZnO (For.)	65	1.8×10^4	1
iZnO-N_2 (Rev.)	2	2.2×10^5	5.1
iZnO-N_2 (For.)	1.1	5.1×10^4	1.6

TABLE 4.2: Extracted device parameters from fits to JV-scans for devices with intrinsic ZnO deposited by spray pyrolysis as ETL (iZnO as-deposited or iZnO-N_2 after annealing at 320 °C under nitrogen).

N_2-annealing (320 °C for 30 minutes) was therefore carried out on iZnO films before device fabrication to study the effect on JV-characteristics. A similar peak in photocurrent around the maximum power point as was observed for the ZnO nanoparticle films was present in reverse bias scans as shown in Figure 4.6(c). This peak was found to become more significant with successive scans in the same direction, suggesting a build-up in charge within the active layer to be at least partly responsible. The nitrogen annealing treatment was found to greatly reduce R_s for both scan directions as extracted from fits in Figure 4.6(b), indicating that trap passivation by N_2 may indeed reduce recombination at the interface between iZnO and perovskite. The shunt resistance was also markedly improved, with an increase in R_{sh} by an order of magnitude in the reverse direction and a five-fold increase for forward bias scans. This result indicated that the more conductive ETL (at least in the in-plane direction) due to grain boundary passivation did not compromise hole-blocking ability in the direction perpendicular to the film surface and may even have improved it. However, fits to scans under illumination gave much larger R_s values than in the dark which was consistent with the hypothesis of band level mismatch which is exacerbated under illumination.

As previously mentioned, titanium dioxide (TiO_2) is the most widely used ETL in perovskite solar cells and so it was grown by spray pyrolysis on fluorine-doped tin oxide (FTO) substrates and devices were fabricated using identical processing for other layers. Figure 4.7(a) shows a typical JV-response for devices employing a 20nm thick layer of TiO_2 as ETL. Cells made with perovskite deposited on as-grown TiO_2 (after a UV-ozone treatment to clean the surface and improve wetting as typically employed in the literature) displayed low J_{sc}, FF and V_{oc}. However, applying a post-annealing treatment of the TiO_2 films (500 °C in air fo 30 minutes) before carrying out subsequent processing steps markedly improved all three JV-scan parameters as shown in Figure 4.7(b). This result indicated that the as-grown films were oxygen deficient resulting in the presence of a high density of trap states and hence poor charge extraction. The improvement was thus attributed to filling of oxygen vacancies in TiO_2 by the high temperature annealing treatment in air which would be reflected by a significant drop in R_s. Successive scans in the reverse bias direction showed improved

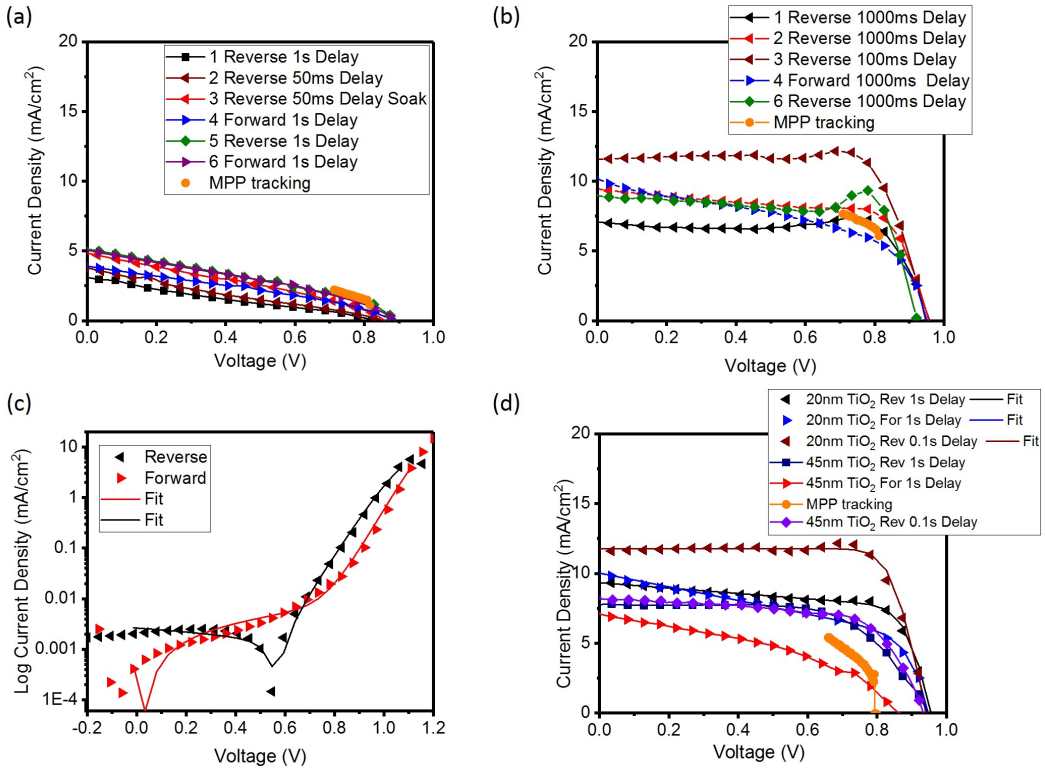

FIGURE 4.7: Current-voltage curves for devices consisting of ITO/TiO_2/Perov/HTL/TiAu where "TiO_2 stands for titanium dioxide grown by spray pyrolysis.(a) JV-curves for devices made with 20nm thick as-grown TiO_2. (b) Current-voltage response of a typical device where the TiO_2 layer was sintered at 500 °C for 30 minutes in air before perovskite deposition. (c) Semilog plots of the JV-curves in the dark for the device shown in (b). (d) Current-voltage curves for a device with 45nm thick TiO_2 layer plotted alongside data from (b) with fits using the one-diode model.

photocurrent, particularly when the scan speed was reduced by using a shorter delay time between data points. Scans in the forward bias direction had approximately the same J_{sc} and V_{oc} but lower FF which is consistent with other reports using similar device structures. Repeated scans over a smaller voltage range around the maximum power point showed the true power conversion efficiency to be between the values calculated using a full scan in either direction. Maximum power point (MPP) tracking demonstrated a promising device efficiency with an increase in power output from 4.9mW/cm^2 to 5.4mW/cm^2 over several minutes under constant illumination. To better characterise the devices, fits to the JV-data were carried out using the One-diode model.

Increasing the thickness of the ETL to approximately 46nm resulted in decreased device performance as shown in Figure 4.7(d), due primarily to increased series resistance as shown in Table 4.3. The large R_s, particularly for forward biased scans, resulted in more severe hysteresis and a lower maximum power extracted from the cells. X-ray diffraction revealed that even after post-annealing at 500 °C in air, the films were amorphous in nature. A high

TiO_2 device	$R_s(\Omega cm^2)$	$R_{sh}(\Omega cm^2)$	n_{id}	J_{sc} (mA/cm^2)	V_{oc} (V)	FF
20nm Rev.(Dark)	8.8	4.6×10^5	2.28	-	-	-
20nm For.(Dark)	2.04	1.1×10^5	2.05	-	-	-
20nm Rev.(Light)	6	515	1.07	9	0.956	0.69
20nm For.(Light)	2.4	202	1.68	10	0.95	0.5
45nm Rev.(Dark)	13.2	1.1×10^5	2.42	-	-	-
45nm Rev.(Light)	11.2	2.4×10^4	2.97	7.75	0.94	0.65

TABLE 4.3: Extracted device parameters for devices with 20nm thick TiO_2 deposited by spray pyrolysis as ETL.

concentration of trap states is a consequence of the disorder inherent in amorphous materials and therefore will adversely affect mobility and the effectiveness of electron extraction from perovskite. This effect is consistent with the measured R_s for TiO_2 films of thickness within the typically employed range. Attempts were made to improve the conductivity by fluorine-doping but the fluorine precursor was not taken up during pyrolysis.

Finally, due to its high mobility even at lower processing temperature as well as improved band level alignment with methylammonium perovskite, tin oxide (SnO_2) was spray coated on FTO and devices fabricated. However, although X-ray reflection showed a nominal thickness of 60-65nm, profilometry revealed the presence of sharp micrometer-scale peaks that protruded from the SnO_2 surface. Consequently devices fabricated with SnO_2 were completely shunted. Grinding the SnO_2 films briefly using an abrasive improved the JV-response but significant shunting remained.

4.3.1 Doped binary oxides

Having established that intrinsic zinc oxide was incompatible with high performing methylammonium lead halide perovskite cells processed under ambient conditions, it was wondered if perhaps doped binary oxides may offer more favourable energy level alignment. There have in fact been reports of high performing devices in which highly doped transparent materials serve as both charge selective layer and electrode [182, 183, 184, 185, 186, 187, 188]. Given the solution-processed nature of the metal oxide film formation, it was relatively simple to dope donor species by addition of the appropriate salt to the alcoholic precursor solution. For example, indium (In) doping could be achieved by adding $InCl_3$ to a solution of zinc acetate dihydrate ($Zn(CH_3COO)_2.2H_2O$) in methanol. Figure 4.8 shows SEM images of ZnO:In films with different In content. Undoped (0%) films were made up of hexagonal-shaped grains which grew in a columnar structure with decreasing grain size towards the film surface. The hexagonal stacks perpendicular to the substrate showed a preferred orienntation along the c axis and reflected the hexagonal wurtzite crystal structure of

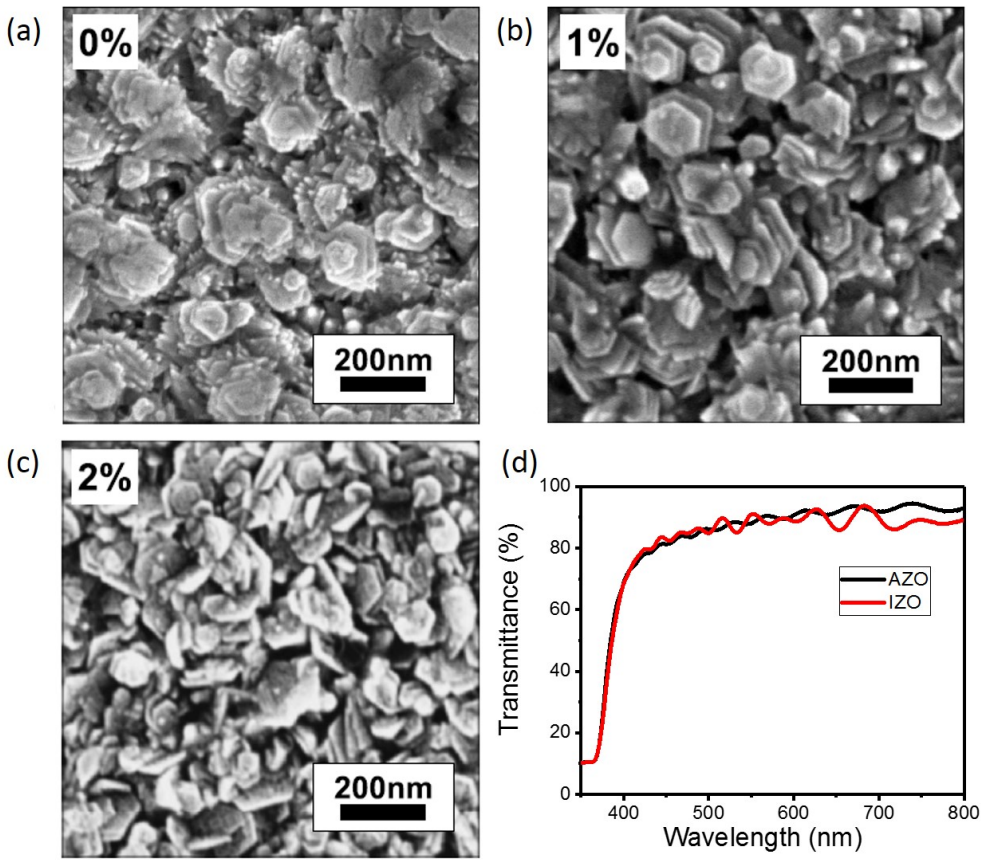

FIGURE 4.8: SEM images of ZnO films deposited via spray pyrolysis with 0%(a), 1% (b) and 2% (c) indium (In) concentration relative to Zn. Adapted from [150]. (d) Transmittance measurements of aluminium-doped (AZO) and In-doped ZnO (IZO) films.

ZnO. The number and angle of tilted stacks increased and grain size decreased as the dopant concentration was raised first to 1% (Figure 4.8(a)) and then 2% (Figure 4.8(b)). This change in preferred nucleation direction may be attributed to etching of ZnO by HCl formed by reaction between $InCl_3$ and H_2O molecules present in the solvent or from dihydrogenated zinc acetate[150]. The resulting films were of a compact nature with high transparency and clearly defined thin-film interference fringes in the visible region (Figure 4.8(d)).

Perovskite films were first deposited on ZnO:In with 2% In (IZO) and on ZnO films doped with 1% Ga and 0.8% Al and devices were fabricated as depicted in Figure 4.9(a). Current-voltage response for cells using either doped oxide was found to be similar with typical behaviour shown in Figure 4.9(b). Scanning in the reverse bias direction from 1.2V to 0V resulted in very little photocurrent output with similar-shaped JV-curves to what was observed previously for devices with ZnO nanoparticle (ZnO-NP) or iZnO deposited by spray pyrolysis on ITO as ETL. Again, slight increases in J_{sc} were found with repeated scans. A more significant increase in photocurrent was observed when the scan range was enlarged

to 1.5V-0V. This suggested that biasing the device at higher voltage raised the maximum current that could be extracted from the cell under illumination. Indeed, when the cell was held at 1.2V for one minute immediately prior to performing a scan in the reverse bias direction, a J_{sc} of over 22mA/cm^2 was observed. However, the nature of this improvement proved transient as subsequent scans decayed back towards the lower values of J_{sc} recorded for earlier scans. This behaviour under bias indicated the presence of significant energy level mismatch at the interface between photoactive layer and IZO.

Attempts were made to improve band-level matching by inserting interlayers between the IZO and perovskite layers. TiO_2 was applied but device performance remained very poor. What's more, the high temperature annealing treatment in air which was found necessary for effective charge extraction was incompatible with IZO whose electrical properties deteriorate massively at even relatively modest temperature treatment ($\geq$200 °C) in the presence of oxygen[150]. Undoped ZnO (iZnO) was also applied between IZO and perovskite (as shown in Figure 4.9(c)) but the resulting current-voltage behaviour (Figure 4.9(d)) was similar to the case of devices with perovskite deposited on ITO/iZnO. It thus became clear that photocurrent extraction for devices using the current setup was not markedly changed by simply raising the Fermi-level of the ETL towards the conduction band via doping. It should also be noted that unlike devices in which perovskite was deposited directly on ITO, shunting was largely absent from those based on IZO interfaced with perovskite as confirmed by R_{sh} of at least 1.6$\times$10$^4\Omega$cm^2 from fitting the dark-JV data (Figure 4.10(c)). One possible explanation for the difference would be that growth of more compact and pinhole-free perovskite films was favoured on IZO over ITO which could be conceivable from the point of view of nucleation dynamics on substrates with greater surface roughness[190]. However, a more likely reason would be linked to the degradation of perovskite in contact with ZnO as discussed previously.

Given that C_{60} was found to improve charge extraction from devices with ZnO-NP ETLs, it was a natural step to apply them to IZO-based devices. Spin coating a layer of C_{60} molecules on IZO before perovskite deposition (as depicted in Figure 4.10(a)) had a dramatic effect on the performance of resulting devices. Figure 4.10(b) shows the current-voltage response of the champion cell for devices consisting of IZO/ C_{60}/ Perov/ P3HT/ TiAu. As was the case for IZO/iZnO/Perov cells, initial scans in the reverse bias direction showed a peak in photocurrent around 0.7V-0.8V but the size of the peak diminished as the delay time between voltage steps was increased leading to stabilized photocurrent output with a FF of 0.67. A degree of scan-dependent hysteresis remained but even forward bias scans recorded PCE of almost 9%. The relatively high performance was all the more remarkable

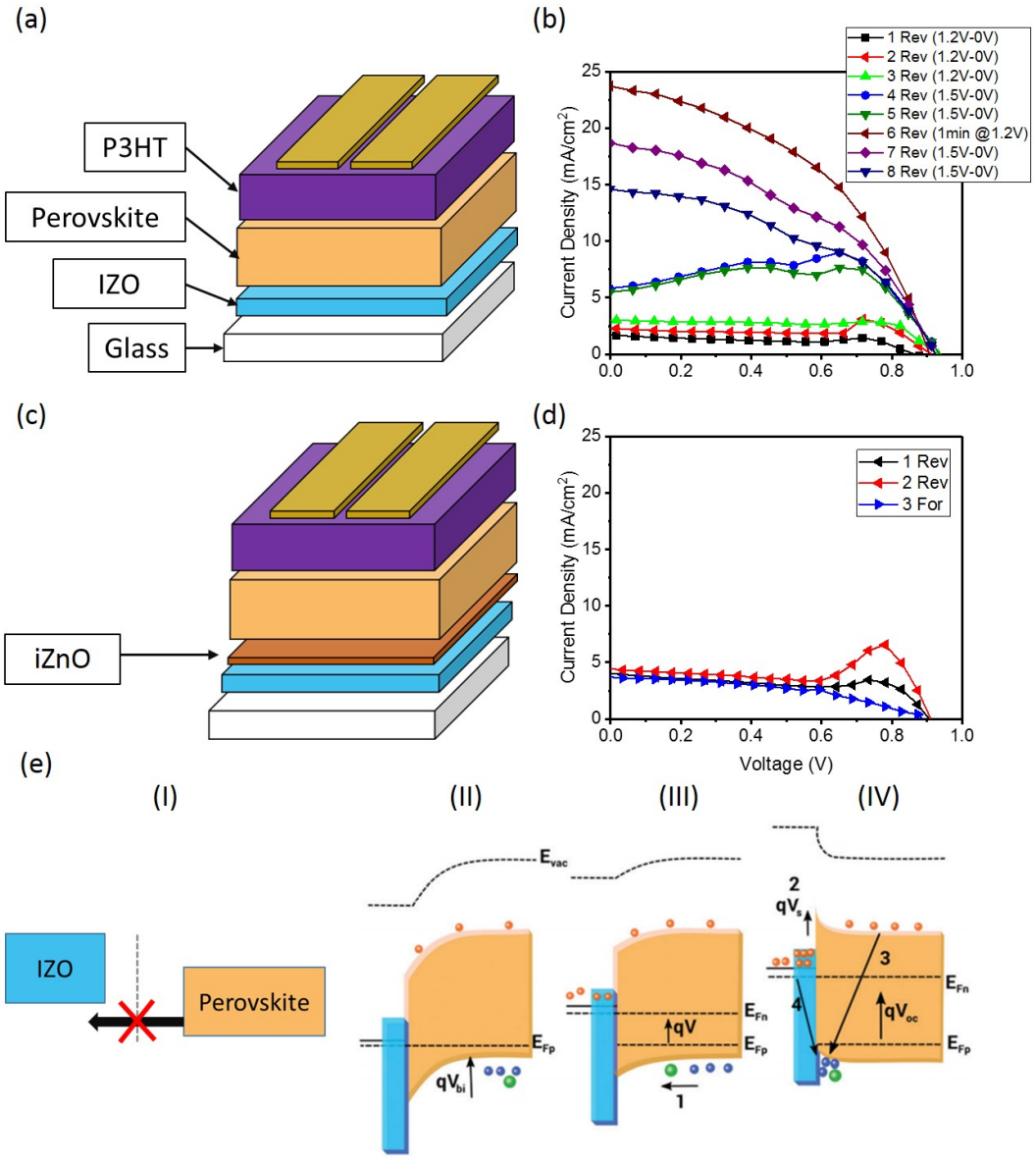

FIGURE 4.9: (a) Schematic of device stack in which ZnO doped with 2wt% indium (IZO) deposited on glass by spray pyrolysis serves as both transparent cathode and ETL. (b) Current-voltage response under illumination of cells using the stack depicted in (a). (c) Schematic of device stack in which a thin (60nm) layer of intrinsic ZnO (iZnO) was grown on IZO prior to perovskite deposition. (d) Current-voltage response of devices depicted in (c). (e) Energy level diagrams for device stack shown in (a). (I) Simplified conduction band diagram depicting energetic barrier to electron injection from perovskite into IZO. (II) Built-in potential at the perovskite/IZO interface under illumination at short circuit conditions (electrons shown in red, holes and cations in blue and green respectively). (III) Under an applied forward bias where "1" indicates kinetic drift of cations and holes towards the interface. (IV) At large forward bias (V_{oc}) the accumulation of cations and holes creates an upward band bending ("2") described by surface voltage V_s. Recombination between accumulated charges and the IZO region ("4") and with electrons in the bulk ("3") are also indicated. Adapted from [189].

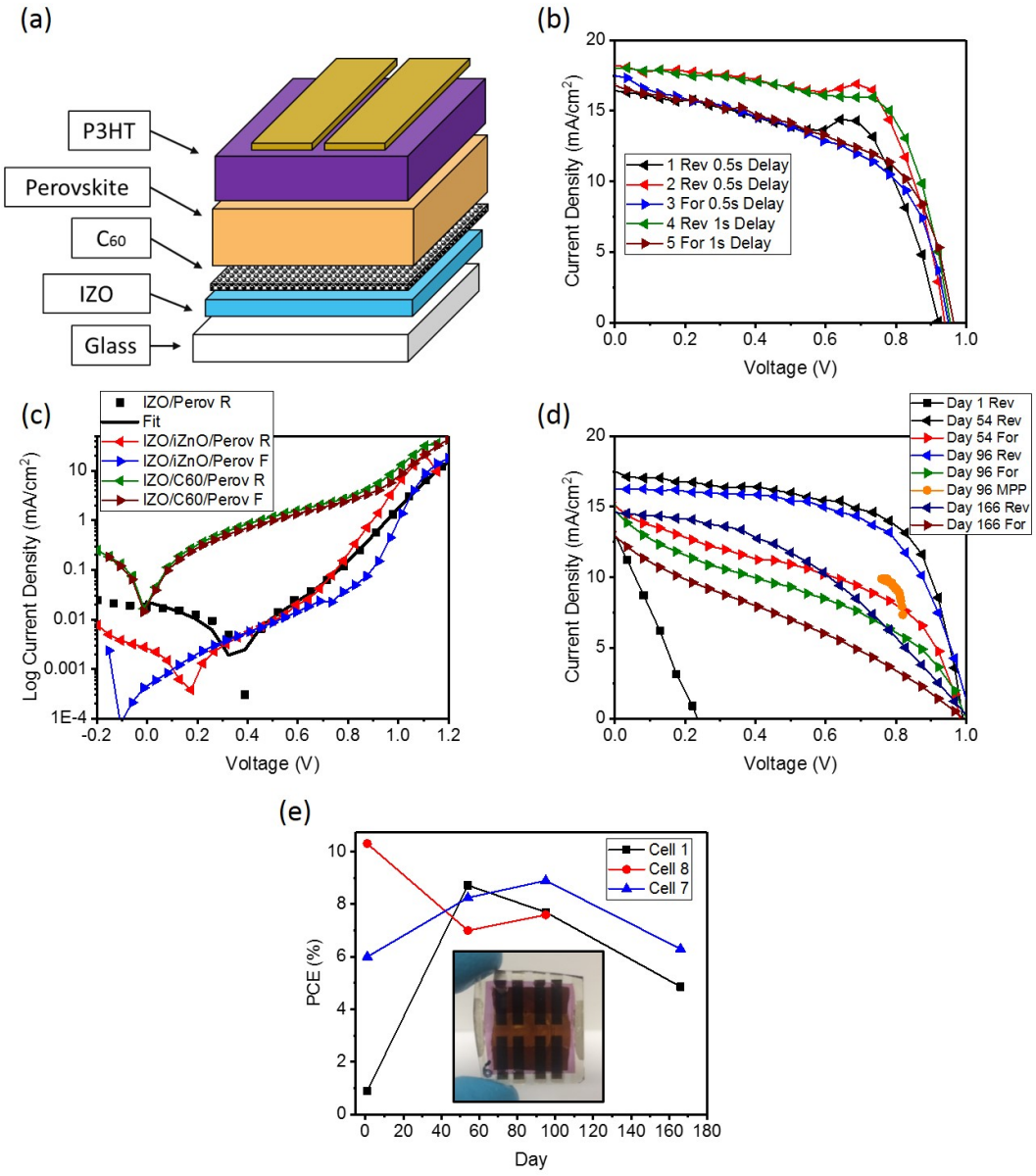

FIGURE 4.10: Current-voltage curves for different device stacks using ZnO doped with 2wt% indium (IZO) deposited by spray pyrolysis as transparent cathode. (a) JV-curves for devices in which IZO serves as both cathode and ETL. (b) Current-voltage response for cells with device stack shown in (a). (c) Semilog plots of the JV-curves in the dark for cell in (b) alongside cells from Figure 4.9. (d) Evolution of JV-curves for a cell with same structure as (a) over a period of months. (e) Plot of PCE against time for different cells on a single device consisting of IZO/C_{60}/Perov/HTL/TiAu. Inset shows device after approximately one year with yellowing visible over the horizontal IZO strip across the central area of the substrate.

given that scans in the dark displayed large current densities under low bias suggesting incomplete film coverage resulting in a large degree of shunting. Two facts combined to explain the result. Firstly, a non-homogeneous thin film of C_{60} molecules was to be expected in the absence of a crosslinking agent given their partial solubility in DMF used for perovskite deposition together with the fact that C_{60} itself was deposited via spin coating. Secondly, a low R_{sh} indicated more incomplete coverage of the photoactive layer relative to devices without fullerenes. Indeed, many cells on the device with champion performance were so severely shunted that PCE remained low. The reason for incomplete perovskite coverage was unclear but an interesting phenomenon occurred over time. An example is illustrated in Figure 4.10(d) where a cell (referred to as "Cell 1") which was initially highly shunted (i.e. on Day 1) displayed much improved R_{sh} when measured again almost two months later, with a V_{oc} of over 1V. After 96 days the performance did begin to deteriorate with a maximum PCE of 7.7% extracted under constant bias (MPP), roughly the average of values suggested by reverse and forward bias scans. A significantly larger R_s was present after 166 days but the cell still displayed a PCE of almost 5% as shown in plot of PCE against time in Figure 4.10(e). The net result was that PCE of the champion cell (referred to as "Cell 8") converged with other cells up to 96 days after initial testing before following a similar trend of gradual deterioration in power output thereafter. One possible explanation for this result would be that a change in photoactive layer morphology brought about by perovskite decomposition could act to fill gaps in the film and improve R_{sh} and hence PCE. Although its exact influence on device performance remains something of an open question, PbI_2 left behind as a decomposition product could fulfill this role, resulting in at least a temporary improvement in cell performance. This hypothesis would be consistent with visible yellowing of the device active area with time (inset of Figure 4.10(e)) and SEM images of aged perovskite films shown in Chapter 5.

4.3.2 Doped binary oxides in conjunction with fullerenes for indium-free fully solution processed solar cells

Performance of devices using C_{60} as surface modifier to improve photoexcited electron extraction from perovskite to IZO was highly encouraging considering the low cost nature of the solution deposition methods used for all layers (i.e. spray pyrolysis and spin coating) coupled with much lower content of indium used in the transparent cathode relative to sputtered ITO (2%-3% $InCl_3$ in IZO films versus approximately 74%-90% In_2O_3 in ITO)[191][192]. However, devices displayed low shunt resistance with many poor-functioning cells on a

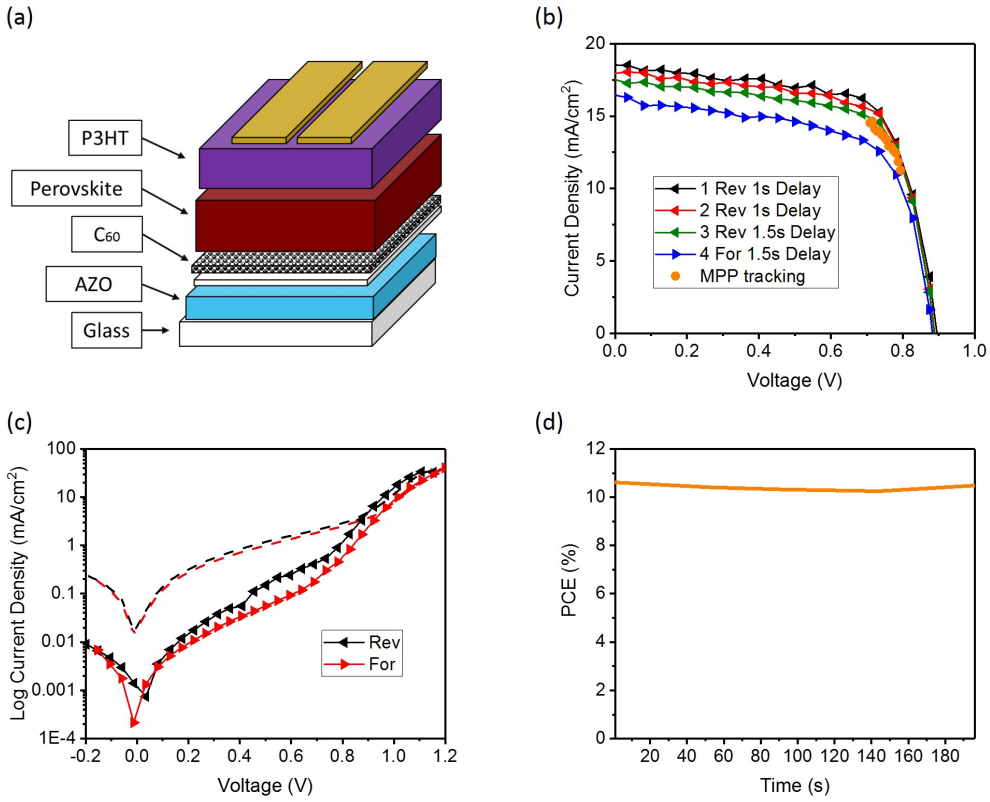

FIGURE 4.11: (a) Current-voltage curves for champion cell with AZO as TCO. (b) Semilog plot of dark-JV curves for AZO cell shown in (a) with IZO/C_{60}/Perov data from Figure **??**(c) represented by dashed lines for comparison. (c) Plot of PCE extracted from maximum power point tracking against time for cell shown in (a).

given freshly prepared device which is undesirable from the point of view of commercialisation. Furthermore, to take full advantage of the financial savings associated with solution processed transparent conducting oxides (TCOs) it would be better to avoid the use of indium entirely. Despite its roughly factor of 2 lower conductivity than the best achieved for ZnO:In, Al-doped ZnO (AZO) maintains excellent transparency (Figure 4.8(d)) and the combination of facile texturing during or after processing coupled with abundance and non-toxicity of its constituents makes AZO a truly low cost and attractive alternative to ITO.

Steps taken to achieve high performing devices using AZO as TCO involved optimizing processing parameters during device fabrication. For example, owing to the micrometer-scale thickness used to guarantee sheet resistance below 80Ω/sq, minimal patterning of AZO was found to be beneficial (due to the combined thickness of other device layers being less than 1μm) as was coating a layer of nail varnish along the etched edge. In this way, any shunting paths created by direct contact between TiAu and AZO along edge of the AZO were avoided. Another measure found to enhance performance involved optimizing the

precursor composition used in fabricating the perovskite layer which forms the basis of experiments carried out in Chapter 5. Finally, deposition conditions for the C_{60}-based ETL were found to be important for reproducibility of device performance as discussed towards the end of this chapter. The combination of these factors resulted in devices with an average PCE of 10.05% and a ratio of standard deviation to mean PCE of 0.07. The current-voltage response of the champion cell is shown in Figure 4.11(a). Although hysteresis remained present with a FF of 0.64 under forward bias and 0.68 for reverse bias scans, applying a constant bias near the maximum power point confirmed that scans in the reverse bias direction were representative of device behaviour under true operating conditions. Furthermore, the maximum power extracted from the cell was stable over at least a few minutes under constant bias and illumination as shown in Figure 4.11(c). At least one factor contributing to the improved performance relative to initial devices fabricated on IZO was increased R_{sh} as suggested by the lower dark current under low bias in Figure 4.11(b).

4.4 Sputtered metal oxides

Sputter coating has been used in recent years for the preparation on hole-blocking layers for solar cells[49] [193] [174][194] [195]. Radio frequency magnetron sputtering (RFMS) in particular has been employed with varying degrees of success, with high efficiencies having been reported even without high temperature treatments [46] [195]. TiO_2 grown by RFMS technique has the advantage of being able to grow uniform pinhole-free films with carefully controlled layer thickness and substrates greater than 3m in width can be coated in industrial scale systems [196] [197]. Additionally, the possibility of low temperature processing is attractive for flexible substrates [198] and thus worthy of attention. In this way, the costs associated with a vacuum-based technique together with the engineering complexity of radio frequency magnetron controlled sputtering can be at least partially offset by relatively large area deposition compatible with roll-to-roll processing

TiO_2 films with thicknesses of 10nm and 20nm were first deposited on ITO-glass substrates and devices fabricated. Figure 4.12(a) shows the JV-response measured from open circuit voltage to short circuit current of a device comprising 10nm thick TiO_2 as ETL sputtered at room temperature with a 5-minute UV ozone treatment to improve wettability and surface coverage by perovskite. Initial scans showed a high series resistance when measuring from 1.2V-(-0.2V). However, increasing the scan range to measure from 1.35V and then from 1.5V to (-0.2V) resulted in an (artificially) decreased series resistance and an associated improvement in fill factor and J_{sc}. Similar to what was observed for devices where

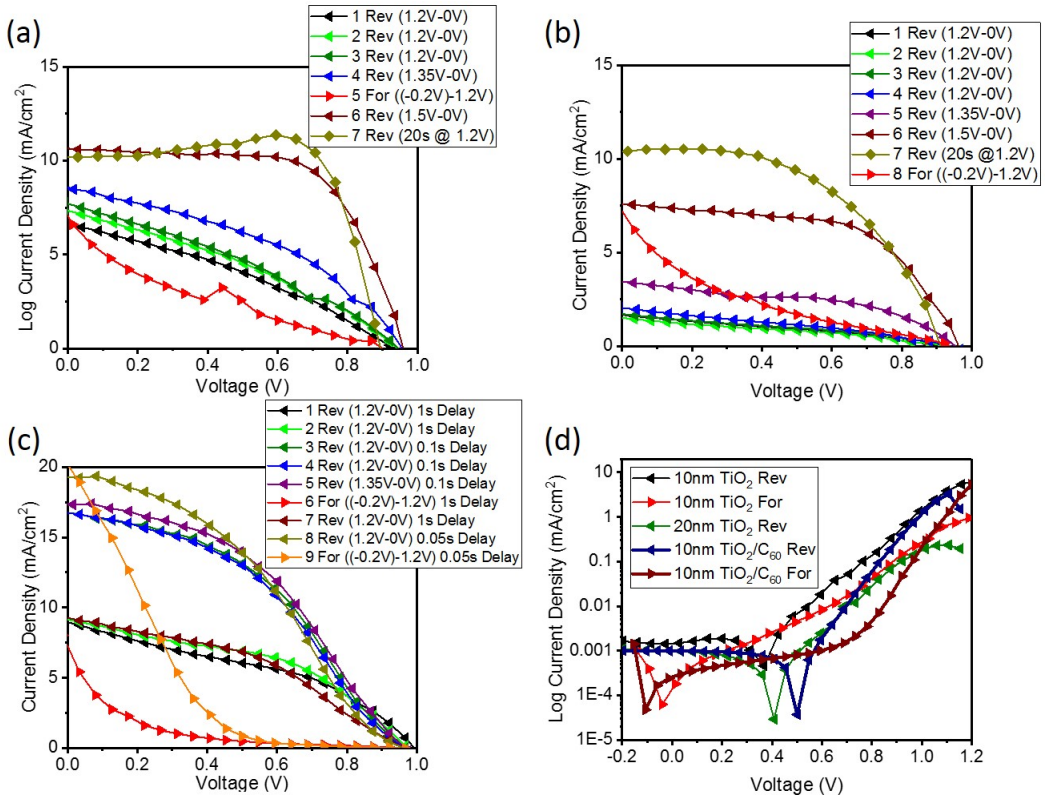

FIGURE 4.12: Current-voltage response of devices with metal oxide ETLs processed at room temperature. (a) Typical response of cells with 10nm thick TiO_2 deposited by RFMS as ETL. (b) Typical response of cells with 20nm thick TiO_2 as ETL (c) JV-response of cells with structure ITO/TiO_2(10nm)/C_{60}/Perov/P3HT/TiAu. (d) Semilog plots of scans performed in the dark for devices in (a), (b) and (c).

IZO was interfaced directly with perovskite, holding the cell at voltages above V_{oc} for 20 seconds immediately prior to performing the scan resulted in an apparent improvement in device performance. However, in the case of TiO_2 the decay in photocurrent was more rapid resulting in a slight peak at around 0.65V. When the scan direction was reversed (i.e. scanning from J_{sc} to V_{oc}), a very pronounced hysteresis was observed with low photocurrents measured. Increasing the thickness of TiO_2 to 20nm resulted in similar device behaviour (Figure 4.12(b)) although the maximum power extracted from cells under the same testing conditions was somewhat lower. This was due to a larger R_s consistent with a thicker ETL and when coupled with the dark-JV curves suggests that shunting is not the limiting factor in such devices.

The severe hysteresis and scan rate-dependent JV can be explained by a combination of possible mechanisms. Defect states are inherent in more amorphous materials and higher densities of such states have been shown to enable significant charge transport at least 0.8 - 2.0eV below the conduction band edge of TiO_2 [199][200]. The presence of such states within

the bandgap may cause unwanted recombination through electron injection from anode to perovskite (shunting effect) or may trap photogenerated electrons resulting in a lower photocurrent. Additionally, the improvement in photocurrent for reverse bias scans after prebiasing the cells at large (greater than V_{oc}) positive voltage would suggest the presence of an energy barrier for electron extraction due to mismatch between the conduction bands (CB) of the active layer and TiO_2. When no bias is applied to the cell, the CB of TiO_2 is raised relative to the CB of perovskite, thereby presenting an energy barrier for the extraction of photoexcited electrons. When the cell is held in reverse bias whilst illuminated, Fermi-level splitting results in an increased barrier to charge extraction as the CB of the ETL is raised further relative to that of the perovskite. Conversely, when the cell is under forward bias, the barrier to electron extraction is reduced and photocurrent is more readily produced.

In an attempt to passivate surface defects and to possibly improve band level matching for electron extraction, devices were fabricated with a layer of C_{60} molecules spin coated from solution onto UV ozone-treated 10nm thick TiO_2 films. Typical JV-curves for such devices under different scan rates and directions is shown in Figure 4.12(c). Although relatively high J_{sc} was recorded for intermediate and fast (i.e. $0.92V/s$) scan rates in the reverse bias direction, the series resistance remained high for all scan speeds. The effect was even more pronounced for scans in the forward bias direction. Such behaviour is consistent both with the high R_s and R_{sh} obtained from fits to the dark-JV curves and with the hypothesis of significant band level mismatch between TiO_2 and perovskite.

Having established that room temperature processed TiO_2 deposited via RFMS from a ceramic target under and argon atmosphere is unsuitable for high efficiency perovskite cells using the current setup, alternative ETLs were sought. Zinc oxide was the obvious candidate due to its improved electrical characteristics allowing for better performance using near ambient processing techniques. Additionally, it was hoped that there would be improved stability of perovskite films in direct contact with sputtered ZnO due to a lack of residual organic species associated with solution processed films. ZnO films with a thickness of 20nm were grown at room temperature (hereafter referred to as "RT-ZnO") from a ceramic target on ITO-coated glass slides.

As seen in Figure 4.13(a), cells with structure ITO/ RT-ZnO/ Perov/ HTL/ TiAu showed reduced hysteresis relative to devices with room temperature sputtered TiO_2 of equal thickness (20nm), although they still behaved similarly to what was observed for iZnO and ZnO-NP ETLs in that J_{sc} remained low. Clearly significant recombination was taking place resulting in only modest photovolatic conversion efficiency. Furthermore, PCE declined with successive scans as shown in Figure 4.13(b). As was the case for devices with spin coated

ZnO-NP films, application of C_{60} as surface modifier had a dramatic effect on photocurrent extracted from cells with RT-ZnO (Figure 4.13(c)) with J_{sc} under reverse bias approaching 20mA/cm^2. However, both J_{sc} and FF declined with successive scans. Device degradation was obvious when a slow scan was performed over a reduced voltage range from 0.8V-0.73V as the photocurrent fell over the 5-minute period from 14mA/cm^2 to 11mA/cm^2 as the applied bias was gradually decreased. Curiously, devices made with C_{60} deposited on ZnO grown at 300 °C were highly shunted. The combination of a low R_{sh} of 400Ωcm^2 extracted from fitting the dark-JV curve with an R_s of over 10Ωcm^2 resulted in modest device performance as shown in Figure 4.13(d). However, annealing the ZnO films at 320 °C under an N_2 atmosphere before coating C_{60} resulted in much improved device performance. As was the case for devices with perovskite coated directly upon N_2 annealed iZnO deposited by spray pyrolysis, a peak in photocurrent remained present for initial reverse bias scans as shown in Figure 4.13(e). However, the peak was less pronounced than for the other device configurations and reduced with successive scans. A significant degree of hysteresis was still present but slow scans in a reduced voltage range around the maximum power point (MPP) ensured that reverse bias scans were indeed representative of the true conversion efficiency under operating conditions with a maximum power output of 14.6% under one sun illumination. The lack of an initial peak in photocurrent upon illuminating the cell around the MPP and steady output thereafter as shown in Figure 4.13(f) suggested a reduction in charge-trapping and an improved stability relative to the non-annealed ETLs.

It was soon realised that as-deposited ZnO rapidly degraded perovskite upon heating no higher than 100 °C. Figure 4.14(a) shows the x-ray diffraction pattern of a freshly deposited perovskite film on ZnO. After heating on a hotplate for 10 minutes at 100 °C, peaks associated with PbI_2 grew significantly at the expense of those associated with perovskite. A control film grown on glass on the other hand saw only an increase in crystallinity upon annealing. Scrubbing the sputtered ZnO films with detergent (Alconox) followed by sonication treatments in acetone, deionised water and IPA was found to improve the stability as perovskite was capable of withstanding at least 10 minutes of annealing with little or no degradation.

Typical JV-scans of a device comprising perovskite on RT-ZnO after copious scrubbing with detergent and solvent washing and sonication steps is shown in Figure 4.14(b). Fitting the data from scans performed in the dark (Figure 4.14(d)) revealed that devices had a strong resistance to shunting with R_{sh} of between 2×10^5Ωcm^2 and 9×10^5Ωcm^2 depending on scan direction. However, R_s of over 20Ωcm^2 for reverse scans and 23.6Ωcm^2 for forward bias resulted in J_{sc} of approximately 6mA/cm^2. As previously discussed, large R_s may be due

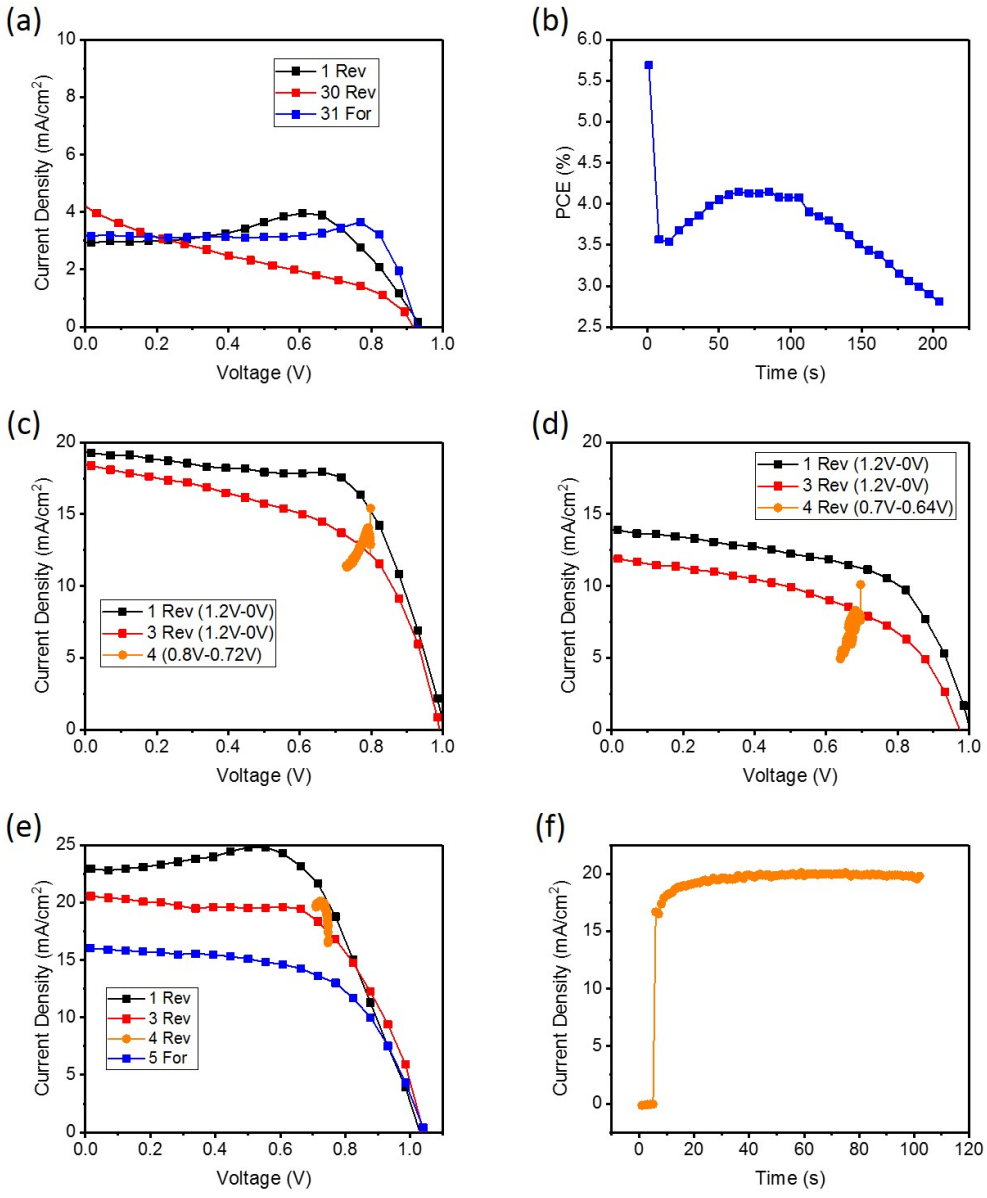

FIGURE 4.13: Current-voltage response of devices with 20nm thick sputtered ZnO ETLs. (a) Device consisting of room temperature deposited ZnO interfaced with perovskite. (b) Evolution of PCE with time for cell shown in (a). (c) JV-response of cells with structure ITO/ZnO(@RT)/C_{60}/Perov/HTL/TiAu. (d) Typical response of a device with the same structure as (c) but where ZnO was grown at 300 °C. (e) JV-response of a device with same structure as (d) but where ZnO film was post-annealed at 320 °C under N_2. (f) evolution of photocurrent under constant bias near the maximum power point for cell shown in (e) going from dark to illumination.

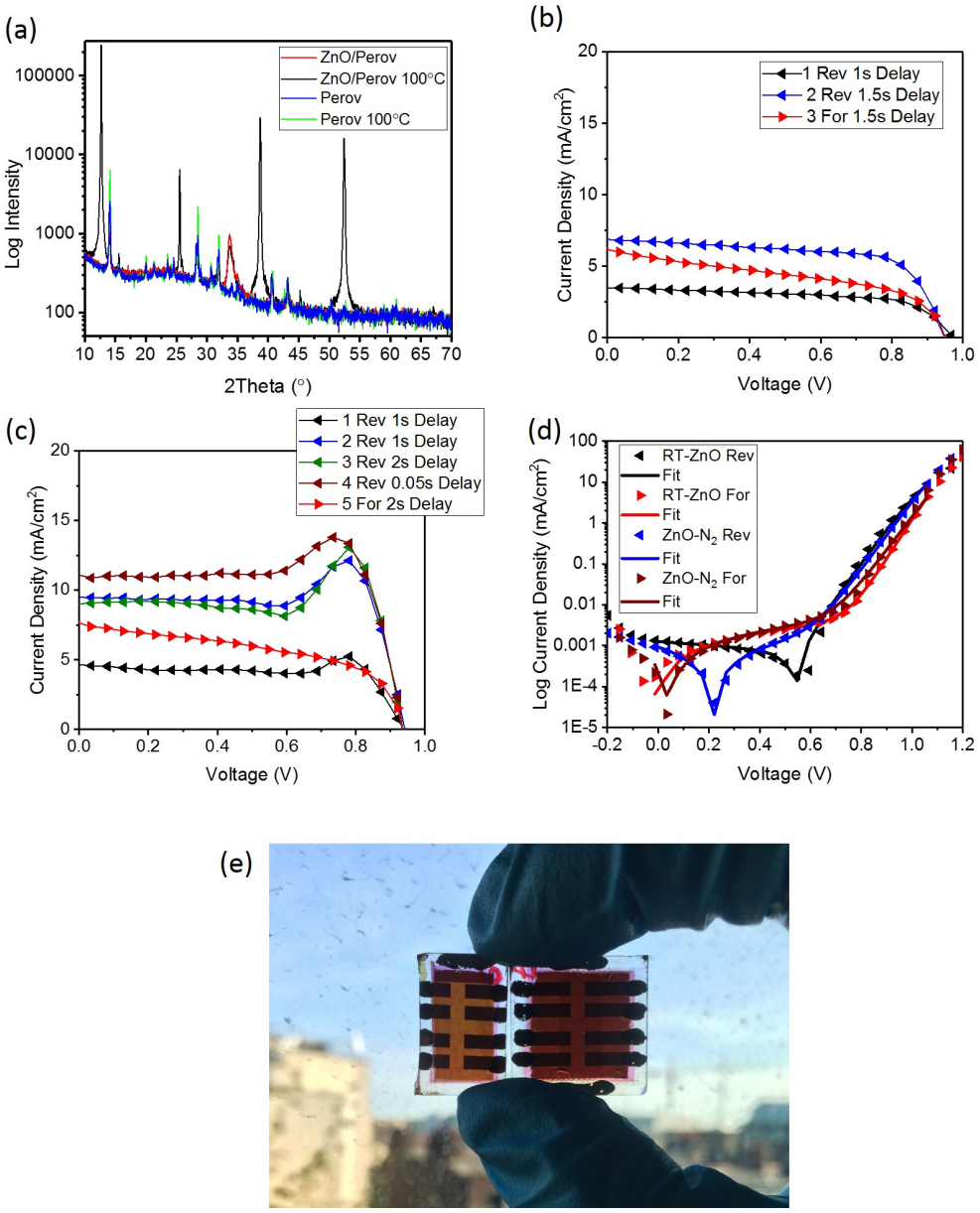

FIGURE 4.14: (a) XRD of perovskite films on glass and on as-grown sputtered ZnO films before and after annealing treatment(b) Current-voltage response of devices with 20nm thick ZnO sputtered at room temperature. (c) Response of devices with ZnO grown at 300 °C and post-annealed under N_2 at 320 °C. (d) Semilog plot of scans performed in the dark for cells shown in (b) and (c) with fits using the diode model. (e) Image of device with N_2-annealed sputtered ZnO film (left) beside a ZnO-free device after a few months storage in ambient conditions in the dark.

	J_{sc} (mA/cm^2)	V_{oc} (V)	FF	PCE(%)
RT-ZnO (Rev.)	6.9	0.95	0.66	4.32
RT-ZnO (For.)	6.04	0.95	0.46	2.68
ZnO-N_2 (Rev.)	11.54	0.94	0.81	8.8
ZnO-N_2 (For.)	7.6	0.94	0.52	3.69

TABLE 4.4: Extracted device parameters for devices with 20nm ZnO deposited by sputtering either at room temperature (RT-ZnO) or at at 300 °C with subsequent annealing at 320 °C under nitrogen (ZnO-N_2).

	R_s(Ωcm^2)	R_{sh}(Ωcm^2)	J_0 (mA/cm^2)	n_{id}
RT-ZnO (Rev.)	6.4	6.9×10^5	2.8×10^{-9}	1.78
RT-ZnO (For.)	1.08	1.95×10^5	2×10^{-10}	1.73
ZnO-N_2 (Rev.)	1.2	2.33×10^5	1.2×10^{-8}	1.99
ZnO-N_2 (For.)	0.23	1.65×10^5	9.3×10^{-9}	2.06

TABLE 4.5: Extracted device parameters for devices with 20nm ZnO deposited by sputtering either at room temperature (RT-ZnO) or at at 300 °C with subsequent annealing at 320 °C under nitrogen (ZnO-N_2).

to recombination caused by defects within or at the surface of the ETL. Therefore, zinc oxide films were annealed under a nitrogen (N_2) atmosphere in an attempt to passivate defects and hence improve device performance. Devices fabricated with N_2-annealed ZnO did indeed show some improvement in photocurrent as shown in Figure 4.14 (c). However, the presence of a peak near the maximum power point which grew as the scan speed decreased in the reverse bias direction resulted in significant hysteresis and signified charge trapping in the device. Accordingly, R_s and FF were measured to be 11.44Ωcm^2 and 0.51 in forward bias direction and 6.43Ωcm^2 and 0.77 in reverse bias respectively as extracted from fits to the data. True conversion efficiency most likely lay therefore between the 3.68% and 8.45% suggested by fits to each scan direction.

4.5 Metal oxide-free electron selective layers

Having observed the effectiveness of solution-processed C_{60} in increasing photocurrent in conjunction with metal oxide ETLs, it seemed natural to establish whether a fullerene-based layer could be used as the sole ETL material. To date, fullerenes and their derivatives such as PCBM have mostly been used in inverted architectures due to the solubility of PCBM in solvents typically used for perovskite deposition and the fact that C_{60} can be coated conformally onto rough perovskite layers via thermal evaporation. However as already mentioned, inverted devices generally require more controlled processing conditions and are

more prone to rapid degradation in humid and oxygen-rich environments. Although pristine C_{60} has limited solubility in most solvents, thereby limiting the maximum attainable film thickness, it was reasoned that the lack of solubilizing chains would improve integrity of the ETL upon exposure to solvents during the deposition of subsequent layers.

Fullerenes were dispersed in dichlorobenzene (DCB) at a concentration of 10mg/mL by mild shaking and were deposited via spin coating at 1500rpm for 50s followed by annealing on a hotplate for 2 minutes at 100 °C. It was found necessary to subject ITO substrates to 10 minutes of UV ozone treatment prior to coating C_{60}. Devices were first fabricated with structure ITO/ C_{60}/ Perovskite/ P3HT/ TiAu as depicted in Figure 4.15(a). Although the JV-response in the dark revealed significant shunting in the absence of a metal oxide hole-blocking layer (Figure 4.15(b) and (d)), initial sweeps showed high J_{sc} in both scan directions. Slow scans around the maximum power point (MPP) confirmed high performance, although the power output tended to degrade under repeated scans and at near constant applied bias under illumination. The exact mechanism of the degradation was unclear but it was evident that a solution-processed C_{60} layer on its own was not sufficient for consistent and reliable device performance.

It was wondered whether a polymer could be used in conjunction with C_{60} to improve surface coverage and shunt resistance. Polyethylenimine (PEI) is a simple aliphatic polymer containing many amine groups organised in either linear, branched or dendritic form. It has found many areas of application, particularly in fields that can exploit its polycationic nature. It has been used as an adhesion promoter in biological applications [201] and as an additive to coatings and printing inks, cosmetics and detergents [202]. Another area of application is in carbon dioxide capture, either impregnated upon a porous scaffold or by cross-linking [203] . Although polyethyleneimines lack π - conjugation and are thus large bandgap insulators, it has been demonstrated that branched PEI and PEI-ethoxylated (PEIE) can act as electrode surface modifiers in organic electronics [204] and as n-type dopant for ETLs in organic photovoltaic (OPV) devices [158]. These properties have naturally begun to find use in perovskite solar cells. For example, a thin layer of PEI has been used as a buffer layer between perovskite and zinc oxide [167] and more recently as a dual functional additive in the fullerene electron accepting layer of an inverted perovskite solar cell [205]. It has also been shown to improve the wetting of perovskite precursor in inverted devices, thereby demonstrating that it is not limited in application to facilitating electron collection [206].

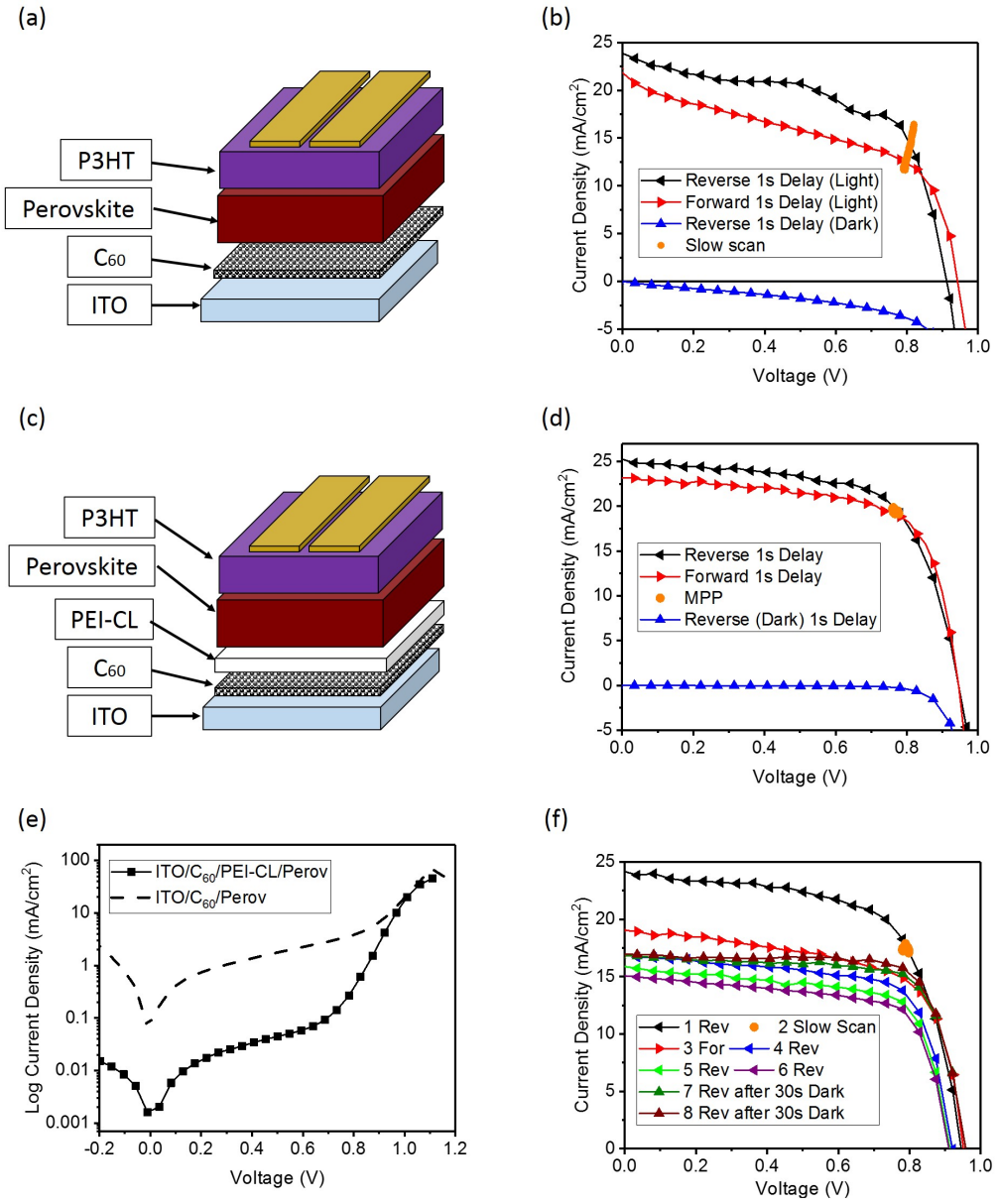

FIGURE 4.15: (a) Schematic of device with C_{60} as ETL between ITO and perovskite. (b) Typical current-voltage response of device shown in (a). (c) Schematic of device with a layer of cross-linked polyethylenimine (PEI-CL) between C_{60} and perovskite. (d) JV-response of champion cell with structure ITO/C_{60}/PEI-CL/Perov/HTL/TiAu. (e) Semilog plot of JV-scans in the dark for cells shown in (b) and (d). (f) Response of cell with same structure as (c) under repeated scans with 1s delay time between voltage steps under illumination and after short rest time in the dark.

In an effort to protect C_{60} from partial removal by DMF during the deposition of perovskite precursors, PEI was first applied on top of the fullerene layer along with the crosslinking agent Poly(propylene glycol) diglycidyl ether (hereafter referred to as "PEI-CL") in a manner developed for OPV fabrication [207]. A device stack consisting of ITO/ C_{60}/ PEI-CL/ Perovskite/ HTL/ TiAu is depicted in Figure 4.15(c). The presence of a thin layer of PEI-CL improved fill factor and reduced hysteresis (Figure 4.15(d)) resulting in a maximum power output of 15.1mW/cm^2. The dark current was markedly reduced relative to C_{60}-only cells as shown in Figure 4.15(e). Furthermore, unlike C_{60}-only devices, cells with a PEI-CL capping layer displayed a much more stable output under constant bias. A curious effect was noted whereby successive reverse bias scans under constant illumination recorded lower J_{sc} and V_{oc} (and hence maximum power output) as shown in Figure 4.15(f). However, upon resting the cell for 30 seconds in the dark before performing a repeat scan the JV-characteristics began to recover, approaching the maximum power output given by the slow scan. This behaviour suggests a certain photoinduced capacitance-voltage (CV) signal which has recently been attributed to bulk polarization as well as polarization states at the interface which may affect carrier transport and recombination [208] [209] [210].

Despite the improved device performance with the polymer capping layer, some cells continued to exhibit shunting behaviour. This was attributed to non-uniform surface coverage of C_{60} on ITO. Indeed, it was observed that C_{60} deposited on clean glass or ITO substrates did not always form a uniform film, even though the substrates were UV-ozone treated. As already mentioned, PEI has been used as an adhesion promoter and so it was reasoned that a layer of PEI deposited on ITO would improve the uniformity of C_{60} coverage. This hypothesis was confirmed visually and via absorption spectroscopy as shown in Figure 4.16(a). Spin coating DMF on top of the films removed a significant portion of C_{60} molecules from both but more of a film remained for the PEI/C_{60} sample. This result corresponds well with a recent publication in which thermally evaporated C_{60} was deposited on PEIE [211]. Cell-to-cell variation in devices comprising ITO/ PEI/ C_{60}/ Perov/ P3HT/ TiAu was lower than that for devices with C_{60}/PEI-CL ETLs, resulting in a higher mean efficiency and lower standard deviation based on 8 cells per substrate. However, PEI/C_{60}-based devices tended to be more shunted due to the lack of protective effect afforded by PEI-CL to C_{60} removal by DMF during perovskite deposition.

These results raised the question of whether device performance could be maximized by combining the two techniques resulting in C_{60} films with good uniformity and thickness after perovskite deposition. As seen in Figure 4.16(b), although the PEI/ C_{60} film was slightly affected during coating of PEI-CL, the resulting stack was much more robust to subsequent

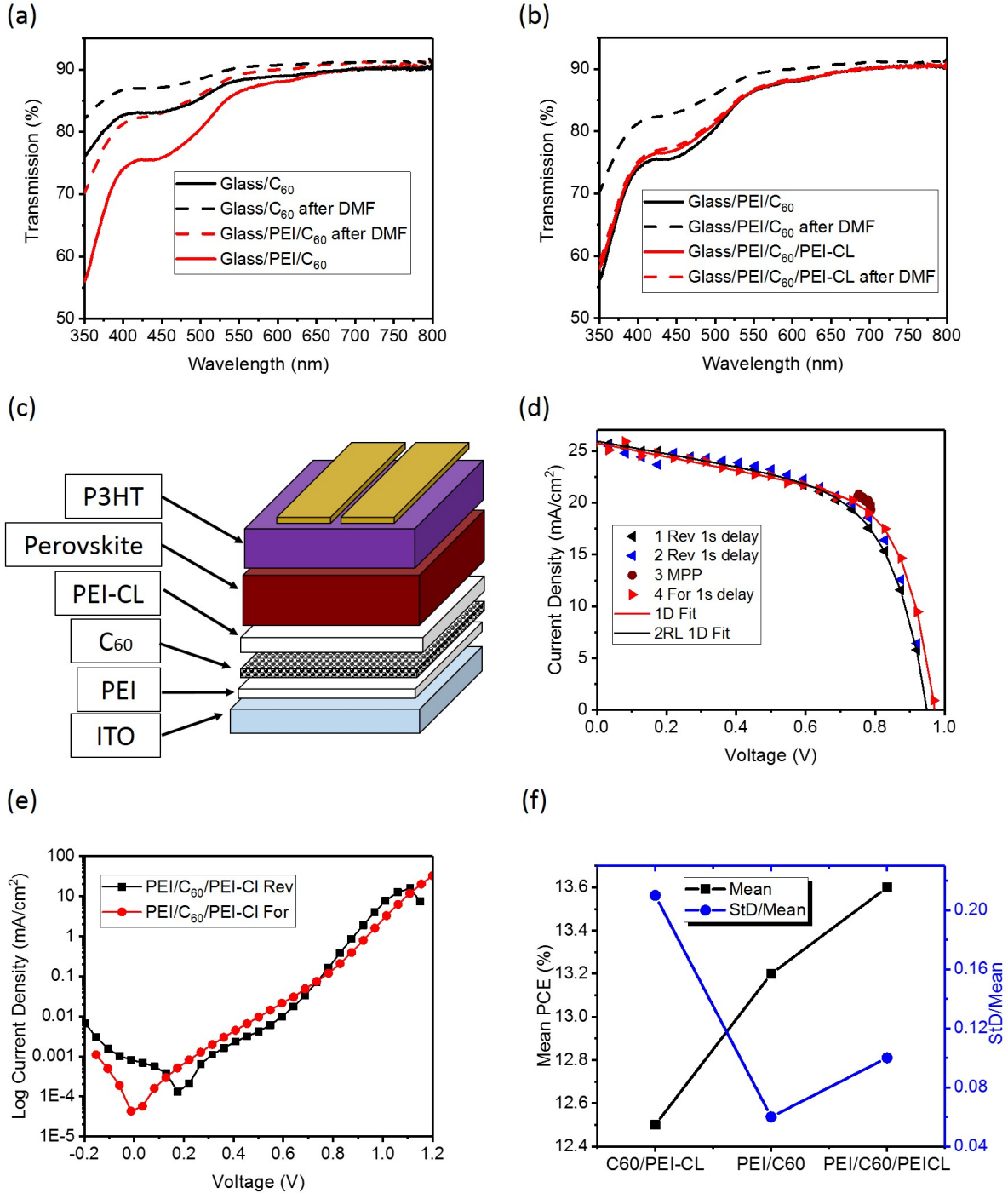

FIGURE 4.16: (a) Transmission measurements of Glass/ C_{60} and Glass/ PEI/ C_{60} before and after spin coating DMF. (b) Transmission measurements of Glass/ PEI/ C_{60} and Glass/ PEI/ C_{60} / PEI-CL before and after spin coating DMF. (c) Schematic of device with C_{60} coated onto a layer of polyethylenimine (PEI) and cross-linked polyethylenimine (PEI-CL) between C_{60} and perovskite. (d) Typical JV curves for cells comprising ITO/ PEI/ C_{60}/ PEI-CL/ Perovskite/ P3HT/ TiAu. (c) . (e) Semilog plot of JV scans in the dark for device shown in (c). (f) Comparison of mean PCE and the ratio of standard deviation to mean PCE (StD/Mean) for a batch of devices with ETLs comprising C_{60}/PEI-CL, PEI/C_{60} and PEI/C_{60}/PEI-CL.

DMF exposure. Devices made with PEI/ C_{60}/ PEI-CL as ETL, depicted in Figure 4.16(c), displayed low dark current under bias (Figure 4.16(e)) which resulted in high efficiency devices as shown in Figure 4.16(d). Fitting the forward bias scan as shown in the figure gave a FF of 0.6, V_{oc} of 0.97V and R_s of 4.16Ωcm^2 which were all improvements on the PEI/C_{60} reference. However, some cells showed similar power conversion efficiency (PCE) to the PEI/C_{60} devices which may be attributed to disruption of the C_{60} film due to interaction between underlying PEI and butanol used to deposit PEI-CL. Figure 4.16(f) compares mean PCE and the ratio of standard deviation to mean PCE (based on 8 cells per device) for three devices each using a different fullerene-based ETL. Mean PCE rose when C_{60} was coated onto ITO whose surface had been modified by application a thin layer of PEI relative to C_{60} on ITO. Transmission measurements of films before and after spin coating DMF suggested that the increased PCE was largely due to improved surface coverage of C_{60} on PEI rather than bare ITO, which resulted in reduced cell-to-cell variation and hence lower ratio between standard deviation and mean PCE (StD/Mean). Devices in which PEI/C_{60} bilayers had been coated with PEI-CL saw a further increase in mean PCE due to protection afforded to the C_{60} layer by the crosslinked polymer. However, the slight increase in mean PCE was accompanied by a larger standard deviation (StD) resulting in a higher StD/Mean.

4.5.1 Optimizing polyethylenimine thickness

As part of device optimization, it was important to test the dependence of device performance on PEI thickness. Figure 4.17(a) shows how mean efficiency (measured via slow scans in the reverse bias direction on fresh devices) varies with increasing PEI concentration. Each data point is accompanied by a standard deviation calculated based on a minimum of 8 cells. As previously mentioned, respectable device efficiencies were achievable with C_{60} coated directly upon ITO, however substrates required UV ozone treatment immediately prior to deposition and still often resulted in poor surface coverage which led to large batch-to-batch variability. Furthermore C_{60}-only devices were significantly shunted with lower V_{oc} and sometimes degraded rapidly under a constant applied load and illumination. When a very dilute solution of PEI in 1-butanol (0.05 mg/mL) was spun on ITO before coating C_{60} there was a corresponding drop in conversion efficiency and an increase in standard deviation. However, increasing the concentration to 0.135mg/mL had a different effect, raising the mean efficiency above 13% with a reduced standard deviation. When the concentration was increased to 0.202 mg/mL and 0.27 mg/mL there was a slight decrease in mean efficiency but it was only at concentrations above 0.337 mg/mL that the mean efficiency dropped below that which could be achieved using C_{60}-only ETLs. Increasing the PEI concentration

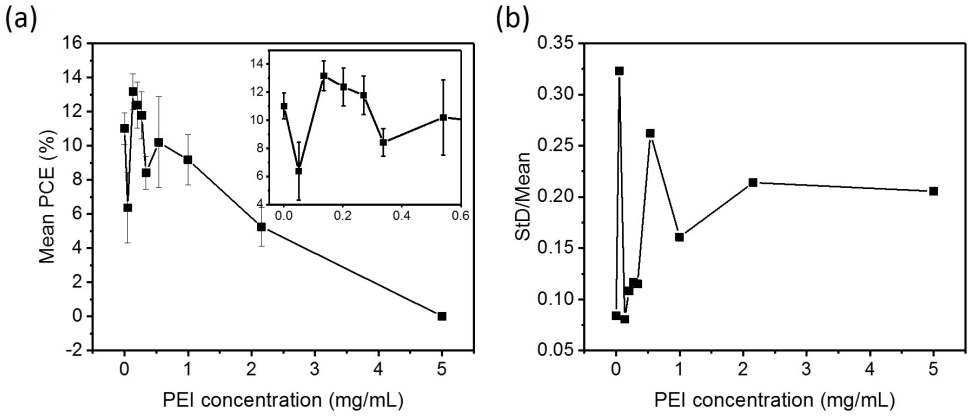

FIGURE 4.17: (a) Variation of mean PCE with concentration (and hence thickness) of the PEI adhesion layer for a batch of devices comprising ITO/PEI/C_{60}/Perov/HTL/TiAu. (b) Ratio of standard deviation to mean PCE against PEI concentration for devices shown in (a).

yet further to 2.16 mg/mL markedly reduced device performance and concentrations of 5 mg/mL and above resulted in negligible device output. Plotting the ratio of standard deviation to mean PCE against PEI concentration as in Figure 4.17(b) revealed a general trend of decreasing ratio as the concentration was reduced.

This trend in device performance may be explained as follows: very low PEI concentration (i.e. 0.05 mg/mL) was insufficient for providing a conformal coating of polymer upon ITO which resulted in regions of different surface energy and hydrophilicity and hence uneven C_{60} coverage. Concentrations above 0.135 mg/mL were enough to fully coat the ITO surface and thus provide improved adhesion of C_{60} molecules during spin coating but the insulating nature of PEI resulted in an increasing R_s as the PEI layer was made thicker with correspondingly lower photocurrent. Although 0.135 mg/mL was found to give the best device performance during thickness optimization studies, some batch-to-batch variation was noted. Presumably this was due to the very dilute solution only barely covering the entire surface of ITO resulting in a heightened sensitivity to any variation in concentration. On the other hand, it was observed that a (nominal) concentration of 0.27 mg/mL was more forgiving in this regard resulting in better batch-to-batch reproducibility. For this reason 0.27 mg/mL was used as the standard PEI concentration for further experiments.

4.5.2 Varying C_{60} concentration

The effect of C_{60} concentration on device performance was studied with the hope of optimizing the metal oxide-free ETL and to gain further insight into device design considerations. The concentration of C_{60} was first varied from 0mg/ml (i.e. perovskite deposited directly on

PEI on ITO) to 10mg/ml which was assumed to be the highest concentration at which C_{60} remained reliably and completely dispersed. Increasing (nominal) C_{60} concentration past 10mg/mL was found to reduce mean efficiency (based on four devices with 8 cells each) as shown in Figure 4.18(b), indicating a dispersibility limit of C_{60} in DCB. The susceptibility of fullerenes to removal by DCB prohibited the build up of a thicker C_{60} film by multiple depositions. Therefore, in an attempt to increase the C_{60} film thickness still further, PEI was deposited on a 10mg/mL coating of C_{60} before spinning another fullerene layer ("2XPEI/C_{60}") as the PEI layer would at least partially protect underlying C_{60}. This process was also repeated a second time to build up an even thicker ETL ("3XPEI/C_{60}") and typical JV-curves (taken in reverse bias direction) for devices made with such films is shown in Figure 4.18(a).

In the absence of a fullerene layer, devices produced very little photocurrent. This would be expected for perovskite films with incomplete coverage as electrons could thus be injected from ITO into the HOMO of the HTL wherever there was no perovskite to prevent direct contact between them. Depositing 1mg/mL C_{60} (in DCB) already markedly improved the photocurrent by reducing recombination losses with further improvements as the concentration was increased first to 2mg/mL and then 5mg/mL and 10mg/mL. It is worth noting however that in the case of 5mg/mL C_{60}, although initial scans were similar to those for 10mg/mL, there was rapid deterioration in J_{sc} with a stabilized output more comparable to cells with 2mg/mL C_{60}. Depositing PEI on top of the fullerenes adversely affected performance which may be explained by the fact that although butanol is a non-solvent for C_{60}, partial removal of underlying PEI would likely affect integrity of the C_{60} film. However, upon spin coating a second C_{60} layer ("2XPEI/C_{60}"), performance largely recovered and was comparable to a single C_{60} deposition. Curiously, measured photocurrent near the MPP was somewhat erratic as seen in Figure 4.18(c) and (d). Repeating the procedure (i.e. three coats of C_{60}) gave a generally higher J_{sc} with more stable photocurrent output as shown in Figure 4.18(e) and (f). Another manner in which to increase C_{60} film thickness would be to spin a higher concentration dispersion. However, mean device efficiencies decreased as the (nominal) C_{60} concentration increased as shown in Figure 4.18(b). This result was likely due to incomplete dispersion of C_{60} which led to pinholes and inhomogeneities from aggregates.

4.5.3 Flexible devices

In order to demonstrate the applicability of polymer-fullerene bilayers to flexible substrates, devices were also fabricated on PET-ITO for comparison. Figure 4.19(a) shows a typical JV-response for devices made on PET. One-diode fits to the data revealed a large R_s of approximately 8.16Ωcm^2 and fill factor of 0.66 resulting in a mean conversion efficiency of

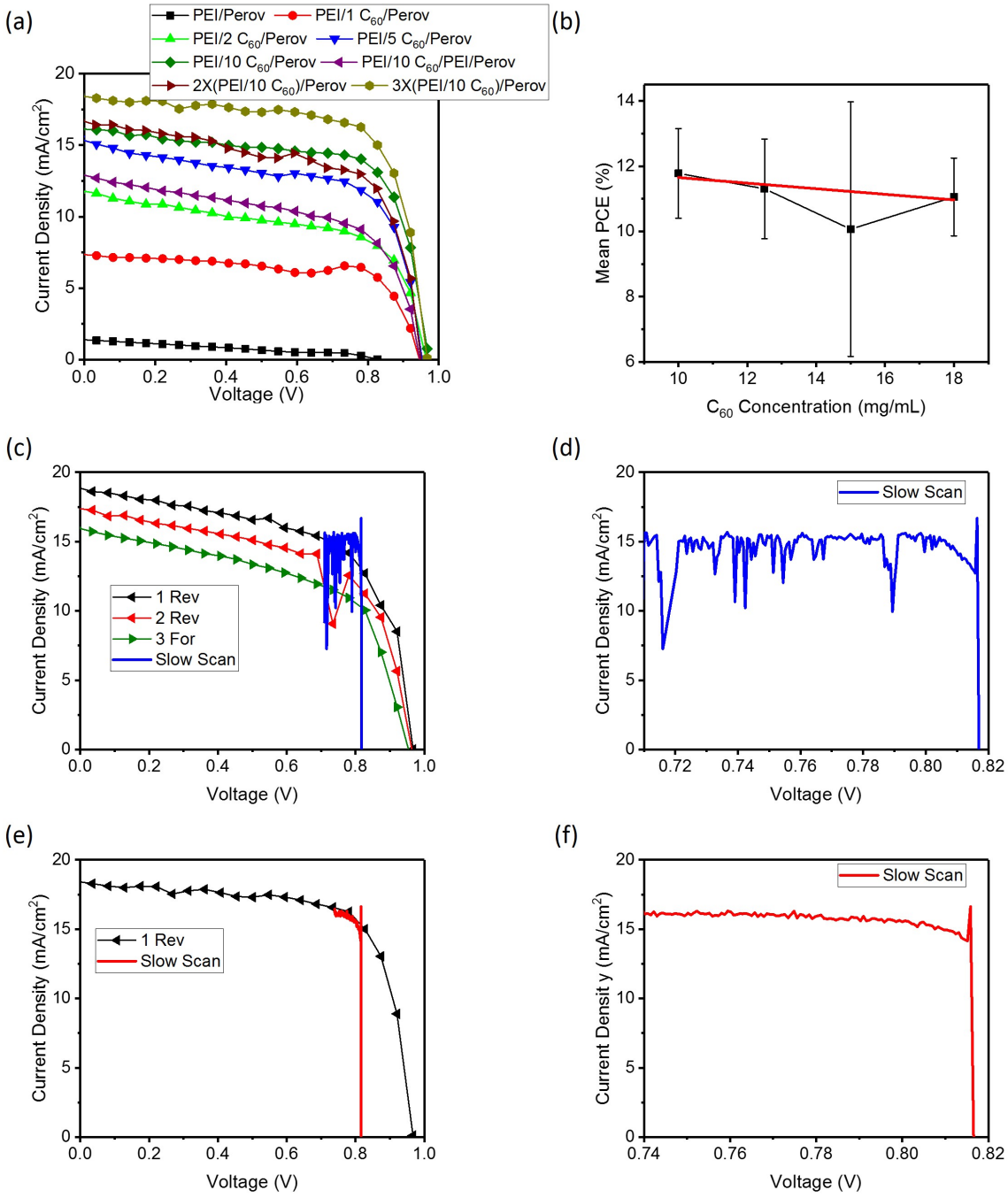

FIGURE 4.18: Variation in photovoltaic response with C_{60} concentration. (a) Typical JV-response for devices made with different concentration C_{60} deposited by spin coating. (b) Effect of higher C_{60} concentration on mean device power conversion efficiency (PCE). (c) JV-curves for device comprising ITO/2XPEI/C_{60}/Perovskite/P3HT/TiAu. (d) Slow scan near the maximum power point for cell shown in (c). (e) JV-curve for device comprising ITO/3XPEI/C_{60}/Perovskite/P3HT/TiAu. (f) Slow scan near the maximum power point for cell shown in (e).

8.38% which was lower than the best achieved on glass substrates. However, this was comparable to the mean efficiency for glass-ITO devices fabricated in the same batch which also displayed high R_s as illustrated in Figure 4.19(b). This led to the conclusion that there was some other factor in device fabrication that sometimes led to high R_s which outweighed the contribution made by a larger sheet resistance of ITO on PET versus glass. The source of this batch-to-batch variability in R_s will be elucidated in the following chapters.

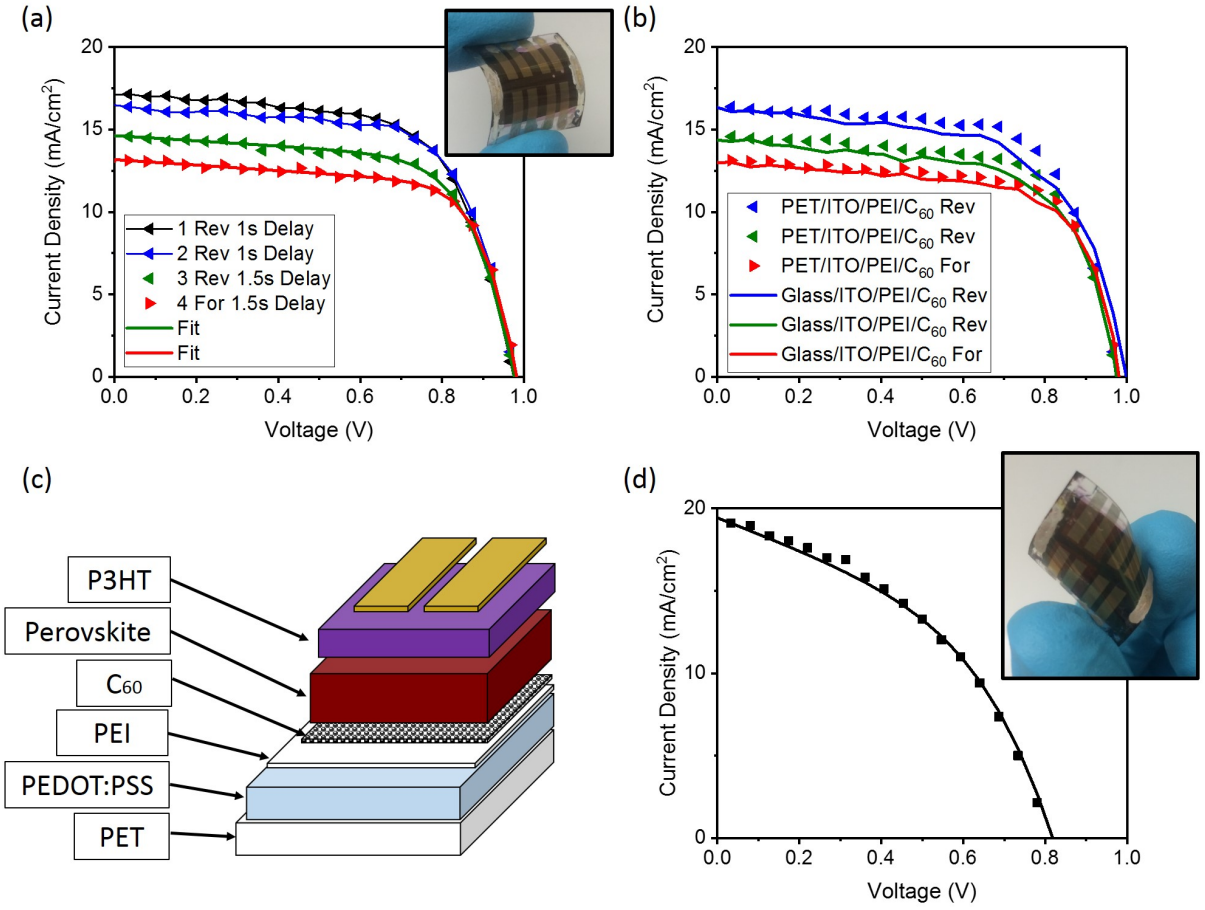

FIGURE 4.19: (a) Typical JV-response of a device comprised of PET/ITO/PEI/C_{60}/Perov/HTL/TiAu. (b) Comparison of cell shown in (a) with control device based on ITO-glass. (c) Schematic of flexible ITO-free device on PET. (d) Response of a cell with structure shown in (c) along with fit using the One Diode model. Inset shows device being flexed.

Finally, in order to really push the versatility of PEI-fullerene bilayers devices were made on top of 50μm thick PET films coated with a layer of the conductive polymer poly (ethylenedioxythiophene) :poly(styrene sulphonate) (PEDOT:PSS) coated from a stock solution of Clevios PH1000 containing 5 vol% dimethylsulphoxide (DMSO) and 0.5 vol% Triton X-100 surfactant in a manner similar to an established method[184]. All of the resulting cells were highly shunted but some maintained a higher V_{oc} as shown in Figure 4.19(c) resulting in a maximum power output of 6.2mW/cm^2. One diode fits to the data gave a FF of 0.42 and R_{sh}

of 101Ωcm^2. The presence of high photocurrents with J_{sc} of almost 20mA/cm^2 suggested that high conversion efficiencies could be achieved through more careful device fabrication, for example by extending the width of the PEDOT:PSS strip shown in the image and masking the disruption caused by the step height by applying nail varnish along the edge to insulate it from the gold counter electrode.

4.6 Liquid-Phase Exfoliated graphene for improved stability of perovskite with ZnO-based TCOs

Although high efficiencies were achieved for perovskite cells using metal oxides in conjunction with fullerenes, it was noted that devices were always affected to a greater or lesser extent by the presence of ZnO. The degree of device susceptibility to degradation ranged from severe in the case of ZnO-NP films and unwashed sputtered films and to more moderate for scrubbed and N_2-annealed films deposited by sputtering and spray pyrolysis. However, all devices with ZnO-based layers regardless of deposition methods and annealing treatments eventually decomposed at least partially, suggesting that ZnO itself may act as a catalyst to perovskite degradation in the presence of air and moisture.

Curiously, although there have been many reports of perovskite solar cells using ZnO-based ETLs, relatively few have studied the stability of resulting devices. However in recent years the instability issues associated with the use of ZnO in perovskites have been begun to be acknowledged and addressed. In addition to the presence of hydroxides and residual acetates and other organic materials noted already, the alkaline nature of ZnO itself has been highlighted as a cause of degradation via deprotonation of methylammonium ions [212, 213, 186, 214, 215], in a process which may be accelerated by heat treatment. Furthermore, ZnO has been reported to have a strong photocataytic effect in the presence of ultraviolet (UV) light [216][217][218]. Most strategies used to combat these issues involve deposition of thin buffer layer of some inert material such as Al_2O_3[60][219][218]. PEI has also been reported as a cost effective buffer material which can be deposited via spin coating[167]. To see whether this strategy could serve to improve the stability of devices used in the current work, ZnO-NP films were coated with different concentration solutions of PEI in 1-butanol followed by perovskite deposition and annealing on a hot plate for 15 minutes. Figure 4.20 shows how perovskite deposited on ZnO-NP films were affected by annealing at 100 °C for 15 minutes with different concentration PEI buffer layers. The protective effect of PEI was clearly evident with increasing concentration as seen by reduced yellowing of the films (Figure 4.20(b)). However, x-ray diffraction patterns for the aged perovskite films confirmed

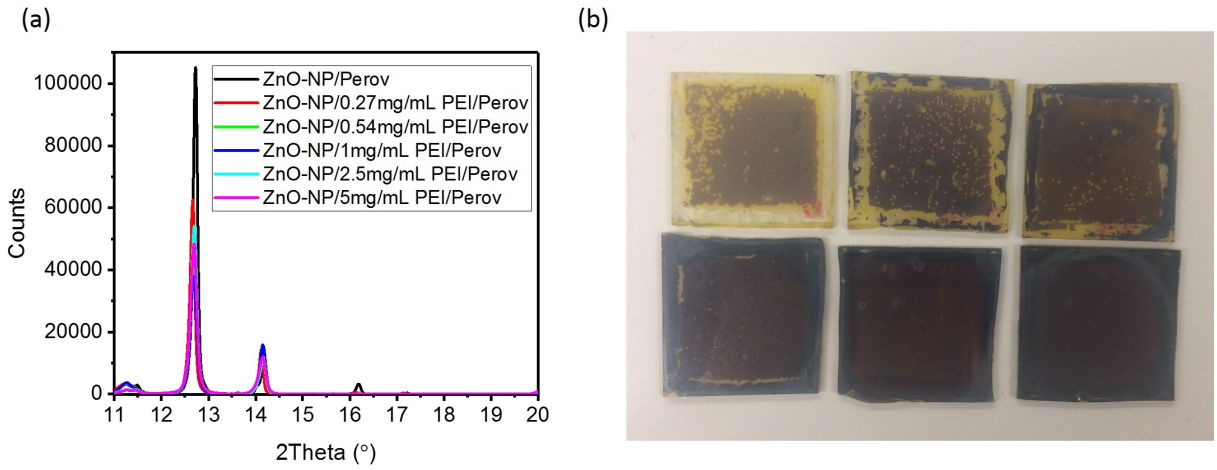

FIGURE 4.20: (a) XRD of perovskite films on ZnO with different concentrations (and hence thickness) of PEI as interlayer after annealing on a hot plate at 100 °C for 15 minutes. (b) Image of films described in (a) (Top row left to right: 0mg/mL, 0.27mg/mL, 0.54mg/mL, 1mg/mL, 2.5mg/mL, 5mg/mL PEI).

that although even solutions as dilute as 0.27mg/mL did provide some level of protection from degradation as signified by a reduced peak at 12.7 ° associated with PbI_2, significant perovskite decomposition still occurred with PEI solutions as concentrated as 5mg/mL (Figure 4.20(a)). This was problematic as the thickness of PEI at such elevated concentration is prohibitive to high performance devices as already demonstrated owing to its insulating nature.

It was wondered whether it might be possible to improve the protective effect of PEI by combining it with a more conductive material. Graphene was an obvious candidate owing to its excellent electrical and barrier properties. There have been some reports of using graphitic materials together with PEI and ethoxylated polythyleneimine (PEIE). For example, graphene oxide (GO)-PEI composite materials have been used as dye and gas adsorbents[220] as well as drug delivery agents in aqueous environments[221]. Reduced graphene oxide (RGO) and PEI composite films have also been fabricated via filtration, demonstrating improved gas barrier properties[222][223]. Solutions of GO grafted PEIE have also been spin coated as ETL in OPVs, outperforming reference devices using either GO or PEIE[224]. However all of these reports used either GO or RGO by oxidation and reduction reactions, thereby damaging the honeycomb lattice structure of graphene resulting in inferior barrier properties and electrical conductivity. Furthermore, the presence of functional groups in GO has been linked to reduced stability of perovskite solar cells[225][226][227][228]. It would thus be advantageous to process graphene in its pristine form. Relatively defect-free individual and few layer graphene sheets may be exfoliated from bulk graphite in liquid

environments by applying energy in the form of ultrasonication or shear mixing. However, to prevent rapid re-aggregation of the nanosheets and obtain significant quantities of dispersed media, high boiling point solvents are typically required due to solubility theory considerations. Accordingly, in the case of molecular solutes, the property most associated with solubility is the cohesive energy density, $E_{C,T}/V$, where $E_{C,T}$is the total molar cohesive energy and V is the molar volume of the solvent[229][230]. The Hildebrand parameter, δ_T, which is the most commonly used solubility parameter, is the square root of $E_{C,T}/V$. Therefore if the cohesive energy density is given by

$$\frac{E_{C,T}}{V} = \frac{E_{C,D}}{V} + \frac{E_{C,P}}{V} + \frac{E_{C,H}}{V} \tag{4.1}$$

where three components represent dispersion, polar and hydrogen bond forces respectively then it follows that the Hansen solubility parameter is given by

$$\delta_T^2 = \delta_D^2 + \delta_P^2 + \delta_H^2 \tag{4.2}$$

It follows that good solvents for a given solute are those that match the various components of the Hansen parameters given by equation4.2. Furthermore, defining R_o as the radius of interaction sphere in Hansen space for a given material and R_a as the distance in Hansen space between two materials based on their partial solubility parameter provides the Relative Energy Difference (RED) which is a useful metric for determining compatibility. The relevant equations linking these parameters are as follows:

$$R_a^2 = 4(\delta_{D2} - \delta_{D1})^2 + (\delta_{P2} - \delta_{P1})^2 + (\delta_{H2} - \delta_{H1})^2 \tag{4.3}$$

$$RED = \frac{R_a}{R_o} \tag{4.4}$$

A RED greater than 1 indicates that the two materials are not soluble where less than one indicates high affinity and 0 perfect compatibility [229][231]. The Hansen solubility parameters of graphene have been evaluated as δ_D = 18.0MPa$^{1/2}$, δ_P = 9.3MPa$^{1/2}$ and δ_H = 7.7MPa$^{1/2}$[230]. It was realised that PEI, which has values of δ_D = 19.6MPa$^{1/2}$, δ_P = 7.6MPa$^{1/2}$ and δ_H = 9MPa$^{1/2}$, could perhaps be highly miscible with graphene, making for a good composite material. Indeed, applying equations 4.3 and 4.4 together with R_o = 6.0 for PEI [231] gave a RED of 0.44 suggesting high compatibility between the materials. It was reasoned therefore that PEI could act analogously to a surfactant forming intimate contact

with graphene flakes and stabilizing them in solvents more suitable for solution processed thin films such as H_2O, IPA or butanol.

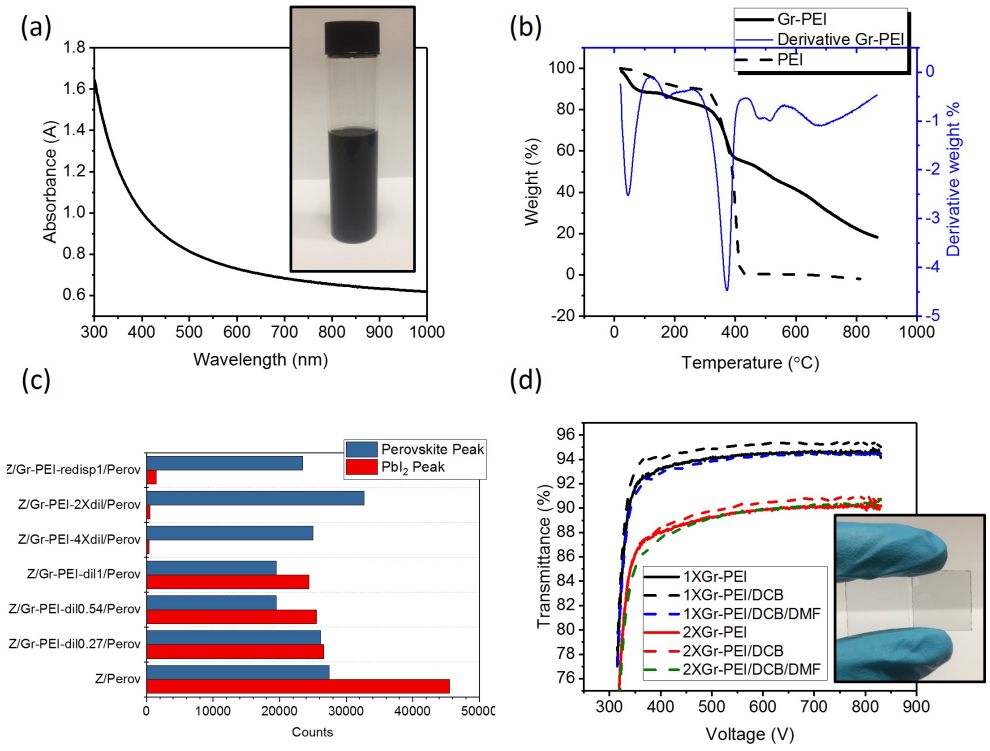

FIGURE 4.21: (a) Absorption spectrum of Gr-PEI hybrid dispersion in butanol diluted 40X (image of stock dispersion shown in inset). (b) Thermogravimetric analysis of Gr-PEI nanohybrid plotted alongside neat PEI for comparison. (c) XRD patterns of perovskite on ZnO-NP layers ("Z" in legend) with different concentration G-PEI composite buffer layers after annealing for 15 minutes at 100 °C. Transmittance measurements of a single coating (1X) of Gr-PEI redispersed in 1mg/mL PEI and two coatings (2X) on glass slides. Image shows high transmittance of composite film (right) alongside blank glass slide (left).

To test this hypothesis, graphite flakes (1.8g) and a solution of PEI (10mg/mL, 60mL) in H_2O were mixed together in a metallic beaker before applying energy using an ultrasonic probe (50% amplitude, 5 hours, 4s on,4s off). As seen in the inset of Figure 4.21(a), the solution turned completely black and remained so long after sonication was stopped indicating successful dispersion of graphitic material. To remove non-dispersed media, the solution was placed in 28mL vials and centrifuged at 2000rpm for 90 minutes. The procedure was found also to be applicable using butanol instead of H_2O. Given the very large bandgap for PEI, it was judged that the hybrid dispersion could be treated as containing only graphene from the point of view of applying the Beer-Lambert law. Various values for the extinction coefficient for graphene have been reported, ranging from $1390 Lg^{-1}m^{-1}$ to $6600 Lg^{-1}m^{-1}$ [91][232][233]. Taking a theoretical value of $4237 Lg^{-1}m^{-1}$ gives a concentration of 0.66mg/mL graphene in the stock solution based on the absorption spectrum of a

diluted dispersion (Figure 4.21(a)).

In order to get an idea of the barrier properties afforded by the presence of graphene, the Gr-PEI stock dispersion was diluted by various amounts and deposited as a buffer on ZnO-NP films before coating perovskite and annealing as carried out previously for PEI. It was assumed that the concentration of PEI in the Gr-PEI stock dispersion was the same as in the starting solution (i.e before sonication and centrifugation steps). As seen in Figure 4.21(c), even a very dilute Gr-PEI solution (0.27mg/mL PEI) resulted in a marked decrease in the intensity of PbI_2 peak, indicating a protective effect offered by the composite buffer layer. However, the intensity of the PbI_2 peak remained high relative to the perovskite phase and gains in barrier effect were marginal as the concentration was increased to 0.54mg/mL and 1mg/mL. Only at concentrations above 2.5mg/mL was the perovskite completely protected from decomposition. Although this was an improvement on the 5mg/mL needed for an effective buffer layer in the case of neat PEI, it was clear that the graphene content was too low to have much of an impact. This was unsurprising given that the absorption spectra suggested a concentration of graphene in the stock dispersion that was roughly 20 times lower than that of PEI. In order to reduce the proportion PEI, the stock dispersion was simply centrifuged at 5000rpm for 90min and the supernatant discarded. The precipitate could then be redispersed in a lower volume of pure solvent by bath sonication with periodic vigorous shaking of the vial. In this way, not only was the proportion of PEI decreased but the concentration of Gr-PEI nanohybrid was also increased. Butanol, H_2O and IPA were all found to be suitable for redispersing the nanohybrid material without need for additional polymer or surfactant, indicating intimate contact between graphene flakes and PEI molecules. The centrifugation and redispersing steps could be repeated to remove any excess PEI. However thermogravimetric analysis (TGA) of the nanohybrid after even a single redispersion step (Figure 4.21(b)) suggested that graphene made up approximately 60% of solids in the mixture. The nanohybrid was redispersed in mg/mL PEI in butanol to ensure good dispersion stability and surface wetting during spin coating. Resulting films coated at 2000rpm on glass slides showed high transparency in the visible spectrum and were only slightly affected by subsequent spin coating of DCB and DMF (Figure 4.21(d)) which indicated suitability as a transparent barrier material for devices. Crucially, although the nanohybrid dispersion contained a much lower PEI content than the stock solution, resulting films remained effective preventing perovskite decomposition as shown in Figure 4.21(c).

Of course, the improved barrier properties afforded Gr-PEI composite layers are of little consequence unless they can be applied in devices without significant loss in PCE. As an initial test, Gr-PEI nanohybrid redispersed in 1mg/mL PEI was spin coated on ITO either

	Mean PCE (%)	StD/Mean	Champion PCE(%)
1XGr-PEI10 redisp 1mg/mL PEI	2.87	0.332	4.27
2XGr-PEI10 redisp 1mg/mL PEI	0.18	0.293	0.25
Gr-PEI10 redisp 1mg/mL PEI	5.76	0.18	6.47
Gr-PEI5 redisp1mg/mL	7.6	0.28	10.47
Gr-PEI5 redisp0.5mg/mL	9	0.19	12.3

TABLE 4.6: Mean, standard deviation divided by mean and champion PCE for devices fabricated with different Gr-PEI composite buffer layers.

once (1XGr-PEI) or twice (2XGr-PEI) and devices were fabricated with structure ITO/Gr-PEI/$_{60}$/Perov/HTL/TiAu. Figure 4.22(a) shows that both device structures resulted in severely shunted devices, particularly in the case of 2XGr-PEI. It was suspected that the high degree of shunting was at least partly due to the relatively hydrophobic nature of the barrier films resulting in poor C_{60} and perovskite coverage. To address this issue, subsequent devices were fabricated with an additional layer of dilute PEI solution (0.27mg/mL) spin coated on 1XGr-PEI before C_{60} deposition. This resulted in a marked improvement in R_{sh} and hence V_{oc} as shown in Figure 4.22(b) and (c). However it was clear that devices had a large series resistance suggesting that the content of PEI in the composite films was still too high. Consequently, fresh stock dispersions were made using a reduced PEI concentration of 5mg/mL (referred to as Gr-PEI5 versus Gr-PEI10 for 10mg/mL stock dispersion used previously) and the nanohybrid was redispersed both in 1mg/mL and 0.5mg/mL PEI. As seen in Table 4.6, devices fabricated with these dispersions saw improvements in PCE, particularly for Gr-PEI5 redisp0.5mg/mL which displayed a champion PCE of 12.3%. As shown in Figure 4.23, both composites also acted as excellent buffer layers to protect perovskite from degradation in the presence of ZnO. These results demonstrate that pristine graphene can be combined with PEI to form a composite material that effectively blocks unwanted decomposition reactions whilst maintaining electron transport. Furthermore, the significant gains in device performance after only a few preliminary optimization steps suggest that much higher PCE could be achieved.

4.7 Conclusions

The aim of this chapter was to determine what materials could best facilitate photoexcited electron extraction from perovskite towards the transparent cathode whilst simultaneously blocking holes. Solution processed ZnO nanoparticles (NPs) films were found to result in significant recombination which limited photocurrent and hence PCE. Modifying the ZnO-NP surface with C_{60} was found to greatly improve charge extraction, suggesting improved

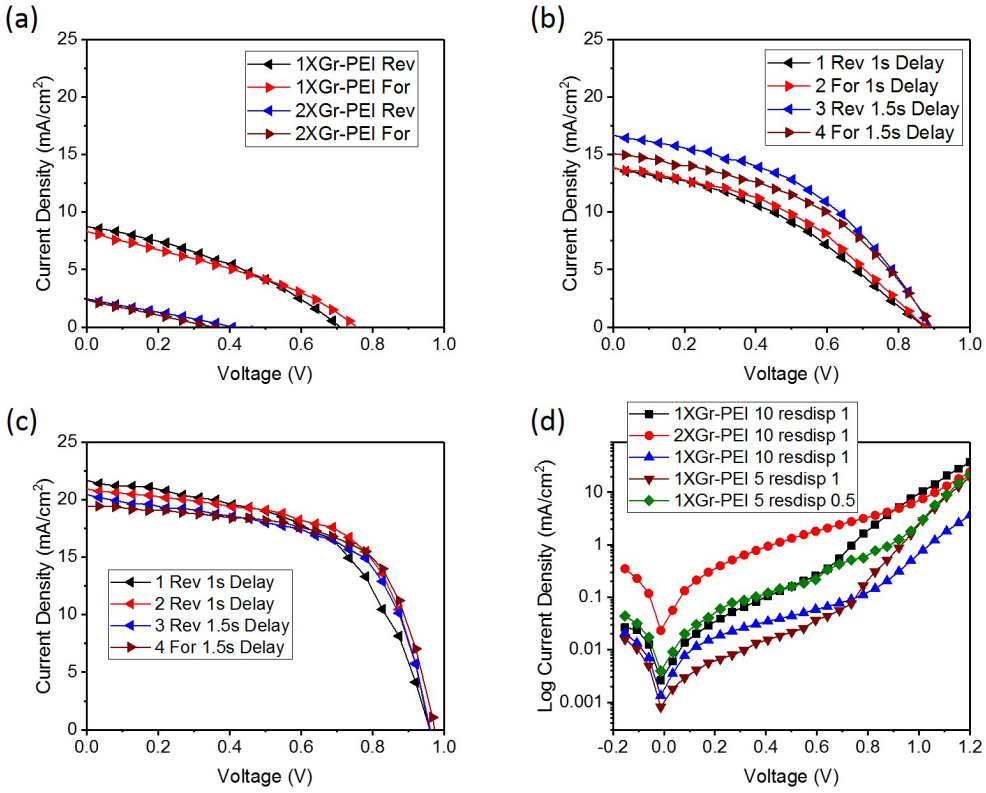

FIGURE 4.22: Current-voltage response of devices with Gr-PEI composite layers. (a) One coat of Gr-PEI redispersed in 1mg/mL PEI (1XGr-PEI) versus two coats (2XGr-PEI) in devices with structure ITO/Gr-PEI/C_{60}/Perov/HTL/TiAu. (b) Response of devices with the same Gr-PEI layer as (a) but with an additional layer of 0.27mg/mL PEI deposited before coating C_{60}. (c) Response of cell with device structure as (b) but in which Gr-PEI from a stock dispersion containing 5mg/mL PEI was redispersed in 0.5mg/mL PEI was used. (d) Typical current-voltage curves in the dark on a semilog scale for devices studied.

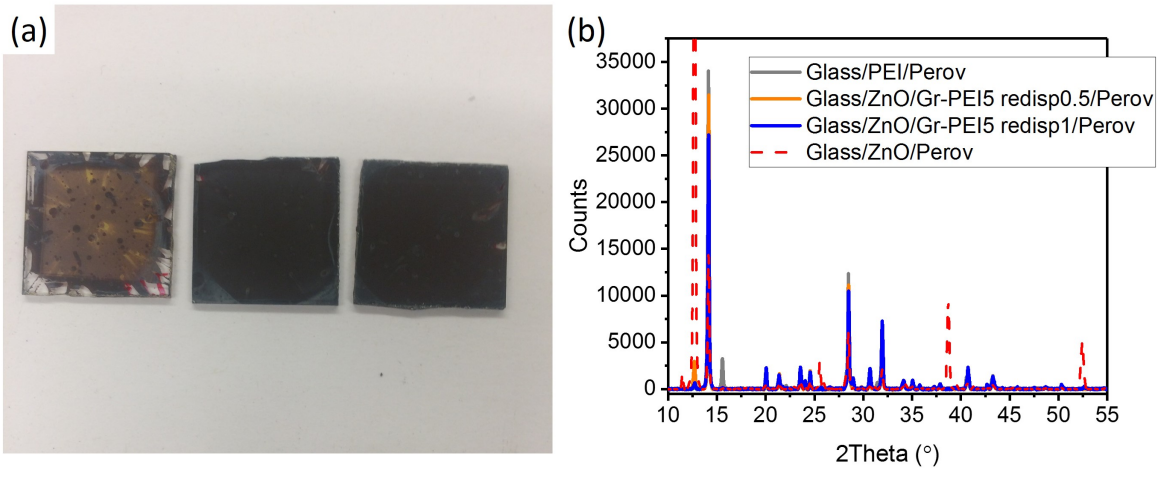

FIGURE 4.23: (a) Image of perovskite films after annealing treatment on ZnO-coated glass slides with no Gr-PEI buffer (left), Gr-PEI5 redisp0.5mg/mL (middle) and Gr-PEI5 redisp1mg/mL (right). (b) XRD patterns for samples shown in (a).

band level matching between the photoactive layer and ETL. However, perovskite was found to degrade significantly when in contact with ZnO-NPs regardless of the presence of a fullerene interlayer which was thought to be a factor in the strong scan-dependent hysteresis observed. Attempts were made to improve stability but degradation persisted. Similar issues were encountered for devices made with intrinsic ZnO films (iZnO) deposited by spray pyrolysis, even after washing steps and surface passivation treatment of iZnO films by annealing under N_2. Minor improvements were observed for devices fabricated on spray pyrolized TiO_2 films annealed at 500 °C in air but J_{sc} remained limited due to elevated series resistance which was attributed to a high density of trap states within the TiO_2 as well as unfavourable alignment between its conduction band and that of the perovskite. ZnO films doped with various metallic donors were also investigated but were found if anything to present an even higher barrier to charge extraction from fabricated devices. However, both indium- and aluminium-doped ZnO worked as effective transparent cathodes when a polymer-fullerene bilayer was employed as ETL, displaying a surprisingly long-lived devices for unencapsulated cells stored under ambient conditions with relatively elevated humidity. Similarly, room temperature sputtered TiO_2 was found to be an extremely ineffective ETL for devices using the current set up as to a lesser extent was ZnO. Observed instability of perovskite on sputter coated ZnO, though somewhat reduced by scrubbing and washing treatments, confirmed the inherent problems associated with processing the two materials together and operating the resulting devices in oxygen and moisture-rich environments. Fullerenes were identified as the most promising electron selective material for devices using the current set up and attempts were made to optimize device performance for fullerene-based ETLs. Polyethylenimine (PEI) was found both to reduce cell-to-cell variability in PCE and to improve device reproducibility by acting variously as an adhesion promoter and (when crosslinked) as a barrier to partial removal of C_{60} molecules during device processing. Optimized devices displayed near negligible hysteresis and high PCE with stabilized power output under illumination. Versatility of the low temperature solution-processed ETL was demonstrated by fabricating flexible devices on ITO-coated PET as well as PET coated with PEDOT:PSS as transparent electrode. Finally, attempts were made to address the aforementioned instabilities associated with the use of ZnO. PEI was found to provide limited protection, especially at thicknesses compatible with effective device performance. However, it was found that graphene could be directly exfoliated in solutions of PEI and enriched Gr-PEI nanohybrid dispersions were demonstrated to protect perovskite films from degradation whilst maintaining effective device performance.

5 Optimizing Precursor Composition for High Performance Perovskite Solar Cells Prepared under High Relative Humidity

5.1 Introduction

As already mentioned, one of the most frequently used techniques for perovskite film fabrication involves dissolving organic and inorganic precursors in a common solvent or solvent mixture followed by deposition upon the desired substrate via spin coating. With this so-called "single-step method" (1Step), perovskite crystallization begins with partial solvent removal during spin coating and is completed via thermal annealing at around 100 °C. In order to obtain dense films with few pinholes, this process is usually carried out in inert or low humidity conditions although this adds to fabrication costs. The "two-step method" (2Step) is also used as it is viewed as a simple method to improve film quality and reproducibility, particularly in non-inert environments. The procedure consists of first depositing the inorganic precursor (typically PbI_2) resulting in a lead salt film which is subsequently reacted with the organic component. The reaction is generally accomplished either by immersing the film in a dilute alcoholic solution of methylammonium iodide (MAI) or spin coating a higher concentration alcoholic solution at elevated temperature creating a bilayer which crystallizes upon annealing. The 2Step method is viewed as offering better control of dense highly crystalline films with few pin-holes and its simple implementation has led to widespread adoption. However, insofar as processing conditions are specified in the literature, the 2Step method is still mostly carried out in humidity controlled environments.

In this chapter the role of halide type and ratio on device performance is explored for

both single-step and two-step perovskite deposited in higher humidity (60-90% relative humidity) conditions. The objective is to determine which method and precursor combination is best suited to processing in ambient environments using simple techniques.

5.2 Single-Step Deposited Perovskite

It has been claimed that certain single-step precursor formulations are suitable for ambient laboratory conditions[184]. However, when such recipes were followed the resulting films were always of a grey semi-transparent nature, with a visible roughness regardless of the substrate onto which they were deposited. Inspection of the films using SEM revealed the presence of many micrometer-sized pinholes as seen in Figure 5.1. Such non-homogeneous films are unsuitable for high-performing devices and may be ascribed to the presence of significant humidity in the air during processing. In order to avoid an excessive number of pinholes, a variant on the single-step method was used in which the solvent was separated from the perovskite precursors by immersing the wet film in diethyl ether before the usual annealing treatment. Using this "solvent-solvent extraction" (SSE) technique[234], significant crystallization occurs in the liquid phase, thereby neutralizing the effect of moisture to attain films with more uniform surface coverage.

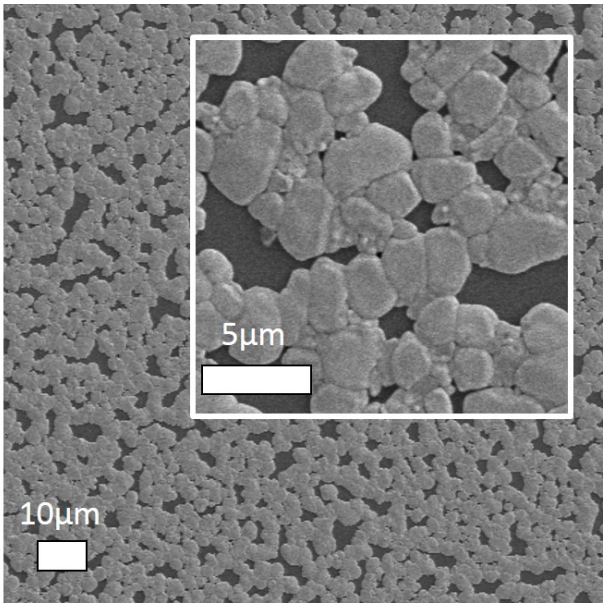

FIGURE 5.1: SEM image of single-step deposited perovskite films on PEDOT:PSS using reported techniques.

The first precursor combination tested was a 50wt% solution of MAI and PbI_2 in the most typically used 1:1 molar ratio. Devices exhibited low photocurrents of 7 mA/cm^2 at short circuit and V_{oc} below 0.5V as shown in Figure 5.2(a) resulting in a conversion efficiency of

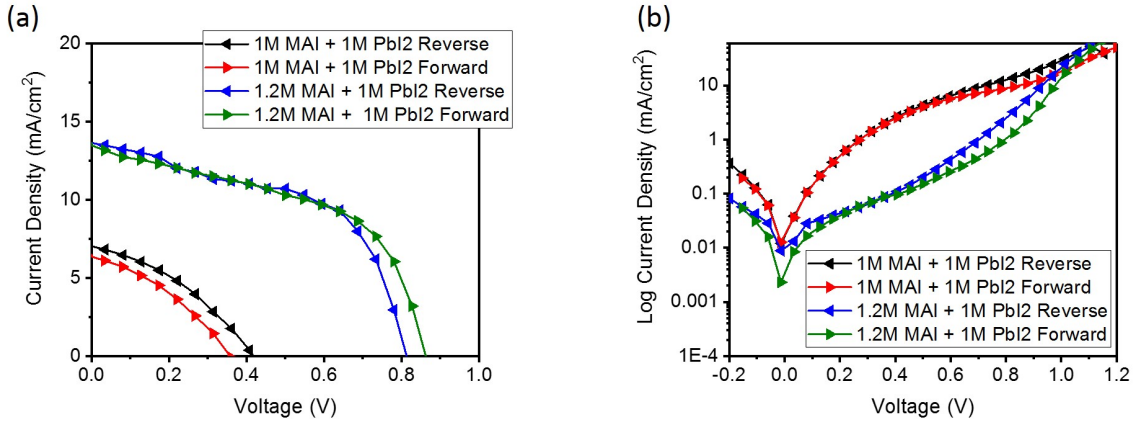

FIGURE 5.2: Effect of MAI:PbI_2 ratio in 1Step perovskite using Solvent-Solvent Extraction method. Typical current-voltage curves under illumination (a) and in the dark (b).

about 1%. This was attributed mainly to poor film morphology resulting in a significant concentration of shunting pathways as indicated by R_{sh} of around 60 Ωcm^2 from fitting and confirmed by dark-JV measurements as shown in Figure 5.2(b). Increasing the molar content of MAI from 1M to 1.2M resulted in a marked improvement with a mean conversion efficiency to 4.5%. The increased performance was attributed mainly to improved shunt resistance as indicated in Figure 5.2(b), although R_{sh} from fitting remained between 120 and 200 Ωcm^2. However, increasing MAI content to 2.2M (as a molar ratio with PbI_2) resulted in highly unstable films that rapidly turned almost completely transparent upon storage in air, even when capped with a 200nm thick protective layer of PMMA.

5.2.1 Effect of halide on device performance

Device performance was significantly improved by partial replacement of PbI_2 with $PbCl_2$ using a precursor ratio of 1M MAI to 0.9M PbI_2 to 0.1M $PbCl_2$. This resulted in a significantly improved device performance, resulting in a mean efficiency of 8.8%. This result could largely be explained by improved morphology of the perovskite film which resulted in reduced shunting as indicated by an increased V_{oc} and lower current densities at low forward bias in the dark as shown in Figure 5.3(a) and (b). Absorption spectra for a mixed iodide-chloride film is shown before and after thermal annealing on a hotplate at 100 °C in Figure 5.3(c). The annealing treatment slightly red shifted the absorption onset and increased absorption at shorter visible wavelengths. This can be explained by full conversion of precursor species to the perovskite phase as shown by the corresponding XRD patterns in Figure 5.3(d). However, increasing the chloride content of the precursor further was found

to be difficult without increasing the molar content of MAI which resulted in very inconsistent and generally poor performing devices. Conversely, increasing the content of $PbCl_2$ was found to be much easier in the case of the 1.2M MAI to 1M lead halide ratio, resulting in a much clearer trend in mean conversion efficiency as shown in Figure 5.4(b).

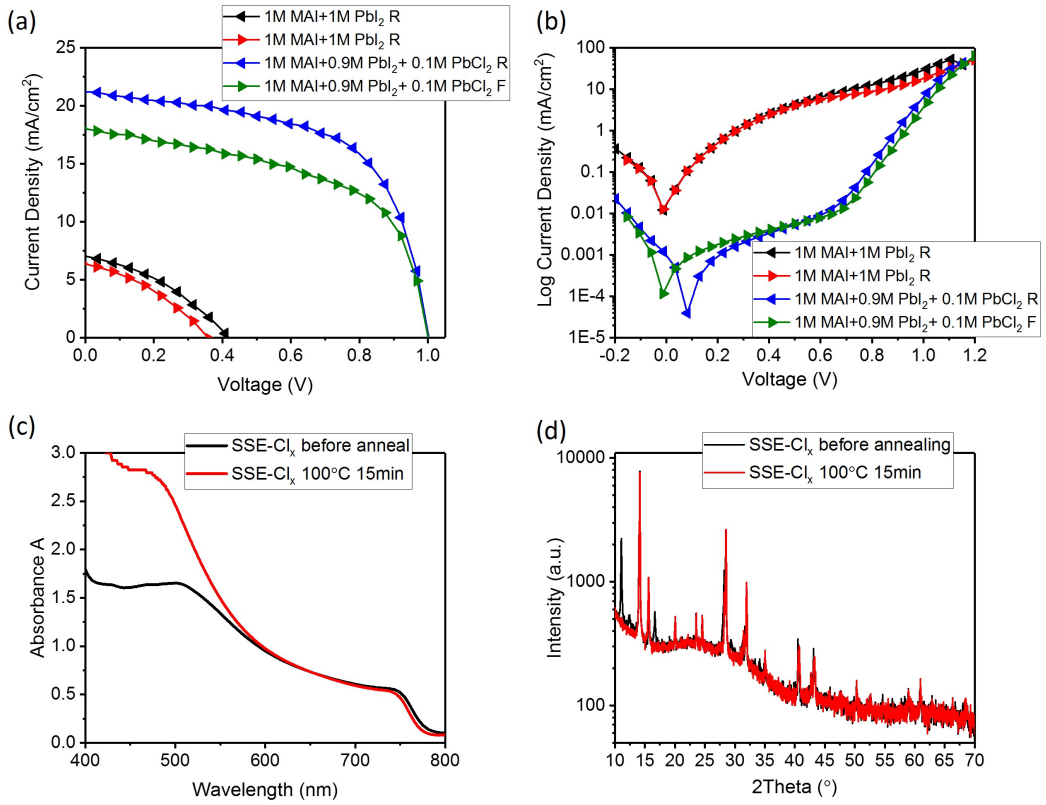

FIGURE 5.3: (a) Current-voltage response of devices with 1M MAI and 1M PbI_2 versus devices with partial substitution of PbI_2 with 0.1M $PbCl_2$. Typical response under illumination. (b) Semilog plots in the dark of devices shown in (a). (c) Absorption spectrum of a 1Step perovskite film made using the Solvent-Solvent Extraction (SSE) method and mixed halides (i.e. Cl_x) before and after thermal annealing. (b) XRD patterns of films shown in (c).

The addition of different molar content of $PbCl_2$ was found not to have much impact on the absorption onset of the perovskite films as shown in Figure 5.4(a), suggesting little change to the optical bandgap. However, mean device efficiency was significantly improved with increasing $PbCl_2$, most notably the ratio of 1.2M MAI to 0.8M PbI_2 to 0.2M $PbCl_2$ resulted in certain cells with efficiencies between 12 and 14% . However, there was a large spread in cell efficiencies due primarily to differences in shunt resistance as indicated by semilog plots of dark current density under applied bias as shown in Figure 5.4(c). The cell with least dark current under low positive bias ("Cell 7" in Figure 5.4(c)) resulted in a champion efficiency of over 15.4% as obtained not only from slow reverse bias scans as shown in Figure 5.4(d) but also under constant bias around the maximum power point. Furthermore

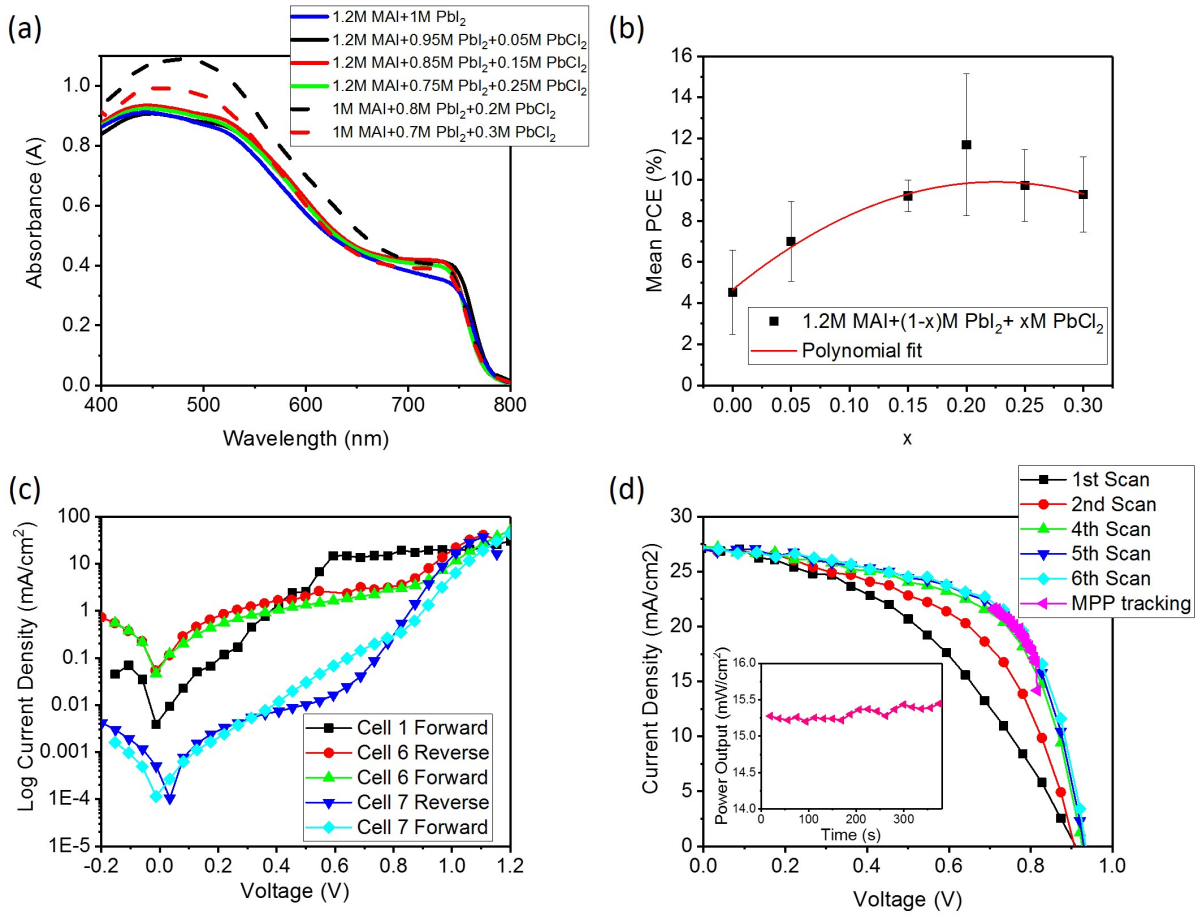

FIGURE 5.4: (a) Absorption spectra for different 1Step perovskite formulations. (b) Plot of mean power conversion efficiency (PCE) against molar content x of $PbCl_2$. (c) Semilog plots of dark current measurements for different cells on a single device made with 0.2M $PbCl_2$ showing large variation in rectifying behaviour. (d) JV-curves for best performing cell with 0.2M $PbCl_2$. Inset shows evolution of power output under constant illumination and bias.

the output was found to increase slightly with time over a 6 minute period as shown in the inset of Figure 5.4(d), thereby demonstrating good device stability under ambient operating conditions. Higher chloride content (i.e. 0.25M) showed no significant improvement and fully dissolved precursor solutions could not be achieved for $PbCl_2$ content greater than 0.3M.

The same procedure of halide substitution was followed by partially replacing PbI_2 with varying molar content of $PbBr_2$ to study the effect on absorption and device performance. As the bromide content was increased, the absorption onset of the perovskite films shifted towards shorter wavelengths as shown in Figure 5.5(a). This was due to subtle changes in the crystal structure and consequently on the electronic band structure, resulting in an increasing bandgap with bromide content which can be approximated by plotting the log of absorption against energy as in Figure 5.5(b).

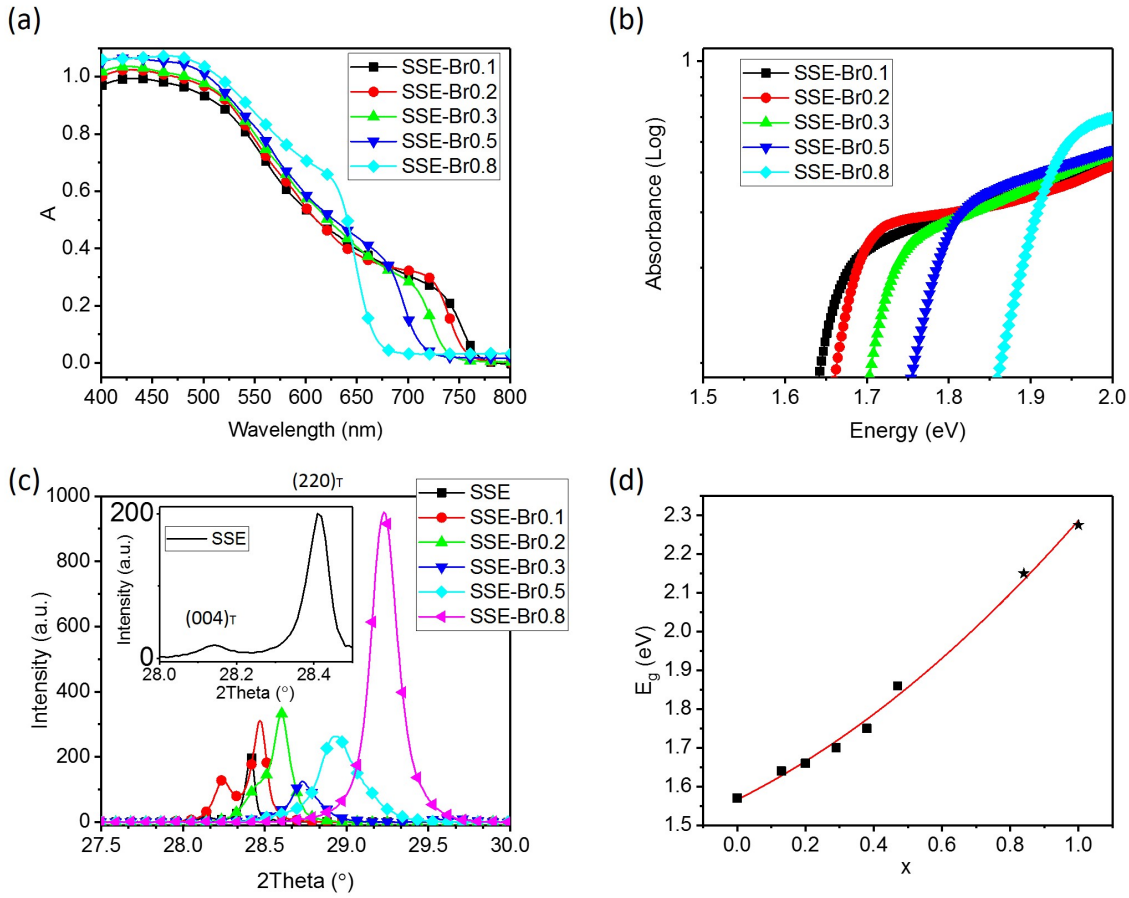

FIGURE 5.5: Characterisation of perovskite films doped with different molar content of $PbBr_2$. (a) Absorption spectra of 1Step films with increasing bromide content (b) Semilog plots of spectra from (a) against photon energy to estimate bandgap (c) X-ray diffraction patterns of films magnified in the region of the tetragonal $(004)_T$ and $(220)_T$ and cubic $(200)_C$ peaks (i.e.27.5-30deg). (d) Plot of energy bandgap versus composition x determined from XRD data along with a second order polynomial fit (red line). Data points represent experimental results except in the case of x=0.84 and x=1 which are from Ref.[35].

It has been demonstrated that methylammonium lead triiodide ($MAPbI_3$) takes on a distorted three-dimensional structure at room temperature, crystallising in the tetragonal perovskite $I4/mcm$ space group whereas methalymmonium lead bromide ($MAPbBr_3$) has a cubic structure of the $Pm\bar{3}m$ space group under the same conditions[235][28]. The difference in crystal structure appears to relate to the size of the ionic radius of I^- and Br^- ions, with the smaller bromide ion better suited to the formation of a cubic structure. It is thus possible to obtain an accurate picture of the perovskite composition by indexing appropriate planes in the XRD patterns. Accordingly, as shown in Figure 5.5(c), $MAPbI_3$ has peaks located at 28.14 ° and 28.4 ° which correspond to the (004) and (220) planes for the tetragonal $I4/mcm$ phase[28]. Defining the proportion of Br ions as "x" for $MAPb(I_{1-x}Br_x)_3$ ($0 \leq x \leq 1$), it can be seen that the peak diffracted by the (004) plane disappears with increasing x by merging with the peak corresponding to (220) as the crystal symmetry improves. The decrease in lattice spacing caused by substitution of I ions with Br results in a shift of the $(200)_c$ towards higher 2θ. Matching peak positions for films of different $PbBr_2$ molar content with reported XRD patterns [35] allowed x to be determined. As already mentioned, systematic shifts in absorption band edge with Br content indicates that the energy band gap (E_g) may be tuned by the alloy composition as has been reported for various alloyed thin films [236] [237] [35]. E_g (estimated from Figure 5.5(b)) is plotted against x in Figure 5.5(d). Nonlinearities in the variation of E_g with composition may be expressed empirically by a quadratic least squares fit to the data (red line) such that [238] [236]

$$E_g(x) = A + Bx + Cx^2 \tag{5.1}$$

where A is the y-intercept, B is the difference in band gap between $MAPbI_3$ and $MAPbBr_3$ with constant subtracted and C is the bowing parameter. The relatively low bowing parameter (C=0.3) obtained would suggest good miscibility between the alloy components and confirms that the entire composition of the compound is made up of $MAPb(I_{1-x}Br_x)_3$.

Devices were fabricated using the structure ITO/ PEI/ C_{60}/ $MAPb(I_{1-x}Br_x)_3$/ P3HT/ TiAu and representative JV-curves for different bromide content are shown in Figure 5.6(a). Similar to the case of chloride addition, a small quantity of Br ions (x=0.13) was found to significantly enhance V_{oc}, increasing it from less than 0.85V to over 1V. The mean V_{oc} measured continued to increase slightly with x as shown in Figure 5.6(b) reaching 1.075V for x = 0.47. The increase in V_{oc} was accompanied by a decrease in J_{sc} as would be expected for a blue shifted absorption onset [28]. It should be noted that both FF and particularly V_{oc} were smaller for bromide-containing devices than theoretically achievable as has been reported in

x	J_{sc}(mA/cm^2)	V_{oc}(V)	FF	PCE(%)
0	13.46	0.82	0.51	4.67
0.13	6.82	1.015	0.61	3.74
0.2	5.4	1.025	0.59	3.51
0.29	4.56	1.063	0.59	2.52
0.38	6.89	18744	0.44	3.12
0.47	4.88	1.075	0.42	1.88

TABLE 5.1: Device characteristics for different bromide content x

recent years [35] [239] [240]. Limited V_{oc} has been attributed at least partly to reversible photoinduced formation of sub-bandgap states, resulting in iodide rich regions which may act as efficient recombination centres [241] [242] as well as band level matching at the interface with charge selective layers [243]. This resulted in a trend of decreasing PCE with increasing bromide content as seen in Figure 5.6(c).

In order to better understand which factors likely caused the limited device performance using the present set up, fits were made to the current-voltage data using the equivalent circuit model. Implementation of the one- and two-diode models requires representative values of certain key parameters if incorrect values for other parameters are to be avoided [244] [245] [246]. This is due to the fact that satisfactory curve fitting may result from a wide parameter set given the implicit nature of the equations used and number of variables. One approach which may be employed in cases where R_{sh} is assumed sufficiently large is to rearrange the equation for current density J derived in Chapter 3 on the basis of the equivalent circuit model such that

$$-\frac{dV}{dJ} = \frac{n_{id}k_bT}{q}(J_{sc} - J)^{-1} + R_s \tag{5.2}$$

The ideality factor n_{id} and R_s may be extracted from the slope and intercept respectively of the plot of $-dV/dJ$ vs $(J_{sc} - J)^{-1}$. Figure 5.6(d) shows such a plot for the case of a reverse scan performed in the dark on a device comprising ITO/ PEI/ C_{60}/ MAPb($I_{1-0.2}Br_{0.2}$)$_3$. The values for R_s and J_0 so obtained may be used as inputs to the diode models. Figure 5.6(e) shows semilog plots of dark-JV scans performed in forward and reverse bias directions on the same cell as Figure 5.6(d) along with fits obtained using the two-diode model. Similarly, Figure 5.6(f) shows a reverse bias scan of the same cell under illumination along with a one-diode fit following the same procedure. The extracted parameters are shown in Table 5.1.

Applying a fit to the reverse bias scan under illumination using the one-diode model with R_s=1.32Ωcm^2 gave an ideality factor of 2.36 with R_{sh} of less than 500Ωcm^2 which together signify poor PN junction quality with large leakage currents. Conversely, the small value

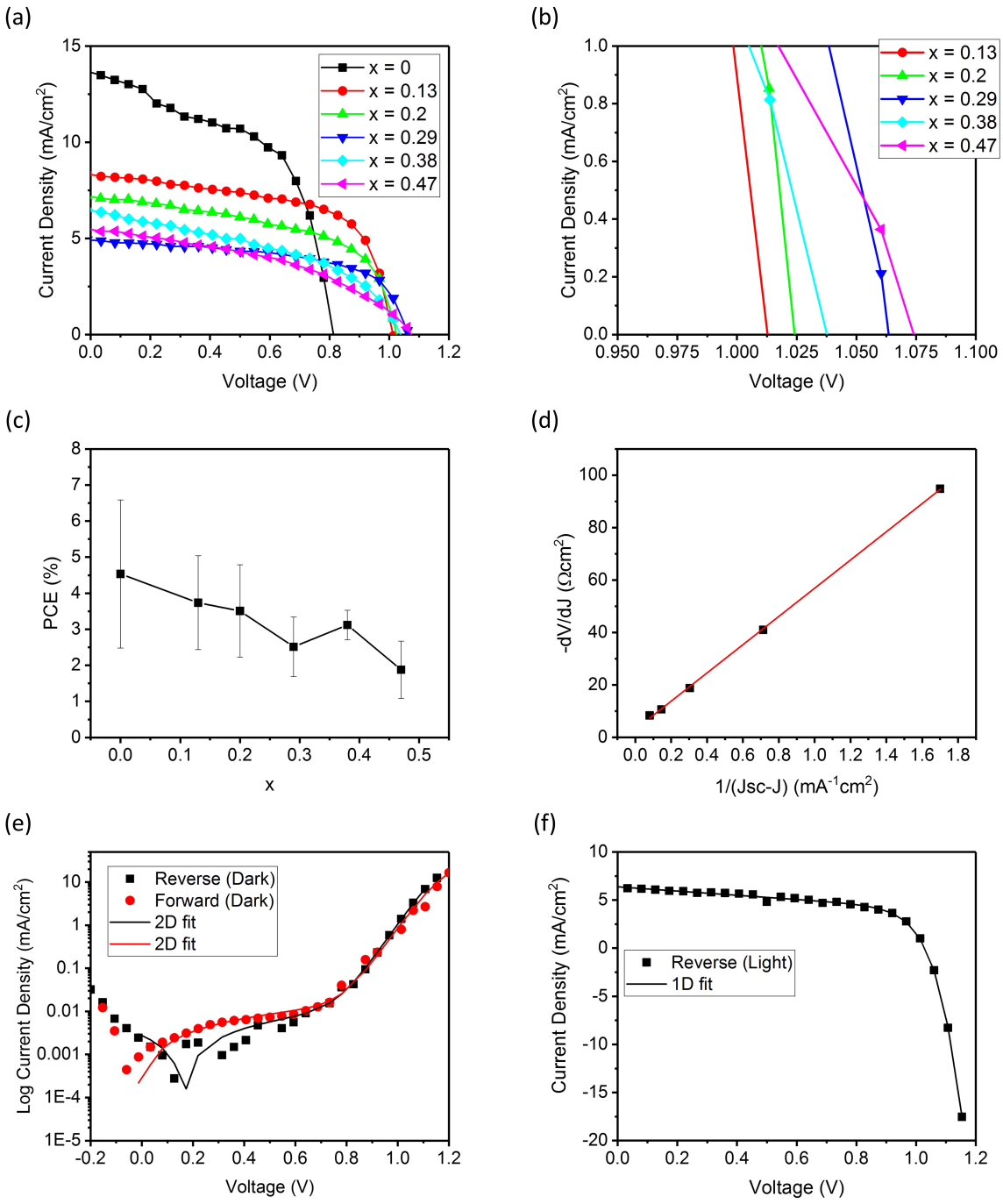

FIGURE 5.6: Photovoltaic response of devices with different molar content of $PbBr_2$. (a) Current-voltage response under illumination. (b) Same plot as (a) showing the open circuit voltage change with bromide content. (c) Mean device efficiency for different Br content. (d) Plot of $-dV/dJ$ vs $(J_{sc} - J)^{-1}$ for a reverse dark scan on a device comprising ITO/ PEI/ C_{60}/ $MAPb(I_{1-0.2}Br_{0.2})_3$ and linear fit to data. (e) Semilog plots of dark-JV scans for the two scan directions along with fitting. (f) Reverse scan under illumination along with fit using one-diode model.

	Diode model	R_s (Ωcm^2)	R_{sh} (Ωcm^2)	n_{id}	J_{01} (mA/cm^2)	J_{02} (mA/cm^2)
Reverse (Light)	1D 2D	1.32 1.32	455 409	2.36 1	1.75×10^{-7} 0	0 6.82×10^{-9}
Reverse (Dark)	1D 2D	3.04 3.04	5.3×10^{4} 6×10^{4}	1.9 1	1.5×10^{-9} 5.65×10^{-19}	0 3.75×10^{-9}
Forward (Dark)	1D 2D	3.32 3.32	7.1×10^{4} 5.85×10^{4}	2.3 1	4.2×10^{-8} 0	0 3.12×10^{-9}

TABLE 5.2: Parameters extracted from JV-characteristics for a device comprising ITO/PEI/C_{60}/MAPb($I_{1-0.2}Br_{0.2}$)$_3$/P3HT/TiAu

measured for J_{01} suggested substantial suppression of the thermal emission rate of electron from the VB to the CB, which would correspond to a higher V_{oc} [247] [248]. Leakage was found to be suppressed in the absence of illumination with an increase in R_{sh} of over two orders of magnitude and one-diode fits to scans performed in the dark gave similar values for n_{id} to the illuminated case. However, two-diode fits in which n_{id1} is set to 1 and n_{id2} is set to 2 provides more quantitative information on the diffusion and recombination processes. The values for J_{01} and J_{02} extracted from the two-diode fits suggested low recombination current leading to reduced shunting but also the presence of a negligible diffusion current contribution, signifying poor charge injection and extraction between the perovskite and the charge selective layers. Such findings are consistent with the reports already mentioned and highlights the necessity of an appropriate choice of charge transport materials as well as ensuring the formation of highly crystalline perovskite films with uniform mixed-halide phases either via additives or by more controlled deposition methods [249] [243][240].

5.3 Two-Step Deposition

As mentioned in the Introduction, the 2Step method in which the inorganic and organic precursors are deposited in separate steps is viewed as offering more dense highly crystalline films with fewer pin-holes. It was thus hoped that use of the 2Step method would overcome the limitations encountered with the 1Step deposited perovskite solar cells, facilitating reproducibly high performing devices.

5.3.1 Dependence of photovoltaic properties on perovskite thickness

An important aspect of device design in the field of photovoltaics is to optimize the thickness of photoactive materials. In the case of perovskite cells this has resulted in a typical film thickness of around 300nm which is sufficient to absorb most incoming photons of energies equal to or higher than the bandgap (if not during the first pass then upon the second after

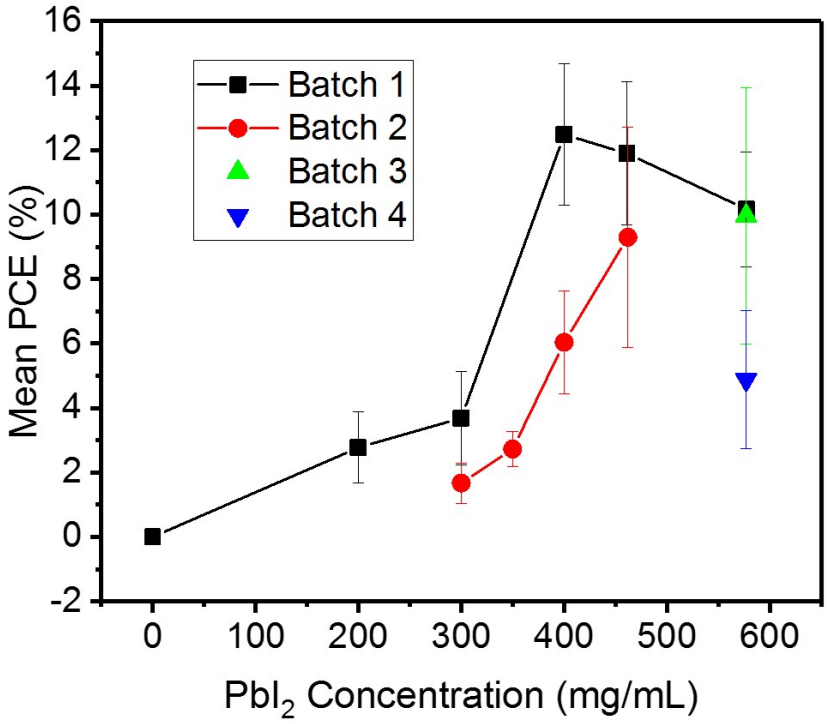

FIGURE 5.7: Mean power conversion efficiency (PCE) versus PbI_2 precursor concentration for devices processed in different batches.

reflecting off the metallic counter electrode) without suffering high recombination losses (i.e. large R_s) due to the limited diffusion length of ≈100nm for triiodide perovskites [250] [54]. In order to find the optimum perovskite layer thickness using the 2Step method, devices were fabricated using PbI_2 solutions of different concentrations in DMF.

Figure 5.7 shows how mean conversion efficiency varied with PbI_2 concentration for devices made in different batches. For the purposes of this discussion, a "batch" refers to a group of solar cells (typically 8 devices each containing 8 cells) fabricated together, with a period of days to weeks between the fabrication of any two batches. At lower concentrations, efficiencies remained below 5% but as the concentration approached 1M (as typically used in the literature) a significant increase in efficiency was observed for the highest performing batch of devices. Although respectable efficiencies were still sometimes achieved for 1.2M solutions of PbI_2, the standard deviation tended to be quite large and some batches had much lower mean efficiencies as shown in the figure. Furthermore, significant batch-to-batch variation was observed in mean efficiency at most concentrations which was problematic for device optimization towards commercial application and explained the humidity controlled and inert processing conditions typically reported in the literature. It was noted during processing that in order to achieve concentrations at or above 1M PbI_2 in DMF it was

necessary to heat the solution above 70 °C with significant precipitation and crystallization occurring shortly after cooling to room temperature. Such an effect has resulted many reports of PbI_2 solutions being deposited at elevated temperature, particularly when higher concentrations (and thus film thickness) are desired. It was posited that this strategy would be disadvantageous for processing in non-controlled environments as the dynamic nature of cooling might increase sensitivity to air temperature and humidity. It was thus out of a desire for reproducibility that solutions were allowed cool to approximately room temperature before spin coating. However, this often resulted in at least partial precipitation of PbI_2 and consequently in the formation of visible pin holes in cast films.

5.3.2 Effect of chloride content on device performance and reproducibility under high relative humidity

It was observed during experimentation that although lead chloride ($PbCl_2$) had quite low solubility in DMF, mixtures of PbI_2 and $PbCl_2$ could be fully dissolved at higher concentrations than either of the lead salts could individually. It was thus reasoned that mixed lead halide solutions could allow for the deposition of films with more reproducible morphology under ambient conditions. Furthermore, mixed halide perovskites have been found to possess longer diffusion lengths than lead triiodide perovskites therefore it was assumed that incorporating $PbCl_2$ as an additive might have the additional advantage of increasing the maximum permissible thickness for the active layer.

As an arbitrary starting point, 20wt% $PbCl_2$ was added to 1M PbI_2 (hereafter referred to as "2Step 20wt%") as this was found to result in a solution that remained fully dissolved at room temperature. Figure 5.8 shows how different batches of devices made with $PbCl_2$ as additive compared with PbI_2-only devices. It was found that some batches significantly outperformed PbI_2-only cells with higher mean efficiency and smaller standard deviation. However, a significant batch-to-batch variation remained resulting in mean conversion efficiencies of anywhere between 8.5% and 15%. Over time it became clear that although the $PbCl_2$ additive tended to improve performance, a sensitivity to ambient humidity during device fabrication remained. In order to determine whether some other $PbCl_2$ content could further improve device performance and reproducibility, the proportion of $PbCl_2$ was varied at a fixed total (nominal) solids concentration of 576mg/mL. As seen in Figure 5.9(a), significant precipitation occurred near room temperature both in the absence of $PbCl_2$ and when the chloride content exceeded 30wt%, even after prolonged stirring at 100 °C. Figure 5.9(b) shows how mean device efficiency varied with $PbCl_2$ content for devices processed under over 90% relative humidity. Mean efficiencies were calculated based on the maximum power

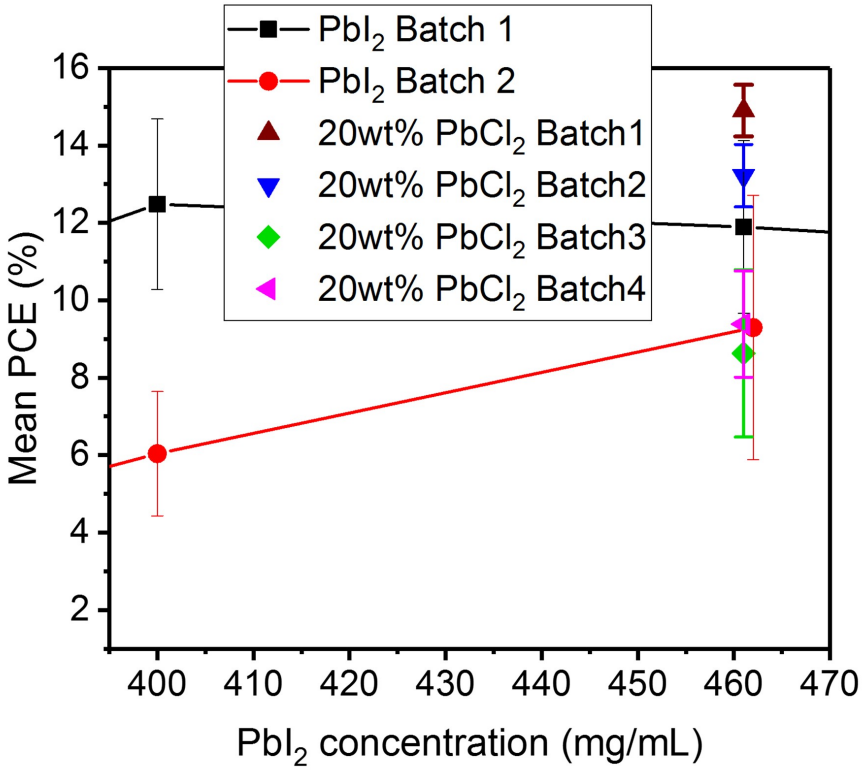

FIGURE 5.8: Effect of the addition of 20wt% $PbCl_2$ to the head halide solution used during deposition of perovskite on mean power conversion efficiency relative to PbI_2-only based perovskite devices.

extracted from JV-scans and so delay times of at least 1.5s were used and values were calculated for both scan directions in order to ensure results indicative of device operation under real world applications.

Although the addition of 2.5wt% $PbCl_2$ was insufficient to fully prevent precipitation of the solution at room temperature, it did notably improve conversion efficiency. However, increasing the chloride content first to 5 wt% and then 10 wt% resulted in a striking reduction in photocurrent and mean efficiency. This trend began to reverse for 15 wt% $PbCl_2$ as photocurrent began gradually to rise. Devices made with 20 wt% $PbCl_2$ tended to display a "burn-in" effect, whereby initial sweeps registered J_{sc} greater than 20 mA/cm^2 with a rapid decay in J_{sc} upon subsequent sweeps before a steady-state value was reached. This effect is illustrated in Figure 5.9(c) which shows a typical cell response for devices incorporating 20 wt% $PbCl_2$ resulting in a stabilised photocurrent of approximately 12 mA/cm^2 and a PCE of 8.63%. Increasing $PbCl_2$ to 25 wt% resulted in a less pronounced burn-in and consequently a higher mean efficiency.

A different sort of burn-in effect took place when $PbCl_2$ content was further increased to 30 wt% as illustrated in Figure 5.9(d), in which fill factor increased with successive scans,

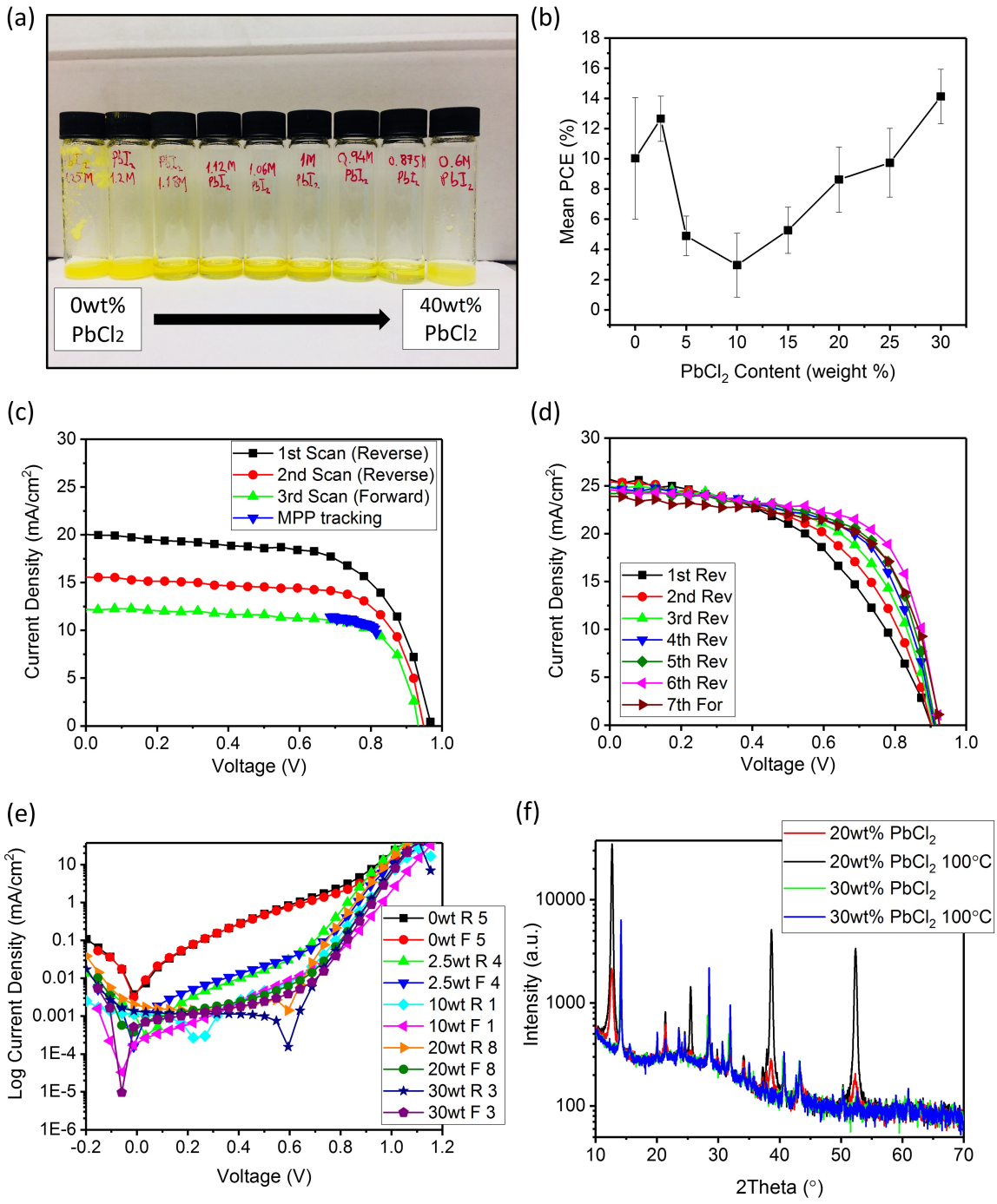

FIGURE 5.9: (a) Solubility of various ratios of PbI_2 to $PbCl_2$. (b) Plot of mean PCE against $PbCl_2$ content in the perovskite precursor solution. (c) Burn-in effect for devices made with 20 wt% $PbCl_2$ (d) Typical JV-response for for devices with 30 wt% $PbCl_2$. (e) JV-response in the dark for devices with different chloride content plotted on a semilog scale. (f) XRD patterns of perovskite films made in high ($\geq$ 70%) humidity conditions with either 20wt% or 30wt% $PbCl_2$ both before and after annealing on a hotplate at 100 °C for 10 minutes.

stabilizing at a higher value than measured initially. Comparing semilog plots of sweeps carried out in the dark revealed a general trend towards lower current densities in the low voltage (i.e. below ≈0.6V) region with increasing $PbCl_2$ content as shown in Figure 5.9(e). Furthermore, it was noted that there was a tendency in the case of reverse bias sweeps for the point of lowest registered current density to shift towards higher positive voltage as the chloride content increased. Lower dark current densities points to the presence of fewer shunting pathways for devices with higher $PbCl_2$ content which would also be consistent with the increased capacitive effect observed for reverse bias scans. This led to the hypothesis that $PbCl_2$ might better mediate perovskite crystallisation under conditions of high ambient humidity, resulting in more densely packed grains with fewer pinholes. The presence of more complete crystallisation was confirmed by the absence of any peaks associated with PbI_2 in XRD patterns of 30wt% $PbCl_2$ films as seen in Figure 5.9(f). Films made 20wt% $PbCl_2$ on the other hand showed a significant PbI_2 (001) peak which grew larger still upon annealing for 10 minutes at 100 °C. This was consistent with the lower photocurrents observed for devices with 20wt% as a larger proportion of the PbI_2 phase would result in higher series resistance and lower optical absorption.

In order to ensure reproducibility of the observed relationship between mean device efficiency and chloride content in the precursor, multiple batches of devices with different $PbCl_2$ content were fabricated over a period of weeks and months. Figure 5.10(a) shows mean efficiency for six batches of devices plotted alongside one another for comparison. Not only did the trend hold between batches (processed under variable humidity but always within the range of 60%–95%) but devices with 30 wt% $PbCl_2$ or more consistently outperformed PbI_2-only devices which displayed higher standard deviation and batch-to-batch variability. This resulted in a trend towards a decreasing ratio between standard deviation and mean efficiency as the chloride content increased as shown in Figure 5.10(b).

Somewhat surprisingly, this trend continued even for devices made with precursor compositions that were above the precipitation threshold. This posed the question of whether moving towards a $PbCl_2$-only formulation would result in further improvements in device performance. However, absorption spectroscopy of the solutions (Figure 5.11(a) and (b)) suggested a non-trivial relationship between the halides at higher $PbCl_2$ content, implying some sort of aggregation effect rather than a simple sum of precursors in the intended ratio. Furthermore, as seen in Figure 5.11(b), $PbCl_2$ was found to have solubility below 30mg/mL in DMF (labelled as "Low concentration") which is far too low to form a sufficiently thick or homogeneous active layer.

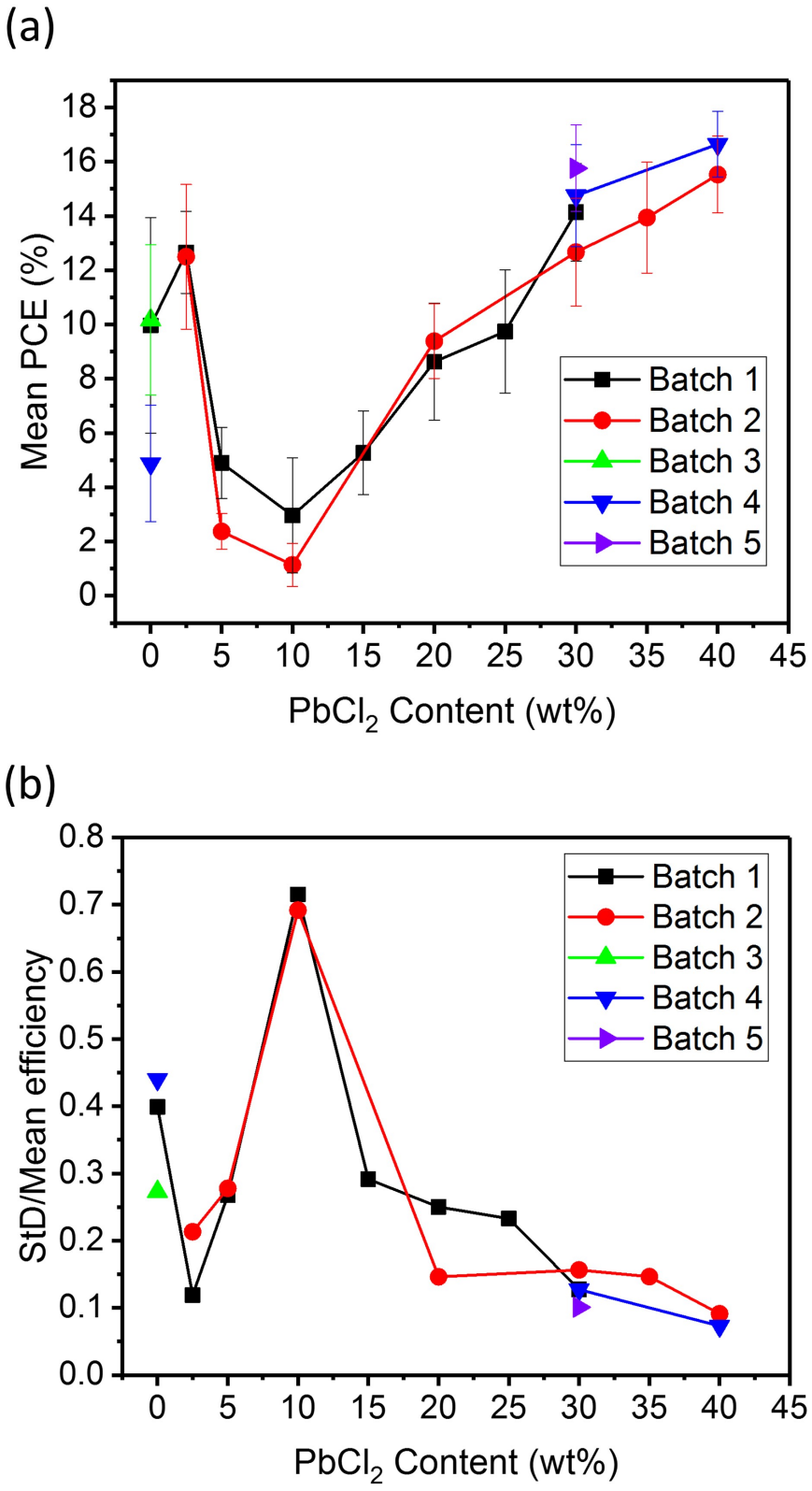

FIGURE 5.10: (a) Plot of mean device efficiency against wt% $PbCl_2$ content in the perovskite precursor for devices made in separate batches (b) Plot of standard deviation (StD)/Mean efficiency against $PbCl_2$ content for the devices shown in (a).

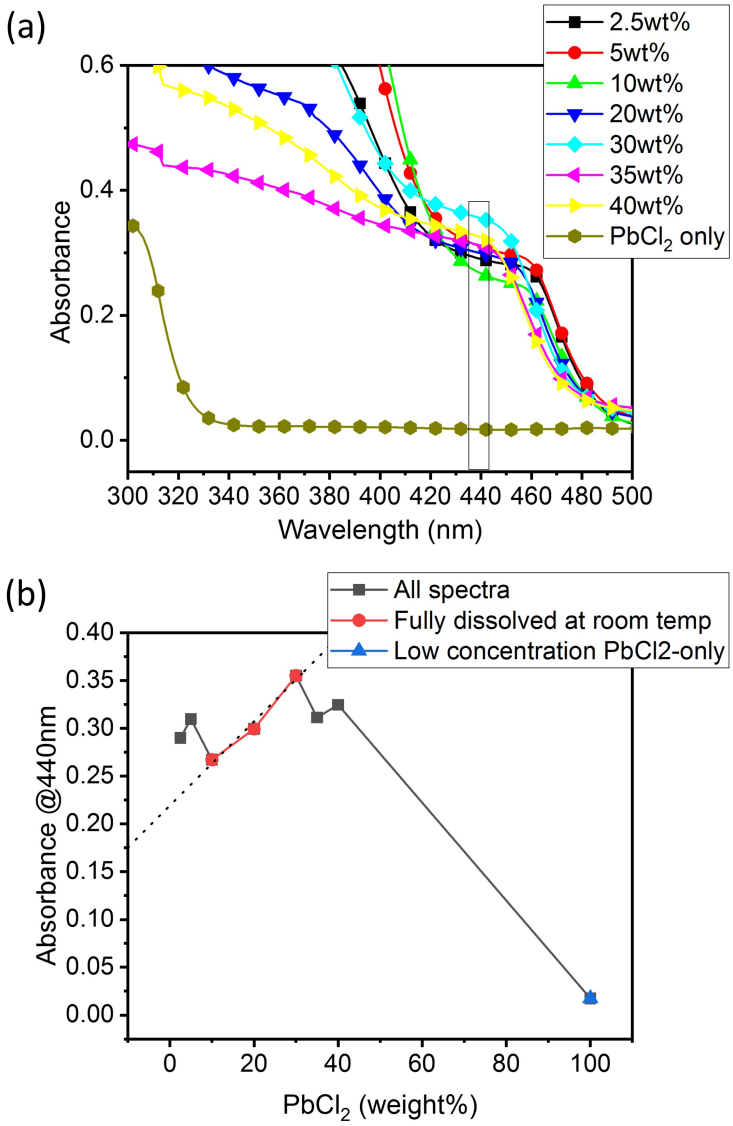

FIGURE 5.11: (a) UV-visible absorption spectra of different precursor compositions and (b) plot of absorption at 440nm against nominal chloride content.

Fits to JV-scans revealed how different solar cell parameters varied with chloride content. As seen in Figure 5.12(a), there was a large increase in both FF and V_{oc} with increasing $PbCl_2$ content up to 5 wt%. The trend was towards a small improvement in FF with increasing chloride content above 20wt% whereas V_{oc} remained largely level over the same range. Observed variations in mean efficiency and standard deviation with chloride content were more adequately reflected in the series resistance and short circuit current density extracted from JV-scans. As seen in Figure 5.12(b), R_s (measured as the inverse slope of the JV-curve at V_{oc}) was highest between 5wt% and 10wt% $PbCl_2$ which corresponded to the lowest values for J_{sc} as would be expected. A clear trend of reduced R_s as the chloride content was increased above 10wt% was accompanied by significant increases in J_{sc},

	Batch 1		Batch 2	
$PbCl_2$	30wt%	40wt%	30wt%	40wt%
R_s (Ωcm^2)	2.15	1.04	0.87	0.48
R_{sh} (Ωcm^2)	248	330	298	442
n_{id}	2.6	3.3	1.99	3.4
J_0	8.5×10^{-6}	2.7×10^{-4}	1.8×10^{-7}	5.7×10^{-4}
FF	0.624	0.637	0.69	0.66
V_{oc} (V)	0.97	0.96	0.947	0.931
J_{sc} (mA/cm^2)	21.1	25.2	22.4	26.5
PCE (%)	12.67	15.5	14.75	16.64

TABLE 5.3: Parameters extracted from JV-characteristics for two separate batches of devices comprising ITO/PEI/C_{60}/2Stepxwt%/P3HT/TiAu where x=30 or x=40.

approaching 27mA/cm^2 for 40wt% $PbCl_2$.

Evaluating series and shunt resistance from the inverse slope of fitted curves around V_{oc} and J_{sc} respectively, though useful as a diagnostic tool, can give misleading results as tiny changes in slope due to variations in illumination intensity, voltage noise or capacitive effects may lead to large variability in the quantities measured. A more rigorous approach is to employ equation 5.2 in order to determine n_{id} and R_s and to use them as constraints in applying fits to the data using the diode models, thereby obtaining sensible values for other extracted device parameters. Figure 5.13 shows typical reverse bias JV data for devices prepared using precursors containing 30wt% and 40wt% $PbCl_2$ along with fits using the one-diode model. In order to better elucidate which device parameters relate to chloride content, fits were performed on two separate batches of devices which are referred to as "Batch 1" and "Batch 2" in Table 5.3.

For both batches, R_s was found to decrease as the chloride content was increased. The inverse relationship was found for the case of shunt resistance as R_{sh} increased with $PbCl_2$ content. Plotting R_s and R_{sh} against PCE for both batches together showed that these trends could be described by polynomial fits as shown in Figure 5.13(d). The increased R_{sh} with chloride content extracted from illuminated JV scans was consistent with lower current densities measured for 40wt% $PbCl_2$ devices as shown in Figure 5.13(c). The combination of lower R_s and higher R_{sh} was also consistent with the marked increase in short-circuit current density and hence PCE with chloride content, as shown by the approximately linear trend between J_{sc} and PCE in Figure 5.13(d). On the other hand, J_0 was found to increase significantly with $PbCl_2$ content, indicating increased thermal emission of electrons from the valence band (VB) to the conduction band (CB) which was consistent with the slight decrease in V_{oc} observed, resulting in larger n_{id} for 40wt% $PbCl_2$ devices.

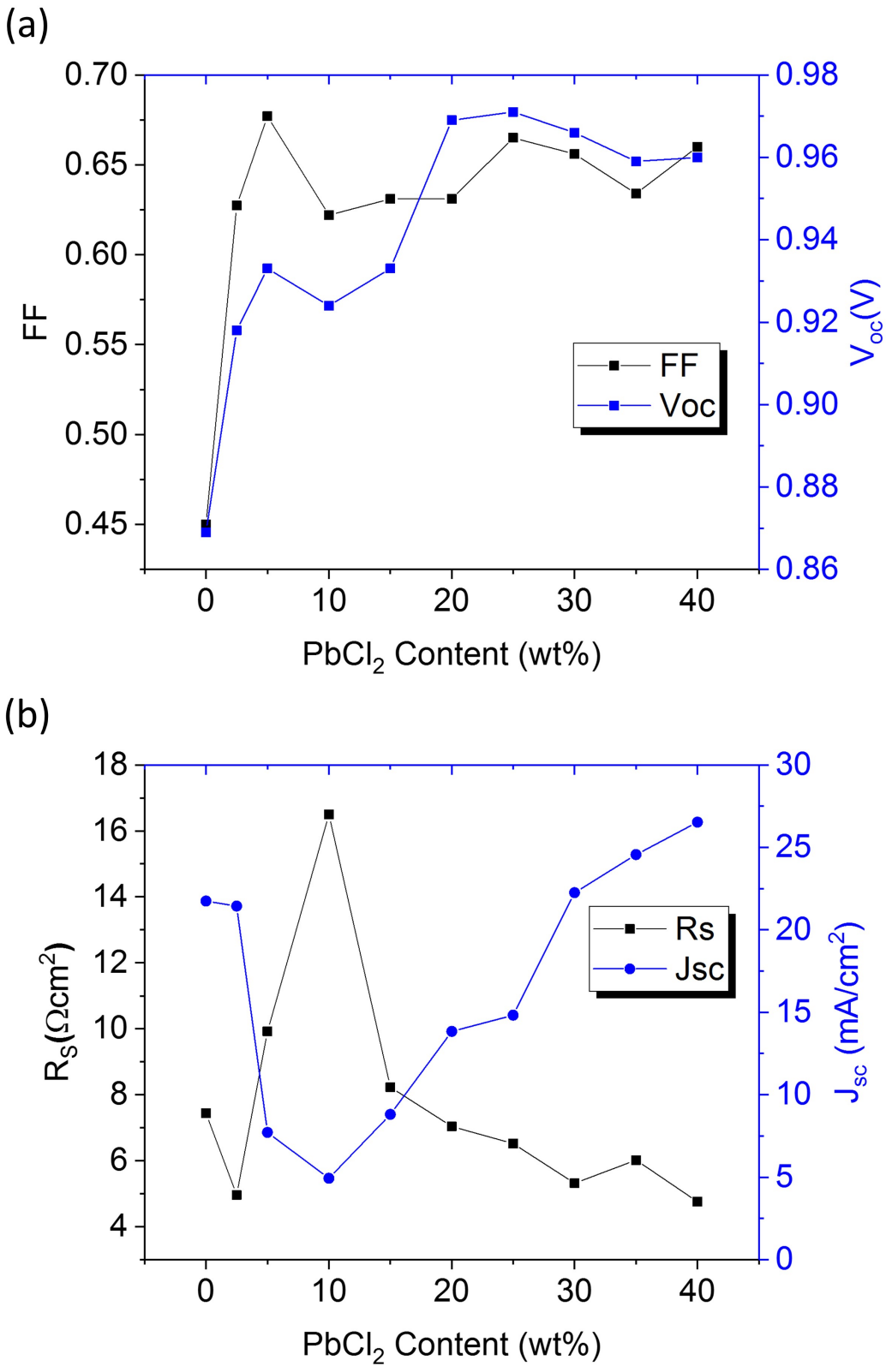

FIGURE 5.12: (a) Plots of fill factor (FF) and open circuit voltage (V_{oc}) versus chloride content and (b) plot of series resistance (R_s) and short circuit current density (J_{sc}) versus chloride content.

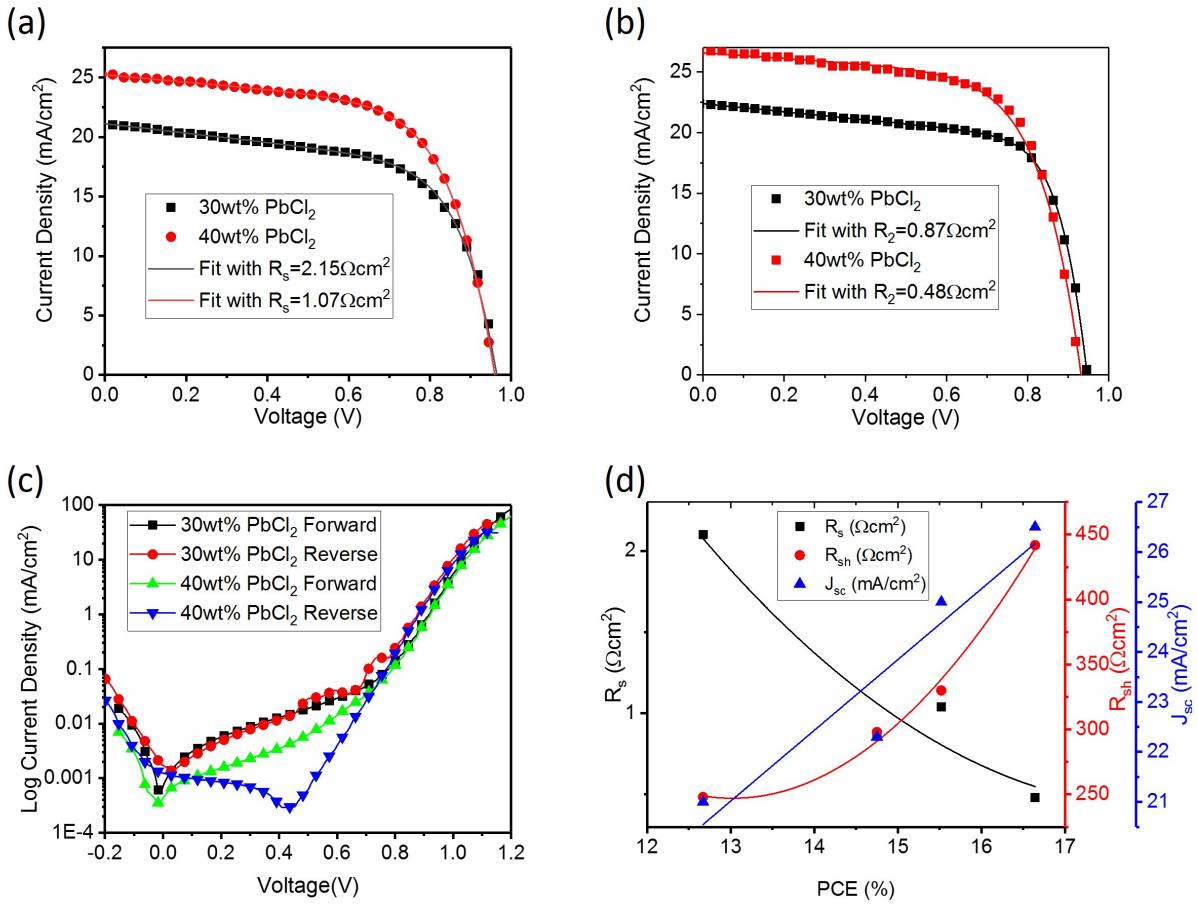

FIGURE 5.13: Difference between 30wt% and 40wt% in two separate batches. (a) Typical response for reverse bias scans for different chloride content in Batch 1. (b) Typical response for reverse bias scans for different chloride content in Batch 2. (c) Semilog plot of devices shown in (a) and (b). (d) Plot of extracted parameters from both batches.

In the case of ITO-based devices, in addition to larger power output regardless of scan direction for higher chloride content, the degree of hysteresis was also reduced to near zero as shown in Figure 5.14(a). An interesting effect which was also manifested at higher chloride content was a discrepancy between maximum power output and hysteresis recorded for cells nearer the edge of devices versus those around the centre. It was found that for both scan directions there was a tendency for mean PCE ("Tot." in the legend) to diverge from PCE recorded for cells near the substrate centre as the proportion of $PbCl_2$ in the precursor was increased.

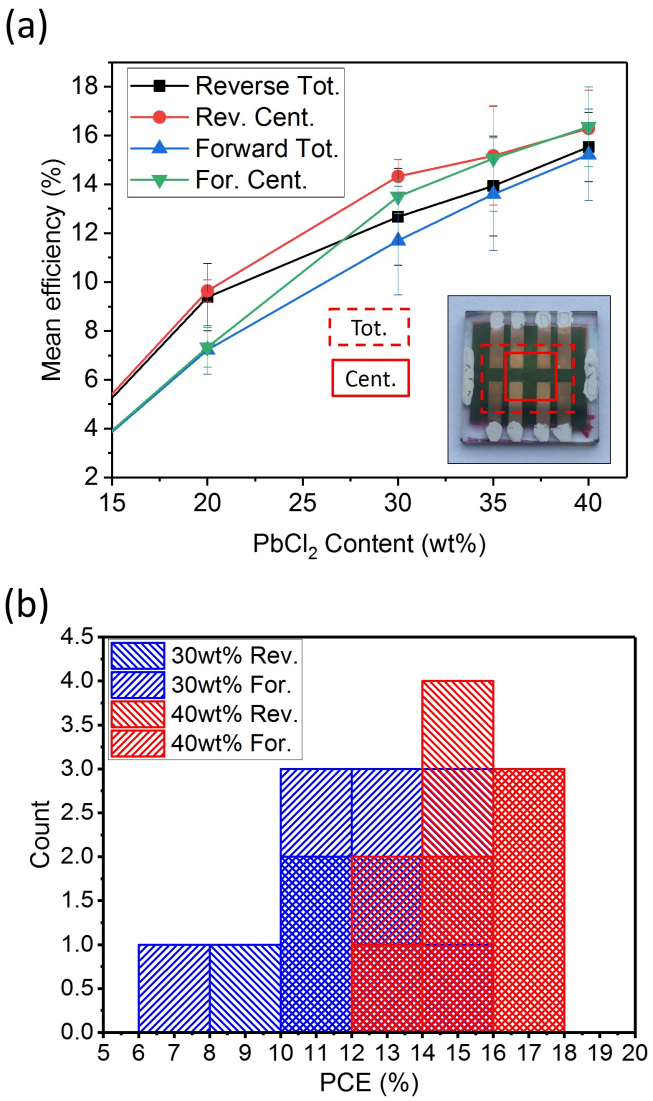

FIGURE 5.14: (a) Mean efficiency versus chloride content based on scans performed in both reverse and forward bias direction. (b) Histogram of PCE distribution for different $PbCl_2$ content based on scan direction.

It was found that mean efficiency calculated as an average of the four central cells on a given device (referred to as "Rev. Cent." and "For. Cent." for reverse and forward bias scans

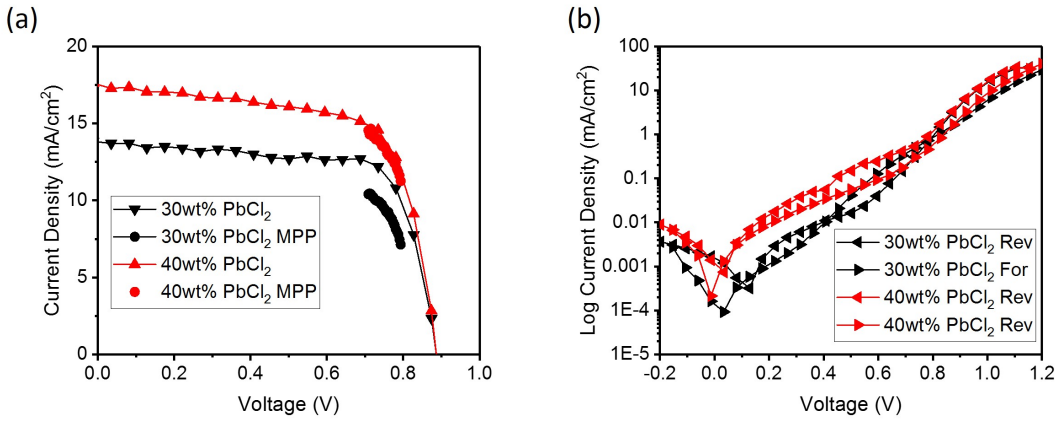

FIGURE 5.15: Difference between devices fabricated using AZO as transparent cathode with either 30wt% or 40wt% $PbCl_2$ in the perovskite layer. (a) JV-response of devices under illumination along with stabilized power under constant bias (MPP). (b) Current-voltage data for devices shown in (a) in the dark plotted on a semilog sale.

respectively) was often significantly higher than that for all eight cells ("Reverse Tot." and "Forward Tot."). The reason for this discrepancy was unclear but it would suggest either that crystallisation tended to remain incomplete towards the substrate edge or else that perovskite decomposition through methylammonium escape proceeds in across the plane of the film with the HTL offering a degree of protection to escape normal to the plane. The net result was a spread in PCE for every $PbCl_2$ content, although deviation from the mean was smaller for 40wt% as seen in Figure 5.14(b).

Devices were also fabricated using different chloride content with AZO as transparent cathode. The resulting device structure consisted of AZO / PEI / C_{60} / 2Step / P3HT / TiAu. In keeping with the trend observed for ITO-based devices, cells with 40wt% $PbCl_2$ in the perovskite precursor outperformed those incorporating only 30wt% as seen in Figure 5.15(a). Table 5.4 shows device parameters extracted from fits to scans performed both in the dark and under illumination using the one-diode model along mean and max PCE. Cells displayed slightly higher Rs than corresponding devices on ITO which may be explained by the larger sheet resistance of AZO relative to ITO and a possible resistive barrier at the interface between perovskite and AZO as suggested in Chapter 4. The larger series resistance values were reflected in lower mean PCE for both cell stacks relative to ITO-based counterparts, although 40wt% devices again showed reduced R_s and significantly enhanced champion PCE despite a larger ideality factor. Curiously, unlike ITO-based devices, R_{sh} tended to be lower for cells incorporating 40wt% $PbCl_2$ though cell-to-cell variability was also lower resulting in a much smaller ratio of standard deviation to mean PCE (StDev./Mean). The

	R_s (Ωcm^2)	R_{sh} (Ωcm^2)	n_{id}	Mean PCE (%)	StDev./ Mean	Max. PCE (%)
30wt% (Dark)	3.6	3.64×10^4	2.2	-	-	-
30wt% (Light)	1.52	2.8×10^3	2.44	6.7	0.356	7.3
40wt% (Dark)	2.92	1.12×10^4	2.8	-	-	-
40wt% (Light)	1.14	1.1×10^3	2.9	10.05	0.07	11

TABLE 5.4: Extracted device parameters for AZO-based devices with different $PbCl_2$ content.

results showed that performance improvements by using high chloride content are not limited to the more typical sputtered ITO and FTO-based device stacks but also apply to much rougher and more reactive substrates such as doped binary oxides deposited by spray pyrolysis.

In order to examine whether it was in fact the case that higher chloride content improved perovskite morphology, films containing 30wt% $PbCl_2$ and films without any chloride were grown under the same conditions and were studied under SEM. In order to mitigate the possibility of precipitates from a highly saturated PbI_2 solution (1.25M) being a source of pinholes, the commonly used concentration of 1M PbI_2 solution was chosen for better comparison with the literature. As seen in Figure 5.16 (a) and (c), PbI_2-only perovskite films tended to be incomplete, leaving many micrometer-sized areas of underlying ITO visible. In contrast, films made with 30 wt% $PbCl_2$ gave continuous and densely packed perovskite with many micrometer-sized grains as shown in Figure 5.16 (b) and (d). It should be noted that the difference in film morphology shown here is particularly dramatic, and is more reflective of batch-to-batch variability for perovskite films using only lead iodide prepared under humid conditions as some batches produced more continuous films with larger grains. However, the chloride-containing films consistently gave dense dark films with few pinholes.

The improved morphology for perovskite films crystallised from lead salt solutions with 30wt% $PbCl_2$ was reflected in device performance and resulted in some devices with FF between 0.73 and 0.75 as shown in Figure 5.17(a). Fits to the JV data under illumination were performed and the series and shunt resistance were evaluated by taking the inverse slope of the fitted curve at V=V_{oc} and V=0 (i.e.$_{sc}$) respectively. This method revealed that the source of high FF was a combination of reduced shunting with R_{sh} of 1248Ωcm^2 for the forward bias and 1872Ωcm^2 for the reverse bias scan direction and a low R_s of 2.99Ωcm^2 and 3.48Ωcm^2 for the former and latter scan directions respectively.

Figure 5.18(a) gives plots and linear fits not for the two scan directions under illumination but also for scans performed in the dark. It can be seen that there was close agreement

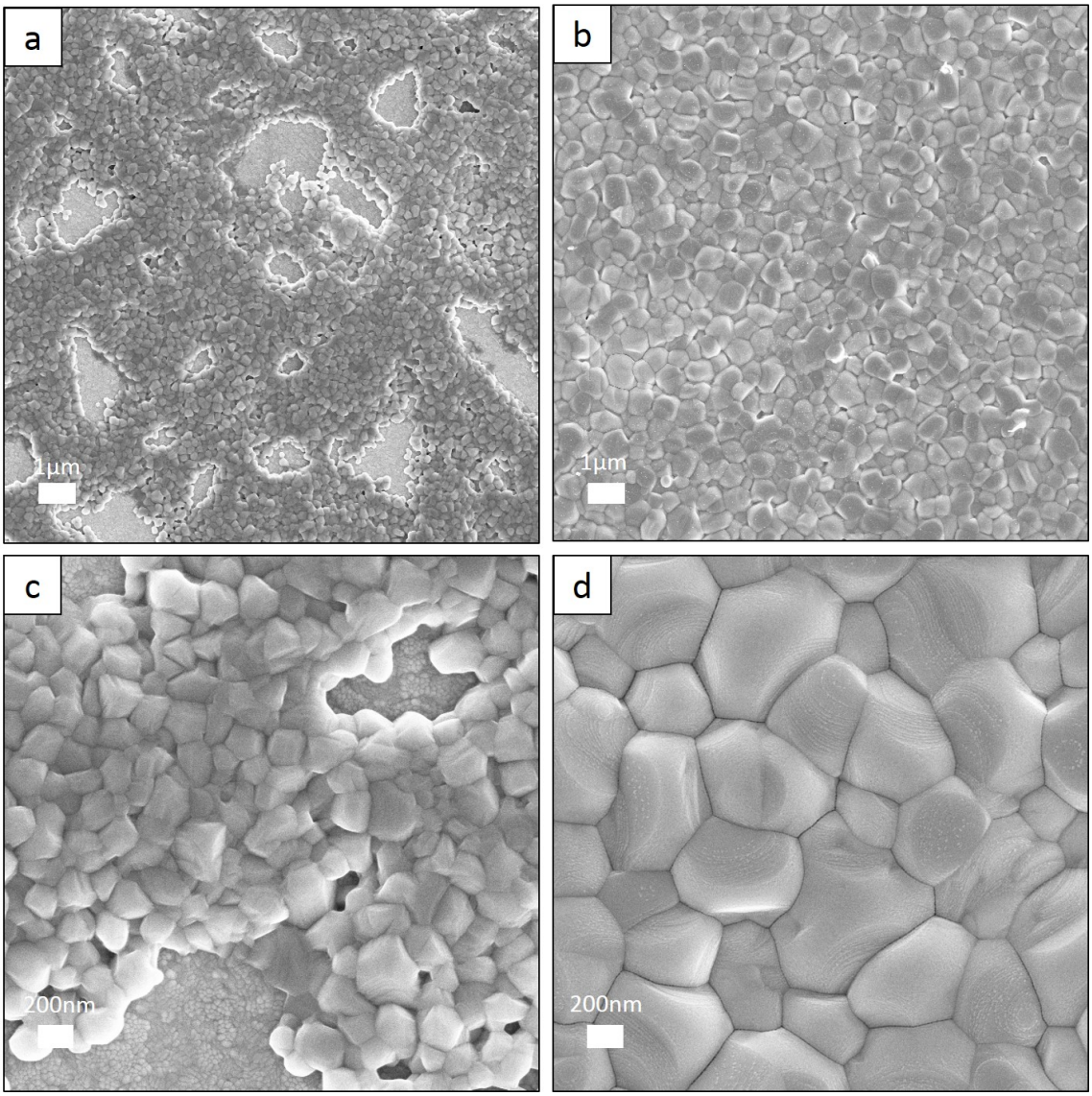

FIGURE 5.16: SEM images of perovskite films produced via the Two-Step method.(a) and (c) Film crystallised from 1M PbI_2 and (b) and (d) crystallised from lead halide film with 30 wt% $PbCl_2$.

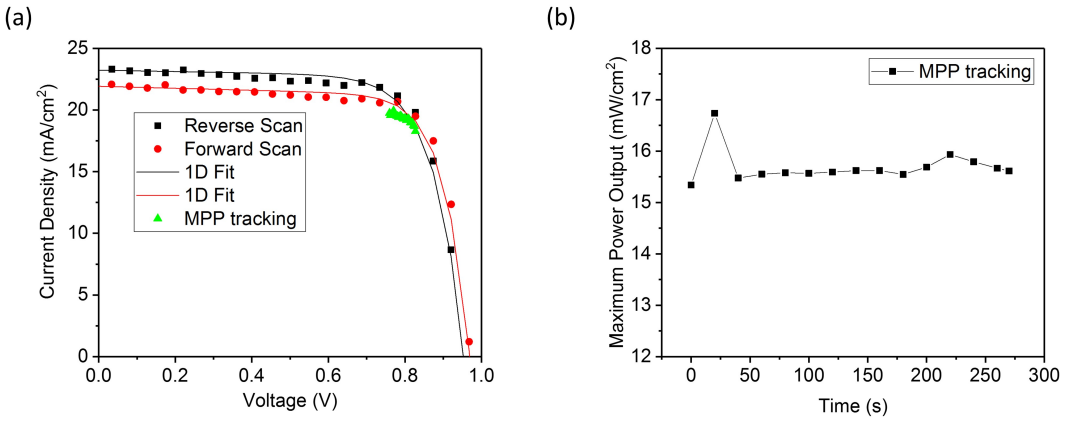

FIGURE 5.17: Current-voltage measurements of device comprising ITO/PEI/C_{60}/2Step30wt%/P3HT/TiAu (a) sweep measured from open circuit to short circuit (Reverse) and from short circuit to open circuit (Forward) as well as under constant bias in the narrow range around the maximum power point (b) Plot of maximum power extracted from the device versus time.

	R_s (Ω cm^2)	R_{sh} (Ω cm^2)	n_{id}	J_{01}(mA/cm^2)	J_{02}(mA/cm^2)
Reverse (Light)	0.74	2274	2.57	1.28×10^{-5}	0
Forward (Light)	0.53	1050	2.29	1.66×10^{-6}	0
Reverse (Dark)	0.59	∞	1	7.75×10^{-17}	2.75×10^{-8}
Forward (Dark)	0.63	1.6×10^{5}	1	4.5×10^{-17}	1.5×10^{-8}

TABLE 5.5: Parameters extracted from fits to current-voltage data for a device comprising ITO/PEI/C_{60}/2Step-30wt%$PbCl_2$/P3HT/TiAu using the one-diode and two-diode models

between forward and reverse bias data under illumination resulting in a derived ideality factor of 2.62 and 2.47 respectively. There was likewise some small difference between the y-intercept for both plots which resulted in a calculated R_s of 0.69 cm^2 for the reverse bias scan and 0.37Ωcm^2 for the forward bias case. These values for R_s were clearly significantly smaller than those evaluated using the inverse slope of the JV-scan but were in close agreement with the result extracted from the dark JV-scans of 0.49 and 0.59Ωcm^2. The value for n_{id} obtained for dark JV scans was invariably lower than that of illuminated scans and was generally in the range 1.5-2. It was thus appropriate to apply two-diode fits to dark-JV data by setting n_{id1}=1 and n_{id2}=2 as the two-diode model is better suited to capturing both diffusion and recombination effects in diodes. Adequate fits were obtained for semilog plots of dark current based on the two-diode model as shown in Figure 5.18 and Table 5.5 shows the parameters extracted from fits to data for the best performing cell using the diode models.

Again, there was a remarkable difference between R_{sh} extracted under illumination versus in the dark with the latter being more than two orders of magnitude greater. The reduced value for the reverse saturation dark current (J_{01}) for the forward bias scan under

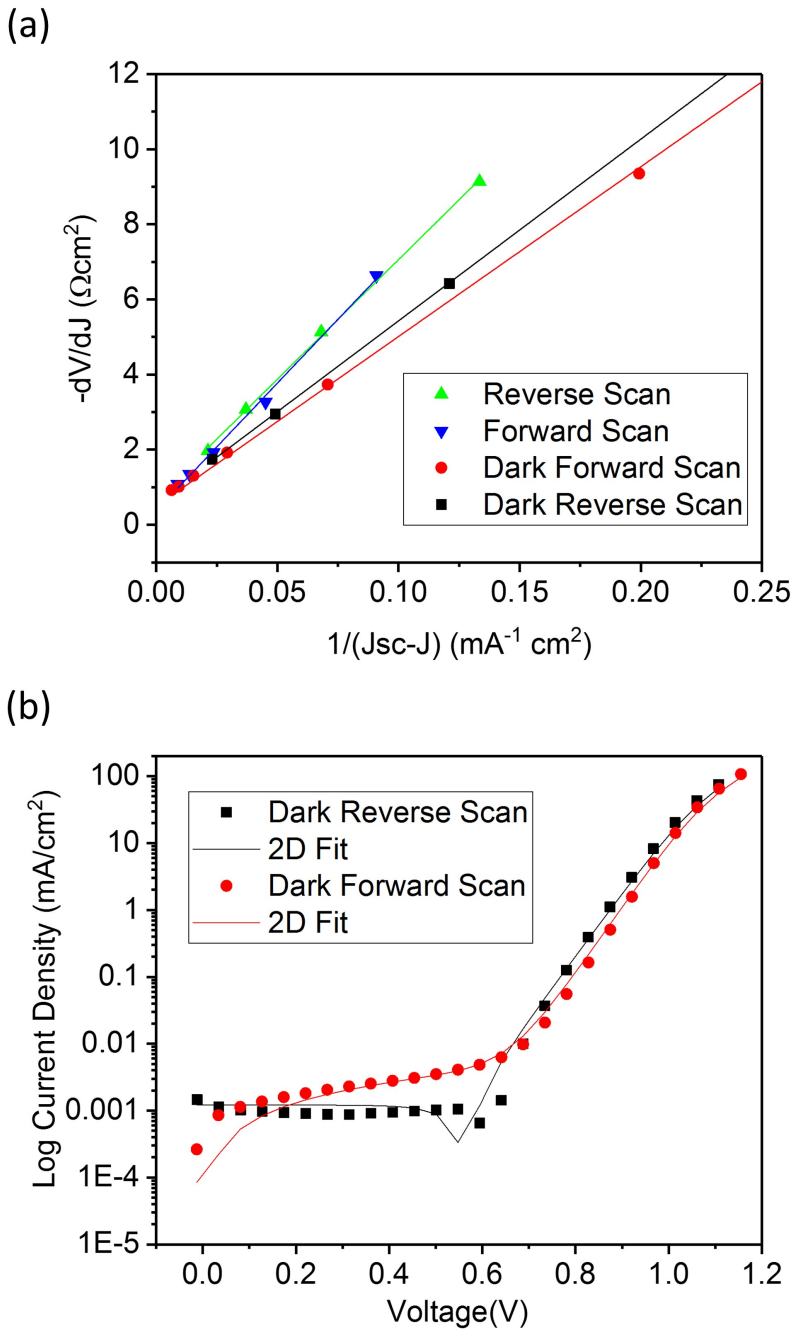

FIGURE 5.18: (a)Plots of $-dV/dJ$ vs $(J_{sc} - J)^{-1}$ and linear fitting curves. (b) Semilog plots of dark-JV scans for the two scan directions along with fitting.

illumination coupled with a lower n_{id} relative to many values reported in the literature [251] [247] [252] [253] [254] [248] were consistent with the very large short-circuit current measured (24.6mA/cm^2). The near negligible value for J_{01} for both scan directions in the dark suggested either that electron injection into the perovskite layer from P3HT or electron extraction from perovskite into the ETL (or both) was greatly suppressed. However, the low recombination current extracted for J_{02} was consistent with the large shunt resistance and signified effective hole-blocking of the ETL.

Such device behaviour is indicative of a high quality active layer and is an impressive result considering all of the processing steps were carried out from solution in humid conditions without high temperature treatments. Furthermore, JV-scans were representative of device performance under true operating conditions as shown by the stable maximum power output at constant bias in Figure 5.17(b). In order to get further verification of the validity of extracted parameters, the FF may be analysed using an empirical equation together with the fit results and experimental data. In ideal solar cells with negligible series resistance ($R_s \approx 0$) and infinite R_{sh}, the FF may be represented by [255] [256] [257] [37]

$$FF_0 = \frac{v_{oc} - ln(v_{oc} + 0.72)}{v_{oc} + 1} \tag{5.3}$$

where $v_{oc} = qV_{oc}/k_BT$ is the dimensionless voltage. Practical devices on the other hand include non-ideal values for R_s and R_{sh} which are accounted for in the expression

$$FF = FF_s(1 - \frac{v_{oc} + 0.7FF_s}{v_{oc}r_p}) \tag{5.4}$$

where FF_s is taken as

$$FF_s = FF_0(1 - 1.1r_s) + \frac{r_s^2}{5.4} \tag{5.5}$$

and where $r_s = J_{sc}R_s/V_{oc}$ and $r_p = J_{sc}R_{sh}/V_{oc}$ are normalised resistances. The FF calculated using the forward bias scan data shown in Table 5.5 was found to be 0.765 which was within 2.5% of that measured experimentally (0.748). Equation 5.4 may thus be used to predict the upper limit for FF in lead halide perovskite devices. Furthermore, given that V_{oc} and n_{id} are dependent on the density of traps states (N_t) [45], and that FF is a function of these parameters as well as J_{sc}, R_s and R_{sh}, it follows that FF is dependent on N_t. Figure 5.19 shows how n_{id}, FF and photovoltaic conversion efficiency (PCE) vary with N_t for devices with R_{sh}=1×10$^5\Omega$cm^2 and R_s of either 6Ωcm^2 (closed triangles and diamonds) or 0.5Ωcm^2 (open triangles and diamonds).

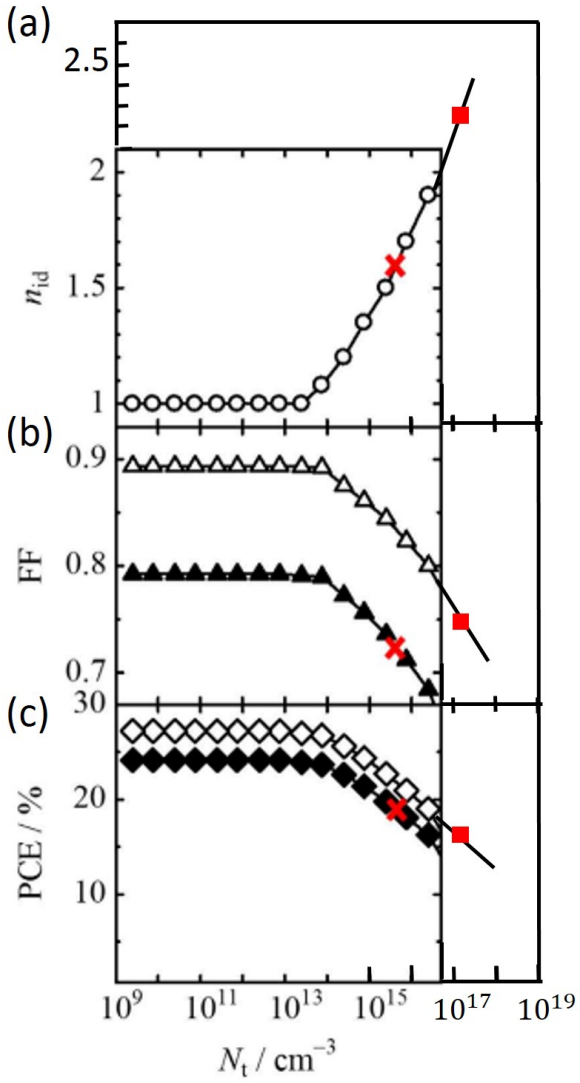

FIGURE 5.19: (a) n_{id}, (b) FF and (c) Photovoltaic conversion efficiency (PCE) plotted against the logarithm of N_t for methylammonium lead iodide perovskite solar cells. Closed triangles and diamonds represent perovskite cells with R_s=6Ωcm^2 and R_{sh}=1×10^{5}Ωcm^2 and open triangle and diamonds represent cells with R_s=0.5Ωcm^2 and R_{sh}=1×10^{5}Ωcm^2. The red "X" marks represent the photovoltaic parameters for the best device measured by [37] under forward bias and the red squares represent the parameters for the best device measured in the current study under forward bias. Adapted from [37].

It can be seen that under both circumstances n_{id} decreases with decreasing density of trap states, reaching unity for $N_t \leq 10^{13}cm^{-3}$ which suggests that direct recombination dominates below that threshold. In the case of devices with R_s=6Ωcm^2, FF increases from 0.7 to 0.79 as N_t is reduced from $10^{16}cm^{-3}$ to $10^{13}cm^{-3}$ which would correspond to an increase in PCE up to a maximum value of ≈24%. However, for devices with a lower R_s of 0.5Ωcm^2, such as is reported for crystalline silicon solar cells as well as the best devices in the current work, the FF may be increased from 0.8 to ≈0.9 over the same interval, and hence the PCE could be increased to ≈27% as shown in Figure 5.19(c). This suggests that the combination of materials and processing conditions used to produce devices resulted in a density of trap states many orders of magnitude large than would be desired. Possible sources of trap states include the ETL/perovskite interface, grain boundaries within the perovskite layer itself and at the perovskite/HTL boundary.

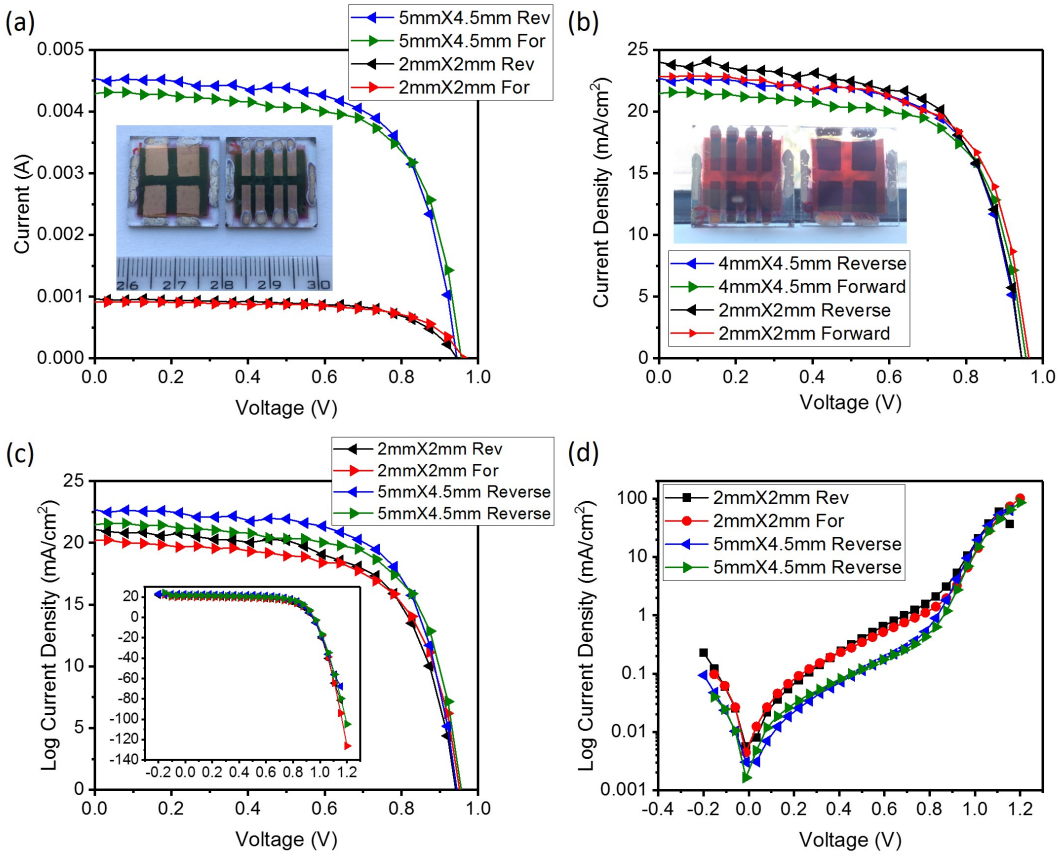

FIGURE 5.20: Current-voltage measurements of device comprising ITO/PEI/C_{60}/2Step30wt%/P3HT/TiAu (a) sweep measured from open circuit to short circuit (Reverse) and from short circuit to open circuit (Forward) as well as under constant bias in the narrow range around the maximum power point (b) Plot of maximum power extracted from the device versus time.

To further validate the processing technique, larger area devices were fabricated to test

scalability. Figure 5.20(a) shows typical current-voltage scans under illumination for two devices with different active device area (as defined by the overlap of ITO and gold electrodes together with a mask) processed in the same batch. From Figure 5.20(b) it can be seen that device performance remained almost unchanged, indicating that the materials and fabrication procedure were not very sensitive to device size. On the contrary, it was found (somewhat surprisingly) that some cells actually outperformed the smaller active area reference devices as seen in Figure 5.20(c). This was judged not to be a result of incorrect scaling as large area cells displayed lower current density at large forward bias as seen in the inset of Figure 5.20(c). Instead, the improvement was attributed to a greater shunt resistance in the large area devices as indicated by lower dark currents under low bias (Figure 5.20(d)). A possible explanation for this counter-intuitive result would be that the wider strip of ITO used for the large area devices resulted in more homogeneous device stack as the relatively large ($\tilde{1}$50nm) step height was further from the substrate centre and the active area.

5.3.3 Device stability relative to literature

An important aspect of device design that needs to be addressed before perovskite solar cells can reach commercialization is that of device lifetime. There is a vast literature on maximizing the efficiency of perovskite solar cells, but comparatively few reports investigate the stability of devices after storage in non-inert environments. Methylammonium lead triiodide perovskite is well known do decompose upon exposure to temperature and especially to moisture through escape of the organic cation, although other degradation mechanisms have also been reported. However many of the materials that tend to give the highest cell performance have also been found to react with perovskite, thereby accelerating the degradation.

In order to provide some idea of the stability of device stacks used in this work, cells were measured repeatedly over a number of weeks and months. Devices were left unencapsulated and were stored in a drawer without humidity control between measurements. Figure 5.21 shows how PCE varied with time for devices containing different $PbCl_2$ content. Device performance was normalised to more easily compare the effect of chloride content as shown in Figure 5.21(b). PbI_2-only cells were reasonably stable over the first few hundred hours, retaining 90% of their initial PCE after 300 hours. However, device performance deteriorated significantly over the subsequent 300 hours resulting in less than 50% of initial performance after 660 hours.

There was a spread in the evolution of PCE with time for the $PbCl_2$-containing devices reflecting a complex relationship between perovskite film morphology and stability. The

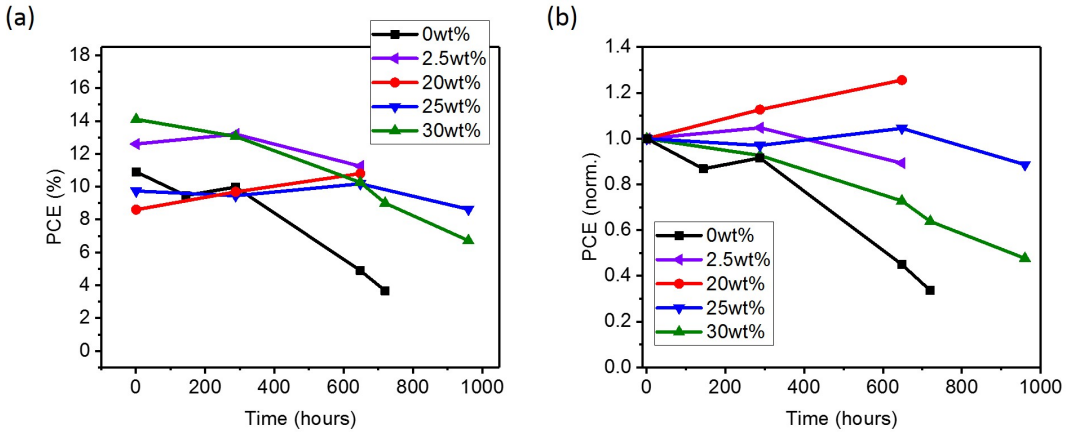

FIGURE 5.21: (a) Device efficiency as a function of time (b) Normalised plot of devices shown in (a).

addition of 2.5wt% $PbCl_2$ was found not only to increase the PCE of fresh devices but also to improve the resistance to degradation, with cells retaining 90% of initial PCE after 660 hours. Devices made with 20wt% $PbCl_2$ actually improved in performance over the same time period, displaying a 25% higher PCE than recorded before ageing. Devices made with 25wt% $PbCl_2$ appeared remarkably stable, losing only 10% of initial performance after nearly 1000 hours. Higher chloride content however seemed to adversely affect stability as 30wt% $PbCl_2$ cells dropped to 50% of their initial PCE over the same time period. It should be noted though that the significantly higher PCE for fresh devices with greater chloride content meant that cells containing 30wt% $PbCl_2$ still had a conversion efficiency of over 10% after 660 hours.

Towards the end of the project it became possible to perform external quantum efficiency (EQE) measurements on devices. These measurements are useful for two reasons; firstly they give information on how devices respond to incident radiation of different wavelengths and secondly the current density at short circuit J_{sc} can be calculated as shown in section3.4.1. The EQE set up required an area of at least 4mm $\times$ 4mm in order to ensure that the assumption of photon flux ratios were correct. For this reason, larger area cells fabricated over one month previously were measured. As seen in Figure 5.23(a), even after 35 days of storage in relatively humid ambient conditions (60%-90% relative humidity [258]) cells displayed over 70% quantum efficiency throughout the visible spectrum and into the UV resulting in an integrated J_{sc} of 17.5mA/cm^2. Current-voltage scans of cells performed on the same day (Figure 5.23(b)) showed that the series resistance had grown significantly relative to scans performed on fresh devices but the measured J_{sc} was in close agreement with that calculated from the EQE which validated the electrical measurement set up.

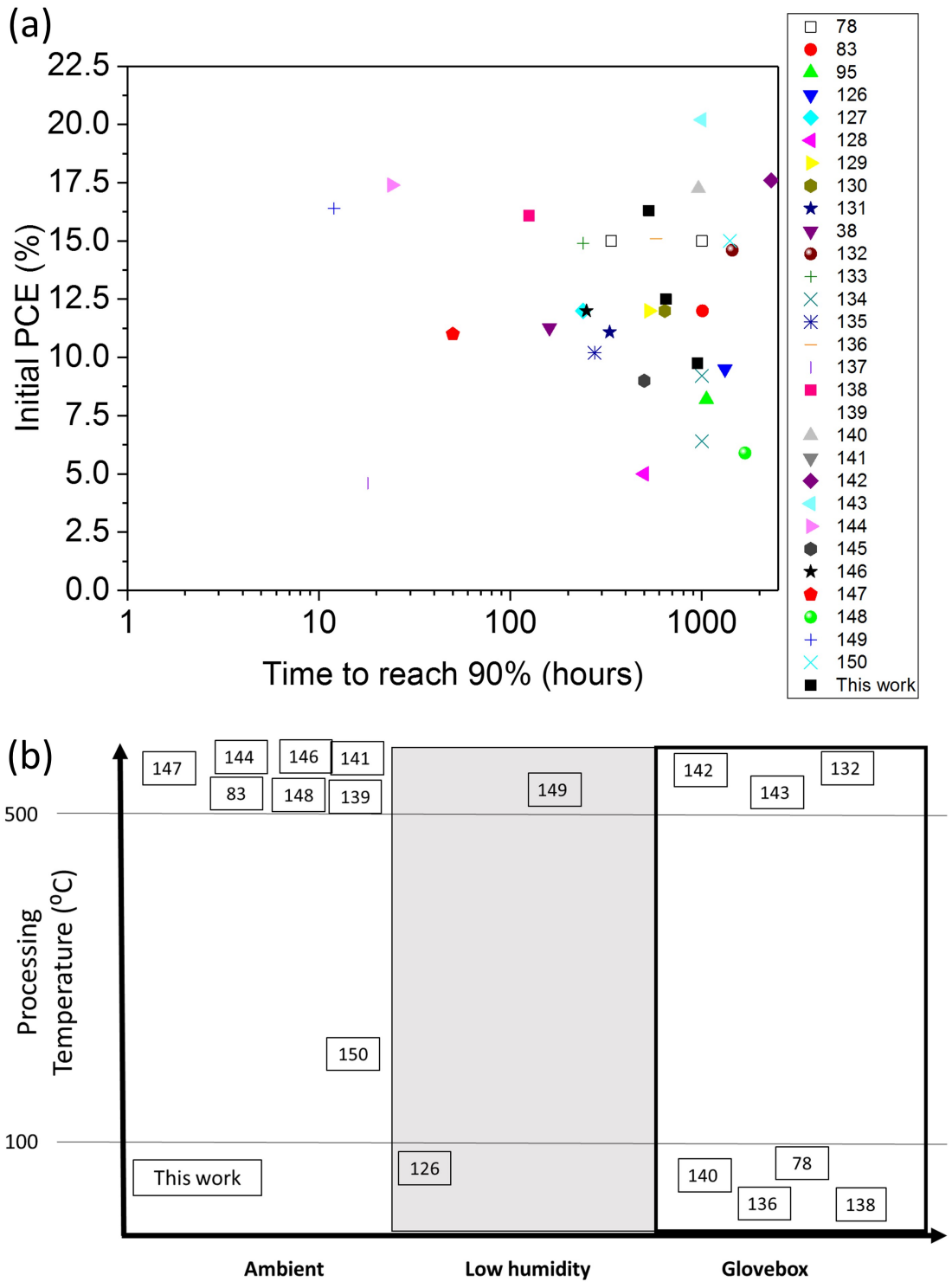

FIGURE 5.22: Device performance and processing relative to literature.(a) Time taken for devices to reach 90% of initial efficiency plotted alongside devices reported in the literature (b) Processing temperature plotted against the degree of humidity for devices shown in (a).

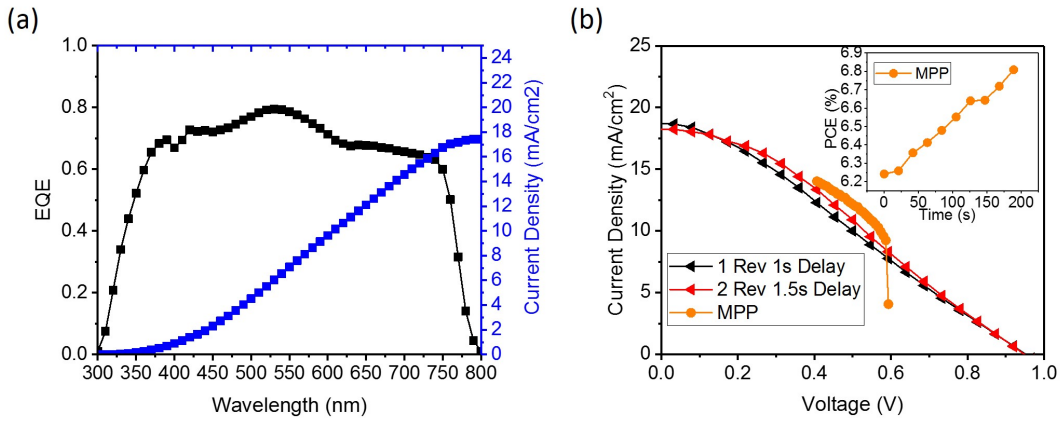

FIGURE 5.23: (a)EQE measurement of large area device made with 30wt% $PbCl_2$ precursor after 35 days of storage in relatively humid (60%-90% rel. hum.[258]) ambient conditions (b) Same day current-voltage measurements of device shown in (a).

To see how device stability compared with the state of the art, all reports in the field of perovskite solar cell research containing stability studies were compiled and the initial efficiencies were plotted against the time taken to reach 90% of initial PCE as shown in Figure 5.22(a). Representative data from this work compares favourably with much of that reported in the literature, with either higher initial PCE or better stability (or both). However, many of the solar cell performances reported used device architectures and materials that required either high temperature sintering steps or inert processing conditions and thus were either stored under inert environments or else were encapsulated to avoid exposure to oxygen and moisture. Conversely, the aim of the present work was to avoid fabrication techniques and processing steps that add cost and limit applicability of perovskite solar cells as an inexpensive technology and as such all processing was carried out below 100 °C and under high humidity. Figure 5.22(b) is a plot of device processing temperature against the degree of climate control during processing (ranging from uncontrolled "ambient" environment with relative humidity in excess of 90% to oxygen and moisture-free glovebox conditions) for the data shown in (a). In this way it can be seen that most (if not all) of the reports that outperformed devices from the current work necessitated either high temperature processing or fabrication under inert conditions and many required encapsulation or storage in low humidity environments to maintain device performance. Conversely, aside from a protective effect against moisture offered to perovskite by the hydrophobic surface of P3HT, the devices studied here were neither properly encapsulated nor were they stored under reduced humidity. Therefore it may be concluded that the device stack and processing procedure used was remarkably stable to degradation, especially considering the inclusion

of an approximately 150nm-thick P3HT layer which is known to degrade significantly in the presence of light and oxygen as will be further detailed in the next chapter. Observed stability of devices incorporating P3HT was attributed to the fact that cells were illuminated through ITO and thus much of the incoming light was absorbed by the perovskite rather than the P3HT itself. Furthermore, P3HT, which neither contained reactive dopants such as lithium salts used in Spiro-OMeTAD nor was hygroscopic and acidic as is the case for PEDOT:PSS, was a more suitable HTL for maximizing device stability in the presence of moisture and oxygen.

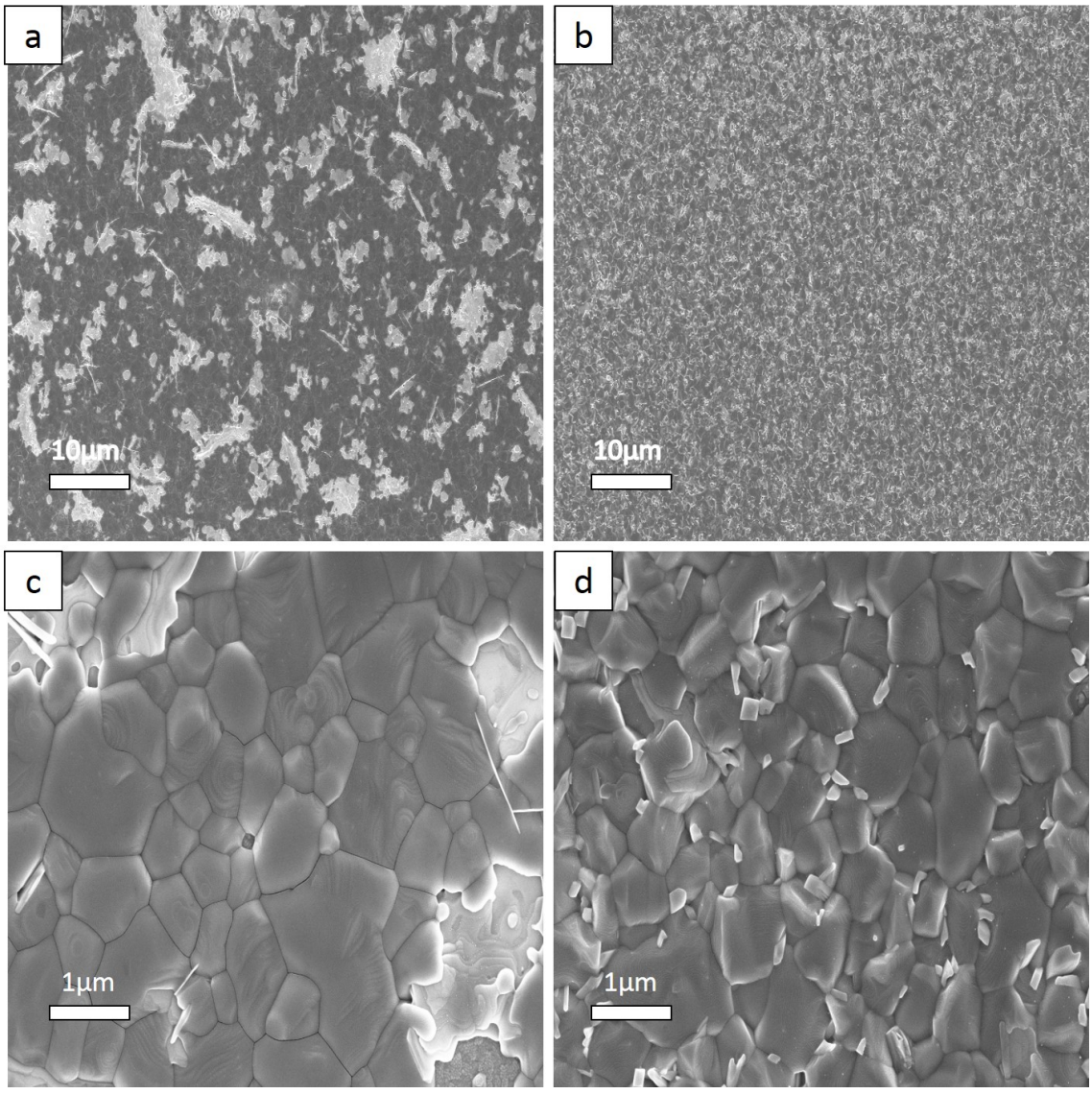

FIGURE 5.24: SEM images of perovskite films produced via the Two-Step method after three weeks in ambient.(a) and (c) Film crystallised from 1M PbI_2 and (b) and (d) crystallised from lead halide film with 30 wt% $PbCl_2$.

Another factor which may have resulted in the relative stability observed was the nature of the perovskite layer itself. Figure 5.24 shows SEM images of films fabricated with

PbI_2-only lead halide precursor and precursor with 30wt% $PbCl_2$ after 3 weeks storage in ambient humidity. Both films were made up of many close-packed micrometer-sized grains, although the PbI_2-only film ((a) and (c)) did contain nanometer and micrometer-scale gaps, revealing underlying ITO. The PbI_2-only film also contained many patches ranging from 1 to 10μm across of some other material which was presumed to be a bi-product of perovskite degradation such as PbI_2. On the other hand, the perovskite film made with 30wt% $PbCl_2$ in the precursor ((b) and (d)) appeared to be more intact, maintaining a densely packed film with no visible pinholes. However, smaller "granules" which appeared to sit atop the film were also present at the grain boundaries and were presumed to signify the early stage of film degradation. Taken together the images are consistent with the device performances observed and indicate that $PbCl_2$ may improve film integrity and stability, as has been suggested previously[259][54][260][261]. These results indicate that devices containing higher $PbCl_2$ content processed in a highly humid environment could likely be competitive with the best reported devices if adequately encapsulated.

5.4 Conclusions

Perovskite films were prepared using Single-Step (1Step) and Two-Step (2Step) methods. Devices fabricated using 1Step deposited perovskite were found to benefit from excess MAI and from partial substitution of PbI_2 with $PbCl_2$. The bandgap was increased by introducing $PbBr_2$ leading towards semi-transparent devices. In the case of perovskite deposited using the 2Step method under highly humid conditions (relative humidity $\geq$ 90%), morphology and device performance was found to vary significantly depending on the content of $PbCl_2$ in the precursor solution. Device performance and reproducibility was greatly improved for chloride content greater than 25wt%, with exceptionally high photocurrents, reduced standard deviation and FF as high as 0.75 for champion cells. The high FF and J_{sc} values were attributed to a high shunt resistance due to a dense and pinhole-free perovskite layer coupled with extremely low series resistance owing to efficient electron extraction by a thin fullerene-based ETL rather than the metal oxides commonly used in the literature. Higher chloride content in the perovskite precursor was found also to be beneficial for improving the conversion efficiency and reducing cell-to-cell variability of devices in which sputtered ITO was replaced by AZO deposited by spray pyrolysis. Taken together these results demonstrate that the addition of large quantities of $PbCl_2$ can be an effective measure for obtaining reproducibly high performance for devices processed using low cost materials

and deposition techniques under uncontrolled humid conditions. Additionally, unencapsulated devices stored in an ambient environment showed respectable longevity compared to previous reports, maintaining high PCE even after hundreds of hours storage.

6 Carbon Nanotubes as Charge Transport and Hole Extraction Material for Improved Stability of Perovskite Solar Cells

6.1 Introduction

The aim of this chapter is to better understand the role of p-type contacts in regular architecture perovskite devices and to develop simple but effective methods to further improve device reproducibility and stability in highly humid conditions. P3HT was chosen as the reference HTL due to its hydrophobic nature and easy solution-processability. The role of P3HT is first examined and then efforts are made to incorporate CNTs into p-type polymers and then into devices. The effect of CNTs and P3HT on device performance and reproducibility are discussed and explanations are offered for the effects observed. Finally, attempts are made to p-dope graphene as back contact material for devices.

6.1.1 Optimizing hole transport layer thickness

In order to better understand the role played by the hole transport layer (HTL), devices were fabricated with a range of P3HT concentrations (and hence thickness) from no HTL (i.e. anode deposited directly onto perovskite) up to 25 mg/mL. The JV-curves are plotted in Figure 6.1 and the cell characteristics extracted from fits to the curves are displayed in Table 6.1. It can be seen that J_{sc} varies with HTL thickness and that the value is dependent upon scan direction. When no P3HT was present, the devices had extremely high series resistance with voltage and fill factor losses due to recombination at the interface between perovskite and the gold anode. It has been demonstrated that perovskite can act as a reasonably effective hole transport material when in intimate contact with a pinhole-free ETL such

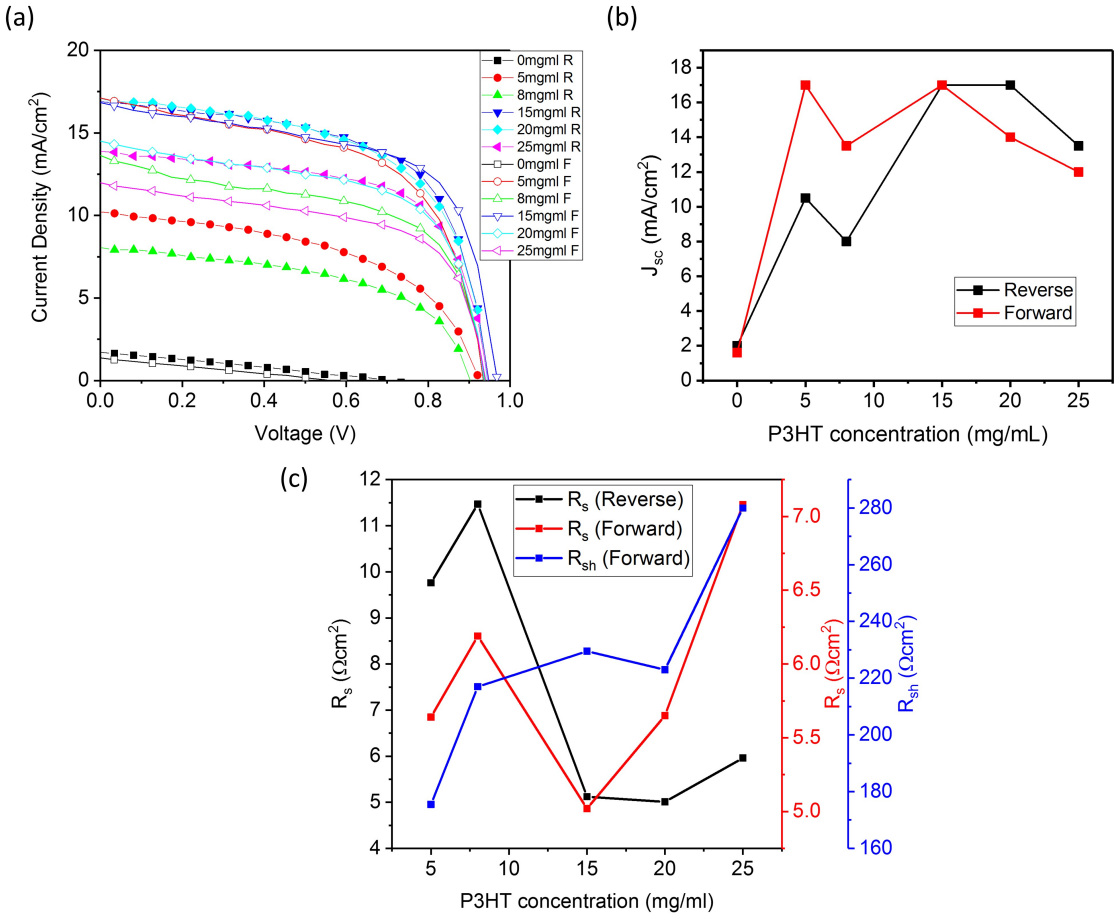

FIGURE 6.1: (a) Current-voltage measurements of devices coated with HTLs deposited from P3HT solutions with different concentration. (b) Plot of short circuit current density (J_{sc}) versus P3HT concentration used during HTL deposition.(c) Plot of R_s and R_{sh} against P3HT concentration.

as TiO_2[32] [262] [263] [264] due to its ambipolar nature. However, this can only be achieved for perovskite with nearly full coverage upon a dense layer of pinhole-free hole-blocking material as a large degree of shunting would result from direct contact between the electrodes and to a lesser extent between the anode and ETL. Furthermore, the iodine/iodide redox system formed due to hydrated intermediate phases during perovskite degradation is particularly reactive with gold [184], resulting in rapid performance losses upon device operation in ambient conditions.

Taking these factors into consideration combined with the fact that devices studied in this work have only a thin solution-processed polymer-C_{60} bilayer as ETL, the poor performance without a P3HT electron blocking layer should come as no surprise. Applying a 5mg/mL P3HT solution on top of the active layer dramatically improved performance, with a sharp decrease in R_s due to a suppression of recombination losses by the shallow LUMO level of the polymer. In addition, the presence of P3HT makes device performance less sensitive to

P3HT conc. (mg/ml)	R_s (Ωcm^2)	R_{sh} (Ωcm^2)	FF	J_{sc} (mA/cm^2)	V_{oc} (V)	PCE (%)
0	370	364	0.25	1.78	0.716	0.3
5	5.64	175.5	0.5	10.6	0.917	4.66
8	6.19	217	0.51	8.36	0.906	3.86
15	5.02	230	0.61	17.25	0.944	9.9
20	5.65	223	0.6	17.56	0.941	9.85
25	7.08	280	0.64	14	0.944	8.5

TABLE 6.1: Device characteristics for HTLs deposited from different concentration P3HT solution

pinholes in the perovskite due to the effective rectifying action at the interface between C_{60} and P3HT as demonstrated in the previous chapter. This resulted in an improvement in FF, V_{oc} and J_{sc}, particularly for forward bias scans. Curiously, increasing the P3HT concentration to 8mg/mL resulted in cells that had slightly lower J_{sc} and V_{oc}. Depositing 15mg/mL P3HT not only decreased R_s and increased FF and V_{oc} further for both scan directions but crucially resulted in negligible hysteresis. Increasing the concentration of P3HT yet further to 20mg/ml did not appreciably change the JV-characteristics under reverse bias but did adversely affect the cells under forward bias. This trend continued as the concentration was increased to 25mg/ml with an increase in R_s for both scan directions resulting in markedly lower J_{sc}. The variation in device parameters can be better understood by plotting R_s for both scan direction as well as R_{sh} against P3HT concentration as in Figure 6.1(c). It can be seen that the point of lowest R_s lies at a concentration of 15mg/ml P3HT and although R_{sh} is notably improved for 25mg/ml P3HT it is at the expense of a large increase in R_s. The larger R_s values at higher concentration can be explained by a thickness-dependent relationship due to the limited conductivity of P3HT. It would appear from these results that a trade-off exists between series and shunt resistances in which higher concentration solutions are required to give full coverage of perovskite films and hence raise R_{sh} but thicker P3HT films are also limited by HTL conductivity. This is consistent with film thicknesses of 200nm-300nm generally reported for the more typically used hole transport layer spiro-OMeTAD, which requires dopants to maintain a sufficiently low R_s and with reduced series resistance with decreasing HTL thickness[265][37].

In addition, although P3HT remains a promising material for commercial application due to the scalability of its synthesis and its compatibility with high-throughput production techniques coupled with reasonable stability (relative to many materials used in OPV)[266][267], it remains prone to photo-induced oxidation leading to the destruction of the π-conjugated

system in a process that is accelerated by the presence of humidity or elevated temperature [268][266][223]. Furthermore, the semi-crystalline nature of P3HT requires some control over morphology in order to guarantee effective charge transport [269][270][271], usually achieved through annealing under inert atmosphere.

6.2 Carbon nanotube-PEDOT:PSS composite electrode

As already mentioned, although there are a variety of methods to synthesize carbon nanomaterials such as CNTs, difficulties remain when it comes to sorting and manipulating them for a desired purpose. One attractive method from an industrial viewpoint is to exploit the fact that many nanomaterials can either be directly exfoliated in the liquid phase (LPE) or else dispersed in suitable solvents. Nanomaterial films may then be deposited from solution. Among the many deposition methods [126][272][273][274][275][276], vacuum filtration has been widely used due to low material waste involved and the ability to produce high quality films with good reproducibility [277][278][279][280]. However, thin film transfer from filter membrane to arbitrary substrates is generally required and can be challenging [281][282]. Dry transfer methods such as using polydimethylsiloxane (PDMS) [283][284][278] [273], though useful, suffers from certain drawbacks associated with direct contact between stamp and film such as mechanically induced damage to the thin film as well as difficulty in transferring to arbitrary substrates due to interfacial energy considerations[284]. Another notable method involves solvent-etchable organic (e.g. mixed cellulose ester) filter membranes and has achieved much success in fabricating nanomaterial-based thin films [285][277][280][286]. However, this method may only be applied to aqueous dispersions such as CNTs or graphene that have been dispersed with the aid of a surfactant in water (H_2O). It is also difficult to fully remove surfactants from thin films which restricts application to high-performance devices. Additionally, heat and pressure are often applied to improve the quality of the transferred film, indicating that the approach is relatively destructive. On the other hand, success in the direct solvent-exfoliation of graphite and other layered materials and nanomaterial bundles for the production of pristine high quality graphene and other two-dimensional materials [287][288][289][290] suggested a need for developing a transfer method toward thin films from non-aqueous dispersions such as CNTs in n-cyclohexyl-2-pyrrolidone (CHP) or graphene in n-methyl -2-pyrrolidone (NMP).

With this in mind, a novel strategy was developed by our group for fabrication and transfer of hybrid (ultra) thin films that was compatible with non-aqueous dispersion systems[291].

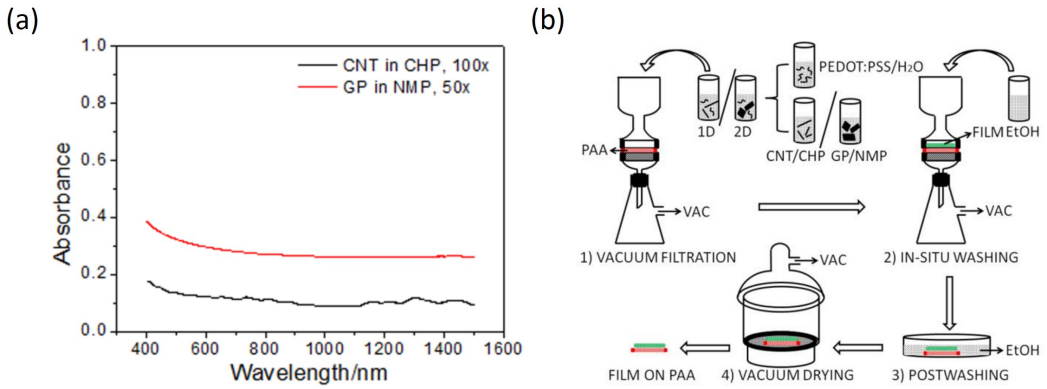

FIGURE 6.2: (a)Absorption spectra of dilute graphene and CNT dispersions.(b) Schematic of the general method for fabrication of hybrid (ultra)thin films supported on PAA membranes

Figure 6.2(b) illustrates the fabrication process for hybrid thin films supported on porous anodic alumina (PAA) membranes. Graphene and CNT dispersions were prepared based on the methods developed by Coleman and co-workers[288][292]. For CNT dispersions, single-walled HiPCO carbon nanotubes at an initial concentration of 0.5mg/ml in CHP were sonicated with a sonic tip (VibraCellCVX, 750 W, power setting 20%, 20 kHz) for 30 minutes followed by centrifugation at 5000rpm for 90 minutes. The supernatant (roughly the top 2/3 of the total volume) was collected and used as stock dispersion. The concentration of 100×diluted samples was determined to be 0.36 mg/mL based on the Beer-Lambert Law using UV-visible-NIR absorption spectroscopy as shown in Figure 6.2(a).

Vacuum filtration was applied to fabricate hybrid thin films using poly (3,4-ethylene dioxythiophene) doped with poly(styrenesulfonate) (PEDOT:PSS) as the matrices. PEDOT:PSS was purchased from Heraeus under the trade name Clevios PH 1000, with initial concentration of 10–13 mg/mL in water. For CNT-based thin films, PEDOT:PSS/H_2O (50× (i.e. 50 times diluted), 1 mL) and SWCNT/CHP (45×, 1 mL) were mixed for vacuum filtration. For CNT-based ultrathin films, PEDOT:PSS/H_2O (500× (i.e. 50 times diluted), 1 mL) and SWCNT/CHP (450×, 1 mL) were mixed for vacuum filtration. Commercially available 20nm (pore size) PAA membranes were used meaning that the system was, in principle, suitable for any component with at least one dimension larger than 20nm [278][283]. In-situ and post washing of the thin films with volatile solvents such as ethanol was carried out in order to efficiently remove remaining high-boiling-point dispersants such as CHP or NMP, thereby facilitating the production of high performance thin film-based structures.

A general method for transferring the as-fabricated hybrid thin films is illustrated in Figure 6.3. A specific configuration of the sample was adopted whereby the film on PAA membrane was placed upside down onto the desired substrate such as glass or PET with

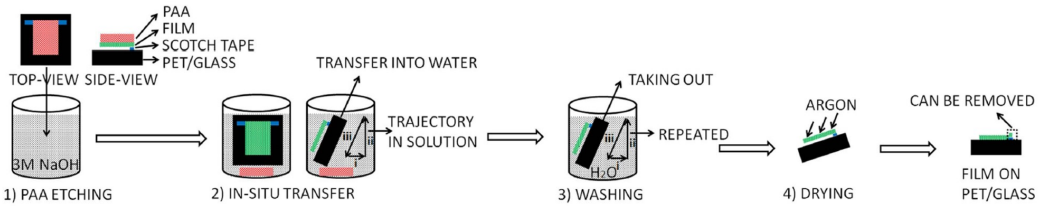

FIGURE 6.3: Schematic illustration of the general method developed for in-situ transfer of hybrid (ultra)thin films.

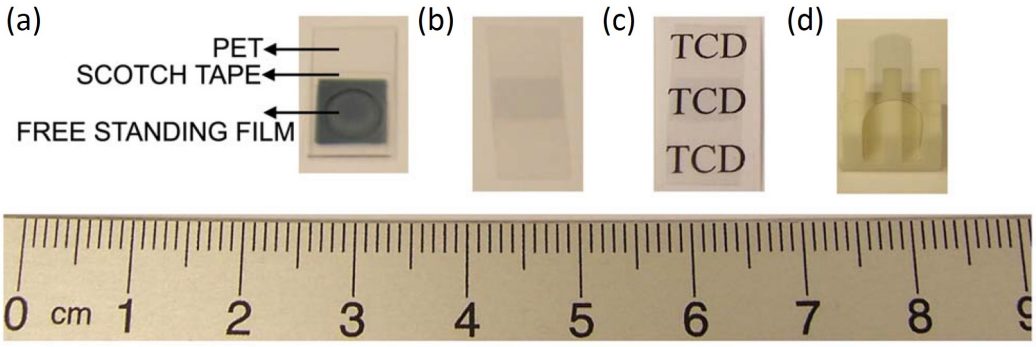

FIGURE 6.4: CNT-doped PEDOT:PSS films obtained via vacuum filtration and in situ transfer (a) composite film transferred onto PET with a 5mm diameter hole. (b) ultrathin film transferred onto PET showing high transparency (c) and mechanical flexibility (d).

one edge attached to the substrate via double-sided scotch tape. The sample was then immersed in sodium hydroxide (NaOH) aqueous solution to etch away the PAA. The chosen configuration enabled flexible fixation of the free-standing thin films on the substrates after removal of the PAA membrane and line-contact mode ensured that free-standing films were directionally guided throughout the etching and washing steps.

In order to avoid bubble and wrinkle issues, the 3M NaOH solution was diluted in a volume ratio (4:1) of aqueous solution to ethanol. Furthermore a specific and repeatable trajectory was adopted as shown in Figure 6.3 in order to keep the process safe and reproducible. A tilting posture was used during both submerging and removing the sample during etching and washing and a large excess of deionised water was used to ensure that no residual NaOH remained on the films. Specifically, the films were washed sequentially in three filled 500ml beakers with three relatively slow (3-5 seconds) wash cycles per beaker. The films were finally dried carefully with argon to avoid bubbles and wrinkles. Photographs of various transferred films are shown in Figure 6.4. To demonstrate that applicability of the method to creating free-standing films, Figure 6.4(a) shows a thin film transferred onto a substrate with a hole. An ultrathin (approx 35nm) film transferred onto PET (50μm thick) (Figure 6.4(b)) displays promising properties such as high transparency and flexibility as

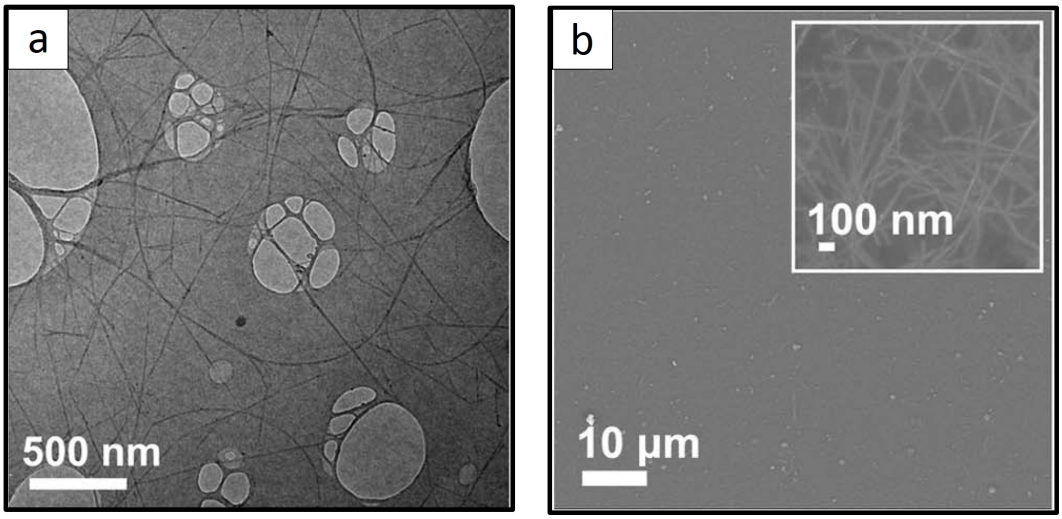

FIGURE 6.5: (a)Transmission electron microscopy image of dropcast CNTs on a copper grid.(b) SEM image of CNT-PEDOT:PSS hybrid thin film.

shown in Figure 6.4(c) and (d) respectively. The quality of hybrid thin films are largely dependent on the dispersion system used to fabricate them. Transmission electron microscope (TEM) images of the dropcast CNTs on copper grids (Figure 6.5(a)) revealed that the CNTs were well dispersed with no visible bundles, indicating the high quality of the dispersion system used. Hybrid thin films formed by the dispersions were characterised by field emission scanning microscopy (FE-SEM) as shown in Figure 6.5(b). Due to the conductive nature of the films, images were taken without prior metallic coatings and were connected to the conducting stage through double-sided conductive tape at the film edges. The InLens detector was used to better reveal CNT networks on the surface of thin films as shown in the inset of Figure 6.5(b). The quality of the stock dispersion was reflected in the highly dispersed and interwoven CNT network present in the hybrid films.

Figure 6.6(a) presents the absorption spectra of thin and ultrathin films. The extremely low absorbance of the ultrathin film indicated high transparency with over 90% transmittance in the visible range and 80% in the NIR as shown in Figure 6.6(b). Four-point probe measurements revealed that the sheet resistance of the ultrathin film as extracted from the IV-curve shown in Figure 6.6(c) was 1850Ω/sq. Although this is significantly higher than the industry standard (100-200Ω/sq), the conductivity was calculated to be as high as 1.54×10^4S/m given that the film thickness was 35nm. Indeed, thicker films (200nm) at a similar conductivity gave a sheet resistance of 360Ω/sq, approaching the industry standard. It should be noted that the CNTs imparted not only improved conductivity relative to undoped PEDOT:PSS (3.7MΩ/sq for a 50nm thick film equivalent to a conductivity of 5 S/m [280]) but also greatly improved durability. Indeed, the hybrid film was highly solvent-resistant, even

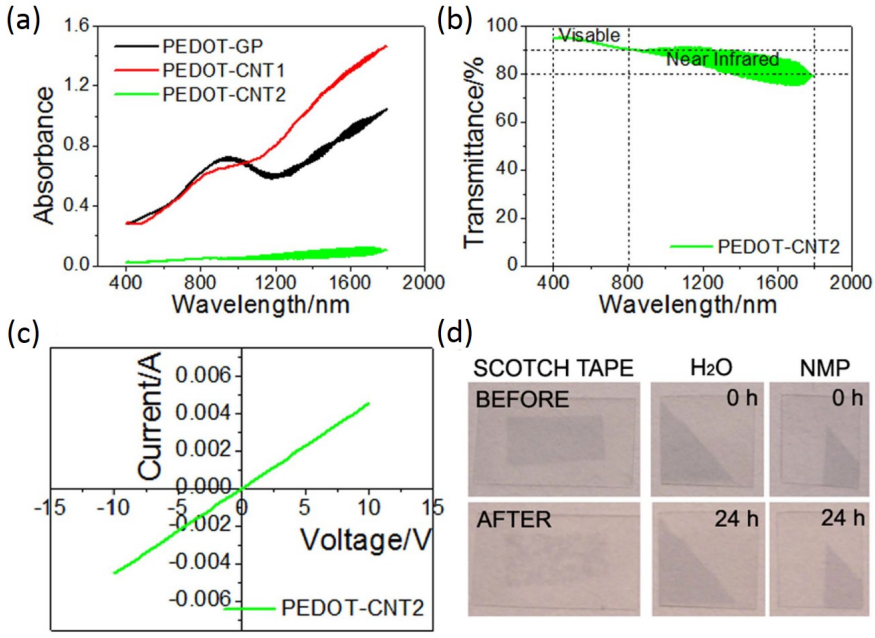

FIGURE 6.6: (a) Absorption spectra of hybrid (ulta)thin films.(b) Transmission spectrum of hybrid ultrathin (35nm) film. (c) IV-curve of ultrathin film. (d) Durability test of ultrathin film.

to H_2O as shown in Figure 6.6(d) which is impressive given the solubility of the polymer matrix in water and its hygroscopic nature. Furthermore, the relatively strong adhesion between the film and PET substrate was demonstrated by the lack of observable damage after rubbing with nitrile gloved fingers and after the application and removal of scotch tape (Figure 6.6(d)).

However, useful as the developed method was for fabrication and transfer of thin films, limitations were encountered in applying it to devices. As regards photovoltaics, it was soon realized that nanohybrid thin films based on CNTs and PEDOT:PSS were best suited to inverted (or normal in the case of OPV) p-i-n structure perovskite solar cells. As already mentioned, although efforts were made to fabricate devices with inverted structure, a combination of a lack of appropriate resources (e.g. evaporation system capable of depositing C_{60}, BCP, LiF, etc.) and inert processing environment (e.g. glovebox) meant that functioning devices were only achieved using regular architecture. Furthermore, while vacuum filtration of some polymers such as PEDOT:PSS was straightforward, it was found that other candidate polymers for the HTL such as P3HT were only partly filtered, with much material passing through the filter membrane. This issue could be addressed either by using a membrane with smaller pore-size or by rendering polymer solutions turbid via addition of non-solvents (or a combination of both measures). However, the presence of an aqueous environment during in-situ transfer was found to be essential. Alternatives such as replacing

water with methanol and/or replacing NaOH with potassium hydroxide (KOH) were tried but found to be unsuccessful. On the other hand, the presence of water is a severe obstacle where methylammonium lead triiodide perovskites are concerned and so other methods of CNT manipulation were sought after.

6.3 Carbon nanotube-P3HT nanohybrid in polymer composite hole transport layer

6.3.1 Sample preparation

Certain aromatic polymers have been shown to facilitate the dispersion of CNTs via wrapping of the rigid-backbone polymer around the tube [293][294]. Furthermore, not only does for example P3HT render CNTs dispersible in common non-polar solvents but the resulting supramolecular nanohybrids have been reported as being predominantly p-type in nature [295][296]. As such P3HT-CNT nanohybrids have been applied in both organic[296][112] and organic-inorganic perovskite solar cells [297][298]. However, concerning the field of perovskite photovoltics, studies have focussed predominantly on regular structured devices using metal oxide scaffolds such as nanoporous TiO_2 and mesoporous Al_2O_3 [297, 298, 299, 300, 301, 302, 303] or else on inverted devices structures [304]. A planar solar cell incorporating CNTs as an interlayer between the perovskite and HTL has been reported, although a high temperature processed TiO_2 ETL was still used and CNTs were of chosen chirality with no metallic CNTs present [305]. On the other hand, incorporating unsorted CNTs into low temperature processed devices has been far less studied, especially with a view towards all layers deposited simply from solution.

In order to disperse CNTs in a solvent compatible with deposition on perovskite, an established procedure was followed [294] [297]. Briefly, 3mg of P3HT was dissolved in 5ml of chlorobenzene (CB) and bath sonicated for 60 minutes before adding 2.5mg of CNTs. The mixture was then treated with an ultrasonic probe for 10 minutes followed by 8 minutes of centrifugation at 10000g to remove non-functionalized CNTs and carbonaceous particles which formed the precipitate. Excess polymer was removed by adding 15ml of toluene and gently heating the mixture for 1 hour to induce aggregation of functionalized CNTs. The aggregates were then removed by 4 minutes centrifugation at 16000g with the supernatant disregarded. The precipitate was redispersed in 5ml toluene and the procedure repeated until the supernatant was colourless. The final pellet consisted of 2-2.2mg of functionalized CNTs which could be redispersed as required.

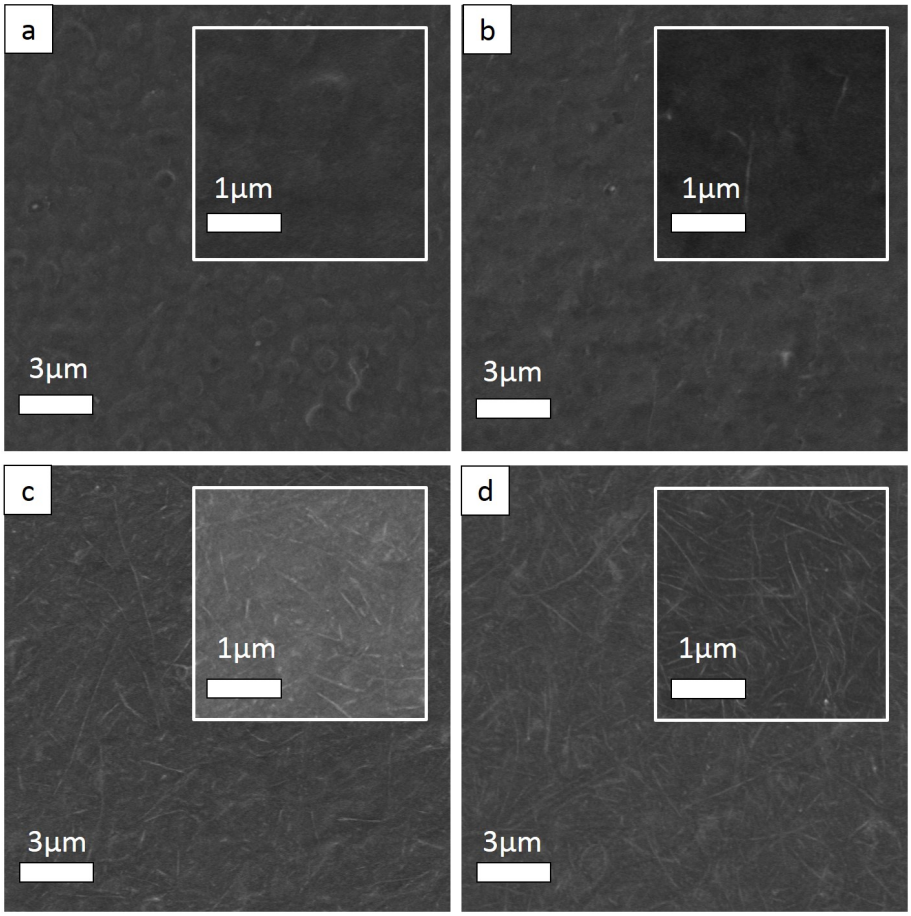

FIGURE 6.7: SEM images of CNT-doped CNT films (a) 0.1wt% CNT, (b) 1wt% CNT, (c) 2wt% CNT and (d) 4wt% CNT.

Figure 6.7 shows SEM images of P3HT films with varying content of CNTs deposited on perovskite. At a concentration of 0.1wt% CNT little or no CNTs are visible in the composite and the HTL largely follows the topography of the underlying perovskite, as seen in Figure 6.7(a). Conversely, the perovskite morphology is less apparent in the case of the 1wt% composite and some CNTs can be discerned at the HTL surface. The CNT network becomes more visible as the concentration is increased to 2wt% and then 4wt%.

Films were measured using a four-point probe setup to test the lateral or in-plane conductivity. As seen in Figure 6.8(b) and Table 6.2, the composite films did indeed become much more conductive in the planar direction, increasing by almost two orders of magnitude between pure P3HT and P3HT with 4wt% CNTs. However, higher content composites proved difficult to produce due to solubility and dispersibility limits. On the other hand, CNT-P3HT nanohybrid-only films (representing 100wt% CNTs) could be achieved by dispersing the hybrid material at a lower concentration in chloroform and depositing in a drop-by-drop fashion [297]. In this way, films made up of a porous network of interwoven CNTs were produced with a sheet resistance R_{sheet} of between 4kΩ/sq and 8kΩ/sq. Hall effect

measurements on these films (Figure 6.8(c)) had a large degree of voltage noise and suggested only a slightly p-type nature with mobility values of less than $0.05\text{cm}^2/\text{Vs}$. However, it should be noted that Hall voltage measurements require homogeneous transport across the entire sheet which makes measurement across complex sheet structures with multiple constituents difficult [144]. Thermogravimetric analysis (TGA) (Figure 6.8(a)) showed that the nanohybrid was composed of approximately 75% CNTs by weight, indicating that only a thin sheath of polymer chains surrounded the nanotubes. This was consistent with results obtained from Differential Scanning Calorimetry (DSC) which showed the nanohybrid to be amorphous, as would be the case for a randomly stacked CNT-dominated network (Figure 6.8(d)). This was in contrast to pure P3HT which showed an endothermic melting peak around $225\,^{\circ}\text{C}$, corresponding to a phase change due to crystallinity [306][307]. For semi-crystalline semiconductor materials the degree of crystallinity can be determined from DSC measurements by analysing the heat flow of the melting peaks [308][306]. The enthalpy change ΔH defined as

$$\Delta H = \int C_p \times dT \tag{6.1}$$

where C_p is the heat capacity with constant pressure. from this it follows that the degree of crystallinity K may be defined as the ratio between the measured enthalpy change from melting ΔH_m and the enthalpy change for a 100% crystalline material ΔH_m^0 or

$$K = \frac{\Delta H_m}{\Delta H_m^0} \times 100[\%] \tag{6.2}$$

The melting enthalpy of a perfect P3HT crystal has been the subject of some disagreement, with values reported between approx 37 J/g and 99 J/g [309][310][311][307]. This variation coupled with a measured ΔH_m of 16 J/g gave a degree of crystallinity between 16% and 43% for P3HT dropcast from chlorobenzene (CB). Slow film growth is a characteristic of dropcast films (especially from high boiling point solvents such as CB) which favours polymer chain ordering resulting in π-π stacking and improved charge carrier transport. Spin coating on the other hand is a more complex dynamic process depending on many factors and generally leads to a lower crystallinity in as-produced films [146][312][147]. As such it may be assumed that spin coated P3HT films used in devices would generally be less crystalline even than the DSC measurements would suggest. In the field of OPV, higher J_{sc}, V_{oc} and FF have been correlated with more crystalline polymer and polymer-fullerene blends, especially those containing P3HT [308][313][**?**]. It would stand to reason therefore that the

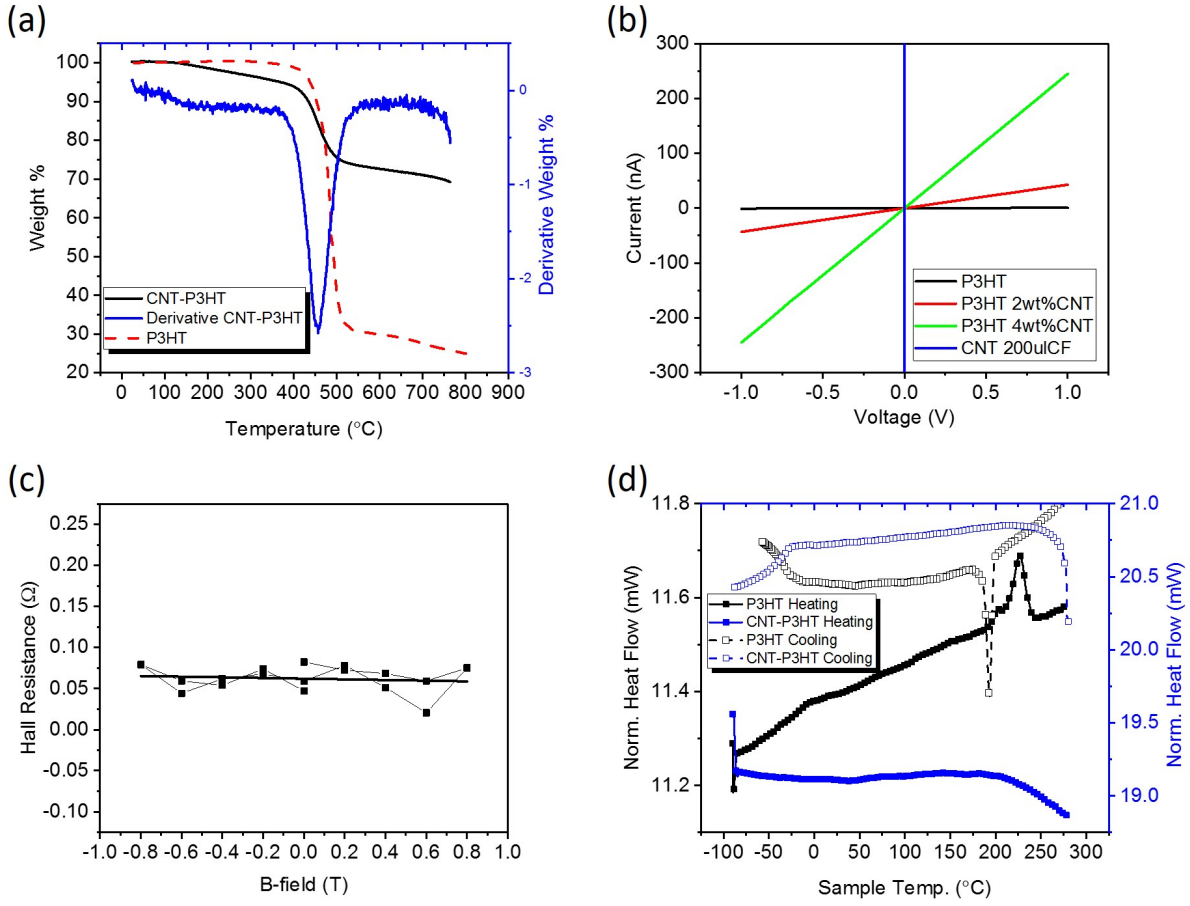

FIGURE 6.8: (a) Thermogravimetric analysis of CNT-P3HT nanohybrid with pure P3HT as reference. (b) Current-voltage measurements of polymer-CNT composite films using four-point probe setup. (c) Hall effect measurement of CNT-P3HT nanohybrid film. (d) Differential Scanning Calorimetry measurement of pure P3HT and CNT-P3HT nanohybrid material.

lack of control over the properties of P3HT films produced by spin coating in ambient conditions is disadvantageous for reproducibility of device performance, especially given that thermal annealing treatments used to improve crystallinity and reduce charge trapping are not applicable to non-inert environments.

As an initial test, P3HT was doped with CNTs and devices were fabricated as depicted in Figure 6.9(a) together with cells using bare P3HT as a reference. Current-voltage scans of devices with and without 1wt% CNTs (Figure 6.9(b)) revealed that addition of 1wt% CNTs adversely affected the maximum power extracted from the cells. In order to gain insight into the cause of the photocurrent difference, fits were made to dark-JV data as shown in Figure 6.9(c) and the extracted device parameters are shown in Table 6.3. One might reasonably expect that he addition of CNTs would decrease series resistance by rendering the HTL more conductive at the expense of a slight decrease in shunt resistance due to greater hole injection into the perovskite. In fact the opposite effect was observed as R_s and R_{sh} both

	R_{sheet} (Ω/sq)	Resistivity (Ωcm)	Conductivity (S/cm)
P3HT	2.16×10^{9}	12960	7.72×10^{-5}
P3HT 2wt% CNT	6.4×10^{7}	576	1.74×10^{-3}
P3HT 4wt% CNT	1.76×10^{7}	264	3.79×10^{-3}
CNT-P3HT nanohybrid	6860	6.17×10^{-2}	16.2

TABLE 6.2: Electrical properties of different polymer nanotube composite films obtained via four point probe measurements.

	Scan direction	R_s (Ωcm^2)	R_{sh} (Ωcm^2)	n_{id}	J_0 (mA/cm^2)
P3HT	Reverse Forward	0.8 0.41	6.23×10^{4} 8.07×10^{4}	2.3 2.24	5.35×10^{-7} 1.02×10^{-8}
P3HT 1wt% CNT	Reverse Forward	1.22 1.09	5.2×10^{5} 1×10^{5}	2.17 2.01	1.44×10^{-7} 3.98×10^{-8}

TABLE 6.3: Parameters extracted from JV-characteristics for devices comprising ITO/PEI/C_{60}/Perovskite/P3HT or P3HT 1wt% CNT/TiAu

increased relative to P3HT-only devices. An explanation compatible with both of the effects would be that the presence of CNTs disrupted whatever crystallinity there was in the film that aided charge extraction but remained below the percolation threshold in the direction normal to the film. This hypothesis would appear to be corroborated by the fact that J_{sc} was observed to recover as the CNT doping was increased to 2wt% and then surpassed the P3HT reference at a CNT loading of 4wt% as shown in Figure 6.9(d).

Thus it may be surmised that a CNT network above the percolation threshold in the direction perpendicular to the plane of the device would guarantee effective charge transport and thus could conceivably provide reproducibly high performance under ambient processing and operating conditions. Additionally, the improved chemical stability of CNTs under irradiation in oxygen and moisture-rich environments would be advantageous towards improving device lifetime. It was soon realized that it would be difficult to achieve such an objective using P3HT solutions-doped with CNTs for a variety of reasons. Firstly, as already mentioned, solutions containing more than 4wt% CNTs proved difficult to obtain. Indeed, even solutions with lower CNT concentration tended to become highly viscous, often taking a gel-like consistency if left undisturbed as the upturned vial with 1wt% CNTs in Figure 6.10 illustrates. Furthermore, although one of the motivations for combining CNTs with P3HT was based on reports of the former protecting the latter from photoinduced degradation[314], this was not found to be true in the case of thin films (at least for the doping levels examined). As shown in Figure 6.10, not only did P3HT-only films turn from

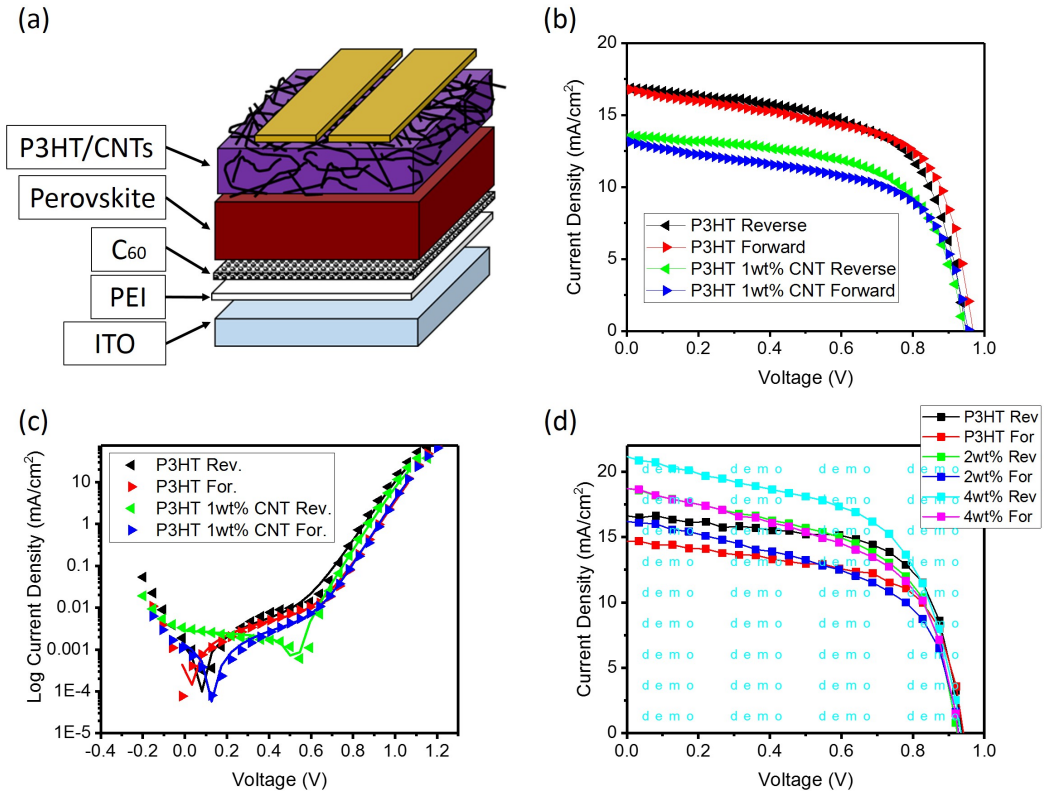

FIGURE 6.9: (a) Schematic of device stack in which HTL is doped with CNTs. (b) Current-voltage curves of cells with neat P3HT as HTL compared with cells incorporating 1wt% CNT, (c) Semilog plots of JV-curves in the dark for devices with HTLs doped with CNTs.(d) Current-voltage response under illumination for devices with different content of CNTs.

magenta to near-colourless after prolonged storage in ambient lab conditions away from direct light exposure, but the same effect was observed for CNT-doped films.

It was therefore decided that a better strategy would be to first deposit a CNT network and then infiltrate the pores with a polymer matrix, in a manner similar to other reports [297, 298, 300, 301, 302, 303, 304]. Specifically, in a procedure adapted from [297], 1.1mg of CNT-P3HT nanohybrid was dispersed in 8mL of chloroform by treatment with an ultrasonic probe (20 min at 20% amplitude) and then 200 μL was dynamically deposited over 100 seconds in a drop-by-drop fashion on a perovskite film spinning at 3000rpm. This resulted in formation of a highly interwoven porous network as shown in Figure 6.11(a). Immediately after this process was complete, a solution of poly(methyl methacrylate) (PMMA) in toluene (50mg/mL, 50μL) was deposited at a spin speed of 2000rpm for 40 seconds. The result, as seen in Figure 6.11(b), was that the CNTs were embedded in the approximately 250nm thick PMMA layer and protruded from it.

The dynamically dispensed CNT-based nanohybrids were first applied in devices with ZnO nanoparticles (NPs) as ETL. The device structure consisted of ITO/ ZnO/ Perovskite/

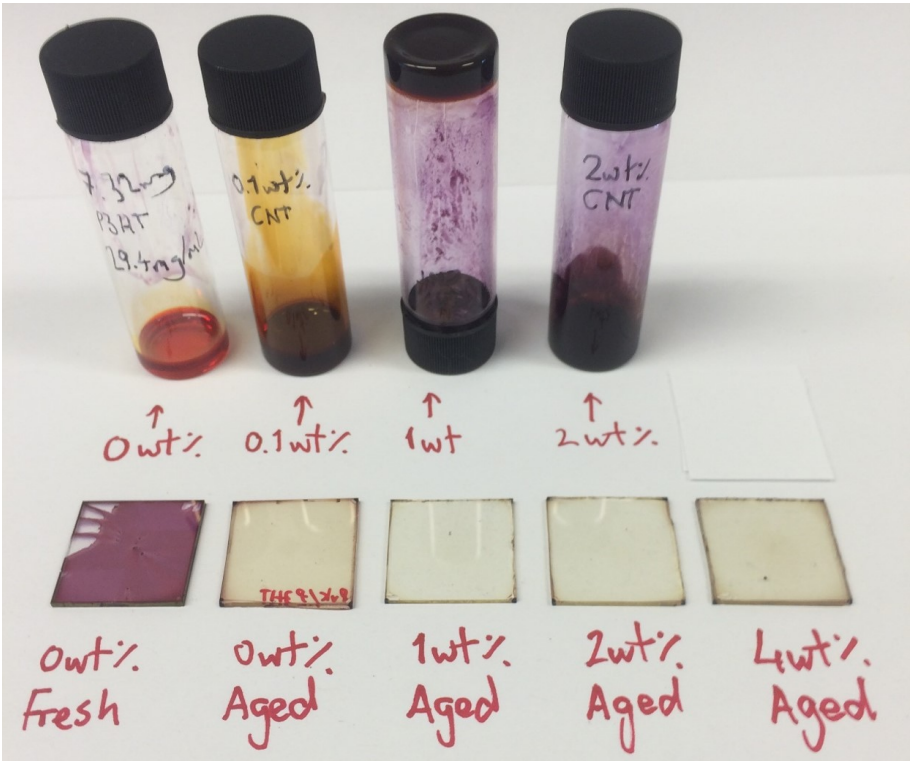

FIGURE 6.10: Dispersions (top row) and thin films (bottom row) for different CNT content. The label "aged" refers to films left in ambient lab conditions not under direct light.

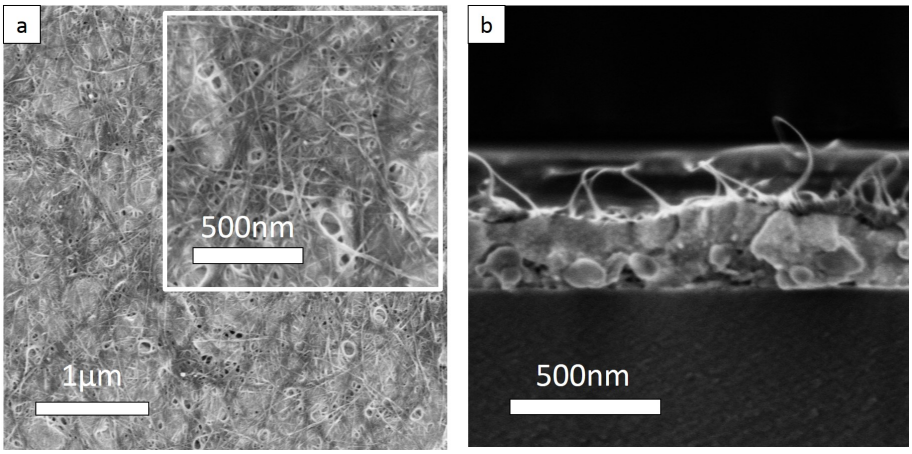

FIGURE 6.11: SEM images of CNT-P3HT nanohybrid films on perovskite. (a) Top view of porous nanohybrid network before coating with PMMA matrix. (b) Cross-section of CNT-PMMA composite.

CNT-P3HT/ PMMA/ TiAu. As shown in Figure 6.12(a), cells with CNT-PMMA composite HTLs displayed higher J_{sc} than P3HT reference devices. However, the JV-curves of both device structures suggested significant current loss due to charge recombination for reasons outlined in Chapter 4. However, when the device stack was altered to include a layer of C_{60} between the ZnO NPs and perovskite as depicted in Figure 6.12(b), both device structures showed improved performance (Figure 6.12(c)). In the case of cells with P3HT as HTL, the improvement consisted of more than a factor of 3 increase in J_{sc} for both scan directions. For devices with CNT-PMMA composite HTLs on the other hand, the improvement was more in FF, shifting the maximum power point (MPP) to higher voltage. MPP-tracking confirmed that true performance under operating conditions for both device structures lay slightly below that suggested by reverse bias scans, consistent with previous reports for perovskite solar cells. The higher power output for P3HT devices indicated that significant current losses due to charge recombination in devices with CNT-PMMA HTLs. Close scrutiny of current-voltage scans in the dark for both device stacks provides a likely cause for the difference in performance.

Figure 6.12(d) shows dark-JV scans for different cells on a single device with P3HT (shades of grey and black) as well as for a device with a CNT-PMMA composite HTL. Most cells in the P3HT-based device displayed relatively low dark currents, signifying that electron injection from ITO into P3HT was effectively suppressed by the combined presence of the ETL and photoactive layers. However, one of the cells was shunted which suggested incomplete ETL and/or perovskite coverage over the cell area. Although the presence of pinholes are detrimental to device performance, in the case of P3HT devices the effect is limited to the area of electrode overlap defining the cell due to the poor charge transport ability of P3HT films in the lateral direction. On the other hand, devices with a more conductive HTL such as a CNT network infiltrated with PMMA are much more susceptible to the presence of pinholes as the entire area of overlap between ITO and HTL effectively acts as a single cell. This would explain the shunting behaviour observed in all of the cells incorporating CNTs.

Although pinholes in the ETL would be an obvious explanation for the presence of shunting pathways, the exact reason wasn't clearly identified and a variety of possibilities exist. As outlined in Chapter 4, ZnO tends to degrade perovskite, especially when deposited from solution as residual hydroxides and organic species accelerate the process. It is therefore conceivable that gaps could be formed in the perovskite film during degradation, increasing the area of direct contact between HTL and ETL. Assuming compact and pinhole-free charge transport layers, direct contact between the ETL and HTL would be of limited concern if the

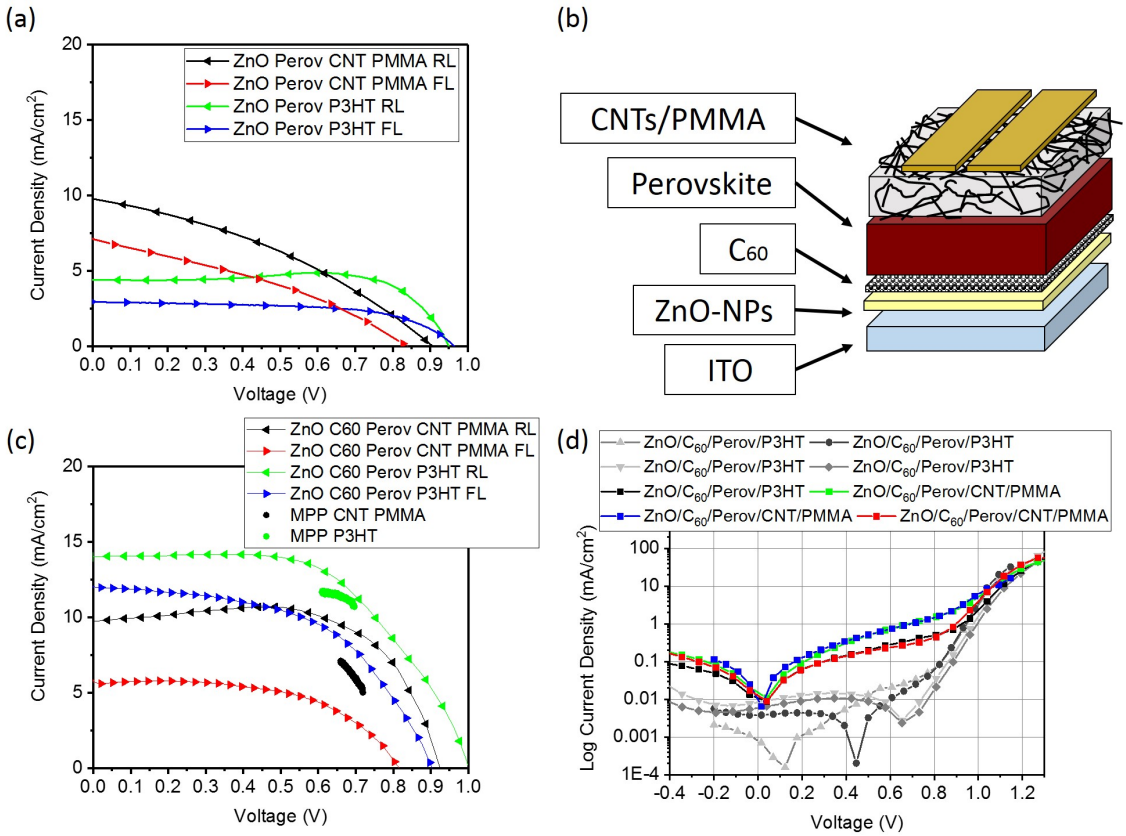

FIGURE 6.12: (a) Device with ZnO nanoparticle ETL and CNT-PMMA composite HTL along with reference device using P3HT as HTL. (b) Schematic of device stack with a sequentially deposited HTL consisting of a CNT network in-filled by a PMMA matrix. (c) Current-voltage response under illumination for device stack depicted in (b) where "ZnO-NPs" refers to sol-gel zinc oxide nanoparticles. Maximum power extracted under true operating conditions ("MPP") included for comparison. (d) Semilog plots of JV-scans in the dark for devices shown in (c).

junction was properly rectifying with diode-like behaviour. However, the presence of defects in either of the charge selective layers such as for example oxygen vacancies (V_o) and oxygen interstitial species (O_i) in ZnO, provide energy levels within the bandgap which can act as trap states and/or shunting pathways [159][315][157] resulting in reduced charge selectivity.

6.3.2 Optimizing deposition on planar devices with fullerene-based electron transport layer

As seen in the previous section, the presence of C_{60} was found to enhance the FF of planar perovskite solar cells with a CNT-based HTL and ZnO ETL. It was wondered therefore, similar to the discussion in Chapter 4, whether forgoing with metal oxides in the ETL could lead to further enhancement in device performance. Potential obstacles were apparent such as

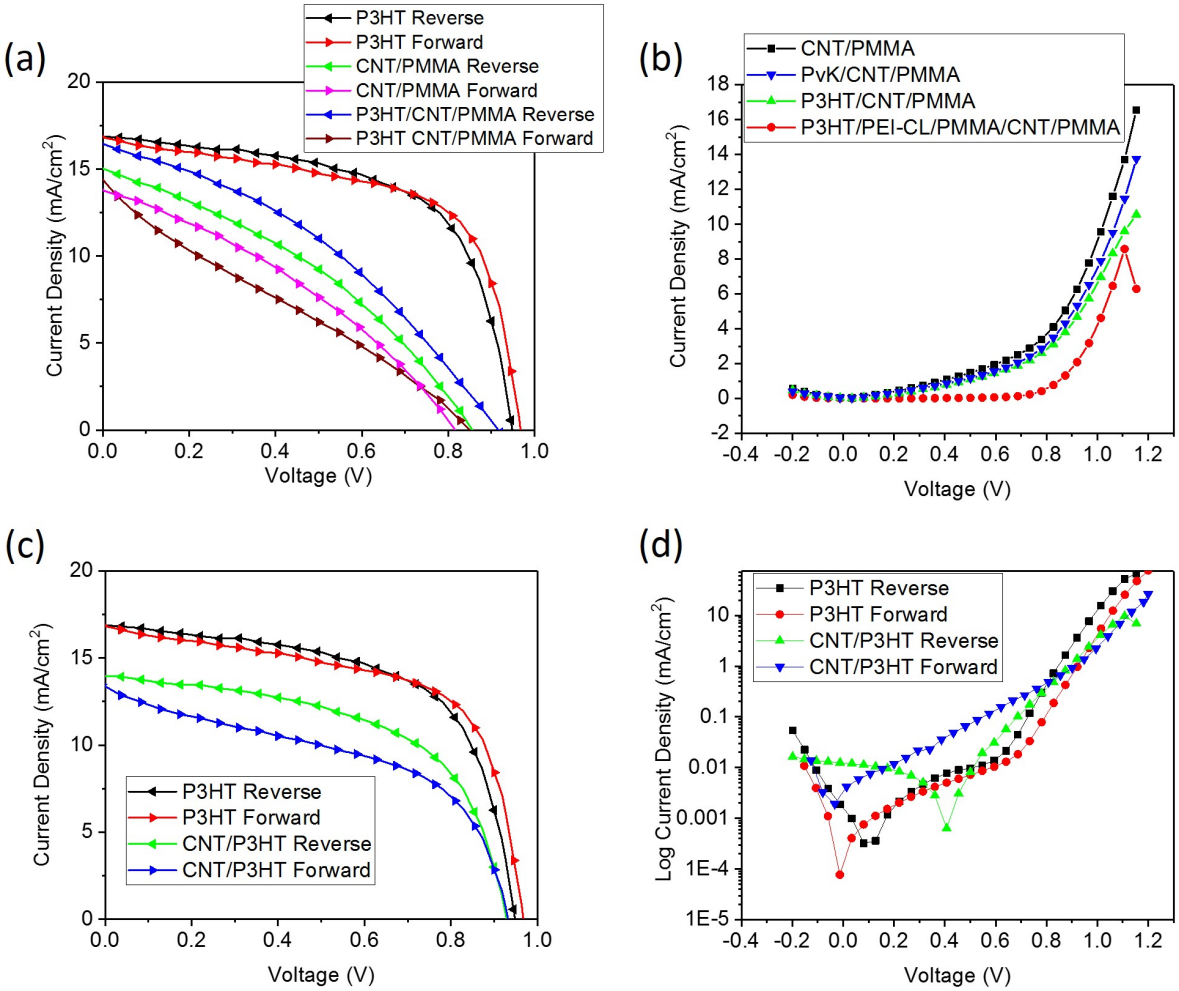

FIGURE 6.13: (a) Current-voltage (JV) sweeps of devices with fullerene-based ETL. (b) JV-sweeps in the dark for devices with fullerene ETLs and various CNT-based HTLs. (c) Current-voltage curves for a device with a CNT HTL infilled with P3HT through sequential deposition along with a P3HT-only device as reference. (d) Dark-JV curves of devices shown in (c).

the fact that C_{60} films obtained via spin coating were of limited thickness to begin with and were susceptible to partial removal by DMF during fabrication of the perovskite layer. This would likely be disadvantageous for a device stack in which good hole-blocking ability by the ETL is of crucial importance such as one with a highly conductive HTL. Furthermore, C_{60} is (slightly) soluble in chloroform (CF) so any solvent that penetrates beneath the perovskite layer during CNT deposition could further damage the ETL.

In an attempt to mitigate these factors, a layer of crosslinked PEI (PEI-CL) was deposited on the PEI/C_{60} bilayer during device fabrication such that the stack consisted of ITO/ PEI/ C_{60}/ PEI-CL/ Perovskite/ CNT/ PMMA/ TiAu. As seen in Figure 6.13(a), devices displayed respectable current densities at short circuit relative to control devices using P3HT as HTL, although FF and V_{oc} were both significantly lower which was a sign that significant

shunting was taking place. In an attempt to address this issue, devices were also fabricated in which polymer layers were coated ontop of the photoactive layer before the drop-by-drop deposited CNT nanobybrid network. Polyvinyl carbazole (Pvk) and P3HT were found to slightly suppress dark current (Figure 6.13(b)) resulting in increased J_{sc} and V_{oc} for reverse bias scans under illumination in the case of P3HT (Figure 6.13(a)). However shunting remained significant and hysteresis was found to increase with inclusion of the polymer interlayer. These results can be explained by the method used to deposit CNTs as it involved repeatedly exposing underlying layers to chloroform which is itself an effective solvent (at least partially) for many compounds including polymers. Depositing different materials sequentially such as P3HT/ PEIC-CL/ PMMA did more effectively suppress shunting but also increased series resistance resulting in a reduction in J_{sc}.

For completeness, devices were also made in which the CNT network was coated with P3HT instead of PMMA using the same procedure as for P3HT-only devices. Cells in which a CNT network was first deposited displayed larger diffusion currents (J_0) and hence ideality factor (n_{id}) as well as increased R_s relative to reference devices. However, compared to cells with CNT/PMMA HTLs, shunting was also largely suppressed. These characteristics taken together would indicate the absence of a clear percolating pathway for charges in the CNT/P3HT stack. The higher viscosity of chlorobenzene (CB) relative to toluene (used as solvent for PMMA) could prevent the P3HT from properly infiltrating the CNT network, resulting in thick polymer layer between the CNTs and anode. Alternatively, the CNT nanohybrids are more readily dispersible in CB than toluene (as exemplified by the toluene washing steps used to separate the nanohybrid from excess P3HT) which when coupled with the longer dwell time of CB during spin coating due to its low vapour pressure, could disrupt the integrity of the CNT network.

In an effort to improve the power output of devices with CNT-based HTLs, an alternative to dynamic drop-by-drop spin coating from CF was sought. During experimentation with CNT-doping of P3HT it had been noted that CNT nanohybrid material could be dispersed up to at least 0.55mg/mL in CB without significant aggregation. It was reasoned therefore that a CNT network of sufficient thickness could be formed by dispensing a single volume (50 μL) of the dispersion. A low spin speed was also chosen (1500rpm) to maximize the network thickness. However devices made using the same concentration solution of PMMA (50mg/mL) produced a near negligible photocurrent as seen in Figure 6.14(a). This was due to an extremely large R_s indicating that the CNT layer was either too thin to provide a pathway through the relatively thick insulating PMMA layer or else was too dense for the PMMA to infiltrate the network and form an effective polymer matrix. Depositing a layer of P3HT

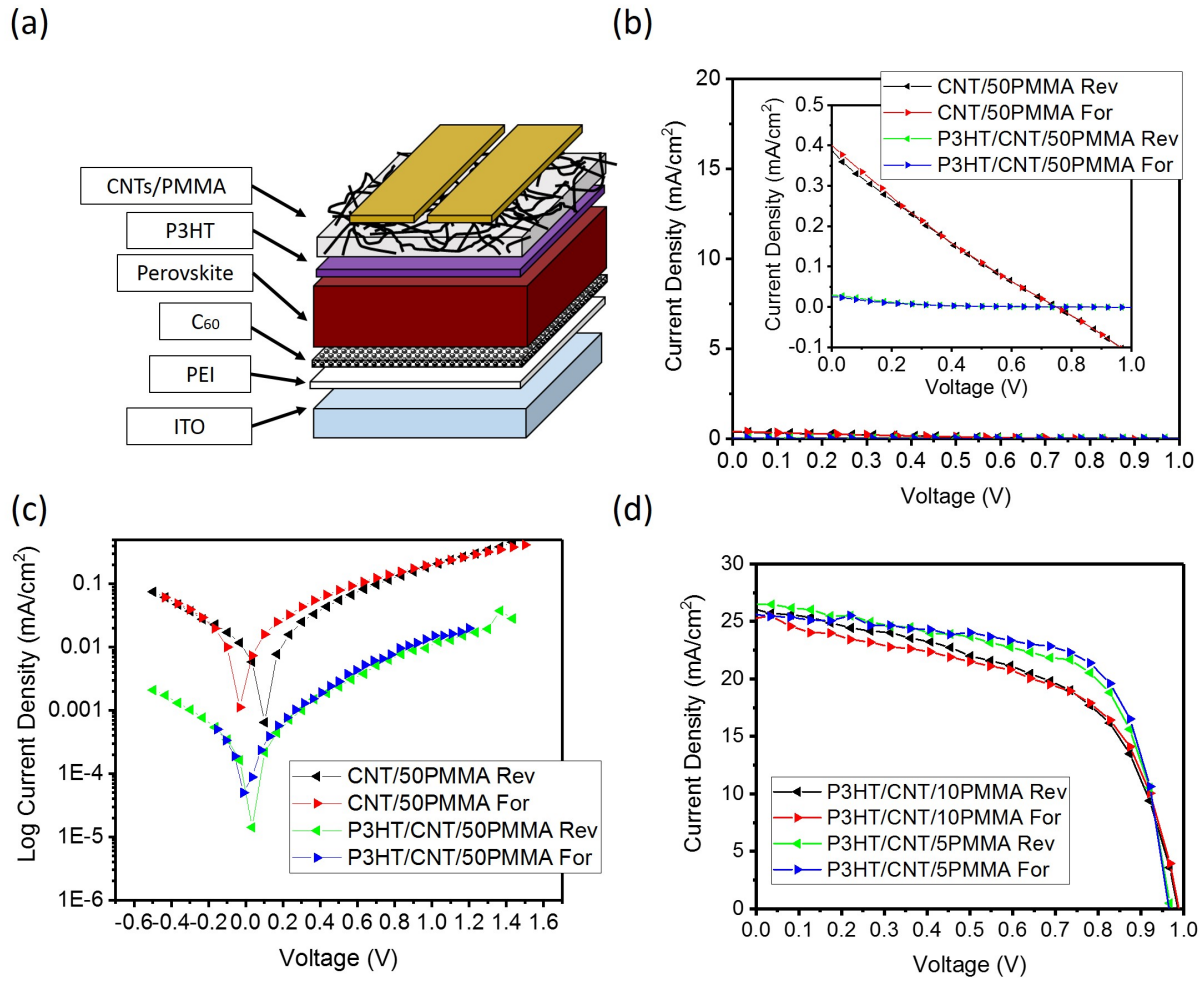

FIGURE 6.14: Current-voltage curves of various device stacks using fullerene-based ETL (a) Device with PMMA layer deposited from 50mg/mL solution . (b) Semilog plots of dark JV-scans of devices in (a). (c) Devices using PMMA capping layer deposted from 5mg/mL and 10mg/mL ("5PMMA" and "10PMMA" respectively).

before the CNT coating resulted in devices producing even less photocurrent, although the dark current was also suppressed as shown in Figure 6.14(b) suggesting reduced shunting. It would seem therefore that although much P3HT appeared to be removed during spin coating of the CNT layer, enough material remained to maintain an electron blocking effect. Keeping the same device structure but decreasing the concentration of PMMA solution to 10mg/mL resulted in a dramatic improvement in performance with a J_{sc} over 25 mA/cm^2, V$_{oc}$ of 0.99V and FF of 0.56 (Figure 6.14(c)). A further improvement in device output resulted from reducing the PMMA concentration to 5 mg/mL as the FF increased to 0.68. It would seem that the combination of a P3HT buffer layer and a sufficiently thin polymer matrix for the CNT-based layer resulted in good charge selectivity and extraction and consequently in high power output.

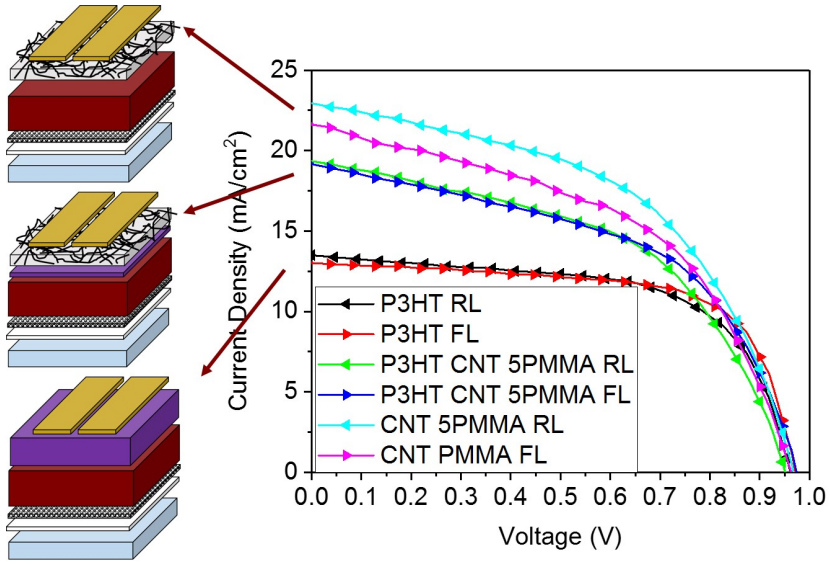

FIGURE 6.15: Current-voltage characteristics for devices with different HTLs produced in a batch with lower overall performance.

However, it was soon realised that devices containing even a thin buffer layer of P3HT suffered from reproducibility issues in ambient processing conditions. Figure 6.15 shows current-voltage curves for devices made in a batch that was generally poor in performance relative to many other batches. All devices used 30wt% $PbCl_2$ in the perovskite precursor as this was previously shown to produce films with good surface coverage and consistently high photovoltaic performance. However, control devices using P3HT as HTL had surprisingly low J_{sc}.

The reason for this result was unclear but it seemed to be related to the presence of a substantial P3HT layer as devices with a HTL consisting of P3HT/CNT/5PMMA (where "5PMMA" refers to a layer PMMA deposited from a 5mg/mL solution) showed improved photocurrent output. This was further corroborated by devices with only a CNT/PMMA composite as HTL which displayed still greater J_{sc} values and power output. This last result suggested that high conversion efficiency was possible for devices in which CNTs were in direct contact with perovskite, somewhat contrary to some previous reports [316][299][302] but in line with others. It is worth noting however that many reports with direct contact between CNTs and perovskite still used prototypical HTLs like PEDOT:PSS, spiro-OMeTAD, or P3HT as polymer matrix [298][300][305][303][304] whereas the current setup used a mixture of semiconducting and metallic CNTs with only a thin insulating polymer layer. Furthermore the result is of greater significance given the absence of metal oxide scaffolds used to guarantee good perovskite coverage and electron extraction by the ETL, thereby signifying both the high quality nature of the perovskite layer used in the present devices and

	CNT/5PMMA	CNT/10PMMA
R_s (Ωcm^2)	0.384	0.84
R_{sh} (Ωcm^2)	2.2×10^3	3.1×10^3
n_{id}	2.65	2.43
J_0 (mA/cm^2)	2.4×10^{-6}	2.8×10^{-6}
FF	0.49	0.57
V_{oc} (V)	0.96	0.97
J_{sc} (mA/cm^2)	21.6	24.4
PCE (%)	10.2	13.6

TABLE 6.4: Device characteristics for different PMMA thickness

efficient electron accepting ability of the solution-processed C_{60} layer. However as shown in Table 6.4, the shunt resistance of devices with a CNT/5PMMA HTL was lower than that typically found in other device architectures, resulting in a FF of only 0.49 in the forward bias direction. Unlike the case for champion batches of devices using the P3HT/CNT/PMMA stack, FF and hence maximum power output was increased for CNT/PMMA devices in which the PMMA concentration was increased from 5mg/mL to 10mg/mL as shown in Figure 6.16(a). Both concentrations of PMMA yielded devices with similar reverse saturation dark current and V_{oc} but CNT/10PMMA HTLs improved the ideality factor and FF as well as the J_{sc}, resulting in an improvement in mean device efficiency under forward bias from 10.2% to 13.6%. The slightly increased R_s was consistent with a thicker insulating polymer matrix but the series resistance remained below 1Ωcm^2 and was offset by a larger R_{sh}. The improvement in shunt resistance may be attributed to better coverage by the PMMA of underlying layers, thereby insulating them from direct contact with the metallic anode, resulting in reduced recombination losses.

In order to see where further gains could be made, devices using CNT/10PMMA as HTL were fabricated with different ETLs. FTO-coated glass substrates were sputter coated with various thicknesses of TiO_2. The substrates were sintered at 500 °C for 30 minutes immediately prior to device fabrication and PEI/C_{60} bilayers were spin coated onto the annealed TiO_2 substrates. As seen in Figure 6.16(c), the presence of even 20nm TiO_2 did significantly suppress dark currents under low positive bias and the trend increased with increasing thickness. However, there was also a trend of decreasing currents at higher positive bias (0.8V-1.2V) reflecting increased resistance to charge extraction. The result, as shown in Figure 6.16(d) and Table 6.5, was that devices with 30nm TiO_2 showed comparable PCE to C_{60}-only devices with a growth in PCE over 5 minutes of constant (MPP) tracking under illumination. Devices with thicker layers of TiO_2 displayed lower photocurrents and hence PCE due to increased R_s.

Tin oxide (SnO_2) has been reported to outperform TiO_2 in planar perovskite cells due

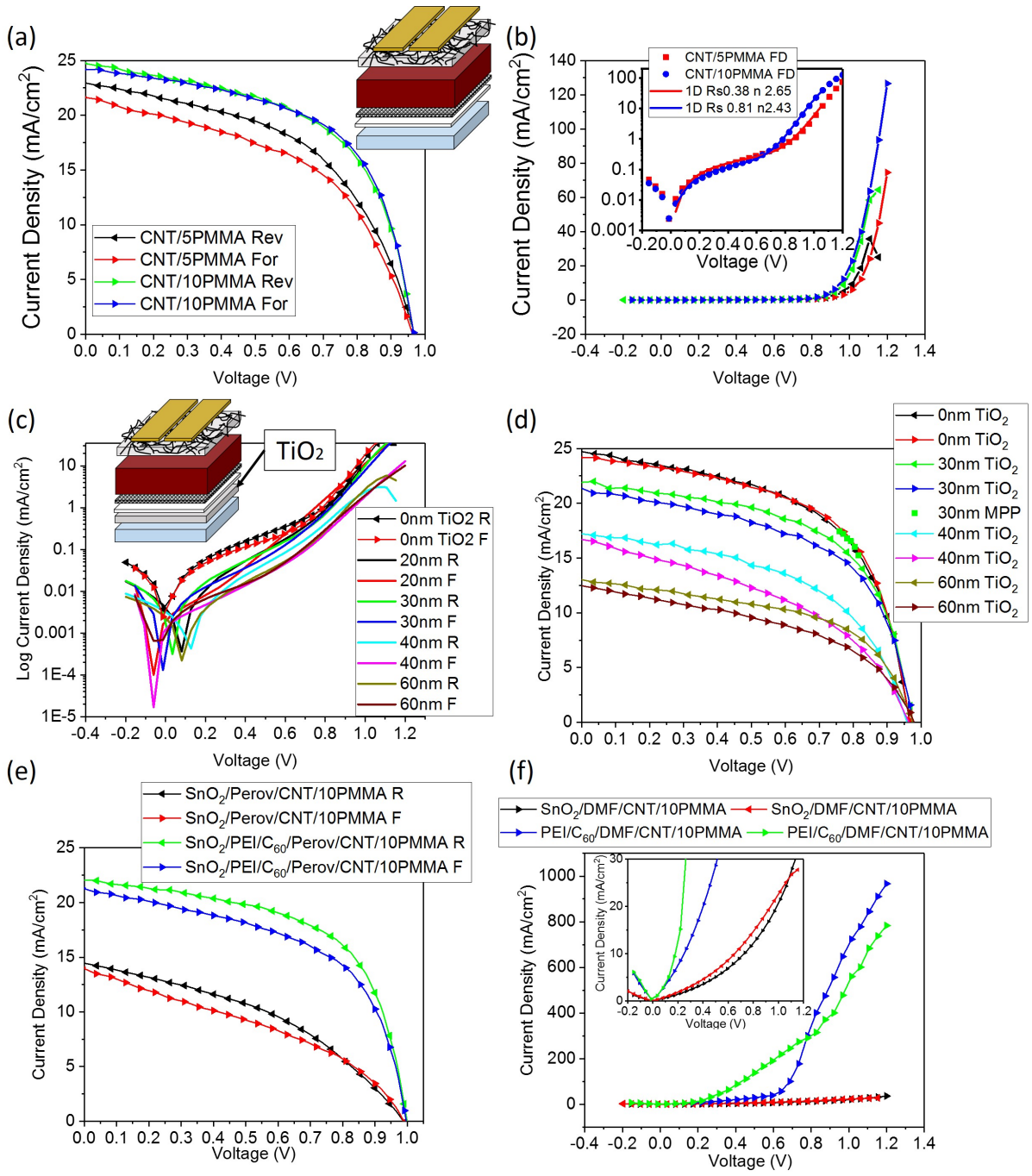

FIGURE 6.16: (a) Current-voltage characteristics for devices capped with PMMA layers deposited from different either 5mg/mL or 10mg/mL.(b) Dark scans for the same devices as in (a). Inset is a semilog plot of forward bias scans with fits using the one-diode model.(c) Dark JV-plots on a semilog scale of devices with structure FTO/TiO_2/PEI/C_{60}/Perov/CNT/10PMMA/TiAu for different TiO_2 thickness. (d) Current-voltage scans under illumination for devices shown in (c) where arrows indicate scan direction. (e) JV-scans for devices with a solution processed SnO_2 ETL and an SnO_2/PEI/C_{60} ETL together with CNT/10PMMA HTL. (f) Current voltage curves of SnO_2/CNT/10PMMA and PEI/C_{60}/CNT/10PMMA diodes in the dark. "DMF" denotes exposure to DMF via spin coating during processing.

	TiO_2 thickness				
	0nm	20nm	30nm	40nm	60nm
Mean PCE (%)	13.6	7.74	11.62	7.72	6.3
StDev./Mean PCE	0.106	0.246	0.145	0.192	0.174

TABLE 6.5: Device characteristics for different TiO_2 thickness.

to higher electron mobility, wider optical gap and a lower conduction-band edge resulting in improved electron collection [317][318][57][319]. An additional advantage of SnO_2 over TiO_2 is the ability to more easily achieve high performing devices at lower synthesis temperatures. A layer of SnO_2 was formed on ITO following an established procedure[320]. Briefly, $SnCl_2.2H_2O$ was dissolved in ethanol at a concentration of 11 mg/mL in an uncapped vial and aged under vigorous stirring for one hour before being twice spin coated on the ITO-glass substrate (3000rpm, 30s) and annealed in air at 150 °C for 30 minutes and 180 °C for one hour. Devices fabricated with structure ITO/SnO_2/Perov/CNT/10PMMA/TiAu displayed a reasonable J_{sc} of around 15mA/cm^2 and a V_{oc} of 1V with little hysteresis which was unlike the other metal oxide ETLs explored in this work. However, the FF was low which suggested plenty of scope for further improvement. Device stacks were also fabricated without a perovskite layer in the hope of gaining some insight into the nature of ETL and HTL junctions. In order to better compare with the full device stack, both SnO_2 and PEI/C_{60} ETLs were coated with DMF prior to depositing the CNT/PMMA composite HTL. As seen in the inset of Figure 6.16(f), neither stack was a particularly good diode but the fact that they displayed any rectifying behaviour was encouraging given the highly conductive nature of the HTL (complete with metallic as well as semiconducting CNTs). Particularly striking was the presence of a distinct knee at 0.6V in the case of the stack with PEI/C_{60} given the extremely thin nature of the ETL after DMF treatment. This result suggested that both the SnO_2 and C_{60} films were relatively pinhole-free insofar as they minimized direct contact between ITO and CNTs. Be that as it may, the large current densities at low bias indicated that the perovskite film must act as an effective barrier to direct contact between ETL and HTL for both stacks. Furthermore, as was the case for devices with TiO_2 and ZnO, coating PEI/C_{60} onto SnO_2 was found to significantly improve J_{sc} and FF, suggesting that C_{60} also facilitated electron injection from the perovskite into SnO_2.

Given the limited performance of metal oxide ETLs used in the current work, an attempt was made to increase the thickness and surface coverage of fullerene-only ETLs in devices incorporating CNT-based HTLs. The method used to achieve more robust C_{60}-based layers was to coat three successive bilayers of PEI and C_{60} (denoted as "3XPEI-C_{60}") as in Chapter 4. Figure 6.17(a) depicts a device stack using such an ETL. Devices using single bilayer ETLs

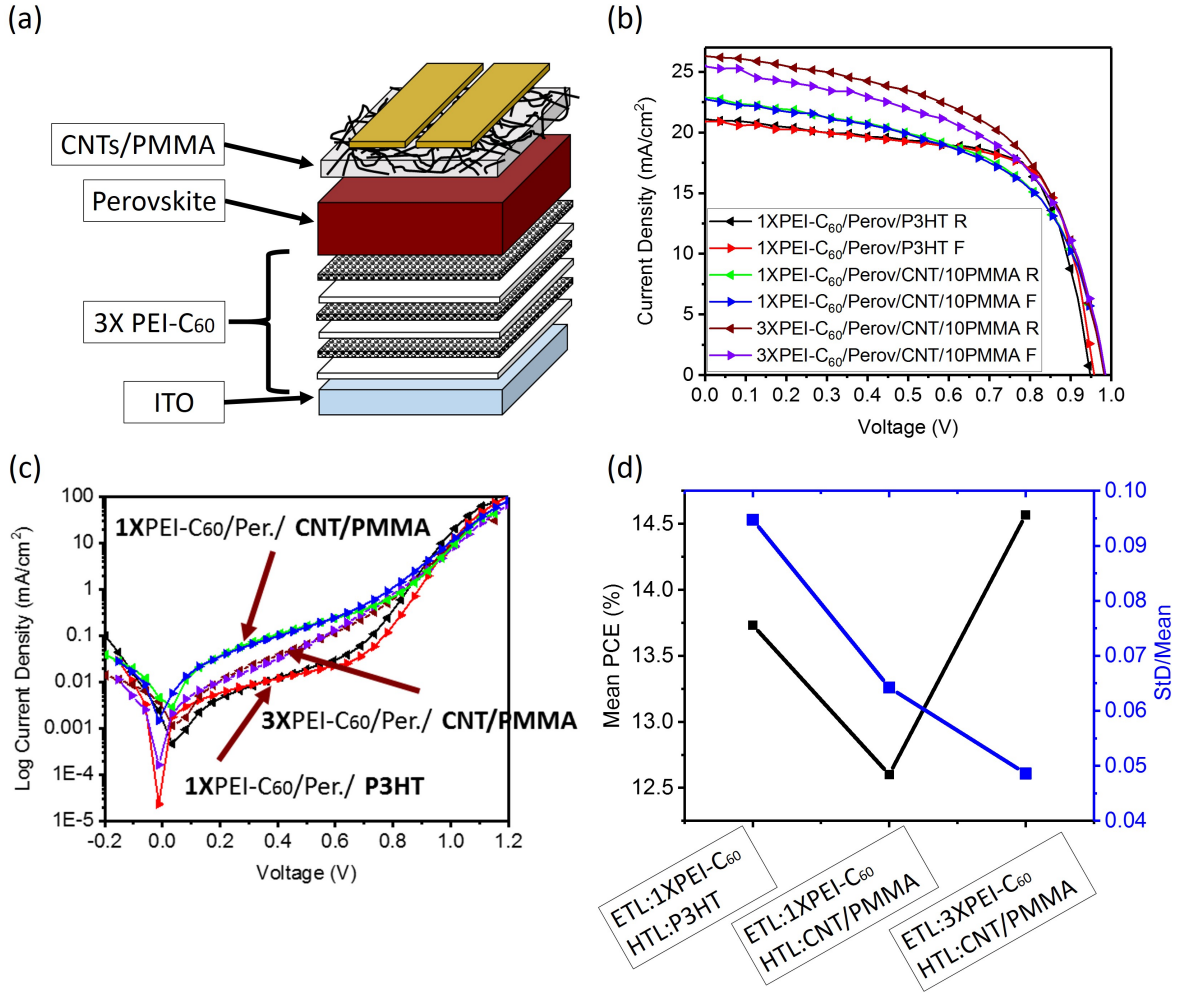

FIGURE 6.17: (a) Schematic of device stack with multiple alternating coats of PEI and C_{60} ("3X PEI-C_{60}"). (b) Current-voltage characteristics for devices with different ETLs and HTLs.(c) Semilog plots of JV-curves in the dark for devices shown in (b). (d) Plot of mean PCE and StD/Mean for different device configurations.

(1XPEI-C_{60}) with either P3HT or CNT/10PMMA composite HTLs were also fabricated for comparison. As seen in Figure 6.17(b), although devices using the CNT-based composite HTL had higher J_{sc} and V_{oc} than P3HT capped devices, they also had a less pronounced knee in the JV-curve resulting in slightly lower PCE.

However, devices with 3XPEI-C_{60} as ETL and CNT/10PMMA as HTL had significantly higher J_{sc} and consequently a greater PCE than even the P3HT reference. Furthermore the combination of a thicker ETL and a CNT-based HTL resulted in the lowest ratio of standard deviation to mean efficiency of the devices studied signifying improved cell-to-cell (as well as batch-to-batch) reproducibility. The difference in mean PCE between the three device

structures (Figure 6.17(d)) can be ascribed to increased shunting losses for cells with 1XPEI-C_{60} and CNT-based HTLs which was at least partly suppressed by a thicker ETL as suggested by the lower dark currents for 3XPEI-C_{60} devices in Figure 6.17(c). Champion cells using 3XPEI-C_{60} had efficiency which increased from 15.2% to 15.6% over 3 minutes of continuous tracking between 0.8V and 0.7V which rivalled that achieved using P3HT/CNT/5PMMA as HTL. This result indicated that high PCE could be achieved in planar devices contacted with purely nanocarbon layers.

6.3.3 Stability relative to neat P3HT

The champion cell using the P3HT/CNT/PMMA composite HTL was tracked over a period of weeks to see how it compared with devices that used P3HT-only HTLs. The cell was left unencapsulated and was stored in a drawer under ambient conditions (with relative humidity generally in the range 60-90% [258]) between measurements. Consistent with what was previously observed for devices made with $PbCl_2$ in the perovskite precursor, the device coated with P3HT/CNT/5PMMA as HTL was much more stable under ambient conditions than the chloride-free device as shown in Figure 6.18(a).

To better compare device stacks using the same perovskite precursor but different HTLs, devices were normalised as in Figure 6.18(b). The CNT-based HTL was found not only to ameliorate initial PCE relative to P3HT but also to improve device stability, retaining 80% of initial conversion efficiency after 900 hours compared to about 55% over the same period for P3HT. This result was all the more remarkable considering the relative thinness of the CNT-based HTL and suggests great promise for further improvements in device stability

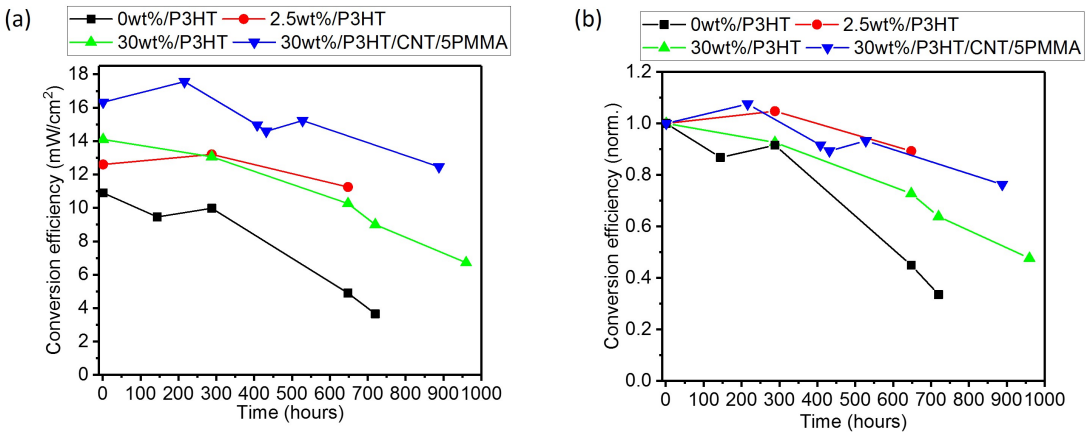

FIGURE 6.18: Stability of champion cell using P3HT/CNT/5PMMA as HTL (a) Absolute efficiency (b) Normalised efficiency.

through increasing the thickness of insulating PMMA or by using an even more hydrophobic polymer matrix.

As mentioned in Chapter 5, towards the end of the project it became possible to perform EQE measurements on some of the larger area devices. The first to be tested was a 9-day old device (shown in the inset of Figure 6.19(a)) consisting of ITO / PEI / C_{60} / 2Step30wt% / CNT / 10PMMA / TiAu. When fresh the cells showed high photocurrent with J_{sc} between 22 and 24mA/cm^2 (Figure 6.19(b)) depending on scan direction, though the cells were also fairly shunted with a low V_{oc} and FF. This came as little surprise given the large electrode overlap area (0.48cm^2) and the proximity of the electrode shown on the left of the image with the ITO contact area. After 9 days the device had degraded significantly with an increase in R_s (R_{sh} remained largely unchanged from dark-JV scans), resulting in a reduced J_{sc} which matched up with the integrated short circuit current density calculated from EQE measurements (Figure 6.19(a)). It is difficult to define the exact degradation mechanism as it is likely that many factors contribute but the fact that quantum efficiency remained high throughout the entire visible range would suggest that the integrity of most of the perovskite layer was largely maintained. A strongly reduced photocurrent at higher forward bias however may indicate formation of a barrier to hole extraction. Given the relatively thin CNT/PMMA HTL used, it is likely following equation 2.1 that PbI_2 crystals would be present on top of the aged perovskite film. Although a general consensus on the nature of energy level alignment of PbI_2 with many of the common perovskite device materials is still lacking[171], PbI_2 has been reported as an n-type semiconductor [321] [322] which can be beneficial towards device performance if present in small quantities near for example the interface with ETL/cathode [323] [324]. It is therefore likely that a PbI_2-rich region near the interface between perovskite and the HTL would effectively act as a Schottky diode of opposite polarity to the main diode. Moderate quantities of PbI_2 would hence result in a moderate back contact barrier to hole extraction which would not greatly impede photocurrent at J_{sc} similar to phenomena observed in chalcogenide-based photovoltaic devices [325].

One-day old devices using the same device stack (Figure 6.19(c) and (d)) were also quite shunted although scans measured in the reverse bias direction registered higher photocurrent than forward bias scans which displayed lower FF and J_{sc}. This suggested the presence of a barrier to photocurrent extraction which was reduced when a positive bias was applied to the cell under full AM1.5 illumination. This hypothesis would be consistent with the observed J_{sc} from the EQE which nearly matched the forward bias scan whose J_{sc} would more likely represent steady state photocurrent at zero bias. Furthermore, given that the EQE measurements were performed at lower light intensity it is conceivable that a photocurrent

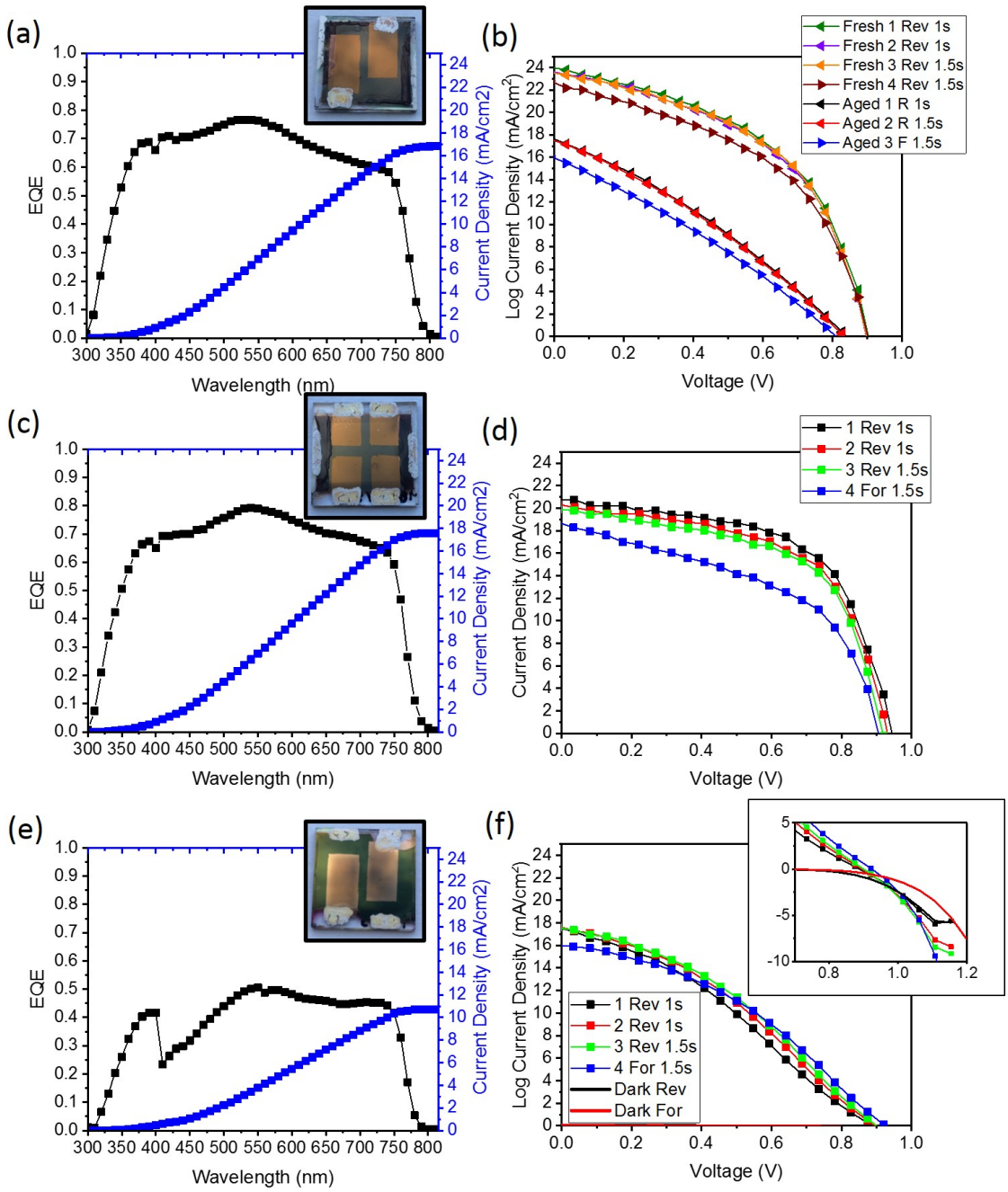

FIGURE 6.19: EQE measurements and JV-scans for different large-area device stacks (a) EQE of 9-day old device (shown in the inset) consisting of ITO / PEI / C_{60} / 2Step30wt% / CNT / 10PMMA / TiAu. (b) JV-curves for device measured the same day as the EQE measurements ("Aged" in the legend) alongside photocurrent when first fabricated ("Fresh"). (c) and (d) measurements performed on the same day for one-day old device consisting of the same stack as (a). (e) and (f) Same day measurements of a one-day old device made in the same batch as the one shown in (c) and (d) but with P3HT as HTL. Inset shows cross-over of light and dark curves.

barrier, which would be sizeable under low light intensity, would be lowered by photodoping of the ETL at AM1.5 illumination [326] [327]. It is also worth noting that in the case of EQE illumination on a limited area of a larger area device containing many micro shunts (such as those studied here), the non-illuminated part will act as a shunting load so that the local shunt resistance as seen from the active area may be smaller than observed macroscopically under JV-analysis [325].

Interestingly, one-day old large area cells with P3HT as HTL (made in the same batch as that shown in (c) and (d)) displayed low EQE throughout the visible range as seen in Figure 6.19(e). There could be many possible explanations but one consistent with the analysis made thus far would be the presence of an even larger barrier near the back contact. In this scenario, the main junction would be put under forward bias, resulting in a reduction in the width of the space charge region or large interface recombination. This would result in low EQE over the entire spectrum but particularly at short wavelengths where carrier collection efficiency would be most affected as seen in the figure. This would also be consistent with the kink in JV curves near V_{oc} and the cross over between dark and illuminated scans as seen in the inset of Figure 6.19(f). The large mismatch between integrated J_{sc} from EQE and that measured by JV scans would suggest that photodoping may significantly reduce the barrier under AM1.5 illumination.

6.4 Spray coating

In the previous sections it was demonstrated that high performing planar perovskite solar cells using CNT-based HTLs can be achieved using simple processing techniques near room temperature and in ambient conditions. To take full advantage of the encapsulating effect of the hydrophobic polymer matrix and highly conductive nature of the CNTs it would be advantageous to deposit relatively thick (order of 200-300nm or more) composite HTLs. However, spin coating is a rather limited method for depositing nanomaterial thin films because it requires either high concentration dispersions or else copious volumes of volatile solvents to build up thicker films in a "drop-by-drop" or layer-by-layer" approach, both of which waste roughly 90% of the solute[146][147]. Furthermore, repeated exposure of the device stacks used in the current work to chloroform during the drop-by-drop deposition of CNT nanohybrid films was found to damage underlying layers to some extent resulting in significant shunting.

As an alternative solution deposition method, spray coating avoids many of these shortcomings in that it offers excellent surface coverage with arbitrary film thickness and low

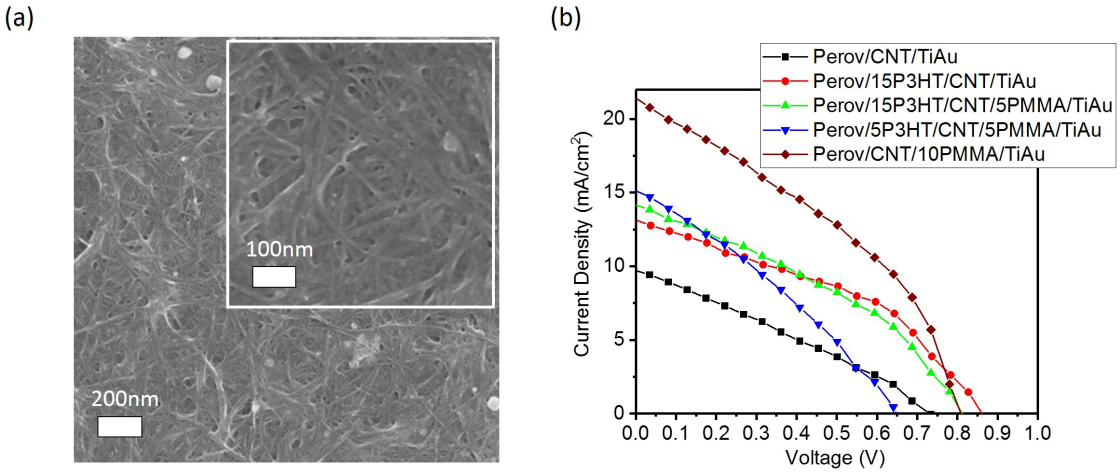

FIGURE 6.20: (a) SEM image of CNT film spray coated from chloroform onto a glass slide. (b) Current-voltage curves for devices with spray coated CNT-based HTLs.

material wastage. More importantly, the solvent is atomized during deposition such that a fine mist of tiny droplets hits the target substrate rather than repeatedly wetting the surface to be coated as with drop-by-drop spin coating. Additionally, the substrate may be easily and controllably heated during spray deposition to further minimize solvent dwell time. In this way it was hoped that spray coating from chloroform would less affect the underlying device layers than drop-by-drop spin coating.

Approximately 6mL of a chloroform dispersion with 0.1375mg/mL CNT nanohybrid gave a 100nm thick CNT film (as determined by profilometry). Figure 6.20(a) shows the spray coated CNT film under SEM. The CNT network appeared more dense with fewer sizeable pores than was observed for networks deposited via drop-by-drop spin coating. The reason for this was unclear but it was reasoned that this deposition method would be more sensitive to the presence of excess polymer in the dispersion.

Spray coated CNT films were incorporated into a variety of HTL structures and resulting devices were tested. Figure 6.20(b) shows typical current-voltage sweeps for different HTL stacks and extracted parameters for all devices are displayed in Table 6.6 . Unfortunately all devices were highly shunted to varying degrees. The relatively large R_s for cells in which TiAu was evaporated onto CNTs deposited directly onto perovskite (Perov/CNT) suggested direct contact between the metallic anode and perovskite layer. Depositing CNTs onto a spin coated P3HT layer (from 15mg/mL solution) before anode evaporation (Perov/15P3HT/CNT) did significantly decrease R_s but R_{sh} was only slightly increased. This behaviour indicated that the P3HT layer was greatly disrupted during the spray deposition step resulting in incomplete surface coverage by P3HT. What's more, the same phenomenon resulted

Device Stack	R_s (Ωcm^2)	R_{sh} (Ωcm^2)	PCE (%)	StD/ PCE
Perov/CNT	4	77	2.21	0.252
Perov/15P3HT/CNT	$\leq$0.2	118	4.36	0.272
Perov/15P3HT/CNT/5PMMA	$\leq$0.2	83	3.95	0.376
Perov/5P3HT/CNT/5PMMA	0.42	64.5	4.28	0.286
Perov/CNT/10PMMA	0.56	65	5.1	0.228

TABLE 6.6: Device characteristics for HTLs using spray deposited CNTs.

whether the substrate (including P3HT) was heated during spray deposition or not which indicated that the P3HT films were extremely sensitive to chloroform (CF). Curiously, spin coating a 5mg/ml PMMA solution (5PMMA) onto the 15P3HT/CNT stack slightly reduced the mean PCE which was ascribed to increased shunting losses, although coating the same solution onto a thinner P3HT/CNT stack (i.e.Perov/5P3HT/CNT/5PMMA) resulted in similar PCE to 15P3HT/CNT. On the other hand, coating a more concentrated PMMA solution (10mg/mL) on CNTs that had been directly sprayed on perovskite (i.e. Perov/CNT/10PMMA) led to increased photocurrent and J_{sc}, resulting in the highest PCE. These results indicated that significant device performance gains could be made by combining a thin P3HT interlayer (or perhaps some other polymer less readily soluble in CF) between the perovskite and CNTs together with depositing a more concentrated PMMA solution to act as an effective polymer matrix for the CNT network.

6.5 P-doping graphene towards hole extraction in perovskite solar cells

Given the success of polymer-assisted exfoliation of graphene for use in ETLs as detailed in Chapter 4, it was wondered whether a similar approach could be used to incorporate graphitic materials in the HTL. P3HT has been proven to enable the deposition of solution processed CNT networks in a manner compatible with perovskite solar cells and so it seemed a logical step to test its applicability towards graphene exfoliation. In a typical procedure, 6mg of P3HT was dissolved in 10mL of CB by bath sonication for one hour. The solution was then combined with 5mg of graphite and the mixture was sonicated using the ultrasonic probe (25% amplitude, 5hrs, 4s on 4s off). The resulting suspension was then centrifuged at 2000rpm for 99 minutes and the sediment discarded. To remove excess polymer, toluene (30mL) was added and the solution was bath sonicated for 10 minutes and then gently heated for one hour at 60 °C before being centrifuged for 4 minutes at 16000g and the

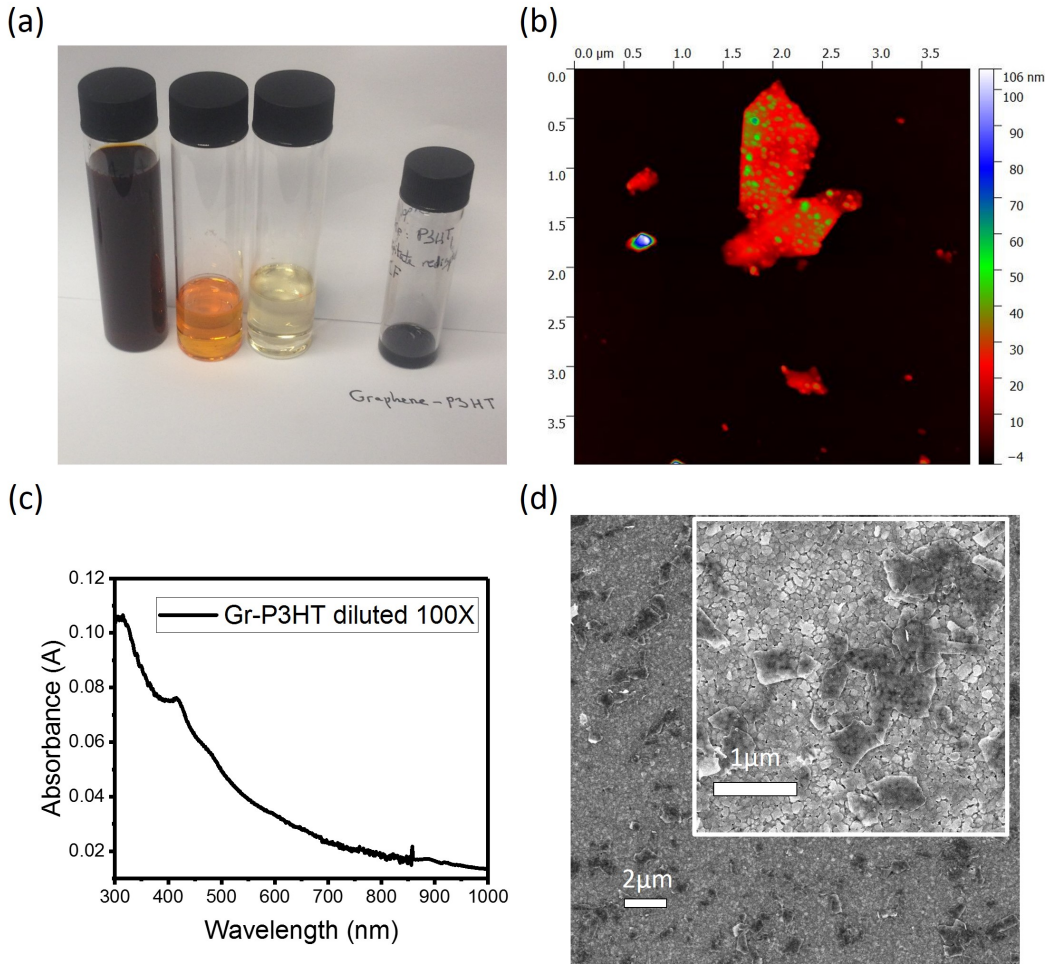

FIGURE 6.21: (a) Image of supernatant after exfoliating graphene in P3HT solution in CB (left), a dilute solution of P3HT extracted by toluene addition and centrifugation (middle left), after repeated toluene addition and centrifugation steps (middle right) and resulting graphene-P3HT (Gr-P3HT) nanohybrid redispersed in CF (right). (b) AFM image of Gr-P3HT material. (c) Absorption spectrum of dilute Gr-P3HT dispersion. (d) SEM image of Gr-P3HT flakes deposited on perovskite substrate via drop-by-drop spin coating.

supernatant discarded. This procedure was repeated twice before redispersing the Gr-P3HT sediment in 1mL CF.

A drop of the Gr-P3HT dispersion placed on an SiO_2 substrate and imaged by AFM confirmed the presence of many micron-sized flakes covered by what was presumed to be trace quantities of P3HT as shown by the raised (green) areas in Figure 6.21(b). However, it was noted during the exfoliation procedure that there was a lot of sediment after the first centrifugation step and that the supernatant was more of a dark red-brown colour than the black observed when fabricating the CNT-P3HT nanohybrids, suggesting a lower yield of well dispersed graphene flakes relative to what was obtained for CNTs. This was confirmed via absorption spectroscopy of the final dispersion as shown in Figure 6.21(c) which indicated a graphene concentration of approximately 0.065mg/mL. This was significantly lower than

the yield and concentration attainable for CNT-P3HT nanohybrids, suggesting a weaker affinity between P3HT and the surface of graphene. Consequently, drop-by-drop spin coating of the dispersion resulted in highly discontinuous surface coverage of perovskite films as shown in Figure 6.21(d), which was unsuitable for effective electron blocking. Following the same procedure outlined in Chapter 4 for Gr-PEI nanohybrids together with Hansen solubility parameters for P3HT taken from the literature[328], gave a calculated Relative Energy Difference (RED) of 1.75 which indicated only moderate affinity. However, the results obtained here would suggest that the degree of interaction between P3HT and graphene may be sufficient for device applications under more optimal processing conditions.

Attempts were also made to use graphene for hole collection instead of the typically used evaporated gold or silver layers. In order to achieve conductivities competitive with metals, graphene grown by chemical vapour deposition (CVD) was used. Hall effect measurements on a large area ($\geq$1.5cm $\times$ 1.5cm) graphene monolayer deposited on glass ()revealed a p-type nature with mobility of 668cm^{2}V/s as would be expected for PMMA-transferred CVD graphene in air. However, simultaneous Van der Pauw measurements recorded a sheet resistance (R_{sheet}) of 1100Ω/sq which is too high as an electrode for solar cells. From equation3.9 it is known that the conductivity can be increased by raising the carrier concentration. Chemical doping via hydrazine exposure, nitric acid treatments or deposition of silver nitrate or gold chloride ($AuCl_3$) [329][330][331]. On the other hand, it was noted from four point probe measurements on transferred graphene films as shown in Figure 6.22(c) that R_{sheet} was significantly lower prior to removal of the PMMA support, with an average sheet resistance of 328Ω/sq. The reason for improved conductivity was likely due firstly to structural damage such as tears and defects introduced during removal of PMMA by acetone and also to some doping effect by PMMA itself. Fortunately, the removal of PMMA is not necessary in the case of applying graphene as a transparent anode in regular architecture devices. In fact, not only would the presence of PMMA be beneficial from the perspective of conductivity but it would serve to improve moisture resistance and hence stability of resulting devices. Further gains were made by coating the graphene-on-copper films with $AuCl_3$ (20nM in nitromethane) and annealing on a hot plate for 5 minutes at 100 °C prior to spinning the PMMA support layer. This resulted in the presence of many nanoparticles of $AuCl_3$ ranging in size from roughly 10nm-100nm over the graphene surface as seen in Figure 6.22(b).Transferred $AuCl_3$-doped ML graphene coated with PMMA had an R_{sheet} of 173Ω/sq, which is highly competitive with other transparent electrode materials including the industry standard, ITO as shown in Figure 6.22(d) and indicates that further lowering of the sheet resistance could be realised by increasing the electrode thickness (i.e. multiple

graphene layers).

6.6 Conclusions

One of the less well studied of the prototypical HTLs used in perovskite solar cells (P3HT) was examined and its shortcomings discussed. Methods for doping CNTs into HTLs to improve robustness and electrical characteristics were considered and developed. It was found that sequentially depositing CNTs and an insulating polymer matrix (PMMA) generally led to improved device performance after optimizing the fabrication procedure. Champion devices using thin stacked P3HT/CNT/PMMA HTL not only matched the best PCE achieved using (thicker) P3HT-only reference devices but led to an improvement in device lifetime. Furthermore batch-to-batch reproducibility issues relating to the use of P3HT were identified and so devices free from P3HT were optimized, approaching the best achieved with P3HT. Spray deposition of CNT layers was also explored as an alternative to spin coating. Although the initial investigation yielded devices with much lower PCE than achieved via spin coating, the results were promising and a route to greatly improved device performance was identified. Overall CNTs were demonstrated as being a promising candidate for high performing low temperature processed planar perovskite solar cells. Finally, attempts were made to incorporate graphene as a p-type material in devices. First, novel graphene-P3HT nanohybrid dispersions were made, although yield and concentration was found too low for easy device application via spin coating. However, even the modest concentrations achieved in chloroform (0.065mg/mL) could prove sufficient for spray deposited films[332]. Graphene grown by CVD was also investigated to replace gold as contact material for hole extraction. Monolayer films doped with $AuCl_3$ and coated with PMMA were found to have sheet resistance below 180Ω/sq, making them competitive with the industrial standard transparent electrodes such as ITO. However, graphene films proved difficult to transfer onto devices without damaging either the electrode or perovskite. It is expected that high performing devices with transparent graphene as top electrode could be achieved with optimized dry transfer techniques such as the PDMS stamp method.

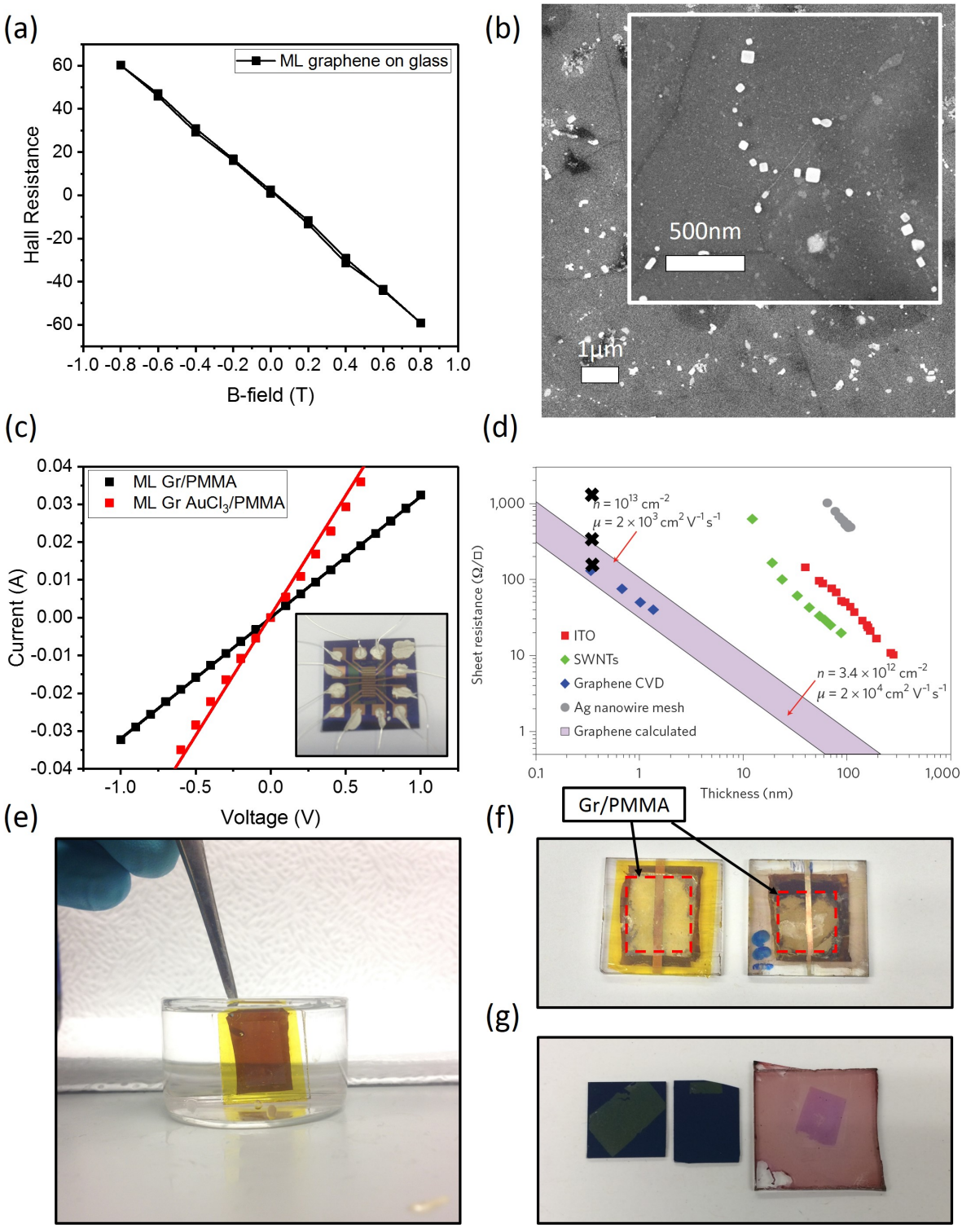

FIGURE 6.22: (a) Hall effect measurement of CVD graphene on glass. (b) SEM image of transferred monolayer (ML) graphene doped with $AuCl_3$. (c) Four point probe measurements of ML graphene with PMMA support both without (black) and with (red) $AuCl_3$ doping. (d) Thickness dependence of sheet resistance for various materials used as transparent electrodes where blue rhombuses show roll-to-roll CVD-grown graphene, grey dots metal nanowires, green rhombuses SWNTs, red squares ITO and black crosses the transferred graphene layers shown in (a) and (c)[120]. (e) Demonstration of the protection offered by CNT/PMMA composite HTL to perovskite during immersion in H_2O. (f) Image of device stacks with CNT/PMMA HTL after aqueous transfer of graphene transparent anodes (Gr/PMMA films are enclosed in red dotted areas). (g) ML graphene coated with PMMA on SiO_2 (left), SiO_2 substrate after removal of Gr/PMMA by PDMS stamp (middle) and Gr-PMMA film transferred by PDMS stamp onto P3HT (right).

7 Conclusions and Further Work

7.1 Conclusions

An ambitious goal was set for this project, namely to achieve high performing solar cells that make use of the superlative properties of carbon allotropes. To add a further constraint and hence difficulty, investigations were limited mainly to low cost materials and processing techniques for two reasons. Firstly, one of the main obstacles to widespread industrial scale adoption of solar photovoltaic-derived energy as an alternative to fossil fuels is the cost associated with current modules commercially available. Production cost should therefore be a major consideration when developing photovoltaic devices. Secondly, it would be extremely advantageous if investigations in the field of photovoltaics were accessible to as large a community of researchers as possible. To this end, the current work focussed primarily on processing devices using materials and equipment available in most research labs. Methylammonium lead triiodide perovskite, as a material that has demonstrated tremendous potential as a low cost replacement or partner for traditional silicon-based solar cells, was used as photoactive material. However, the vast majority of research output on high performing perovskite solar cells to date has focussed on carefully controlled oxygen and moisture-free processing conditions using reactive charge selective materials resulting in inherently unstable devices. Furthermore, device fabrication has often involved relatively slow and costly vacuum-based steps including thermal evaporation and ALD or else high temperature treatments rendering devices incompatible with flexible substrates.

Accordingly, attempts were made to optimise each of the three main device layers for processing under ambient conditions with generally high ($\geq$60%) humidity outside of cleanroom environments. It was found that many of the typically used metal oxides were unsuitable in their as-deposited state in conjunction with ambient processed perovskite towards well-functioning devices. Sol-gel ZnO nanoparticle films for example resulted in generally low photocurrents with a high degree of scan-dependent hysteresis. Furthermore, the films were found to cause rapid perovskite decomposition, even after multiple washing steps and

annealing. Similar problems were encountered for ZnO films deposited by spray pyrolysis and room temperature sputtering. Annealing of sputtered ZnO under N_2 did result in some increase in the amount and stability of photocurrent extracted under illumination. Conversely spray pyrolized ZnO doped with indium or aluminium and annealed under N_2 resulted in an even greater barrier to charge extraction. Air annealing at 500 °C was found absolutely necessary to obtain even modest device efficiencies for TiO_2 deposited either via spray pyrolysis or sputtering. Surface modification by spin coating a solution of C_{60} was found to improve the charge extraction ability of all metal oxides to varying degrees. Polyethylenimine (PEI) with and without a crosslinking agent was variously used to promote adhesion and integrity of solution processed C_{60} layers resulting in metal oxide-free high performing devices after some optimization. PEI was also found capable of facilitating graphene exfoliation at concentrations and in solvents suitable for spin coating. Consequently, graphene-PEI composite layers were demonstrated to protect perovskite from degradation by ZnO whilst simultaneously maintaining device performance.

After experimenting with a variety of crystallization techniques, a variant on the two-step method was found most applicable to processing perovskite layers under conditions of high humidity. Incorporating 20wt% $PbCl_2$ into the lead halide precursor was found to increase the maximum attainable total dissolved solids concentration, leading to better device efficiencies than achieved using PbI_2-only solutions deposited at room temperature. However, significant batch-to-batch variation in PCE was found to persist for chloride containing devices depending on ambient humidity during fabrication, which was ascribed to incomplete crystallization of the perovskite as determined via XRD. This prompted a systematic study of the variation of device parameters with $PbCl_2$ content. It was found that lead chloride in excess 30wt% consistently resulted in full crystallization and consequently high performance even for devices processed under highly humid ($\geq$90% rel. hum.) conditions. Champion batches displayed not only J_{sc} equal to the highest reported but also FF as high as 0.75. Fitting to JV-characteristics in the dark and under illumination revealed that the observed device performance was due to a combination of high perovskite coverage and low resistance to charge extraction. Furthermore, unencapsulated devices showed respectable device stability compared to the literature.

Investigations were also made into optimizing the HTL towards further improvements in device performance and stability. The limitations of P3HT were highlighted and methods were developed to fabricate composite films of CNTs in p-type polymers. A high loading of CNTs in P3HT was found necessary to guarantee improved charge extraction and hence device performance, due presumably to the interplay between crystallinity of P3HT and

percolation in CNT networks. This fact coupled with the observation of P3HT-bleaching regardless of CNT-doping lead to adoption of stacked composite structures in which CNT networks were infilled by subsequent deposition of a polymer matrix. Drop-by-drop spin coating of CNTs from CF followed by PMMA, though effective in guaranteeing high conductivity and good barrier properties to moisture ingress, also resulted in significant shunting losses in planar devices with C_{60}-based ETLs. However, dispersing P3HT-wrapped CNTs at a higher concentration in CB and coating on P3HT followed by PMMA resulted in excellent device performance, despite the fact that P3HT was mostly removed during processing. Decent performance was also maintained without spin coating P3HT in the stack which allowed the conclusion to be drawn that P3HT was also a contributing factor to batch-to-batch variation in PCE as some batches had higher R_s and lower FF for P3HT capped devices relative to CNT/PMMA composite HTLs. By optimizing the ETL and CNT-based HTL, devices with PCE approaching the best achieved with P3HT were obtained. This was an encouraging result as CNT/PMMA HTLs gave much more consistent PCE than P3HT. Furthermore, the champion device based on a stacked P3HT/CNT/PMMA HTL proved more stable than comparable P3HT-only devices. A preliminary study of CNT-based HTLs deposited from CF by spray coating revealed similar shunting issues to drop-by-drop spin coated films but the PCEs were for some device stacks were promising, suggesting that significant performance gains could easily be made with further optimization. Finally, attempts were made to incorporate graphene as a p-type contact material in devices. Graphene was successfully dispersed in chlorinated solvents by means of non-covalent functionalisation with P3HT, though the yield was too low for spin coating. CVD-grown graphene was also effectively doped with $AuCl_3$ resulting in transparent electrodes with sheet resistance below 180Ω/sq, thereby suitable for application as device anode. Although wet transfer techniques resulted in decomposition of the perovskite layer even in the presence of a protective CNT/PMMA composite layer, it is anticipated that such graphene films could be applied to the current device stacks using dry transfer techniques.

All in all, the work carried out in this thesis suggests that carbon nanomaterials are well-suited to improving device performance, reproducibility and stability of perovskite solar cells processed under ambient and high humidity conditions. Simple solution-processing techniques were shown to be capable of producing devices with consistently high PCE without need for high temperature treatments or glovebox conditions. It is hoped that the results detailed here will help open up the exciting field of perovskite photovoltaics to a wider research community.

7.2 Further work

Some pressing questions have been raised in the course of work carried out during this project regarding the role of primary and secondary phases in perovskite films on the alignment of energy levels with respect to those of charge selective materials. As discussed in 6, the distribution of PbI_2-rich and MAI-rich phases in the film may be important in determining the performance of resulting devices depending on the device stack used, particularly in the case of planar devices. The presence of a PbI_2 layer near the ETL in devices with indium-doped ZnO (a reasonable assumption given reported decomposition effects of ZnO in contact with perovskites) seemed to provide improvement in shunt resistance, particularly in the dark as seen in section 4.3.1. However, this improvement was generally accompanied by increased hysteresis and a larger barrier to photocurrent extraction. Conversely, perovskite films with less of a PbI_2 signature tended to display a voltage-dependent collection function with higher J_{sc} and a sloped JV-response under low forward bias which would be consistent with a p-doped rather than intrinsic photoactive layer [33]. As such, a systematic study of the effect of doping on the energy levels and surface passivation of perovskite films via ultraviolet photoelectron spectroscopy (UPS) and x-ray photoelectron spectroscopy (XPS) would be useful together with electrochemical impedance spectroscopy (EIS) studies of the films in device stacks. The results of such investigations would help determine the likelihood of illumination-dependent shunt paths in perovskite films due to photoconductive secondary phases as has been reported for certain lead iodide-based species [333] [334]. Additionally, possible photodoping effects of either the ETL or perovskite layer under AM1.5 illumination suggested by the mismatch between J_{sc} from EQE and JV analysis for fresh devices could be investigated by varying the light intensity incident on devices and measuring the photoresponse as well as performing SCLC measurements on ETL only devices with C_{60} both in the dark and under illumination.

In addition to maximizing device performance through optimizing the morphology and composition of perovskite films, there is also plenty of scope for further improvements in device stability. As already discussed, there is a growing body of evidence indicating instability in perovskite solar cells with metal-based electrodes [335] [336] [184], with carbon a more stable alternative [337]. Over the course of this work it has been demonstrated that planar devices with thin C_{60} and CNT-based charge selective layers fabricated and tested under highly humid conditions could compete with porous metal oxide-based devices in terms of PCE.

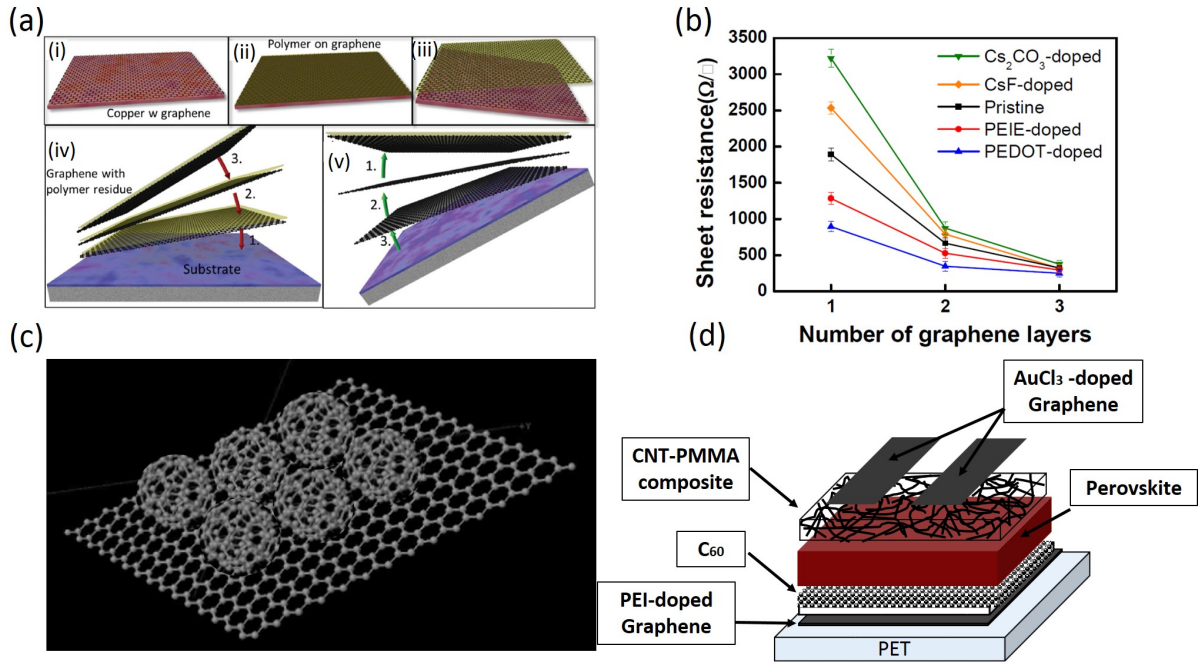

FIGURE 7.1: All-carbon contacted perovskite solar cell (a) Graphene stack production (i) CVD-graphene on copper foil (ii) coated by polymer for transfer (iii) After dissolving copper the graphene is transferred onto another piece of graphene on copper and the process is repeated until the desired number of layers has been transferred (iv) conventional graphene transfer resulting in support polymer residue (v) modified transfer without polymer residue transferred onto desired substrate [338]. (b) Sheet resistance against number of layers for differently doped graphene electrodes [339]. (c) C_{60} molecules on a graphene substrate. (d) Schematic of an all-carbon contacted perovskite solar cell using CNT-based HTL, C_{60} ETL and transferred CVD-graphene electrodes.

In order to take full advantage of stability improvements offered by these materials, deposition of layers of arbitrary thickness would be necessary, particularly for CNT composite layers with hydrophobic polymers. Although this can be achieved by dry transfer of relatively thick CNT networks grown on filter membranes, a solution-based technique such as spray deposition would be cheaper and therefore more advantageous. Preliminary results obtained for spray coated CNT networks on devices used in this work indicate that control over a C_{60} film thickness and uniformity is a necessary prerequisite to avoiding a high degree of shunting. This could be achieved via thermal evaporation which is the method most commonly used for C_{60} film fabrication. However, an approach more in keeping with low cost devices would be to spray coat C_{60} as has been demonstrated to controllably coat films ranging in thickness from monolayer to at least 100nm [340]. As for optimizing spray-coated CNT-based layers, the use of dilute CNT dispersions should allow the polymer component to be deposited in the same step as the CNTs to guarantee homogeneous distribution of the polymer matrix in the resulting film. In the event that single-step deposited composites

prove unsuitable, a hierarchically stacked arrangement may be used. Thus by optimizing spray coating conditions for the C_{60} and CNT-based layers it should be possible to achieve high performing devices with improved stability.

Furthermore, PEI-C_{60} bilayers are suitable for fabricating regular planar perovskite cells using graphene as transparent cathode instead of ITO. PEIE has been shown to n-dope CVD graphene resulting in transparent electrodes with low work function (4.2eV) and improved conductivity [339] [341]. Following equation3.37, combining PEI-doping with a stack of multiple graphene layers produced by a modified polymer-assisted transfer method scheme illustrated in Figure 7.1(a) would likely result in relatively crack-free graphene electrodes with good barrier properties and low sheet resistance as shown in Figure 2.10(b). These PEI-coated graphene layers could then be coated with C_{60} either by spin or spray coating (as represented in Figure 2.10(c)) before fabricating devices. If $AuCl_3$-doped graphene electrodes studied in 6 were successfully transferred onto a n-doped graphene / PEI /C_{60} / Perovskite / CNT-PMMA stack then the resulting device would be entirely carbon contacted as illustrated in Figure 2.10(d). If fabricated on a PET then the device would be both highly flexible and (depending on the perovskite bandgap and thickness) semi-transparent.

Bibliography

[1] 2018 Doomsday Clock Statement bulletin of the atomic scientists. https://thebulletin.org/doomsday-clock/current-time/. Accessed: 2018-10-02.

[2] John Rafferty. Anthropocene Epoch britannica. https://www.britannica.com/science/Anthropocene-Epoch. Accessed: 2018-10-01.

[3] Yadvinder Malhi. The concept of the anthropocene. *Annual Review of Environment and Resources*, 42:77–104, 2017.

[4] Rebecca Lindsey. Climate Change: Atmosphheric Carbon Dioxide. https://www.climate.gov/news-features/understanding-climate/climate-change-atmospheric-carbon-dioxide. Accessed: 2018-10-02.

[5] James Hansen, Makiko Sato, Paul Hearty, Reto Ruedy, Maxwell Kelley, Valerie Masson-Delmotte, Gary Russell, George Tselioudis, Junji Cao, Eric Rignot, et al. Ice melt, sea level rise and superstorms: evidence from paleoclimate data, climate modeling, and modern observations that 2 c global warming could be dangerous. *Atmospheric Chemistry and Physics*, 16(6):3761–3812, 2016.

[6] Tobias Friedrich, Axel Timmermann, Michelle Tigchelaar, Oliver Elison Timm, and Andrey Ganopolski. Nonlinear climate sensitivity and its implications for future greenhouse warming. *Science Advances*, 2(11):e1501923, 2016.

[7] Natalia Shakhova, Igor Semiletov, Orjan Gustafsson, Valentin Sergienko, Leopold Lobkovsky, Oleg Dudarev, Vladimir Tumskoy, Michael Grigoriev, Alexey Mazurov, Anatoly Salyuk, et al. Current rates and mechanisms of subsea permafrost degradation in the east siberian arctic shelf. *Nature communications*, 8:15872, 2017.

[8] Caspar A Hallmann, Martin Sorg, Eelke Jongejans, Henk Siepel, Nick Hofland, Heinz Schwan, Werner Stenmans, Andreas Müller, Hubert Sumser, Thomas Hörren, et al. More than 75 percent decline over 27 years in total flying insect biomass in protected areas. *PloS one*, 12(10):e0185809, 2017.

[9] Gerardo Ceballos, Paul R Ehrlich, and Rodolfo Dirzo. Biological annihilation via the ongoing sixth mass extinction signaled by vertebrate population losses and declines. *Proceedings of the National Academy of Sciences*, 114(30):E6089–E6096, 2017.

[10] Keeling Curvescripps institution of oceanography. https://scripps.ucsd.edu/programs/keelingcurve/pdf-downloads/. Accessed: 2018-10-02.

[11] Timothy D Searchinger, Tim Beringer, Bjart Holtsmark, Daniel M Kammen, Eric F Lambin, Wolfgang Lucht, Peter Raven, and Jean-Pascal van Ypersele. Europe's renewable energy directive poised to harm global forests. *Nature communications*, 9(1):3741, 2018.

[12] Natural Resources Defense Council. Money to burnii: Solar and wind can reliably supply the united kingdom's new electricity needs more cost-effectively than biomass. 2017.

[13] Renewable Energy Policy Network for the 21st Century. Renewables 2018 global status report. 2018.

[14] William Shockley and Hans J Queisser. Detailed balance limit of efficiency of p-n junction solar cells. *Journal of applied physics*, 32(3):510–519, 1961.

[15] Alexis De Vos. Detailed balance limit of the efficiency of tandem solar cells. *Journal of Physics D: Applied Physics*, 13(5):839, 1980.

[16] William Grylls Adams and RE Day. The action of light on selenium. *Proceedings of the Royal Society of London*, 25(171-178):113–117, 1876.

[17] Alan Chodos. April 25, 1954: Bell labs demonstrates the first practical silicon solar cell.

[18] Daryl M Chapin, CS Fuller, and GL Pearson. A new silicon p-n junction photocell for converting solar radiation into electrical power. *Journal of Applied Physics*, 25(5):676–677, 1954.

[19] Ran Fu, David J Feldman, Robert M Margolis, Michael A Woodhouse, and Kristen B Ardani. Us solar photovoltaic system cost benchmark: Q1 2017. Technical report, National Renewable Energy Lab.(NREL), Golden, CO (United States), 2017.

[20] GA Chamberlain. Organic solar cells: A review. *Solar cells*, 8(1):47–83, 1983.

[21] Ching W Tang. Two-layer organic photovoltaic cell. *Applied Physics Letters*, 48(2):183–185, 1986.

[22] Amaresh Mishra and Peter Bäuerle. Small molecule organic semiconductors on the move: promises for future solar energy technology. *Angewandte Chemie International Edition*, 51(9):2020–2067, 2012.

[23] Gustav Rose. De novis quibusdam fossilibus quae in montibus. 1839.

[24] Veerle Keppens. Structure of materials: An introduction to crystallography, diffraction, and symmetry. *The Journal of the Acoustical Society of America*, 124(3):1385–1386, 2008.

[25] Encyclopaedia Britannica. Rose family.

[26] Joseph S Manser, Jeffrey A Christians, and Prashant V Kamat. Intriguing optoelectronic properties of metal halide perovskites. *Chemical reviews*, 116(21):12956–13008, 2016.

[27] Akihiro Kojima, Kenjiro Teshima, Tsutomu Miyasaka, and Yasuo Shirai. Novel photoelectrochemical cell with mesoscopic electrodes sensitized by lead-halide compounds (2). In *Meeting Abstracts*, number 7, pages 397–397. The Electrochemical Society, 2006.

[28] Akihiro Kojima, Kenjiro Teshima, Yasuo Shirai, and Tsutomu Miyasaka. Organometal halide perovskites as visible-light sensitizers for photovoltaic cells. *Journal of the American Chemical Society*, 131(17):6050–6051, 2009.

[29] Jeong-Hyeok Im, Chang-Ryul Lee, Jin-Wook Lee, Sang-Won Park, and Nam-Gyu Park. 6.5% efficient perovskite quantum-dot-sensitized solar cell. *Nanoscale*, 3(10):4088–4093, 2011.

[30] Hui-Seon Kim, Chang-Ryul Lee, Jeong-Hyeok Im, Ki-Beom Lee, Thomas Moehl, Arianna Marchioro, Soo-Jin Moon, Robin Humphry-Baker, Jun-Ho Yum, Jacques E Moser, et al. Lead iodide perovskite sensitized all-solid-state submicron thin film mesoscopic solar cell with efficiency exceeding 9%. *Scientific reports*, 2:591, 2012.

[31] Michael M Lee, Joël Teuscher, Tsutomu Miyasaka, Takurou N Murakami, and Henry J Snaith. Efficient hybrid solar cells based on meso-superstructured organometal halide perovskites. *Science*, page 1228604, 2012.

[32] Lioz Etgar, Peng Gao, Zhaosheng Xue, Qin Peng, Aravind Kumar Chandiran, Bin Liu, Md K Nazeeruddin, and Michael Gratzel. Mesoscopic ch3nh3pbi3/tio2 heterojunction solar cells. *Journal of the American Chemical Society*, 134(42):17396–17399, 2012.

[33] Xingshu Sun, Reza Asadpour, Wanyi Nie, Aditya D Mohite, and Muhammad Ashraful Alam. A physics-based analytical model for perovskite solar cells. *IEEE Journal of Photovoltaics*, 5(5):1389–1394, 2015.

[34] Anders Hagfeldt, Gerrit Boschloo, Licheng Sun, Lars Kloo, and Henrik Pettersson. Dye-sensitized solar cells. *Chemical reviews*, 110(11):6595–6663, 2010.

[35] Jun Hong Noh, Sang Hyuk Im, Jin Hyuck Heo, Tarak N Mandal, and Sang Il Seok. Chemical management for colorful, efficient, and stable inorganic–organic hybrid nanostructured solar cells. *Nano letters*, 13(4):1764–1769, 2013.

[36] Osbel Almora, Clara Aranda, Isaac Zarazua, Antonio Guerrero, and Germa Garcia-Belmonte. Noncapacitive hysteresis in perovskite solar cells at room temperature. *ACS Energy Letters*, 1(1):209–215, 2016.

[37] Hyung Do Kim and Hideo Ohkita. Potential improvement in fill factor of lead-halide perovskite solar cells. *Solar RRL*, 1(6), 2017.

[38] Michael Saliba, Taisuke Matsui, Konrad Domanski, Ji-Youn Seo, Amita Ummadisingu, Shaik M Zakeeruddin, Juan-Pablo Correa-Baena, Wolfgang R Tress, Antonio Abate, Anders Hagfeldt, et al. Incorporation of rubidium cations into perovskite solar cells improves photovoltaic performance. *Science*, 354(6309):206–209, 2016.

[39] Manda Xiao, Fuzhi Huang, Wenchao Huang, Yasmina Dkhissi, Ye Zhu, Joanne Etheridge, Angus Gray-Weale, Udo Bach, Yi-Bing Cheng, and Leone Spiccia. A fast deposition-crystallization procedure for highly efficient lead iodide perovskite thin-film solar cells. *Angewandte Chemie*, 126(37):10056–10061, 2014.

[40] Nam Joong Jeon, Jun Hong Noh, Young Chan Kim, Woon Seok Yang, Seungchan Ryu, and Sang Il Seok. Solvent engineering for high-performance inorganic–organic hybrid perovskite solar cells. *Nature materials*, 13(9):897, 2014.

[41] Samuel D Stranks, Pabitra K Nayak, Wei Zhang, Thomas Stergiopoulos, and Henry J Snaith. Formation of thin films of organic–inorganic perovskites for high-efficiency solar cells. *Angewandte Chemie International Edition*, 54(11):3240–3248, 2015.

[42] Yani Chen, Minhong He, Jiajun Peng, Yong Sun, and Ziqi Liang. Structure and growth control of organic–inorganic halide perovskites for optoelectronics: From polycrystalline films to single crystals. *Advanced Science*, 3(4), 2016.

[43] Julian Burschka, Norman Pellet, Soo-Jin Moon, Robin Humphry-Baker, Peng Gao, Mohammad K Nazeeruddin, and Michael Grätzel. Sequential deposition as a route to high-performance perovskite-sensitized solar cells. *Nature*, 499(7458):316, 2013.

[44] Sneha A Kulkarni, Tom Baikie, Pablo P Boix, Natalia Yantara, Nripan Mathews, and Subodh Mhaisalkar. Band-gap tuning of lead halide perovskites using a sequential deposition process. *Journal of Materials Chemistry A*, 2(24):9221–9225, 2014.

[45] Guan-Woo Kim, Gyeongho Kang, Jinseck Kim, Gang-Young Lee, Hong Il Kim, Limok Pyeon, Jaechol Lee, and Taiho Park. Dopant-free polymeric hole transport materials for highly efficient and stable perovskite solar cells. *Energy & Environmental Science*, 9(7):2326–2333, 2016.

[46] Cong Chen, Yu Cheng, Qilin Dai, and Hongwei Song. Radio frequency magnetron sputtering deposition of tio 2 thin films and their perovskite solar cell applications. *Scientific reports*, 5:17684, 2015.

[47] Qi Chen, Huanping Zhou, Ziruo Hong, Song Luo, Hsin-Sheng Duan, Hsin-Hua Wang, Yongsheng Liu, Gang Li, and Yang Yang. Planar heterojunction perovskite solar cells via vapor-assisted solution process. *Journal of the American Chemical Society*, 136(2):622–625, 2013.

[48] Rui Sheng, Anita Ho-Baillie, Shujuan Huang, Sheng Chen, Xiaoming Wen, Xiaojing Hao, and Martin A Green. Methylammonium lead bromide perovskite-based solar cells by vapor-assisted deposition. *The Journal of Physical Chemistry C*, 119(7):3545–3549, 2015.

[49] Mingzhen Liu, Michael B Johnston, and Henry J Snaith. Efficient planar heterojunction perovskite solar cells by vapour deposition. *Nature*, 501(7467):395, 2013.

[50] Lidon Gil-Escrig, Araceli Miquel-Sempere, Michele Sessolo, and Henk J Bolink. Mixed iodide–bromide methylammonium lead perovskite-based diodes for light emission and photovoltaics. *The journal of physical chemistry letters*, 6(18):3743–3748, 2015.

[51] M Ibrahim Dar, Neha Arora, Peng Gao, Shahzada Ahmad, Michael Gratzel, and Mohammad Khaja Nazeeruddin. Investigation regarding the role of chloride in organic–inorganic halide perovskites obtained from chloride containing precursors. *Nano letters*, 14(12):6991–6996, 2014.

[52] Giulia Grancini, Sergio Marras, Mirko Prato, Cinzia Giannini, Claudio Quarti, Filippo De Angelis, Michele De Bastiani, Giles E Eperon, Henry J Snaith, Liberato Manna, et al.

The impact of the crystallization processes on the structural and optical properties of hybrid perovskite films for photovoltaics. *The journal of physical chemistry letters*, 5(21):3836–3842, 2014.

[53] Wei Zhang, Michael Saliba, David T Moore, Sandeep K Pathak, Maximilian T Hörantner, Thomas Stergiopoulos, Samuel D Stranks, Giles E Eperon, Jack A Alexander-Webber, Antonio Abate, et al. Ultrasmooth organic–inorganic perovskite thin-film formation and crystallization for efficient planar heterojunction solar cells. *Nature communications*, 6:6142, 2015.

[54] Samuel D Stranks, Giles E Eperon, Giulia Grancini, Christopher Menelaou, Marcelo JP Alcocer, Tomas Leijtens, Laura M Herz, Annamaria Petrozza, and Henry J Snaith. Electron-hole diffusion lengths exceeding 1 micrometer in an organometal trihalide perovskite absorber. *Science*, 342(6156):341–344, 2013.

[55] Hui-Seon Kim and Nam-Gyu Park. Parameters affecting i–v hysteresis of ch3nh3pbi3 perovskite solar cells: effects of perovskite crystal size and mesoporous tio2 layer. *The journal of physical chemistry letters*, 5(17):2927–2934, 2014.

[56] Jiangjian Shi, Xin Xu, Dongmei Li, and Qingbo Meng. Interfaces in perovskite solar cells. *Small*, 11(21):2472–2486, 2015.

[57] Juan Pablo Correa Baena, Ludmilla Steier, Wolfgang Tress, Michael Saliba, Stefanie Neutzner, Taisuke Matsui, Fabrizio Giordano, T Jesper Jacobsson, Ajay Ram Srimath Kandada, Shaik M Zakeeruddin, et al. Highly efficient planar perovskite solar cells through band alignment engineering. *Energy & Environmental Science*, 8(10):2928–2934, 2015.

[58] Joseph S Manser, Makhsud I Saidaminov, Jeffrey A Christians, Osman M Bakr, and Prashant V Kamat. Making and breaking of lead halide perovskites. *Accounts of chemical research*, 49(2):330–338, 2016.

[59] Jianqing Chen, Xin Cai, Donghui Yang, Dan Song, Jiajia Wang, Jinghua Jiang, Aibin Ma, Shiquan Lv, Michael Z Hu, and Chaoying Ni. Recent progress in stabilizing hybrid perovskites for solar cell applications. *Journal of Power Sources*, 355:98–133, 2017.

[60] Tomas Leijtens, Giles E Eperon, Sandeep Pathak, Antonio Abate, Michael M Lee, and Henry J Snaith. Overcoming ultraviolet light instability of sensitized tio 2 with meso-superstructured organometal tri-halide perovskite solar cells. *Nature communications*, 4:2885, 2013.

[61] Gagan Flora, Deepesh Gupta, and Archana Tiwari. Toxicity of lead: a review with recent updates. *Interdisciplinary toxicology*, 5(2):47–58, 2012.

[62] Bekele Hailegnaw, Saar Kirmayer, Eran Edri, Gary Hodes, and David Cahen. Rain on methylammonium lead iodide based perovskites: possible environmental effects of perovskite solar cells. *The journal of physical chemistry letters*, 6(9):1543–1547, 2015.

[63] Douglas Fabini. Quantifying the potential for lead pollution from halide perovskite photovoltaics, 2015.

[64] Po-Yen Chen, Jifa Qi, Matthew T Klug, Xiangnan Dang, Paula T Hammond, and Angela M Belcher. Environmentally responsible fabrication of efficient perovskite solar cells from recycled car batteries. *Energy & Environmental Science*, 7(11):3659–3665, 2014.

[65] Harold W Kroto, James R Heath, Sean C O'Brien, Robert F Curl, and Richard E Smalley. C60: Buckminsterfullerene. *Nature*, 318(6042):162–163, 1985.

[66] Sumio Iijima. Helical microtubules of graphitic carbon. *nature*, 354(6348):56, 1991.

[67] Sumio Iijima and Toshinari Ichihashi. Single-shell carbon nanotubes of 1-nm diameter. *nature*, 363(6430):603–605, 1993.

[68] Pavel Nikolaev, Michael J Bronikowski, R Kelley Bradley, Frank Rohmund, Daniel T Colbert, KA Smith, and Richard E Smalley. Gas-phase catalytic growth of single-walled carbon nanotubes from carbon monoxide. *Chemical physics letters*, 313(1):91–97, 1999.

[69] Richard E Smalley and Boris I Yakobson. The future of the fullerenes. *Solid state communications*, 107(11):597–606, 1998.

[70] Jason H Hafner, Michael J Bronikowski, Bobak R Azamian, Pavel Nikolaev, Andrew G Rinzler, Daniel T Colbert, Ken A Smith, and Richard E Smalley. Catalytic growth of single-wall carbon nanotubes from metal particles. *Chemical Physics Letters*, 296(1):195–202, 1998.

[71] Alan M Cassell, Jeffrey A Raymakers, Jing Kong, and Hongjie Dai. Large scale cvd synthesis of single-walled carbon nanotubes. *The Journal of Physical Chemistry B*, 103(31):6484–6492, 1999.

[72] Santiago Esconjauregui, Caroline M Whelan, and Karen Maex. The reasons why metals catalyze the nucleation and growth of carbon nanotubes and other carbon nanomorphologies. *Carbon*, 47(3):659–669, 2009.

[73] Olivier Berné and Alexander GGM Tielens. Formation of buckminsterfullerene (c60) in interstellar space. *Proceedings of the National Academy of Sciences*, 109(2):401–406, 2012.

[74] Rainer D Beck, Pamela St. John, Marcos M Alvarez, Francois Diederich, and Robert L Whetten. Resilience of all-carbon molecules c60, c70, and c84: A surface-scattering time-of-flight investigation. *The Journal of Physical Chemistry*, 95(21):8402–8409, 1991.

[75] W Edward Billups. *Buckminsterfullerenes*. John Wiley & Sons, 1993.

[76] Yizheng Jin, Richard J Curry, Jeremy Sloan, Ross A Hatton, Lok Cee Chong, Nicholas Blanchard, Vlad Stolojan, Harold W Kroto, and S Ravi P Silva. Structural and optoelectronic properties of c 60 rods obtained via a rapid synthesis route. *Journal of Materials Chemistry*, 16(37):3715–3720, 2006.

[77] Christos D Dimitrakopoulos and Patrick RL Malenfant. Organic thin film transistors for large area electronics. *Advanced materials*, 14(2):99–117, 2002.

[78] Ming-Liang Zhang and Han-Ying Guo. Superconductivity in alkali-doped c60. *Communications in Theoretical Physics*, 23(3):271, 1995.

[79] Yoshihiro Iwasa. Superconductivity: Revelations of the fullerenes. *Nature*, 466(7303):191–192, 2010.

[80] Julieta Coro, Margarita Suárez, Lays SR Silva, Katlin IB Eguiluz, and Giancarlo R Salazar-Banda. Fullerene applications in fuel cells: A review. *International Journal of Hydrogen Energy*, 41(40):17944–17959, 2016.

[81] Lothar Dunsch and Shangfeng Yang. The recent state of endohedral fullerene research. *INTERFACE-PENNINGTON-*, 15(2):34, 2006.

[82] Qihai Liu, Quanjun Cui, Xudong Joshua Li, and Li Jin. The applications of buckminsterfullerene c60 and derivatives in orthopaedic research. *Connective tissue research*, 55(2):71–79, 2014.

[83] Hari Singh Nalwa. *Handbook of Organic Conductive Molecules and Polymers, Volume 2, Conductive Polymers: Synthesis and Electrical Properties*. Chichester: John Wiley and Sons, 1997.

[84] Mildred S Dresselhaus, Gene Dresselhaus, and Peter C Eklund. *Science of fullerenes and carbon nanotubes: their properties and applications*. Academic press, 1996.

[85] NS Sariciftci, David Braun, C Zhang, VI Srdanov, AJ Heeger, G Stucky, and F Wudl. Semiconducting polymer-buckminsterfullerene heterojunctions: Diodes, photodiodes, and photovoltaic cells. *Applied physics letters*, 62(6):585–587, 1993.

[86] T Dürkop, SA Getty, Enrique Cobas, and MS Fuhrer. Extraordinary mobility in semiconducting carbon nanotubes. *Nano letters*, 4(1):35–39, 2004.

[87] Phaedon Avouris, Marcus Freitag, and Vasili Perebeinos. Carbon-nanotube photonics and optoelectronics. *Nature photonics*, 2(6):341–350, 2008.

[88] Xueshen Wang, Qunqing Li, Jing Xie, Zhong Jin, Jinyong Wang, Yan Li, Kaili Jiang, and Shoushan Fan. Fabrication of ultralong and electrically uniform single-walled carbon nanotubes on clean substrates. *Nano letters*, 9(9):3137–3141, 2009.

[89] Min-Feng Yu, Oleg Lourie, Mark J Dyer, Katerina Moloni, Thomas F Kelly, and Rodney S Ruoff. Strength and breaking mechanism of multiwalled carbon nanotubes under tensile load. *Science*, 287(5453):637–640, 2000.

[90] Jonathan N Coleman, Umar Khan, Werner J Blau, and Yurii K Gun'ko. Small but strong: a review of the mechanical properties of carbon nanotube–polymer composites. *Carbon*, 44(9):1624–1652, 2006.

[91] Mustafa Lotya, Yenny Hernandez, Paul J King, Ronan J Smith, Valeria Nicolosi, Lisa S Karlsson, Fiona M Blighe, Sukanta De, Zhiming Wang, IT McGovern, et al. Liquid phase production of graphene by exfoliation of graphite in surfactant/water solutions. *Journal of the American Chemical Society*, 131(10):3611–3620, 2009.

[92] Alexander A Green and Mark C Hersam. Solution phase production of graphene with controlled thickness via density differentiation. *Nano letters*, 9(12):4031–4036, 2009.

[93] PM Allemand, A Koch, Fred Wudl, Y Rubin, F Diederich, MM Alvarez, SJ Anz, and RL Whetten. Two different fullerenes have the same cyclic voltammetry. *Journal of the American Chemical Society*, 113(3):1050–1051, 1991.

[94] Niyazi S Sariciftci, L Smilowitz, Alan J Heeger, and F Wudl. Photoinduced electron transfer from a conducting polymer to buckminsterfullerene. *Science*, pages 1474–1476, 1992.

[95] JJM Halls, K Pichler, RH Friend, SC Moratti, and AB Holmes. Exciton diffusion and dissociation in a poly (p-phenylenevinylene)/c60 heterojunction photovoltaic cell. *Applied Physics Letters*, 68(22):3120–3122, 1996.

[96] Satoru Suzuki, Chris Bower, Yoshio Watanabe, and Otto Zhou. Work functions and valence band states of pristine and cs-intercalated single-walled carbon nanotube bundles. *Applied Physics Letters*, 76(26):4007–4009, 2000.

[97] Masashi Shiraishi and Masafumi Ata. Work function of carbon nanotubes. *Carbon*, 39(12):1913–1917, 2001.

[98] Yi Jia, Anyuan Cao, Xi Bai, Zhen Li, Luhui Zhang, Ning Guo, Jinquan Wei, Kunlin Wang, Hongwei Zhu, Dehai Wu, et al. Achieving high efficiency silicon-carbon nanotube heterojunction solar cells by acid doping. *Nano letters*, 11(5):1901–1905, 2011.

[99] Feijiu Wang, Daichi Kozawa, Yuhei Miyauchi, Kazushi Hiraoka, Shinichiro Mouri, Yutaka Ohno, and Kazunari Matsuda. Considerably improved photovoltaic performance of carbon nanotube-based solar cells using metal oxide layers. *Nature communications*, 6:6305, 2015.

[100] Sumit Chaudhary, Haiwei Lu, Astrid M Müller, Christopher J Bardeen, and Mihrimah Ozkan. Hierarchical placement and associated optoelectronic impact of carbon nanotubes in polymer-fullerene solar cells. *Nano Letters*, 7(7):1973–1979, 2007.

[101] Jao Van De Lagemaat, Teresa M Barnes, Garry Rumbles, Sean E Shaheen, Timothy J Coutts, Chris Weeks, Igor Levitsky, Jorma Peltola, and Paul Glatkowski. Organic solar cells with carbon nanotubes replacing in 2 o 3: Sn as the transparent electrode. *Applied Physics Letters*, 88(23):233503, 2006.

[102] Ross Ulbricht, Sergey B Lee, Xiaomei Jiang, Kanzan Inoue, Mei Zhang, Shaoli Fang, Ray H Baughman, and Anvar A Zakhidov. Transparent carbon nanotube sheets as 3-d charge collectors in organic solar cells. *Solar Energy Materials and Solar Cells*, 91(5):416–419, 2007.

[103] Hongwei Zhu, Jinquan Wei, Kunlin Wang, and Dehai Wu. Applications of carbon materials in photovoltaic solar cells. *Solar Energy Materials and Solar Cells*, 93(9):1461–1470, 2009.

[104] Zhibin Yang, Tao Chen, Ruixuan He, Guozhen Guan, Houpu Li, Longbin Qiu, and Huisheng Peng. Aligned carbon nanotube sheets for the electrodes of organic solar cells. *Advanced Materials*, 23(45):5436–5439, 2011.

[105] Jianxin Geng and Tingying Zeng. Influence of single-walled carbon nanotubes induced crystallinity enhancement and morphology change on polymer photovoltaic devices. *Journal of the American Chemical Society*, 128(51):16827–16833, 2006.

[106] Cheng Li, Yuhong Chen, Yubing Wang, Zafar Iqbal, Manish Chhowalla, and Somenath Mitra. A fullerene–single wall carbon nanotube complex for polymer bulk heterojunction photovoltaic cells. *Journal of Materials Chemistry*, 17(23):2406–2411, 2007.

[107] Shenqiang Ren, Marco Bernardi, Richard R Lunt, Vladimir Bulovic, Jeffrey C Grossman, and Silvija Gradecak. Toward efficient carbon nanotube/p3ht solar cells: Active layer morphology, electrical, and optical properties. *Nano letters*, 11(12):5316–5321, 2011.

[108] Vincent C Tung, Jen-Hsien Huang, Jaemyung Kim, Alexander J Smith, Chih-Wei Chu, and Jiaxing Huang. Towards solution processed all-carbon solar cells: a perspective. *Energy & Environmental Science*, 5(7):7810–7818, 2012.

[109] Michael S Arnold, Jeramy D Zimmerman, Christopher K Renshaw, Xin Xu, Richard R Lunt, Christine M Austin, and Stephen R Forrest. Broad spectral response using carbon nanotube/organic semiconductor/c60 photodetectors. *Nano letters*, 9(9):3354–3358, 2009.

[110] Rishabh M Jain, Rachel Howden, Kevin Tvrdy, Steven Shimizu, Andrew J Hilmer, Thomas P McNicholas, Karen K Gleason, and Michael S Strano. Polymer-free near-infrared photovoltaics with single chirality (6, 5) semiconducting carbon nanotube active layers. *Advanced Materials*, 24(32):4436–4439, 2012.

[111] Marc P Ramuz, Michael Vosgueritchian, Peng Wei, Chenggong Wang, Yongli Gao, Yingpeng Wu, Yongsheng Chen, and Zhenan Bao. Evaluation of solution-processable carbon-based electrodes for all-carbon solar cells. *ACS nano*, 6(11):10384–10395, 2012.

[112] Maogang Gong, Tejas A Shastry, Yu Xie, Marco Bernardi, Daniel Jasion, Kyle A Luck, Tobin J Marks, Jeffrey C Grossman, Shenqiang Ren, and Mark C Hersam. Polychiral semiconducting carbon nanotube–fullerene solar cells. *Nano letters*, 14(9):5308–5314, 2014.

[113] Kostya S Novoselov, Andre K Geim, Sergei V Morozov, D Jiang, Y_ Zhang, Sergey V Dubonos, Irina V Grigorieva, and Alexandr A Firsov. Electric field effect in atomically thin carbon films. *science*, 306(5696):666–669, 2004.

[114] KS Novoselov, D Jiang, F Schedin, TJ Booth, VV Khotkevich, SV Morozov, and AK Geim. Two-dimensional atomic crystals. *Proceedings of the National Academy of Sciences of the United States of America*, 102(30):10451–10453, 2005.

[115] Andre Konstantin Geim. Graphene: status and prospects. *science*, 324(5934):1530–1534, 2009.

[116] Abhay Shukla, Rakesh Kumar, Javed Mazher, and Adrian Balan. Graphene made easy: High quality, large-area samples. *Solid State Communications*, 149(17):718–721, 2009.

[117] Thomas Moldt, Axel Eckmann, Philipp Klar, Sergey V Morozov, Alexander A Zhukov, Kostya S Novoselov, and Cinzia Casiraghi. High-yield production and transfer of graphene flakes obtained by anodic bonding. *Acs Nano*, 5(10):7700–7706, 2011.

[118] Yoshiyuki Miyamoto, Hong Zhang, and David Tománek. Photoexfoliation of graphene from graphite: an ab initio study. *Physical review letters*, 104(20):208302, 2010.

[119] S Dhar, A Roy Barman, GX Ni, X Wang, XF Xu, Y Zheng, S Tripathy, Ariando, A Rusydi, KP Loh, et al. A new route to graphene layers by selective laser ablation. *Aip Advances*, 1(2):022109, 2011.

[120] Francesco Bonaccorso, Antonio Lombardo, Tawfique Hasan, Zhipei Sun, Luigi Colombo, and Andrea C Ferrari. Production and processing of graphene and 2d crystals. *Materials today*, 15(12):564–589, 2012.

[121] William S Hummers Jr and Richard E Offeman. Preparation of graphitic oxide. *Journal of the American Chemical Society*, 80(6):1339–1339, 1958.

[122] Yanfei Xu, Guankui Long, Lu Huang, Yi Huang, Xiangjian Wan, Yanfeng Ma, and Yongsheng Chen. Polymer photovoltaic devices with transparent graphene electrodes produced by spin-casting. *Carbon*, 48(11):3308–3311, 2010.

[123] Xuan Wang, Linjie Zhi, Nok Tsao, Željko Tomović, Jiaoli Li, and Klaus Müllen. Transparent carbon films as electrodes in organic solar cells. *Angewandte Chemie International Edition*, 47(16):2990–2992, 2008.

[124] Qian Zhang, Xiangjian Wan, Fei Xing, Lu Huang, Guankui Long, Ningbo Yi, Wang Ni, Zhibo Liu, Jianguo Tian, and Yongsheng Chen. Solution-processable graphene mesh transparent electrodes for organic solar cells. *Nano Research*, 6(7):478–484, 2013.

[125] Dimitrios Konios, Constantinos Petridis, George Kakavelakis, Maria Sygletou, Kyriaki Savva, Emmanuel Stratakis, and Emmanuel Kymakis. Reduced graphene oxide micromesh electrodes for large area, flexible, organic photovoltaic devices. *Advanced Functional Materials*, 25(15):2213–2221, 2015.

[126] Zhiyong Liu, Dawei He, Yongsheng Wang, Hongpeng Wu, and Jigang Wang. Solution-processable functionalized graphene in donor/acceptor-type organic photovoltaic cells. *Solar Energy Materials and Solar Cells*, 94(7):1196–1200, 2010.

[127] Dingshan Yu, Kyusoon Park, Michael Durstock, and Liming Dai. Fullerene-grafted graphene for efficient bulk heterojunction polymer photovoltaic devices. *The journal of physical chemistry letters*, 2(10):1113–1118, 2011.

[128] T Kim, JH Kang, SJ Yang, SJ Sung, YS Kim, and CR Park. Facile preparation of reduced graphene oxide-based gas barrier films for organic photovoltaic devices. *Energy & Environmental Science*, 7(10):3403–3411, 2014.

[129] Héctor A Becerril, Jie Mao, Zunfeng Liu, Randall M Stoltenberg, Zhenan Bao, and Yongsheng Chen. Evaluation of solution-processed reduced graphene oxide films as transparent conductors. *ACS nano*, 2(3):463–470, 2008.

[130] Cecilia Mattevi, Goki Eda, Stefano Agnoli, Steve Miller, K Andre Mkhoyan, Ozgur Celik, Daniel Mastrogiovanni, Gaetano Granozzi, Eric Garfunkel, and Manish Chhowalla. Evolution of electrical, chemical, and structural properties of transparent and conducting chemically derived graphene thin films. *Advanced Functional Materials*, 19(16):2577–2583, 2009.

[131] Anupama B Kaul. Two-dimensional layered materials: Structure, properties, and prospects for device applications. *Journal of Materials Research*, 29(3):348–361, 2014.

[132] Cristina Gómez-Navarro, R Thomas Weitz, Alexander M Bittner, Matteo Scolari, Alf Mews, Marko Burghard, and Klaus Kern. Electronic transport properties of individual chemically reduced graphene oxide sheets. *Nano letters*, 7(11):3499–3503, 2007.

[133] Lewis Gomez De Arco, Yi Zhang, Cody W Schlenker, Koungmin Ryu, Mark E Thompson, and Chongwu Zhou. Continuous, highly flexible, and transparent graphene films by chemical vapor deposition for organic photovoltaics. *ACS nano*, 4(5):2865–2873, 2010.

[134] J Clayden, N Greeves, and S Warren. Organic chemistry. 2nd, 2012.

[135] Li Li Zhang and XS Zhao. Carbon-based materials as supercapacitor electrodes. *Chemical Society Reviews*, 38(9):2520–2531, 2009.

[136] Jean-Christophe Charlier, Xavier Blase, and Stephan Roche. Electronic and transport properties of nanotubes. *Reviews of modern physics*, 79(2):677, 2007.

[137] Junbo Wu, Mukul Agrawal, Héctor A Becerril, Zhenan Bao, Zunfeng Liu, Yongsheng Chen, and Peter Peumans. Organic light-emitting diodes on solution-processed graphene transparent electrodes. *ACS nano*, 4(1):43–48, 2009.

[138] Sagar Sarkar and Priya Mahadevan. Role of the a-site cation in determining the properties of the hybrid perovskite ch 3 nh 3 pbbr 3. *Physical Review B*, 95(21):214118, 2017.

[139] Bayrammurad Saparov and David B Mitzi. Organic–inorganic perovskites: structural versatility for functional materials design. *Chemical reviews*, 116(7):4558–4596, 2016.

[140] Oscar Grånäs, Dmitry Vinichenko, and Efthimios Kaxiras. Establishing the limits of efficiency of perovskite solar cells from first principles modeling. *Scientific reports*, 6:36108, 2016.

[141] T Umebayashi, K Asai, T Kondo, and A Nakao. Electronic structures of lead iodide based low-dimensional crystals. *Physical Review B*, 67(15):155405, 2003.

[142] Federico Brivio, Keith T Butler, Aron Walsh, and Mark Van Schilfgaarde. Relativistic quasiparticle self-consistent electronic structure of hybrid halide perovskite photovoltaic absorbers. *Physical Review B*, 89(15):155204, 2014.

[143] Reference Air Mass 1.5 Spectra nrel. https://www.nrel.gov/grid/solar-resource/spectra-am1.5.html. Accessed: 2018-09-25.

[144] Mathias Schubert, Philipp Kühne, Vanya Darakchieva, and Tino Hofmann. Optical hall effect—model description: tutorial. *JOSA A*, 33(8):1553–1568, 2016.

[145] JR Connolly. Diffraction basics, part 2. *Introduction to X-Ray Powder Diffraction*, 2012.

[146] K Norrman, A Ghanbari-Siahkali, and NB Larsen. 6 studies of spin-coated polymer films. *Annual Reports Section" C"(Physical Chemistry)*, 101:174–201, 2005.

[147] Spin Coating. A guide to theory and techniques,[online] dostupné z: https://www.ossila. com/pages/spin-coating [7] a. buckley et al. *Organic Light-Emitting Diodes (OLEDs): Materials, Devices and Applications*, 2013.

[148] Elisabetta Arca, Karsten Fleischer, and Igor Shvets. Tuning the crystallographic, morphological, optical and electrical properties of zno: Al grown by spray pyrolysis. *Thin Solid Films*, 555:9–12, 2014.

[149] KO Ukoba, AC Eloka-Eboka, and FL Inambao. Review of nanostructured nio thin film deposition using the spray pyrolysis technique. *Renewable and Sustainable Energy Reviews*, 2017.

[150] D Ali, MZ Butt, C Coughlan, D Caffrey, IV Shvets, and K Fleischer. Nitrogen grain-boundary passivation of in-doped zno transparent conducting oxide. *Physical Review Materials*, 2(4):043402, 2018.

[151] Mohammad-Mehdi Bagheri-Mohagheghi and Mehrdad Shokooh-Saremi. Electrical, optical and structural properties of li-doped sno2 transparent conducting films deposited by the spray pyrolysis technique: a carrier-type conversion study. *Semiconductor science and technology*, 19(6):764, 2004.

[152] Eric A Meulenkamp. Synthesis and growth of zno nanoparticles. *The Journal of Physical Chemistry B*, 102(29):5566–5572, 1998.

[153] Xiaohui Ju, Wei Feng, Xuequan Zhang, Varutt Kittichungchit, Tetsuro Hori, Hiroki Moritou, Akihiko Fujii, and Masanori Ozaki. Fabrication of organic photovoltaic cells with double-layer zno structure. *Solar Energy Materials and Solar Cells*, 93(9):1562–1567, 2009.

[154] Michael Hartel, Song Chen, Benjamin Swerdlow, Hsien-Yi Hsu, Jesse Manders, Kirk Schanze, and Franky So. Defect-induced loss mechanisms in polymer–inorganic planar heterojunction solar cells. *ACS applied materials & interfaces*, 5(15):7215–7218, 2013.

[155] Aleksandra B Djurišić, Xiang Liu, and Yu Hang Leung. Zinc oxide films and nanomaterials for photovoltaic applications. *physica status solidi (RRL)-Rapid Research Letters*, 8(2):123–132, 2014.

[156] Yulia Galagan, Henri Fledderus, Harrie Gorter, Hero H t Mannetje, Santhosh Shanmugam, Rajesh Mandamparambil, Johan Bosman, Jan-Eric JM Rubingh, Jean-Pierre Teunissen, Ahmed Salem, et al. Roll-to-roll slot–die coated organic photovoltaic (opv) modules with high geometrical fill factors. *Energy Technology*, 3(8):834–842, 2015.

[157] Dou Li, Wenjing Qin, Shengchen Zhang, Dongyue Liu, Zhenyang Yu, Jing Mao, Linfeng Wu, Liying Yang, and Shougen Yin. Effect of uv-ozone process on the zno interlayer in the inverted organic solar cells. *RSC Advances*, 7(10):6040–6045, 2017.

[158] Jian Wang, Liang Xu, Bo Zhang, Yun-Ju Lee, and Julia WP Hsu. n-type doping induced by electron transport layer in organic photovoltaic devices. *Advanced Electronic Materials*, 3(2), 2017.

[159] Zong-Liang Tseng, Chien-Hung Chiang, and Chun-Guey Wu. Surface engineering of zno thin film for high efficiency planar perovskite solar cells. *Scientific reports*, 5:13211, 2015.

[160] Warda Hadouchi, Jean Rousset, Denis Tondelier, Bernard Geffroy, and Yvan Bonnassieux. Zinc oxide as a hole blocking layer for perovskite solar cells deposited in atmospheric conditions. *RSC Advances*, 6(72):67715–67723, 2016.

[161] Juan Dong, Yanhong Zhao, Jiangjian Shi, Huiyun Wei, Junyan Xiao, Xin Xu, Jianheng Luo, Jing Xu, Dongmei Li, Yanhong Luo, et al. Impressive enhancement in the cell performance of zno nanorod-based perovskite solar cells with al-doped zno interfacial modification. *Chemical Communications*, 50(87):13381–13384, 2014.

[162] Mulmudi Hemant Kumar, Natalia Yantara, Sabba Dharani, Michael Graetzel, Subodh Mhaisalkar, Pablo P Boix, and Nripan Mathews. Flexible, low-temperature, solution processed zno-based perovskite solid state solar cells. *Chemical Communications*, 49(94):11089–11091, 2013.

[163] Dae-Yong Son, Jeong-Hyeok Im, Hui-Seon Kim, and Nam-Gyu Park. 11% efficient perovskite solar cell based on zno nanorods: an effective charge collection system. *The Journal of Physical Chemistry C*, 118(30):16567–16573, 2014.

[164] Naoyuki Shibayama, Hiroyuki Kanda, Shin-ichi Yusa, Shota Fukumoto, Ajay K Baranwal, Hiroshi Segawa, Tsutomu Miyasaka, and Seigo Ito. All-inorganic inverse perovskite solar cells using zinc oxide nanocolloids on spin coated perovskite layer. *Nano convergence*, 4(1):18, 2017.

[165] Waldo JE Beek, Martijn M Wienk, Martijn Kemerink, Xiaoniu Yang, and René AJ Janssen. Hybrid zinc oxide conjugated polymer bulk heterojunction solar cells. *The Journal of Physical Chemistry B*, 109(19):9505–9516, 2005.

[166] Dianyi Liu and Timothy L Kelly. Perovskite solar cells with a planar heterojunction structure prepared using room-temperature solution processing techniques. *Nature photonics*, 8(2):133, 2014.

[167] Yuanhang Cheng, Qing-Dan Yang, Jingyang Xiao, Qifan Xue, Ho-Wa Li, Zhiqiang Guan, Hin-Lap Yip, and Sai-Wing Tsang. Decomposition of organometal halide perovskite films on zinc oxide nanoparticles. *ACS applied materials & interfaces*, 7(36):19986–19993, 2015.

[168] Weihai Zhang, Juan Xiong, Li Jiang, Jianying Wang, Tao Mei, Xianbao Wang, Haoshuang Gu, Walid A Daoud, and Jinhua Li. Thermal stability-enhanced and high-efficiency planar perovskite solar cells with interface passivation. *ACS applied materials & interfaces*, 9(44):38467–38476, 2017.

[169] U Koch, A Fojtik, H Weller, and A Henglein. Photochemistry of semiconductor colloids. preparation of extremely small zno particles, fluorescence phenomena and size quantization effects. *Chemical Physics Letters*, 122(5):507–510, 1985.

[170] C Roldan-Carmona, P Gratia, I Zimmermann, G Grancini, P Gao, Michael Graetzel, and Mohammad Khaja Nazeeruddin. High efficiency methylammonium lead triiodide perovskite solar cells: the relevance of non-stoichiometric precursors. *Energy & Environmental Science*, 8(12):3550–3556, 2015.

[171] T Jesper Jacobsson, Juan-Pablo Correa-Baena, Meysam Pazoki, Michael Saliba, Kurt Schenk, Michael Grätzel, and Anders Hagfeldt. Exploration of the compositional space for mixed lead halogen perovskites for high efficiency solar cells. *Energy & Environmental Science*, 9(5):1706–1724, 2016.

[172] Dongqin Bi, Wolfgang Tress, M Ibrahim Dar, Peng Gao, Jingshan Luo, Clémentine Renevier, Kurt Schenk, Antonio Abate, Fabrizio Giordano, Juan-Pablo Correa Baena, et al. Efficient luminescent solar cells based on tailored mixed-cation perovskites. *Science advances*, 2(1):e1501170, 2016.

[173] Cheol Hyoun Ahn, Young Yi Kim, Dong Chan Kim, Sanjay Kumar Mohanta, and Hyung Koun Cho. A comparative analysis of deep level emission in zno layers deposited by various methods. *Journal of Applied Physics*, 105(1):013502, 2009.

[174] Jinli Yang, Braden D Siempelkamp, Edoardo Mosconi, Filippo De Angelis, and Timothy L Kelly. Origin of the thermal instability in ch3nh3pbi3 thin films deposited on zno. *Chemistry of Materials*, 27(12):4229–4236, 2015.

[175] J McK Nobbs and FC Gillespie. Properties of thin films of zinc oxide prepared by a chemical spray method. *Journal of Physics and Chemistry of Solids*, 31(10):2353–2359, 1970.

[176] JC Manifacier, JP Fillard, and JM Bind. Deposition of in2o3 sno2 layers on glass substrates using a spraying method. *Thin solid films*, 77(1-3):67–80, 1981.

[177] MS Tomar and FJ Garcia. A zno/p-cuinse2 thin film solar cell prepared entirely by spray pyrolysis. *Thin Solid Films*, 90(4):419–423, 1982.

[178] V Vasu and A Subrahmanyam. Electrical and optical properties of pyrolytically sprayed sno2 film—dependence on substrate temperature and substrate-nozzle distance. *Thin Solid Films*, 189(2):217–225, 1990.

[179] AF Aktaruzzaman, GL Sharma, and LK Malhotra. Electrical, optical and annealing characteristics of zno: Al films prepared by spray pyrolysis. *Thin solid films*, 198(1-2):67–74, 1991.

[180] A Crossay, S Buecheler, L Kranz, J Perrenoud, CM Fella, YE Romanyuk, and AN Tiwari. Spray-deposited al-doped zno transparent contacts for cdte solar cells. *Solar Energy Materials and Solar Cells*, 101:283–288, 2012.

[181] AU Ubale and YS Sakhare. Growth of nanocrystalline mgse thin films by spray pyrolysis. *Vacuum*, 99:124–126, 2014.

[182] Dianyi Liu, Jinli Yang, and Timothy L Kelly. Compact layer free perovskite solar cells with 13.5% efficiency. *Journal of the American Chemical Society*, 136(49):17116–17122, 2014.

[183] Seong Sik Shin, Woon Seok Yang, Jun Hong Noh, Jae Ho Suk, Nam Joong Jeon, Jong Hoon Park, Ju Seong Kim, Won Mo Seong, and Sang Il Seok. High-performance flexible perovskite solar cells exploiting zn 2 sno 4 prepared in solution below 100 c. *Nature communications*, 6:7410, 2015.

[184] Martin Kaltenbrunner, Getachew Adam, Eric Daniel Głowacki, Michael Drack, Reinhard Schwödiauer, Lucia Leonat, Dogukan Hazar Apaydin, Heiko Groiss, Markus Clark Scharber, Matthew Schuette White, et al. Flexible high power-per-weight perovskite solar cells with chromium oxide–metal contacts for improved stability in air. *Nature materials*, 14(10):1032, 2015.

[185] Like Huang, Jie Xu, Xiaoxiang Sun, Yangyang Du, Hongkun Cai, Jian Ni, Juan Li, Ziyang Hu, and Jianjun Zhang. Toward revealing the critical role of perovskite coverage in highly efficient electron-transport layer-free perovskite solar cells: an energy band and equivalent circuit model perspective. *ACS applied materials & interfaces*, 8(15):9811–9820, 2016.

[186] Xingyue Zhao, Heping Shen, Ye Zhang, Xin Li, Xiaochong Zhao, Meiqian Tai, Jingfeng Li, Jianbao Li, Xin Li, and Hong Lin. Aluminum-doped zinc oxide as highly stable electron collection layer for perovskite solar cells. *ACS applied materials & interfaces*, 8(12):7826–7833, 2016.

[187] Li Deng, Jiale Xie, Baohua Wang, Tao Chen, and Chang Ming Li. Chlorinated fluorine doped tin oxide electrodes with high work function for highly efficient planar perovskite solar cells. *Applied Physics Letters*, 110(26):263901, 2017.

[188] A Baltakesmez, M Biber, and S Tüzemen. Inverted planar perovskite solar cells based on al doped zno substrate. *Journal of radiation research and applied sciences*, 11(2):124–129, 2018.

[189] Yaoguang Rong, Yue Hu, Sandheep Ravishankar, Huawei Liu, Xiaomeng Hou, Yusong Sheng, Anyi Mei, Qifei Wang, Daiyu Li, Mi Xu, et al. Tunable hysteresis effect for perovskite solar cells. *Energy & Environmental Science*, 10(11):2383–2391, 2017.

[190] Yan Li, Bin Ding, Qian-Qian Chu, Guan-Jun Yang, Mingkui Wang, Chang-Xin Li, and Chang-Jiu Li. Ultra-high open-circuit voltage of perovskite solar cells induced by nucleation thermodynamics on rough substrates. *Scientific reports*, 7:46141, 2017.

[191] Indium Tin Oxide indium corporation. http://www.indium.com/inorganic-compounds/indium-compounds/indium-tin-oxide/. Accessed: 2018-09-16.

[192] Jian Du, Xin-liang Chen, Cai-chi Liu, Jian Ni, Guo-fu Hou, Ying Zhao, and Xiaodan Zhang. Highly transparent and conductive indium tin oxide thin films for solar cells grown by reactive thermal evaporation at low temperature. *Applied Physics A*, 117(2):815–822, 2014.

[193] Weijun Ke, Guojia Fang, Jing Wang, Pingli Qin, Hong Tao, Hongwei Lei, Qin Liu, Xin Dai, and Xingzhong Zhao. Perovskite solar cell with an efficient tio2 compact film. *ACS applied materials & interfaces*, 6(18):15959–15965, 2014.

[194] Sawanta S Mali, Chang Kook Hong, AI Inamdar, Hyunsik Im, and Sang Eun Shim. Efficient planar nip type heterojunction flexible perovskite solar cells with sputtered tio2 electron transporting layers. *Nanoscale*, 9(9):3095–3104, 2017.

[195] Atsushi Kogo, Shinichi Iwasaki, Masashi Ikegami, and Tsutomu Miyasaka. An ultrathin sputtered tio2 compact layer for mesoporous brookite-based plastic ch3nh3pbi3-x cl x solar cells. *Chemistry Letters*, 46(4):530–532, 2017.

[196] Reiner Kukla. Magnetron sputtering on large scale substrates: an overview on the state of the art. *Surface and Coatings Technology*, 93(1):1–6, 1997.

[197] Konstanty Marszalek. *LARGE AREA DEPOSITION SPUTTERING COATERS*, pages 44–54. 01 2014.

[198] Anja Blondeel, Peter Persoone, and Wilmert De Bosscher. Rotatable magnetron sputter technologyfor large area glass and web coating. *Vakuum in Forschung und Praxis*, 21(3):6–13, 2009.

[199] Michael A Henderson, William S Epling, Charles HF Peden, and Craig L Perkins. Insights into photoexcited electron scavenging processes on tio2 obtained from studies of the reaction of o2 with oh groups adsorbed at electronic defects on tio2 (110). *The Journal of Physical Chemistry B*, 107(2):534–545, 2003.

[200] Andrew G Scheuermann, Jonathan D Prange, Marika Gunji, Christopher ED Chidsey, and Paul C McIntyre. Effects of catalyst material and atomic layer deposited tio 2 oxide thickness on the water oxidation performance of metal–insulator–silicon anodes. *Energy & Environmental Science*, 6(8):2487–2496, 2013.

[201] A Baker, M Saltik, H Lehrmann, I Killisch, V Mautner, G Lamm, G Christofori, and M Cotten. Polyethylenimine (pei) is a simple, inexpensive and effective reagent for condensing and linking plasmid dna to adenovirus for gene delivery. *Gene therapy*, 4(8):773, 1997.

[202] Sigma-Aldrich. Polyethylenimine, branched, 2018.

[203] Enrico Andreoli, Eoghan P Dillon, Laurie Cullum, Lawrence B Alemany, and Andrew R Barron. Cross-linking amine-rich compounds into high performing selective co 2 absorbents. *Scientific reports*, 4:7304, 2014.

[204] Yinhua Zhou, Canek Fuentes-Hernandez, Jaewon Shim, Jens Meyer, Anthony J Giordano, Hong Li, Paul Winget, Theodoros Papadopoulos, Hyeunseok Cheun, Jungbae Kim, et al. A universal method to produce low–work function electrodes for organic electronics. *Science*, 336(6079):327–332, 2012.

[205] Sujuan Dong, Yangyang Wan, Yaling Wang, Yin Yang, Yahui Wang, Xinyu Zhang, Huanqi Cao, Wenjing Qin, Liying Yang, Cong Yao, et al. Polyethylenimine as a dual functional additive for electron transporting layer in efficient solution processed planar heterojunction perovskite solar cells. *RSC Advances*, 6(63):57793–57798, 2016.

[206] Pengwei Li, Chao Liang, Yiqiang Zhang, Fengyu Li, Yanlin Song, and Guosheng Shao. Polyethyleneimine high-energy hydrophilic surface interfacial treatment toward efficient and stable perovskite solar cells. *ACS applied materials & interfaces*, 8(47):32574–32580, 2016.

[207] Yasemin Udum, Patrick Denk, Getachew Adam, Dogukan H Apaydin, Andreas Nevosad, Christian Teichert, Matthew S White, Niyazi S Sariciftci, and Markus C Scharber. Inverted bulk-heterojunction solar cell with cross-linked hole-blocking layer. *Organic electronics*, 15(5):997–1001, 2014.

[208] Ting Wu, Liam Collins, Jia Zhang, Pei-Ying Lin, Mahshid Ahmadi, Stephen Jesse, and Bin Hu. Photoinduced bulk polarization and its effects on photovoltaic actions in perovskite solar cells. *ACS nano*, 11(11):11542–11549, 2017.

[209] Satyaprasad P Senanayak, Bingyan Yang, Tudor H Thomas, Nadja Giesbrecht, Wenchao Huang, Eliot Gann, Bhaskaran Nair, Karl Goedel, Suchi Guha, Xavier Moya, et al. Understanding charge transport in lead iodide perovskite thin-film field-effect transistors. *Science Advances*, 3(1):e1601935, 2017.

[210] Daehee Seol, Gill Sang Han, Changdeuck Bae, Hyunjung Shin, Hyun Suk Jung, and Yunseok Kim. Screening effect on photovoltaic performance in ferroelectric ch 3 nh 3 pbi 3 perovskite thin films. *Journal of Materials Chemistry A*, 3(40):20352–20358, 2015.

[211] Jaewon Ha, Hoyeon Kim, Hyunwoo Lee, Kyung-Geun Lim, Tae-Woo Lee, and Seunghyup Yoo. Device architecture for efficient, low-hysteresis flexible perovskite solar cells: Replacing tio2 with c60 assisted by polyethylenimine ethoxylated interfacial layers. *Solar Energy Materials and Solar Cells*, 161:338–346, 2017.

[212] Aleksandra Djurišić, Fangzhou Liu, and Ho Won Tam. Improving the performance of zno-based perovskite solar cells. 01 2017.

[213] Jingbi You, Lei Meng, Tze-Bin Song, Tzung-Fang Guo, Yang Michael Yang, Wei-Hsuan Chang, Ziruo Hong, Huajun Chen, Huanping Zhou, Qi Chen, et al. Improved air stability of perovskite solar cells via solution-processed metal oxide transport layers. *Nature nanotechnology*, 11(1):75, 2016.

[214] Zong-Liang Tseng, Chien-Hung Chiang, Sheng-Hsiung Chang, and Chun-Guey Wu. Surface engineering of zno electron transporting layer via al doping for high efficiency planar perovskite solar cells. *Nano Energy*, 28:311–318, 2016.

[215] Putao Zhang, Fu Yang, Gaurav Kapil, Qing Shen, Taro Toyoda, Kenji Yoshino, Takashi Minemoto, Shyam S Pandey, Tingli Ma, and Shuzi Hayase. Enhanced performance of zno based perovskite solar cells by nb2o5 surface passivation. *Organic Electronics*, 2018.

[216] Min Tu, Hayder A Abbood, Zhening Zhu, Hailing Li, and Zhonghong Gao. Investigation of the photocatalytic effect of zinc oxide nanoparticles in the presence of nitrite. *Journal of hazardous materials*, 244:311–321, 2013.

[217] NikAthirah Yusoff, Li-Ngee Ho, Soon-An Ong, Yee-Shian Wong, and WanFadhilah Khalik. Photocatalytic activity of zinc oxide (zno) synthesized through different methods. *Desalination and Water Treatment*, 57(27):12496–12507, 2016.

[218] Peng Zhang, Jiang Wu, Yafei Wang, Hojjatollah Sarvari, Detao Liu, Zhi David Chen, and Shibin Li. Enhanced efficiency and environmental stability of planar perovskite solar cells by suppressing photocatalytic decomposition. *Journal of Materials Chemistry A*, 5(33):17368–17378, 2017.

[219] Shibin Li, Peng Zhang, Hao Chen, Yafei Wang, Detao Liu, Jiang Wu, Hojjatollah Sarvari, and Zhi David Chen. Mesoporous pbi2 assisted growth of large perovskite grains for efficient perovskite solar cells based on zno nanorods. *Journal of Power Sources*, 342:990–997, 2017.

[220] Zhu-Yin Sui, Yi Cui, Jian-Hua Zhu, and Bao-Hang Han. Preparation of three-dimensional graphene oxide–polyethylenimine porous materials as dye and gas adsorbents. *ACS applied materials & interfaces*, 5(18):9172–9179, 2013.

[221] Liang Yan, Ya-Nan Chang, Lina Zhao, Zhanjun Gu, Xiaoxiao Liu, Gan Tian, Liangjun Zhou, Wenlu Ren, Shan Jin, Wenyan Yin, et al. The use of polyethylenimine-modified graphene oxide as a nanocarrier for transferring hydrophobic nanocrystals into water to produce water-dispersible hybrids for use in drug delivery. *Carbon*, 57:120–129, 2013.

[222] Hongyu Liu, Tapas Kuila, Nam Hoon Kim, Bon-Cheol Ku, and Joong Hee Lee. In situ synthesis of the reduced graphene oxide–polyethyleneimine composite and its gas barrier properties. *Journal of materials chemistry a*, 1(11):3739–3746, 2013.

[223] Minwoo Park, Joon-Suh Park, Il Ki Han, and Jin Young Oh. High-performance flexible and air-stable perovskite solar cells with a large active area based on poly (3-hexylthiophene) nanofibrils. *Journal of Materials Chemistry A*, 4(29):11307–11316, 2016.

[224] Jeongmo Kim, Heeryung Lee, Seung Joo Lee, Wilson Jose da Silva, Abd Rashid bin Mohd Yusoff, and Jin Jang. Graphene oxide grafted polyethylenimine electron transport materials for highly efficient organic devices. *Journal of Materials Chemistry A*, 3(44):22035–22042, 2015.

[225] Muge Acik and Seth B Darling. Graphene in perovskite solar cells: device design, characterization and implementation. *Journal of Materials Chemistry A*, 4(17):6185–6235, 2016.

[226] Johann Bouclé and Nathalie Herlin-Boime. The benefits of graphene for hybrid perovskite solar cells. *Synthetic Metals*, 222:3–16, 2016.

[227] Solar Applications of Graphene cheap tubes. https://www.cheaptubes.com/solar-applications-of-graphene/. Accessed: 2018-09-20.

[228] Eng Liang Lim, Chi Chin Yap, Mohammad Hafizuddin Hj Jumali, Mohd Asri Mat Teridi, and Chin Hoong Teh. A mini review: Can graphene be a novel material for perovskite solar cell applications? *Nano-Micro Letters*, 10(2):27, 2018.

[229] Charles M Hansen. *Hansen solubility parameters: a user's handbook*. CRC press, 2002.

[230] Yenny Hernandez, Mustafa Lotya, David Rickard, Shane D Bergin, and Jonathan N Coleman. Measurement of multicomponent solubility parameters for graphene facilitates solvent discovery. *Langmuir*, 26(5):3208–3213, 2009.

[231] Luigi-Jules Vandi, Meng Hou, Martin Veidt, R Truss, M Heitzmann, and R Paton. Interface diffusion and morphology of aerospace grade epoxy co-cured with thermoplastic polymers. In *28th International Congress of the Aeronautical Sciences (ICAS), Brisbane, Australia, Sept*, pages 23–28, 2012.

[232] Mustafa Lotya, Paul J King, Umar Khan, Sukanta De, and Jonathan N Coleman. High-concentration, surfactant-stabilized graphene dispersions. *ACS nano*, 4(6):3155–3162, 2010.

[233] Keith R Paton and Jonathan N Coleman. Relating the optical absorption coefficient of nanosheet dispersions to the intrinsic monolayer absorption. *Carbon*, 107:733–738, 2016.

[234] Yuanyuan Zhou, Mengjin Yang, Wenwen Wu, Alexander L Vasiliev, Kai Zhu, and Nitin P Padture. Room-temperature crystallization of hybrid-perovskite thin films via solvent–solvent extraction for high-performance solar cells. *Journal of Materials Chemistry A*, 3(15):8178–8184, 2015.

[235] Albrecht Poglitsch and Daniel Weber. Dynamic disorder in methylammoniumtrihalogenoplumbates (ii) observed by millimeter-wave spectroscopy. *The Journal of chemical physics*, 87(11):6373–6378, 1987.

[236] Chin-Tsar Hsu. Variation with composition of the properties in znsxse1- x. *Journal of crystal growth*, 193(1-2):33–38, 1998.

[237] Min Wang, Guang Tao Fei, Yu Gang Zhang, Ming Guang Kong, and LD Zhang. Tunable and predetermined bandgap emissions in alloyed znsxse1–x nanowires. *Advanced Materials*, 19(24):4491–4494, 2007.

[238] Horst Hartmann, Regina Mach, and Burkhardt Selle. *Wide gap II-VI compounds as electronic materials*. Akad. d. Wiss. d. DDR, Zentralinst. für Elektronenphysik, 1982.

[239] Daniel J Slotcavage, Hemamala I Karunadasa, and Michael D McGehee. Light-induced phase segregation in halide-perovskite absorbers. *ACS Energy Letters*, 1(6):1199–1205, 2016.

[240] Giulia Longo, Cristina Momblona, Maria-Grazia La-Placa, Lidón Gil-Escrig, Michele Sessolo, and Henk J Bolink. Fully vacuum-processed wide band gap mixed-halide perovskite solar cells. *ACS Energy Letters*, 3(1):214–219, 2018.

[241] Eric T Hoke, Daniel J Slotcavage, Emma R Dohner, Andrea R Bowring, Hemamala I Karunadasa, and Michael D McGehee. Reversible photo-induced trap formation in mixed-halide hybrid perovskites for photovoltaics. *Chemical Science*, 6(1):613–617, 2015.

[242] Alex J Barker, Aditya Sadhanala, Felix Deschler, Marina Gandini, Satyaprasad P Senanayak, Phoebe M Pearce, Edoardo Mosconi, Andrew J Pearson, Yue Wu, Ajay Ram Srimath Kandada, et al. Defect-assisted photoinduced halide segregation in mixed-halide perovskite thin films. *ACS Energy Letters*, 2(6):1416–1424, 2017.

[243] Jin Hyuck Heo, Dae Ho Song, and Sang Hyuk Im. Planar ch3nh3pbbr3 hybrid solar cells with 10.4% power conversion efficiency, fabricated by controlled crystallization in the spin-coating process. *Advanced Materials*, 26(48):8179–8183, 2014.

[244] Gerado L Araujo, Andres Cuevas, and Jose M Ruiz. The effect of distributed series resistance on the dark and illuminated current—voltage characteristics of solar cells. *IEEE Transactions on Electron Devices*, 33(3):391–401, 1986.

[245] J Appelbaum, A Chait, and D Thompson. Parameter estimation and screening of solar cells. *Progress in Photovoltaics: Research and Applications*, 1(2):93–106, 1993.

[246] Jürgen Carstensen, Alireza Abdollahinia, Andreas Schütt, and Helmut Föll. Characterization of the grid design by fitting of the distributed serial grid resistance to cello resistance maps and global iv curves. In *Proc. 24th European Photovoltaic Solar Energy Conference*, 2009.

[247] Jingbi You, Yang Yang, Ziruo Hong, Tze-Bin Song, Lei Meng, Yongsheng Liu, Chengyang Jiang, Huanping Zhou, Wei-Hsuan Chang, Gang Li, et al. Moisture assisted perovskite film growth for high performance solar cells. *Applied Physics Letters*, 105(18):183902, 2014.

[248] Peizhe Liao, Xiaojuan Zhao, Guolong Li, Yan Shen, and Mingkui Wang. A new method for fitting current–voltage curves of planar heterojunction perovskite solar cells. *Nano-Micro Letters*, 10(1):5, 2018.

[249] Seungchan Ryu, Jun Hong Noh, Nam Joong Jeon, Young Chan Kim, Woon Seok Yang, Jangwon Seo, and Sang Il Seok. Voltage output of efficient perovskite solar cells with high open-circuit voltage and fill factor. *Energy & Environmental Science*, 7(8):2614–2618, 2014.

[250] Guichuan Xing, Nripan Mathews, Shuangyong Sun, Swee Sien Lim, Yeng Ming Lam, Michael Grätzel, Subodh Mhaisalkar, and Tze Chien Sum. Long-range balanced electron-and hole-transport lengths in organic-inorganic ch3nh3pbi3. *Science*, 342(6156):344–347, 2013.

[251] Weijun Ke, Guojia Fang, Jiawei Wan, Hong Tao, Qin Liu, Liangbin Xiong, Pingli Qin, Jing Wang, Hongwei Lei, Guang Yang, et al. Efficient hole-blocking layer-free planar halide perovskite thin-film solar cells. *Nature communications*, 6:6700, 2015.

[252] Juan Dong, Jiangjian Shi, Dongmei Li, Yanhong Luo, and Qingbo Meng. Controlling the conduction band offset for highly efficient zno nanorods based perovskite solar cell. *Applied Physics Letters*, 107(7):073507, 2015.

[253] Yukun Wang, Dezhi Yang, Xiaokang Zhou, Saad M Alshehri, Tansir Ahamad, Agafonov Vadim, and Dongge Ma. Vapour-assisted multi-functional perovskite thin films for solar cells and photodetectors. *Journal of Materials Chemistry C*, 4(31):7415–7419, 2016.

[254] Jing Chen, Jia Xu, Li Xiao, Bing Zhang, Songyuan Dai, and Jianxi Yao. Mixed-organic-cation (fa) x (ma) 1–x pbi3 planar perovskite solar cells with 16.48% efficiency via a low-pressure vapor-assisted solution process. *ACS applied materials & interfaces*, 9(3):2449–2458, 2017.

[255] Martin A Green. Solar cell fill factors-general graph and empirical expressions. *Solid State Electronics*, 24:788, 1981.

[256] Martin A Green. Accuracy of analytical expressions for solar cell fill factors. *Solar Cells*, 7(3):337–340, 1982.

[257] Boyuan Qi and Jizheng Wang. Fill factor in organic solar cells. *Physical Chemistry Chemical Physics*, 15(23):8972–8982, 2013.

[258] daily-data met eireann. http://archive.met.ie/climate/daily-data.asp. Accessed: 2018-09-11.

[259] James M Ball, Michael M Lee, Andrew Hey, and Henry J Snaith. Low-temperature processed meso-superstructured to thin-film perovskite solar cells. *Energy & Environmental Science*, 6(6):1739–1743, 2013.

[260] Bert Conings, Linny Baeten, Christopher De Dobbelaere, Jan D'Haen, Jean Manca, and Hans-Gerd Boyen. Perovskite-based hybrid solar cells exceeding 10% efficiency with high reproducibility using a thin film sandwich approach. *Advanced Materials*, 26(13):2041–2046, 2014.

[261] Chun-Yu Chang, Cheng-Ya Chu, Yu-Ching Huang, Chien-Wen Huang, Shuang-Yuan Chang, Chien-An Chen, Chi-Yang Chao, and Wei-Fang Su. Tuning perovskite morphology by polymer additive for high efficiency solar cell. *ACS applied materials & interfaces*, 7(8):4955–4961, 2015.

[262] Jiangjian Shi, Juan Dong, Songtao Lv, Yuzhuan Xu, Lifeng Zhu, Junyan Xiao, Xin Xu, Huijue Wu, Dongmei Li, Yanhong Luo, et al. Hole-conductor-free perovskite organic lead iodide heterojunction thin-film solar cells: High efficiency and junction property. *Applied Physics Letters*, 104(6):063901, 2014.

[263] Sigalit Aharon, Bat El Cohen, and Lioz Etgar. Hybrid lead halide iodide and lead halide bromide in efficient hole conductor free perovskite solar cell. *The Journal of Physical Chemistry C*, 118(30):17160–17165, 2014.

[264] Feng Hao, Constantinos C Stoumpos, Zhao Liu, Robert PH Chang, and Mercouri G Kanatzidis. Controllable perovskite crystallization at a gas–solid interface for hole conductor-free solar cells with steady power conversion efficiency over 10%. *Journal of the American Chemical Society*, 136(46):16411–16419, 2014.

[265] Antonio Abate, Tomas Leijtens, Sandeep Pathak, Joël Teuscher, Roberto Avolio, Maria E Errico, James Kirkpatrik, James M Ball, Pablo Docampo, Ian McPherson, et al. Lithium salts as "redox active" p-type dopants for organic semiconductors and their

impact in solid-state dye-sensitized solar cells. *Physical Chemistry Chemical Physics*, 15(7):2572–2579, 2013.

[266] Mikkel Jørgensen, Kion Norrman, Suren A Gevorgyan, Thomas Tromholt, Birgitta Andreasen, and Frederik C Krebs. Stability of polymer solar cells. *Advanced materials*, 24(5):580–612, 2012.

[267] Sarah Holliday, Raja Shahid Ashraf, Andrew Wadsworth, Derya Baran, Syeda Amber Yousaf, Christian B Nielsen, Ching-Hong Tan, Stoichko D Dimitrov, Zhengrong Shang, Nicola Gasparini, et al. High-efficiency and air-stable p3ht-based polymer solar cells with a new non-fullerene acceptor. *Nature communications*, 7:11585, 2016.

[268] Holger Hintz, H-J Egelhaaf, Larry Luer, Jens Hauch, Heiko Peisert, and Thomas Chassé. Photodegradation of p3ht- a systematic study of environmental factors. *Chemistry of Materials*, 23(2):145–154, 2010.

[269] LJA Koster, VD Mihailetchi, and PWM Blom. Bimolecular recombination in polymer/fullerene bulk heterojunction solar cells. *Applied physics letters*, 88(5):052104, 2006.

[270] Mariano Campoy-Quiles, Toby Ferenczi, Tiziano Agostinelli, Pablo G Etchegoin, Youngkyoo Kim, Thomas D Anthopoulos, Paul N Stavrinou, Donal DC Bradley, and Jenny Nelson. Morphology evolution via self-organization and lateral and vertical diffusion in polymer: fullerene solar cell blends. *Nature materials*, 7(2):158, 2008.

[271] Xin Song, Nicola Gasparini, Long Ye, Huifeng Yao, Jianhui Hou, Harald Ade, and Derya Baran. Controlling blend morphology for ultrahigh current density in non-fullerene acceptor-based organic solar cells. *ACS Energy Letters*, 3(3):669–676, 2018.

[272] Sondra L Hellstrom, Hang Woo Lee, and Zhenan Bao. Polymer-assisted direct deposition of uniform carbon nanotube bundle networks for high performance transparent electrodes. *Acs Nano*, 3(6):1423–1430, 2009.

[273] Matthew A Meitl, Yangxin Zhou, Anshu Gaur, Seokwoo Jeon, Monica L Usrey, Michael S Strano, and John A Rogers. Solution casting and transfer printing single-walled carbon nanotube films. *Nano Letters*, 4(9):1643–1647, 2004.

[274] Neerja Saran, Kunjal Parikh, Dong-Seok Suh, Edgar Munoz, Harsha Kolla, and Sanjeev K Manohar. Fabrication and characterization of thin films of single-walled carbon nanotube bundles on flexible plastic substrates. *Journal of the American Chemical Society*, 126(14):4462–4463, 2004.

[275] Yoshiaki Abe, Ryo Tomuro, and Masahito Sano. Highly efficient direct current electrodeposition of single-walled carbon nanotubes in anhydrous solvents. *Advanced Materials*, 17(18):2192–2194, 2005.

[276] Xuesong Li, Weiwei Cai, Jinho An, Seyoung Kim, Junghyo Nah, Dongxing Yang, Richard Piner, Aruna Velamakanni, Inhwa Jung, Emanuel Tutuc, et al. Large-area synthesis of high-quality and uniform graphene films on copper foils. *science*, 324(5932):1312–1314, 2009.

[277] Zhuangchun Wu, Zhihong Chen, Xu Du, Jonathan M Logan, Jennifer Sippel, Maria Nikolou, Katalin Kamaras, John R Reynolds, David B Tanner, Arthur F Hebard, et al. Transparent, conductive carbon nanotube films. *Science*, 305(5688):1273–1276, 2004.

[278] Daihua Zhang, Koungmin Ryu, Xiaolei Liu, Evgueni Polikarpov, James Ly, Mark E Tompson, and Chongwu Zhou. Transparent, conductive, and flexible carbon nanotube films and their application in organic light-emitting diodes. *Nano letters*, 6(9):1880–1886, 2006.

[279] Samuli Kivistö, Tommi Hakulinen, Antti Kaskela, Brad Aitchison, David P Brown, Albert G Nasibulin, Esko I Kauppinen, Antti Härkönen, and Oleg G Okhotnikov. Carbon nanotube films for ultrafast broadband technology. *Optics express*, 17(4):2358–2363, 2009.

[280] Sukanta De, Philip E Lyons, Sophie Sorel, Evelyn M Doherty, Paul J King, Werner J Blau, Peter N Nirmalraj, John J Boland, Vittorio Scardaci, Jerome Joimel, et al. Transparent, flexible, and highly conductive thin films based on polymer- nanotube composites. *Acs Nano*, 3(3):714–720, 2009.

[281] Frank Hennrich, Sergei Lebedkin, Sharali Malik, Joseph Tracy, Matthias Barczewski, Harald Rösner, and Manfred Kappes. Preparation, characterization and applications of free-standing single walled carbon nanotube thin films. *Physical Chemistry Chemical Physics*, 4(11):2273–2277, 2002.

[282] Ji Won Suk, Alexander Kitt, Carl W Magnuson, Yufeng Hao, Samir Ahmed, Jinho An, Anna K Swan, Bennett B Goldberg, and Rodney S Ruoff. Transfer of cvd-grown monolayer graphene onto arbitrary substrates. *ACS nano*, 5(9):6916–6924, 2011.

[283] Yangxin Zhou, Liangbing Hu, and George Grüner. A method of printing carbon nanotube thin films. *Applied physics letters*, 88(12):123109, 2006.

[284] Jie Song, Fong-Yu Kam, Rui-Qi Png, Wei-Ling Seah, Jing-Mei Zhuo, Geok-Kieng Lim, Peter KH Ho, and Lay-Lay Chua. A general method for transferring graphene onto soft surfaces. *Nature nanotechnology*, 8(5):356, 2013.

[285] Sukanta De, Thomas M Higgins, Philip E Lyons, Evelyn M Doherty, Peter N Nirmalraj, Werner J Blau, John J Boland, and Jonathan N Coleman. Silver nanowire networks as flexible, transparent, conducting films: extremely high dc to optical conductivity ratios. *ACS nano*, 3(7):1767–1774, 2009.

[286] Goki Eda, Giovanni Fanchini, and Manish Chhowalla. Large-area ultrathin films of reduced graphene oxide as a transparent and flexible electronic material. *Nature nanotechnology*, 3(5):270, 2008.

[287] Yenny Hernandez, Valeria Nicolosi, Mustafa Lotya, Fiona M Blighe, Zhenyu Sun, Sukanta De, IT McGovern, Brendan Holland, Michele Byrne, Yurii K Gun'Ko, et al. High-yield production of graphene by liquid-phase exfoliation of graphite. *Nature nanotechnology*, 3(9):563, 2008.

[288] Jonathan N Coleman, Mustafa Lotya, Arlene O'Neill, Shane D Bergin, Paul J King, Umar Khan, Karen Young, Alexandre Gaucher, Sukanta De, Ronan J Smith, et al. Two-dimensional nanosheets produced by liquid exfoliation of layered materials. *Science*, 331(6017):568–571, 2011.

[289] Valeria Nicolosi, Manish Chhowalla, Mercouri G Kanatzidis, Michael S Strano, and Jonathan N Coleman. Liquid exfoliation of layered materials. *Science*, 340(6139):1226419, 2013.

[290] Keith R Paton, Eswaraiah Varrla, Claudia Backes, Ronan J Smith, Umar Khan, Arlene O'Neill, Conor Boland, Mustafa Lotya, Oana M Istrate, Paul King, et al. Scalable production of large quantities of defect-free few-layer graphene by shear exfoliation in liquids. *Nature materials*, 13(6):624, 2014.

[291] Yong Zhang, John J Magan, and Werner J Blau. A general strategy for hybrid thin film fabrication and transfer onto arbitrary substrates. *Scientific reports*, 4:4822, 2014.

[292] Shane D Bergin, Zhenyu Sun, Philip Streich, James Hamilton, and Jonathan N Coleman. New solvents for nanotubes: approaching the dispersibility of surfactants. *The Journal of Physical Chemistry C*, 114(1):231–237, 2009.

[293] Adrian Nish, Jeong-Yuan Hwang, James Doig, and Robin J Nicholas. Highly selective dispersion of single-walled carbon nanotubes using aromatic polymers. *Nature nanotechnology*, 2(10):640, 2007.

[294] T Schuettfort, HJ Snaith, A Nish, and RJ Nicholas. Synthesis and spectroscopic characterization of solution processable highly ordered polythiophene–carbon nanotube nanohybrid structures. *Nanotechnology*, 21(2):025201, 2009.

[295] Nanditha M Dissanayake and Zhaohui Zhong. Unexpected hole transfer leads to high efficiency single-walled carbon nanotube hybrid photovoltaic. *Nano letters*, 11(1):286–290, 2010.

[296] G Dinesha MR Dabera, KDG Imalka Jayawardena, MR Ranga Prabhath, Iskandar Yahya, Y Yuan Tan, N Aamina Nismy, Hidetsugu Shiozawa, Markus Sauer, G Ruiz-Soria, Paola Ayala, et al. Hybrid carbon nanotube networks as efficient hole extraction layers for organic photovoltaics. *ACS nano*, 7(1):556–565, 2012.

[297] Severin N Habisreutinger, Tomas Leijtens, Giles E Eperon, Samuel D Stranks, Robin J Nicholas, and Henry J Snaith. Carbon nanotube/polymer composites as a highly stable hole collection layer in perovskite solar cells. *Nano letters*, 14(10):5561–5568, 2014.

[298] Severin N Habisreutinger, Tomas Leijtens, Giles E Eperon, Samuel D Stranks, Robin J Nicholas, and Henry J Snaith. Enhanced hole extraction in perovskite solar cells through carbon nanotubes. *The journal of physical chemistry letters*, 5(23):4207–4212, 2014.

[299] Molang Cai, Vincent Tiing Tiong, Tubuxin Hreid, John Bell, and Hongxia Wang. An efficient hole transport material composite based on poly (3-hexylthiophene) and bamboo-structured carbon nanotubes for high performance perovskite solar cells. *Journal of Materials Chemistry A*, 3(6):2784–2793, 2015.

[300] Kerttu Aitola, Kári Sveinbjörnsson, Juan-Pablo Correa-Baena, Antti Kaskela, Antonio Abate, Ying Tian, Erik MJ Johansson, Michael Grätzel, Esko I Kauppinen, Anders Hagfeldt, et al. Carbon nanotube-based hybrid hole-transporting material and selective contact for high efficiency perovskite solar cells. *Energy & Environmental Science*, 9(2):461–466, 2016.

[301] Feijiu Wang, Masaru Endo, Shinichiro Mouri, Yuhei Miyauchi, Yutaka Ohno, Atsushi Wakamiya, Yasujiro Murata, and Kazunari Matsuda. Highly stable perovskite solar cells with an all-carbon hole transport layer. *Nanoscale*, 8(23):11882–11888, 2016.

[302] Xiaoli Zheng, Haining Chen, Zhanhua Wei, Yinglong Yang, He Lin, and Shihe Yang. High-performance, stable and low-cost mesoscopic perovskite (ch 3 nh 3 pbi 3) solar cells based on poly (3-hexylthiophene)-modified carbon nanotube cathodes. *Frontiers of Optoelectronics*, 9(1):71–80, 2016.

[303] Kerttu Aitola, Konrad Domanski, Juan-Pablo Correa-Baena, Kári Sveinbjörnsson, Michael Saliba, Antonio Abate, Michael Grätzel, Esko Kauppinen, Erik MJ Johansson, Wolfgang Tress, et al. High temperature-stable perovskite solar cell based on low-cost carbon nanotube hole contact. *Advanced Materials*, 29(17):1606398, 2017.

[304] Il Jeon, Seungju Seo, Yuta Sato, Clement Delacou, Anton Anisimov, Kazu Suenaga, Esko I Kauppinen, Shigeo Maruyama, and Yutaka Matsuo. Perovskite solar cells using carbon nanotubes both as cathode and as anode. *The Journal of Physical Chemistry C*, 121(46):25743–25749, 2017.

[305] Rachelle Ihly, Anne-Marie Dowgiallo, Mengjin Yang, Philip Schulz, Noah J Stanton, Obadiah G Reid, Andrew J Ferguson, Kai Zhu, Joseph J Berry, and Jeffrey L Blackburn. Efficient charge extraction and slow recombination in organic–inorganic perovskites capped with semiconducting single-walled carbon nanotubes. *Energy & Environmental Science*, 9(4):1439–1449, 2016.

[306] Florian Machui, Silke Rathgeber, Ning Li, Tayebeh Ameri, and Christoph J Brabec. Influence of a ternary donor material on the morphology of a p3ht: Pcbm blend for organic photovoltaic devices. *Journal of Materials Chemistry*, 22(31):15570–15577, 2012.

[307] Chad R Snyder, Ryan C Nieuwendaal, Dean M DeLongchamp, Christine K Luscombe, Prakash Sista, and Shane D Boyd. Quantifying crystallinity in high molar mass poly (3-hexylthiophene). *Macromolecules*, 47(12):3942–3950, 2014.

[308] Christian Müller, Toby AM Ferenczi, Mariano Campoy-Quiles, Jarvist M Frost, Donal DC Bradley, Paul Smith, Natalie Stingelin-Stutzmann, and Jenny Nelson. Binary organic photovoltaic blends: a simple rationale for optimum compositions. *Advanced Materials*, 20(18):3510–3515, 2008.

[309] Sudip Malik and Arun K Nandi. Crystallization mechanism of regioregular poly (3-alkyl thiophene) s. *Journal of Polymer Science Part B: Polymer Physics*, 40(18):2073–2085, 2002.

[310] Cameron S Lee and Mark D Dadmun. Important thermodynamic characteristics of poly (3-hexyl thiophene). *Polymer*, 55(1):4–7, 2014.

[311] Felix Peter Vinzenz Koch, Martin Heeney, and Paul Smith. Thermal and structural characteristics of oligo (3-hexylthiophene) s (3ht) n, n= 4–36. *Journal of the American Chemical Society*, 135(37):13699–13709, 2013.

[312] Jin Yeong Na, Boseok Kang, Dong Hun Sin, Kilwon Cho, and Yeong Don Park. Understanding solidification of polythiophene thin films during spin-coating: Effects of spin-coating time and processing additives. *Scientific reports*, 5:13288, 2015.

[313] Donato Spoltore, Wibren D Oosterbaan, Samira Khelifi, John N Clifford, Aurelien Viterisi, Emilio Palomares, Marc Burgelman, Laurence Lutsen, Dirk Vanderzande, and Jean Manca. Effect of polymer crystallinity in p3ht: Pcbm solar cells on band gap trap states and apparent recombination order. *Advanced Energy Materials*, 3(4):466–471, 2013.

[314] Prasanta J Goutam, Dilip K Singh, Pravat K Giri, and Parameswar K Iyer. Enhancing the photostability of poly (3-hexylthiophene) by preparing composites with multiwalled carbon nanotubes. *The Journal of Physical Chemistry B*, 115(5):919–924, 2011.

[315] Pietro Camarda, Fabrizio Messina, Lavinia Vaccaro, Simonpietro Agnello, Gianpiero Buscarino, Reinhard Schneider, Radian Popescu, Dagmar Gerthsen, Roberto Lorenzi, Franco Mario Gelardi, et al. Luminescence mechanisms of defective zno nanoparticles. *Physical Chemistry Chemical Physics*, 18(24):16237–16244, 2016.

[316] Jiyong Lee, Mini Mol Menamparambath, Jae-Yeol Hwang, and Seunghyun Baik. Hierarchically structured hole transport layers of spiro-ometad and multiwalled carbon nanotubes for perovskite solar cells. *ChemSusChem*, 8(14):2358–2362, 2015.

[317] Weijun Ke, Guojia Fang, Qin Liu, Liangbin Xiong, Pingli Qin, Hong Tao, Jing Wang, Hongwei Lei, Borui Li, Jiawei Wan, et al. Low-temperature solution-processed tin oxide as an alternative electron transporting layer for efficient perovskite solar cells. *Journal of the American Chemical Society*, 137(21):6730–6733, 2015.

[318] Jiaxing Song, Enqiang Zheng, Ji Bian, Xiao-Feng Wang, Wenjing Tian, Yoshitaka Sanehira, and Tsutomu Miyasaka. Low-temperature sno 2-based electron selective contact for efficient and stable perovskite solar cells. *Journal of Materials Chemistry A*, 3(20):10837–10844, 2015.

[319] Jeremy Barbe, Max L Tietze, Marios Neophytou, Banavoth Murali, Erkki Alarousu, Abdulrahman El Labban, Mutalifu Abulikemu, Wan Yue, Omar F Mohammed, Iain

McCulloch, et al. Amorphous tin oxide as a low-temperature-processed electron-transport layer for organic and hybrid perovskite solar cells. *ACS applied materials & interfaces*, 9(13):11828–11836, 2017.

[320] Lijian Zuo, Hexia Guo, Sarthak Jariwala, Nicholas De Marco, Shiqi Dong, Ryan DeBlock, David S Ginger, Bruce Dunn, Mingkui Wang, Yang Yang, et al. Polymer-modified halide perovskite films for efficient and stable planar heterojunction solar cells. *Science advances*, 3(8):e1700106, 2017.

[321] Qiaogang Song, Tong Lin, Xue Sun, Bei Chu, Zisheng Su, Huishan Yang, Wenlian Li, and Chun Sing Lee. Electronic level alignment at an indium tin oxide/pbi2 interface and its applications for organic electronic devices. *ACS applied materials & interfaces*, 10(10):8909–8916, 2018.

[322] Qi Wang, Yuchuan Shao, Haipeng Xie, Lu Lyu, Xiaoliang Liu, Yongli Gao, and Jinsong Huang. Qualifying composition dependent p and n self-doping in ch3nh3pbi3. *Applied Physics Letters*, 105(16):163508, 2014.

[323] Duyen H Cao, Constantinos C Stoumpos, Christos D Malliakas, Michael J Katz, Omar K Farha, Joseph T Hupp, and Mercouri G Kanatzidis. Remnant pbi2, an unforeseen necessity in high-efficiency hybrid perovskite-based solar cells? *Apl Materials*, 2(9):091101, 2014.

[324] Jingjing Chang, Hai Zhu, Juanxiu Xiao, Furkan Halis Isikgor, Zhenhua Lin, Yue Hao, Kaiyang Zeng, Qing-Hua Xu, and Jianyong Ouyang. Enhancing the planar heterojunction perovskite solar cell performance through tuning the precursor ratio. *Journal of Materials Chemistry A*, 4(20):7943–7949, 2016.

[325] Roland Scheer and Hans-Werner Schock. *Chalcogenide photovoltaics: physics, technologies, and thin film devices*. John Wiley & Sons, 2011.

[326] Yulia Tolstova, Stefan T Omelchenko, Raymond E Blackwell, Amanda M Shing, and Harry A Atwater. Polycrystalline cu 2 o photovoltaic devices incorporating zn (o, s) window layers. *Solar Energy Materials and Solar Cells*, 160:340–345, 2017.

[327] Zhouhui Xia, Pengfei Li, Yuqiang Liu, Tao Song, Qiaoliang Bao, Shuit-Tong Lee, and Baoquan Sun. Black phosphorus induced photo-doping for high-performance organic-silicon heterojunction photovoltaics. *Nano Research*, 10(11):3848–3856, 2017.

[328] Florian Machui, Stefan Langner, Xiangdong Zhu, Steven Abbott, and Christoph J Brabec. Determination of the p3ht: Pcbm solubility parameters via a binary solvent

gradient method: Impact of solubility on the photovoltaic performance. *Solar Energy Materials and Solar Cells*, 100:138–146, 2012.

[329] Ki Kang Kim, Alfonso Reina, Yumeng Shi, Hyesung Park, Lain-Jong Li, Young Hee Lee, and Jing Kong. Enhancing the conductivity of transparent graphene films via doping. *Nanotechnology*, 21(28):285205, 2010.

[330] Dong Hee Shin, Jong Min Kim, Chan Wook Jang, Ju Hwan Kim, Sung Kim, and Suk-Ho Choi. Annealing effects on the characteristics of aucl3-doped graphene. *Journal of Applied Physics*, 113(6):064305, 2013.

[331] Dong Hee Shin, Jong Min Kim, Sang Woo Seo, Ju Hwan Kim, Sung Kim, and Suk-Ho Choi. Si heterojunction solar cells employing graphene transparent conductive electrodes co-doped with gold chlorides and silver nanowires. *Journal of Alloys and Compounds*, 726:1047–1052, 2017.

[332] Beatriz Mendoza-Sánchez, Bertold Rasche, Valeria Nicolosi, and Patrick S Grant. Scaleable ultra-thin and high power density graphene electrochemical capacitor electrodes manufactured by aqueous exfoliation and spray deposition. *Carbon*, 52:337–346, 2013.

[333] Zhu Xinghua, Yang Dingyu, Wei Zhaorong, Sun Hui, Wang Zhiguo, and Zu Xiaotao. Photoconductive properties of lead iodide films prepared by electron beam evaporation. *Journal of Semiconductors*, 31(8):083002, 2010.

[334] Yifang Wang, Jie Zhang, Jia Huang, Haoyu Zhang, and Zhiyong Fu. A lead-iodide based single crystal semiconductor: exploring multi-orientation photoconductive behaviour via intervening isopropyl viologen component between the inorganic [pb 2 i 6] 2- n wires. *CrystEngComm*, 20(15):2089–2092, 2018.

[335] Hyungcheol Back, Geunjin Kim, Junghwan Kim, Jaemin Kong, Tae Kyun Kim, Hongkyu Kang, Heejoo Kim, Jinho Lee, Seongyu Lee, and Kwanghee Lee. Achieving long-term stable perovskite solar cells via ion neutralization. *Energy & Environmental Science*, 9(4):1258–1263, 2016.

[336] Konrad Domanski, Juan-Pablo Correa-Baena, Nicolas Mine, Mohammad Khaja Nazeeruddin, Antonio Abate, Michael Saliba, Wolfgang Tress, Anders Hagfeldt, and Michael Gratzel. Not all that glitters is gold: metal-migration-induced degradation in perovskite solar cells. *ACS nano*, 10(6):6306–6314, 2016.

[337] Anyi Mei, Xiong Li, Linfeng Liu, Zhiliang Ku, Tongfa Liu, Yaoguang Rong, Mi Xu, Min Hu, Jiangzhao Chen, Ying Yang, et al. A hole-conductor–free, fully printable mesoscopic perovskite solar cell with high stability. *Science*, 345(6194):295–298, 2014.

[338] Christian Wirtz, Nina C Berner, and Georg S Duesberg. Large-scale diffusion barriers from cvd grown graphene. *Advanced Materials Interfaces*, 2(14):1500082, 2015.

[339] Jan-Kai Chang, Wei-Hsiang Lin, Jieh-I Taur, Ting-Hao Chen, Guo-Kai Liao, Tun-Wen Pi, Mei-Hsin Chen, and Chih-I Wu. Graphene anodes and cathodes: tuning the work function of graphene by nearly 2 ev with an aqueous intercalation process. *ACS applied materials & interfaces*, 7(31):17155–17161, 2015.

[340] J Červenka and CFJ Flipse. Fullerene monolayer formation by spray coating. *Nanotechnology*, 21(6):065302, 2010.

[341] Zheng Yan, Jun Yao, Zhengzong Sun, Yu Zhu, and James M Tour. Controlled ambipolar-to-unipolar conversion in graphene field-effect transistors through surface coating with poly (ethylene imine)/poly (ethylene glycol) films. *Small*, 8(1):59–62, 2012.